Reconstruction of the spatial and temporal variability of the surface to subsurface ocean dynamics of the North West Pacific during the Pliocene and Pleistocene

Dissertation

zur Erlangung des Doktorgrades
Dr. rer. nat.

der Mathematisch-Naturwissenschaftlichen Fakultät
der Christian-Albrechts-Universität zu Kiel

vorgelegt von

Lara Jacobi

Kiel, 2023

Erster Gutachter: Prof. Dr. Dirk Nürnberg

Zweiter Gutachter: Prof. Dr. Martin Frank

Eingereicht am: 6. März 2023
Tag der Disputation: 26. April 2023
Zum Druck genehmigt: November 2023

Eidesstattliche Erklärung

Hiermit erkläre ich des Eides statt, dass ich die vorliegende Abhandlung, abgesehen von der Beratung durch meine Betreuer, nach Inhalt und Form selbstständig erarbeitet habe und keine anderen als die von mir aufgeführten Quellen und Hilfsmittel verwendet wurden.

Diese Arbeit ist unter Einhaltung der Regeln guter wissenschaftlicher Praxis der Deutschen Forschungsgemeinschaft entstanden und wurde weder in Auszügen noch in ganzer Form an einer anderen Stelle im Rahmen eines Prüfungsverfahrens eingereicht.

Teile dieser Arbeit wurden zur Veröffentlichung in einer Fachzeitschrift eingereicht oder sind in Vorbereitung eingereicht zu werden.

Es wurde kein akademischer Grad entzogen.

Kiel, den 6. Dezember 2023

Lara Jacobi

Abstract

The North Pacific is an essential component of the global climate system as it acts as a significant natural carbon sink and neutralizes a part of the anthropogenic release of CO_2. The efficiency of the North Pacific carbon sink depends on a range of variable factors, including gyre circulation, the wind system, influences from tropical and subpolar regions, and internal reorganizations like stratification changes. A change of this complex system has likely contributed to the dramatic climate change at the onset of the Northern Hemisphere glaciation ~2.7 Ma years ago. Thus, a detailed investigation of the North Pacific ocean-climate system of the past is crucial to understand how the ongoing climate change influences this region and will affect future global climate. However, long-term sediment records from the pelagic North Pacific are rare and up to now only isolated regions have been investigated.

This thesis presents a set of six sediment cores from a meridional transect from Hess Rise to the subarctic North Pacific retrieved during R/V SONNE expeditions 202 in 2009 and 264 in 2018. The stratigraphy of these cores is based on benthic oxygen isotope records, which were correlated to the global benthic isotope stack LR04 (Lisiecki and Raymo, 2005), the correlation of prominent patterns in X-ray fluorescence (XRF) scans of various elements, radiocarbon dating, as well as magneto-, tephra- and bio-stratigraphic approaches. Pliocene and Pleistocene changes in (sub)-surface temperatures ((sub)-SST) and the ice-volume corrected stable oxygen istotopic composition of seawater ($\delta^{18}O_{sw\text{-}ivc}$; approximating salinities) are reconstructed via combined Mg/Ca and $\delta^{18}O$ analyses of the shallow-dwelling foraminifera *Globigerina bulloides* and the near-thermocline-dwelling *Neogloboquadrina pachyderma* and *incompta*. Changes in biological productivity are investigated via XRF-based Ba/Ti, Ca/Ti and Si/Ti ratios, $CaCO_3$ content and alkenone concentrations. The terrigenous input via wind is assessed via XRF-based Fe concentrations.

The new records reveal significantly different upper ocean conditions and a different productivity pattern in the western North Pacific during the Pliocene than during the Pleistocene. Higher SST and sub-SST in the late Pliocene at sites SO264-45 and -53 were linked to warmer global temperatures and less seasonality. A significant SST decrease with increasing latitude indicates that the frontal system separating the subpolar and subtropical gyres was either slightly shifted northward relative to its present position or was less pronounced than it is today. Moreover, it is confirmed that there has been no salinity-driven stratification (at least within the upper ~130 m of the water column) throughout the late Pliocene, yet we show that there was a constant thermocline. At ~2.7 Ma, a dramatic decrease in (sub)-SST and productivity at sites SO264-45 and -53 occurred while aeolian dust input increased due to increased wind speed or aridification of Asia, or both. We associate these changes with the intensification of Northern Hemisphere Glaciation (iNHG) and the onset of a permanent halocline that hindered nutrients from reaching the surface layer and with increased seasonality. During the Pleistocene, productivity was lower than during the Pliocene. Productivity and carbonate deposition of the northern sites SO264-45, -53. -55, -66 increased during the deglaciations and early interglacials of the Pleistocene, followed by a decrease during late inter-glacials and early glacials. This pattern was closely linked to variations of nutrient availability and utilization induced by changes in the supply of nutrients from the sub-polar marginal seas, changes in stratification, or both. The contrasting development of dust supply and productivity at these sites during the Pliocene and Pleistocene suggests that dust fertilization neither caused the high primary productivity in the North Pacific during the late Pliocene nor limited the primary productivity during the late Pleistocene. The records south of 40°N (SO264-15 and SO202-37) show different productivity patterns that reflect the different nutrient regimes of the subtropical and subpolar gyre. Further, the carbonate deposition at southernmost site SO202-37 is only weakly correlated to the productivity signals but instead follows deep Pacific carbonate chemistry changes, which caused variations in carbonate dissolution.

Moreover, abrupt and pronounced (~4°C) changes in SST at site SO264-45 (at 480 ka and 280 ka) indicate that the Subarctic Front (SAF) was temporally located north of this site. We propose that such shifts of the frontal system have been induced by changes in the strength of the Kuroshio Extension, e.g., caused by sustained La Niña-like conditions in the tropical Pacific, which led to enhanced transport of tropical ocean heat into the Kuroshio-Oyashio transition zone via the Kuroshio Current. These shifts, however, did not affect the productivity at this site, which continuously followed the typical sub-polar gyre pattern.

Kurzfassung

Der Nordpazifik ist ein wesentlicher Bestandteil des globalen Klimasystems, da er heute als bedeutende natürliche Kohlenstoffsenke fungiert und einen Teil der vom Menschen verursachten Freisetzung von CO_2 neutralisiert. Die Effizienz des Nordpazifiks als Kohlenstoffsenke hängt von verschiedenen variablen Faktoren ab, darunter die Gyrenzirkulation, das Windsystem, Einflüsse aus tropischen und subpolaren Regionen und Reorganisationen der internen Struktur der Wassersäule und der Stratifizierung. Eine Veränderung dieses komplexen Systems hat wahrscheinlich zu dem dramatischen Klimawandel zu Beginn der Vergletscherung der nördlichen Hemisphäre vor ~2,7 Mio. Jahren beigetragen. Daher ist eine detaillierte Untersuchung des Nordpazifischen Ozean-Klimasystems der Vergangenheit von entscheidender Bedeutung, um zu verstehen, wie der aktuelle Klimawandel diese Region beeinflussen und sich auf das zukünftige globale Klima auswirken wird. Sedimentkerne aus dem pelagischen Nordpazifik, die zeitlich weit zurückreichen, sind jedoch selten daher wurden bisher nur wenige, isolierte Regionen untersucht.

In dieser Arbeit werden sechs Sedimentkerne vorgestellt, die auf den FS-SONNE Expeditionen 202 (2009) und 264 (2018) gewonnen wurden und einen meridionalen Transekt vom Hess Rise bis zum subarktischen Nordpazifik abdecken. Die Stratigraphie dieser Kerne basiert auf benthischen Sauerstoff-Isotopendaten, die mit dem globalen benthischen Sauerstoffisotopen Datensatz LR04 (Lisiecki und Raymo, 2005) korreliert wurden, sowie der Korrelation auffälliger Muster in Röntgenfluoreszenz (XRF)-Scans verschiedener Elemente, Radiocarbondatierungen und magneto-, tephra- und biostratigraphischen Ansätzen. Pliozäne und pleistozäne Veränderungen der (Sub-)Oberflächentemperatur ((Sub-)SST) und die Eisvolumen korrigeierte stabile Sauerstoffisotopenzusammensetzung des Wassers ($\delta^{18}O_{sw\text{-}ivc;}$ in Abhängigkeit von der Salinität) werden durch kombinierte Mg/Ca- und $\delta^{18}O$-Analysen der oberflächennah lebenden Foraminifere *Globigerina bulloides* und der nahe der Thermokline lebenden *Neogloboquadrina pachyderma* und *incompta* rekonstruiert. Veränderungen in der biologischen Produktivität werden anhand von XRF-basierten Ba/Ti-, Ca/Ti- und Si/Ti-Verhältnissen, $CaCO_3$-–Gehalt und Alkenon-Konzentrationen untersucht. Der terrigene Eintrag durch Wind wird mittels XRF-basierten Fe-Gehalten ermittelt.

Die neuen Aufzeichnungen zeigen, dass sich die Eigenschaften des Oberflächenwassers und die marine Primärproduktivität im westlichen Nordpazifik im Pliozän deutlich vom Pleistozän unterschieden. Höhere SST und Sub-SST-Werte im späten Pliozän an den Kernlokationen SO264-45 und -53 waren mit wärmeren globalen Temperaturen und geringerer Saisonalität assoziiert. Ein deutlicher SST-Abfall mit zunehmender geographischer Breite deutet darauf hin, dass das Frontensystem, welches die subpolare und subtropische Gyre trennt, entweder relativ zu seiner heutigen Position leicht nach Norden verschoben oder weniger ausgeprägt war, als heute. Darüber hinaus wird bestätigt, dass es während des gesamten späten Pliozäns keine salzgehaltsbedingte Stratifizierung (zumindest in den oberen ~130 m), aber eine konstante Thermokline gab. Vor ~2,7 Ma kam es an den Kernlokationen von SO264-45 und -53 zu einer dramatischen Abnahme der (Sub)-SST und der Produktivität, während der äolische Staubeintrag als Folge von höhreren Windgeschwindigkeiten, einer Aridifizierung von Asien oder einer Kombination der beiden Prozesse zunahm. Diese Veränderungen werden mit der

Intensivierung der Vergletscherung der nördlichen Hemisphäre (iNHG) und dem Auftreten einer permanenten Halokline in Verbindung gebracht. Diese verhinderte, dass Nährstoffe die Oberflächenschicht erreichten und verstärkte die Saisonalität.

Während des Pleistozäns war die Produktivität geringer als im Pliozän. An den nördlichen Kernlokationen SO264-45, -53. -55, -66 nahmen die Produktivität und die Karbonatablagerung während den späten Deglazialen und frühen Interglazialen des Pleistozäns zu, gefolgt von einem Rückgang am Ende der Interglaziale und dem Beginn der Glaziale. Dieses Muster war eng gekoppelt an Veränderungen der Nährstoffverfügbarkeit und -nutzung, die entweder durch Änderungen des Nährstofftransports aus den subpolaren Randmeeren oder der Schichtung oder durch eine Kombination aus beidem gesteuert wurden. Die gegensätzliche Entwicklung von Staubeintrag und Produktivität während des Pliozäns und Pleistozäns an diesen Lokationen deutet darauf hin, dass Staubdüngung weder die hohe Primärproduktivität im Nordpazifik während des späten Pliozäns verursacht noch die Primärproduktivität während des späten Pleistozäns eingeschränkt hat. Die Sedimentkerne südlich von 40°N (SO264-15 und SO202-37) zeigen ein anderes Produktivitätsmuster, das die unterschiedlichen Nährstoffregime der subtropischen und subpolaren Gyre widerspiegelt. Die Karbonatdeposition des Kerns SO202-37 korreliert nur schwach mit den Produktivitätssignalen, folgt dafür aber den Veränderungen der Karbonatchemie im tiefen Pazifik und hängt daher mit Schwankungen der Karbonatlösung zusammen.

Darüber hinaus deuten abrupte und ausgeprägte (~4°C) Veränderungen der SST an der Lokation von Kern SO264-45 (bei 480 ka und 280 ka) darauf hin, dass sich die Subarktische Front (SAF) zeitweise nördlich dieser Kernposition befand. Es wird vorgeschlagen, dass solche Verschiebungen des Frontensystems durch Veränderungen in der Stärke der Kuroshio-Extension verursacht wurden, z.B. hervorgerufen durch anhaltende La-Niña-ähnliche Bedingungen im tropischen Pazifik, die zu einem verstärkten Transport tropischer Wärme in die Kuroshio-Oyashio-Übergangszone über den Kuroshio-Strom führten. Diese mögliche Verschiebung wirkte sich jedoch nicht auf die Produktivität an dieser Lokation aus, die kontinuierlich dem typischen Muster der subpolaren Gyre folgte.

Contents

1. Introduction

1.1. Motivation and principal objectives

The current climate change has long since ceased to be a topic that is only discussed by scientists and nowadays appears in the media essentially every day. Even children act as climate activists as they understand that the current conditions do not represent natural changes of the climate system but are drastically influenced by human activities. Although the scientific community studying climate change has steadily increased since the First World Climate Conference (1979) in Geneva (Pachauri et al., 2014), there is still a lack of knowledge when it comes to understanding the global climate system, especially internal amplification mechanisms that contribute to the natural climate change (Pachauri et al., 2014). To understand, predict and take action against anthropogenic climate change, it is, therefore, crucial to understand the entire climate system. One key method is the investigation of past climate variability beyond instrumental records. These investigations provide the necessary information for model studies of future climate. Marine sediments are one of the most important archives of past climatic and environmental conditions. As the North Pacific can act as a sink or source of atmospheric carbon dioxide (CO_2), it plays an important role for both current and past climate variations. Therefore, the investigation of upper ocean paleoceanography and its controlling factors as well as biological productivity, which influences the ocean-atmosphere greenhouse gas exchange, will contribute to a more comprehensive understanding of the great jigsaw called earth's climate.

The modern Pacific, with a surface area of ~47% of the world's ocean, represents 32% of the net global ocean CO_2 sink (Takahashi et al., 2009; Tanhua et al., 2013). While the equatorial Pacific generally act as a CO_2 source and the areas north and south of 50°N/50°S only contribute weakly to the overall CO_2 reduction, the areas between ~15 and ~50°S and ~15 and ~50°N act as strong sinks (Takahashi et al., 2009; Tanhua et al., 2013). Under modern conditions, nutrient- and CO_2-rich waters reach the surface due to Ekman divergence (Gargett, 1991; Talley, 1995). This way, previously sequestered CO_2 is released into the atmosphere, and phytoplankton growth is stimulated. Through photosynthesis during phytoplankton growth, the upwelled nutrients and CO_2 are absorbed from the water masses. The eventual export of organic matter subsequently lowers the pCO_2 of surface waters, causing the surface layer to reabsorb a portion of the CO_2 that was initially released from the upwelled water (Jaccard et al., 2010). Therefore, the strength and efficiency of the biological carbon pump that control the uptake of CO_2 are linked to plankton composition and productivity, which are altered under changing ocean conditions. In the modern subarctic North Pacific, the upwelling of nutrient-rich waters to the surface is dampened by strong stratification (Warren, 1983; Gargett, 1991; Haug et al., 1999). This stratification, however, has not always been as strong as under modern conditions. In the Pliocene, for example, a lack of permanent salinity-driven stratification has been associated with higher nutrient supply to the surface ocean and higher primary productivity (Haug et al., 1999; Sigman et al., 2004).

Studying the more recent history of the climate during the late Pleistocene can provide valuable information on rapid changes in the climate system during glacial-interglacial cycles and thus help to gain a better understanding of processes that have driven the climate. Another advantage of studying the Pleistocene is that the development of age models for sediment cores or dating of individual samples is easier for the more recent past than for older epochs. Moreover, there is widespread availability of microfossils from the Pleistocene, which are better preserved than in older epochs. However, analogies to the ongoing climate change have not existed during the Pleistocene, as modern CO_2 concentrations even exceed CO_2 concentrations of peak interglacials of the Pleistocene (Bereiter et al., 2014; Vega et al., 2020). Therefore, it is necessary to go further back in time, e.g. to the Pliocene. The Pliocene is the most recent epoch with atmospheric CO_2 concentrations comparable to modern post-industrial values (Bereiter et al., 2014; Chalk et al., 2017; Vega et al., 2020), while the tectonic boundary conditions of the oceans were similar to modern ones. The high atmospheric CO_2 concentrations in the Pliocene were accompanied by ~2-3°C higher global mean temperatures and ~20 m higher sea level than during pre-industrial times (Dutton et al., 2015; Dumitru et al., 2019). Thus, in order to understand future climate change, it is helpful to understand how the Pliocene climate worked.

Despite the great importance of the North Pacific for the ocean-atmosphere carbon interaction, previous studies covering glacial-interglacial cycles of the Pleistocene or even reaching back into the Pliocene are rare. Moreover, the few existing sites are limited to coastal regions and few isolated areas from the subarctic Pacific, Hess Rise or Shatsky Rise. The great depth of the North Pacific is responsible for this limited spatial coverage as the availability of carbonate-bearing sediment records is restricted to, e.g., seamount areas, where the water depth does not exceed the depth of the calcite compensation depth, which lies at about ~4000 m in the open North Pacific (Chen et al., 2021). Yet carbonate-bearing sediments are a valuable tool for reconstructions of the past state of the ocean as, e.g., the foraminiferal calcite is a well-established signal carrier ($\delta^{18}O$, $AMS^{14}C$) for the development of age models and used as a proxy for e.g., paleo water-temperature. Another constraint are the generally low sedimentation rates in the North Pacific, which makes high-resolution records rare and represents an obstacle for developing precise age models.

In this thesis, I aim to contribute to fill the gap in the spatial resolution of sediment archives from the North Pacific and shed light on the long-term evolution of upper ocean hydrography as well as changes in primary productivity spanning the time from the late Pliocene to the late Pleistocene and to link them to regional variations in the North Pacific as well as large-scale variations. For this, a new set of six sediment records from the Emperor Seamount Chain and Hess rise is used which may eventually be part of a new reference transect for the North Pacific. Via geochemical and sedimentological proxy data, age models are developed and past (sub)surface temperature, $\delta^{18}O_{sw\text{-}ivc}$ (approximating salinity), export production, and dust supply via wind are reconstructed. By combining these proxy records, we address the following questions:

- Which are the main driving mechanisms for past primary productivity in the pelagic North Pacific? To what extent did eolian dust fertilization changes influence primary productivity and carbon export efficiency? How did shifts in the frontal system in the Kuroshio-Oyashio transition zone impact primary productivity?

- Are there different past productivity regimes along the meridional transect between the Hess Rise and the Emperor Seamount Chain north of the SAF? To what extent did carbonate productivity and preservation change along this transect?
- What are the main drivers of past upper ocean circulation in the pelagic North Pacific? To what extent do climate variations on glacial-interglacial timescales, changes in the tropical Pacific, and variations of the westerly winds influence upper ocean circulation at the northern boundary of the Kuroshio-Oyashio transition zone?
- What was driving the primary productivity at the northern boundary of the Kuroshio Oyashio transition zone in the Pliocene, and what were the differences between the Pliocene and Pleistocene primary productivity in this region?
- How did upper ocean characteristics change during the fundamental reorganization of the global climate in the late Pliocene? Have there also been significant changes in the frontal system of the Kuroshio-Oyahio transition zone?

1.2. Oceanography of the North Pacific and site selection

Ocean circulation exerts a fundamental control on heat transport, marine biological productivity, and ocean-atmosphere CO_2 exchange (Sigman et al., 2010); thus, it is crucial to understand upper ocean circulation in the North Pacific. Today the North Pacific is dominated by two large-scale wind-driven gyre systems: the cyclonic subpolar gyre (SPG) in the north and the anticyclone subtropical gyre (STG) in the south (Qiu, 2002; Wang et al., 2020). The subpolar gyre can further be separated into the Alaskan gyre to the east and the western subarctic gyre to the west. The latter hosts a strong western boundary current, the Oyashio Current (figure 1.1). It originates from the East Kamchatka Current and is further fed by cold, low saline, nutrient-rich water from the Bering Sea and the Sea of Okhotsk. At around 40°N, the Oyashio Current splits, and one path contributes to the northeastward flowing Subarctic Current (Qiu, 2019). The productivity of the Oyashio Current-dominated region is limited by a strong salinity-driven stratification and light limitation. However, in winter, nutrients reach the surface through wind-induced mixing, which causes extensive phytoplankton blooms in spring when the light limitation declines (Liu et al., 2004; Yatsu et al., 2013).

In the subtropical gyre a strong western boundary current also prevails, the Kuroshio Current (figure 1.1). It originates from the warm, saline Pacific North Equatorial Current (NEC) and transports heat from the West Pacific warm pool (WPWP) to the northern regions. The strength and velocity transport of the Kuroshio Current is influenced by the main driver of upper ocean circulation in the tropical Pacific, the El Niño-Southern Oscillation, ENSO (Joh & Di Lorenzo, 2019; Hu et al., 2015). After separating from the Japanese coast at 35°N, the Kuroshio Current enters the open basin of the North Pacific Ocean, where it is renamed and called the Kuroshio Extension (Qiu, 2002). Primary productivity in the Kuroshio Current-dominated regions is generally lower than in the Oyashio Current-dominated regions (Yatsu et al., 2013) and limited by nutrient availability (Polovina et al., 1995). Moreover, the water column is less stratified throughout the year. Thus, nutrient upwelling through wintertime mixing does not result in as intense spring phytoplankton blooms as in the Oyashio Current regions (Polovina et al., 1995; Yatsu et al., 2013).

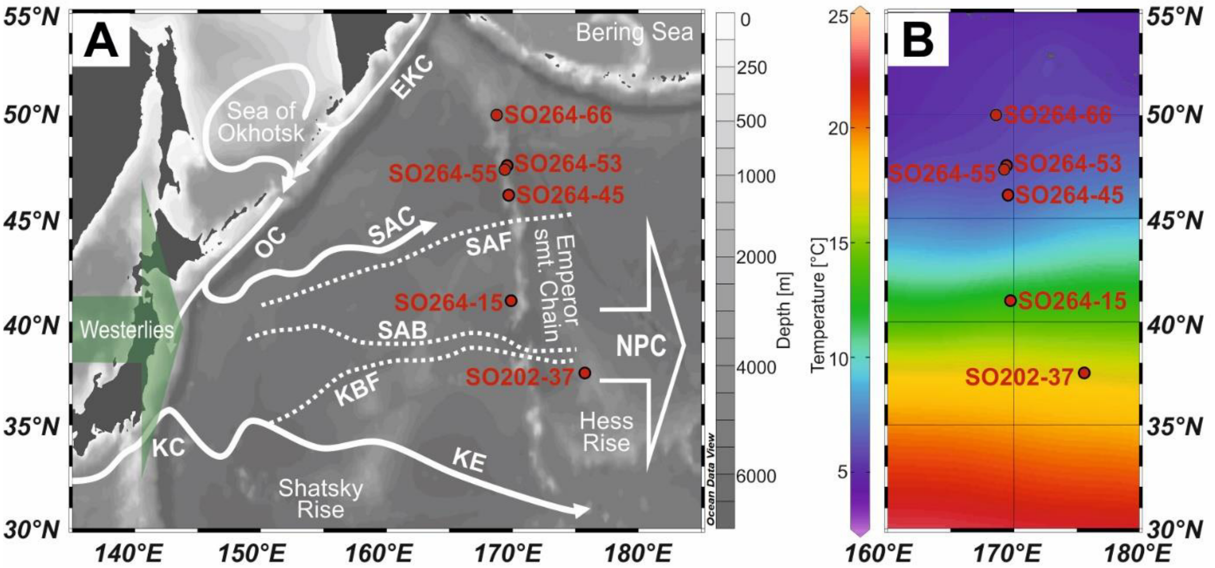

Figure 1.1 **A**: Bathymetric map illustrated with Ocean Data View (Schlitzer, 2019) showing the position of the core sites (red dots) of this thesis. Approximate paths and positions of major surface currents and fronts in the Kuroshio-Oyashio transition area are indicated based on Yasuda et al. (2003): EKC = East Kamchatka Current, KC = Kuroshio Current, KE= Kuroshio Extension, NPC = North Pacific Current, OC = Oyashio Current, SAC = Subarctic Current; KBF = Kuroshio Bifurcation Front, SAB = Subarctic Boundary, SAF = Subarctic Front. The modern position of the westerlies is indicated as green arrow. **B**: Temperature transect illustrated with Ocean Data View (Schlitzer, 2019) based on data from the World Ocean Atlas 2018 (Locarnini et al., 2018; Zweng et al., 2019).

Between the Kuroshio Current/Extension and the Oyashio/Subarctic Current, there is the Kuroshio-Oyashio transition zone, marked by pronounced latitudinal sea surface temperature, salinity, and nutrient gradients (figure 1.1). Several fronts occur that separate the two regimes: the Subarctic Front (SAF), which marks the northern end of the transitional zone (Favorite, 1976); the Subarctic Boundary (SAB), a near-surface salinity front south of the SAF (Yasuda, 2003) and the Kuroshio Bifurcation Front (KBF). The Kuroshio-Oyashio transition zone and its borders are characterized by numerous meanders and mesoscale eddies that form due to the dia- and isopycnal mixing between Kuroshio and Oyashio water with vertically different temperature, salinity, and velocity structures (Yasuda et al., 1996, 2002; Shimizu et al., 2001; Isoguchi et al., 2006; Mitnik et al., 2020). Due to this mixing, nutrients, mainly provided from the Oyashio Current, are upwelled and cause high primary productivity in the Kuroshio-Oyashio transition zone (Sasai et al., 2007; Yatsu et al., 2013).
Further, surface ocean circulation in the North Pacific is closely linked to atmospheric circulation, mainly the mid-latitude westerly winds. Although gyre circulation is primarily driven by wind (e.g. Howell et al., 2012), changes in both systems can significantly influence each other’s circulation patterns (Toggweiler et al., 2006).

In order to reconstruct the development of this highly variable region in the past we chose five sediment cores from the Emperor Seamount Chain and one core from Hess Rise retrieved during R/V SONNE expeditions SO264 in 2018 and SO202 in 2009, respectively. Detailed information of these cores are given in table 1.1, scientific chapters I-III, as well as the respective cruise reports (Gersonde, 2012; Nürnberg, 2018). Together these cores form a meridional transect spanning several oceanographic features indicated in figure 1.1. We selected these cores because they are not disturbed, retrieved in relatively shallow water depth (ensuring good carbon preservation) and allow the development of reliable age models. Three of the SO264 records (-45, -53 and -55) are from Minnetonka Seamount, located close to the modern positon of the SAF (figure 1.1). Thus, they enable the detailed investigation of shifts of the frontal system in the Kuroshio-Oyashio transition zone and the productivity in this highly variable region. SO264-66 is the northernmost core of our transect and located South of Detroit Seamount in the Oyashio current dominated regime, while SO264-15 is located further south at 'East of Ninigi Seamount' in the center of the Kuroshio-Oyashio transition zone. The southernmost core is SO202-37 from Hess Rise and is located in the southern part of the Kuroshio-Oyashio transition zone.

Table 1.1: Site information of sediment cores used in this thesis including site name, seamount, position, and water depth.

Site	Area/Seamount	Latitude (°N)	Longitue (°E)	Water depth (m)
SO264-66	South of Detroit	50°15.067'N	168°17.821'E	2751
SO264-53	Minnetonka	47°38.934'N	169°20.417'E	2325
SO264-55	Minnetonka	47°10.553'N	169°25.291'E	2936
SO264-45	Minnetonka	46°33.792'N	169°36.072'E	2425
SO264-15	East of Ninigi	41°36.917'N	170°25.340'E	3662
SO202-37	North of Hess Rise	37°46.07'N	176°16.13'E	3568

1.3. Paleoclimate reconstructions from proxy records

In order to investigate the questions and topics addressed in chapter 1.1, we use several proxies mainly based on the isotopic and elemental composition of the shells of foraminifera and the sediment composition revealed by X-ray fluorescence (XRF) core scanning. Yet, for some cores, also carbonate content (calculated from total carbon vs. total organic carbon), alkenone concentrations, and the percentage abundance of the sand fraction in the sediment were measured.

Foraminifera have a broad abundance in most marine environments with a continuous export flux of shells to the ocean floor and a high preservation potential in ocean sediments reaching back to the Lower Cretaceous (Imbrie and Kipp, 1971; Kucera et al., 2005; Schiebel and Hemleben, 2017). Therefore, foraminifera are highly suitable for paleoceanographic investigations. During their life cycle, foraminifera build their calcium carbonate shells using elements from ambient seawater. This way, they preserve the contemporaneous elemental and isotopic composition of the oceans, providing unique insights into the past surface and deep ocean conditions and thus, environmental changes (Kucera and Schönfeld, 2007; Schiebel and

Hemleben, 2017). The ratio of incorporated magnesium and calcium (Mg/Ca), for example, is mainly controlled by water temperature, for which it has become a well-established proxy (Nürnberg, 1995; Nürnberg et al., 1996; Lea et al., 1999). Yet also seawater salinity and carbonate chemistry, diagenetic effects like calcite dissolution and species-specific differences need to be considered when referring to past water temperature derived from Mg/Ca ratios of foraminifera (e.g. Gray & Evans, 2019; Lea et al., 1999; Nürnberg et al., 1996; Regenberg et al., 2006).

The ratio of the stable oxygen-isotopes ^{18}O and ^{16}O (δ^{18}O) is also linked to water temperature (e.g. Emiliani, 1955; Shackleton, 1967) but simultaneously connected to the isotopic composition of the ambient seawater (e.g. related to global ice volume), vital effects, and the carbonate ion concentration and pH at calcification (Mulitza et al., 2003). The δ^{18}O of benthic foraminifera is one of the most essential tools for developing age models (Lisiecki and Raymo, 2005), while the δ^{18}O of planktic foraminifera is used to reconstruct, e.g., sea surface temperature. Combining Mg/Ca and δ^{18}O measurements of foraminiferal calcite allows to quantify the δ^{18}O of seawater, which is correlated to seawater salinity (e.g. Lea et al., 1999; Elderfield and Ganssen, 2000; Nürnberg, 2000).

By investigating foraminifera from different habitat depths, e.g., above and below the thermocline, these methods further allow to obtain a reconstruction of the temperature and salinity development in different depths with age and thus of stratification.

The elemental sediment composition revealed through XRF scanning, on the other hand, offers information on various environmental and climatic aspects such as primary productivity, ice-rafted debris, aeolian dust flux, sediment provenance, porosity/water content, grain size or the amount of rainfall (Croudace and Rothwell, 2015). XRF scan records are also well-established for the development of age models (Croudace and Rothwell, 2015). The great advantage of XRF scanning is that it is a non-destructive method that allows relatively fast and high-resolution analyses of sediment composition (Croudace and Rothwell, 2015; Gebregiorgis et al., 2020). This study focusses on elements that provide insights into primary productivity and terrestrial input, e.g., Al, Si, Ca, Ti, Fe, and Ba.

Detailed information on the individual proxies used can be found in the respective scientific chapters.

1.4. Outline of the thesis and declaration of contribution

This thesis is divided into three scientific chapters. The initial ideas and research questions of all three chapters are based on the project of the BMBF (German Ministry of Education and Research) 03G0264A: “SO264 SONNE-Emperor – The Plio/Pleistocene to Holocene development of the pelagic North Pacific from surface to depth – assessing its role for the global carbon budget and Earth´s climate” proposed by Dirk Nürnberg and Ralf Tiedemann. Each of these scientific chapters is designed as an individual manuscript. Chapter I has been submitted and is currently under review in Frontiers in Marine Science, while chapters II and III are in preparation for submission to peer-reviewed journals. In addition, the introduction establishes an overview of the North Pacific and its importance for paleoceanographic investigations and the research topics that are addressed in detail in the individual chapters. The thesis further comprises an overarching conclusion and outlook of possible future studies.

Scientific chapter I presents the development of sea surface and subsurface temperature, $\delta^{18}O_{sw\text{-}ivc}$, terrigenous input via dust, and productivity at site SO264-45 in the North Pacific over the past 650 ka. It discusses different influences on upper ocean temperature and $\delta^{18}O_{sw\text{-}ivc}$, such as variations in the strength of the Oyashio Current, glacial/interglacial changes of the front system in the Kuroshio-Oyashio transition zone, wind-induced changes, as well as long term La Niña-like events in the tropical Pacific which may have enhanced the Kuroshio Current/Extension resulting in shifts of the Subarctic Front. Further, it investigates why productivity shows a different evolution than the upper ocean temperature and draws a connection between the glacial/interglacial variability of primary productivity and changes in nutrient supply.

Contributions to chapter I: The scientific crew of SO264 and myself collected the samples at sea under the lead of chief scientists Dirk Nürnberg and Lester Lembke-Jene. Weng-si Chao and myself performed the XRF scanning with help from Lester Lembke-Jene. With help from Nadine Gehre and student assistants, I washed the samples, picked foraminifera, and prepared the samples for geochemical measurements that were carried out by Nadine Gehre and Sebastian Fessler. Dirk Nürnberg and I developed the age model and analyzed the data. I produced all figures as well as tables and wrote the entire manuscript, Weng-si Chao, Lester Lembke-Jene, Ralf Tiedemann, and Dirk Nürnberg contributed ideas and feedback throughout the whole process of designing the study as well as during writing and improving the manuscript.

Scientific chapter II examines the biological export production and deep sea carbonate deposition along a meridional transect from Hess Rise to the subarctic Northwest Pacific over the last five glacial cycles (500 ka). It discusses carbonate dissolution and possible influencing factors for productivity such as the availability of nutrients in connection to upper ocean stratification and shifts of the gyre circulation. A special focus of this chapter is the differences between the subtropical and subpolar productivity regimes and variations in deep-sea carbonate chemistry.

Contributions to chapter II: Weng-si Chao, Lester Lembke-Jene, and Ralf Tiedemann designed the study. Weng-si Chao and myseld carried out the XRF scanning. Weng-si Chao, student assistants, and myself carried out the lab work. Weng-si Chao, Lester Lembke-Jene, Ralf Tiedemann, Dirk Nürnberg, and myself developed the age model. Weng-si Chao and Lester Lembke-Jene wrote the manuscript with inputs from all co-authors. All authors discussed the data and contributed to the final manuscript version.

Scientific chapter III investigates the upper ocean temperature, $\delta^{18}O_{sw\text{-}ivc,}$ terrigenous input via dust, and productivity of calcareous and siliceous organisms in the North Pacific at two sites (SO264-45 and -53) that are located close to each other at the Emperor Seamount chain. The focus of this chapter is the comparison of the late Pleistocene situation that has extensively been discussed in scientific chapters I and II and the late Pliocene situation. It compares the different evolution of productivity, upper ocean temperature, and wind during these time periods. Further, it discusses in detail the dramatic change in all the above mentioned systems in connection to the intensification of the Northern Hemisphere glaciation. The findings are put in a global context and emphasize the unique role of the North Pacific for global climate.

Contributions to chapter III: The scientific crew of SO264 and myself collected the samples at sea under the lead of chief scientists Dirk Nürnberg and Lester Lembke-Jene. Weng-si Chao and I performed the XRF scanning with help from Lester Lembke-Jene. With help from Nadine Gehre and student assistants, I washed the samples, picked foraminifera, and prepared the samples for geochemical measurements that were carried out by Nadine Gehre and Sebastian Fessler. Dirk Nürnberg and I developed initial age models of the cores that were later finalized by myself. I analyzed and interpreted the data, made all figures and tables, and wrote the entire manuscript. Weng-si Chao, Lester Lembke-Jene, and Dirk Nürnberg contributed ideas and feedback.

1.5. References

Bereiter, B., Eggleston, S., Schmitt, J., Nehrbass-Ahles, C., Stocker, T. F., Fischer, H., et al. (2014). Revision of the EPICA Dome C CO2 record from 800 to 600-kyr before present. *Geophys. Res. Lett.* 42, 542–549. doi: 10.1002/2014GL061957.

Chalk, T. B., Hain, M. P., Foster, G. L., Rohling, E. J., Sexton, P. F., Badger, M. P. S., et al. (2017). Causes of ice age intensification across the mid-pleistocene transition. *Proc. Natl. Acad. Sci. U. S. A.* 114, 13114–13119. doi: 10.1073/pnas.1702143114.

Chen, J., Zou, J., Zhu, A., Shi, X., Nürnberg, D., Lembke-Jene, L., et al. (2021). Geochemistry of Surface Sediments From the Emperor Seamount Chain, North Pacific. *Front. Earth Sci.* 9, 1–15. doi: 10.3389/feart.2021.674842.

Croudace, I. W., and Rothwell, R. G. (2015). *Micro-XRF Studies of Sediment Cores*. Available at: http://link.springer.com/10.1007/978-94-017-9849-5.

Dumitru, O. A., Austermann, J., Polyak, V. J., Fornós, J. J., Asmerom, Y., Ginés, J., et al. (2019). Constraints on global mean sea level during Pliocene warmth. *Nature* 574, 233–236. doi: 10.1038/s41586-019-1543-2.

Dutton, A., Carlson, A. E., Long, A. J., Milne, G. A., Clark, P. U., DeConto, R., et al. (2015). Sea-level rise due to polar ice-sheet mass loss during past warm periods. *Science (80-.).* 349. doi: 10.1126/science.aaa4019.

Elderfield, H., and Ganssen, G. (2000). Past temperature and δ18O of surface ocean waters inferred from foraminiferal Mg/Ca ratios. *Nature* 405, 442–445. doi: 10.1038/35013033.

Emiliani, C. (1955). Pleistocene Temperatures. *J. Geol.* 63, 538–578. doi: 10.1086/626295.

Gargett, A. E. (1991). Physical processes and the maintenance of nutrient-rich euphotic zones. *Limnol. Oceanogr.* 36, 1527–1545. doi: 10.4319/lo.1991.36.8.1527.

Gebregiorgis, D., Giosan, L., Hathorne, E. C., Anand, P., Nilsson-Kerr, K., Plass, A., et al. (2020). What Can We Learn From X-Ray Fluorescence Core Scanning Data? A

Paleomonsoon Case Study. *Geochemistry, Geophys. Geosystems* 21, 1–17. doi: 10.1029/2019GC008414.

Gersonde, R. (2012). The Expedition of the Research Vessel " Sonne "to the subpolar North Pacific and the Bering Sea in 2009 (SO202-INOPEX). 2009, 127–282.

Gray, W. R., and Evans, D. (2019). Nonthermal Influences on Mg/Ca in Planktonic Foraminifera: A Review of Culture Studies and Application to the Last Glacial Maximum. *Paleoceanogr. Paleoclimatology* 34, 306–315. doi: 10.1029/2018PA003517.

Haug, G. H., Sigman, D. M., Tiedemann, R., Pedersen, T. F., and Sarnthein, M. (1999). Onset of permanent stratification in the subarctic Pacific Ocean. *Nature* 401, 779–782. Available at: http://www.nature.com/nature/journal/v401/n6755/abs/401779a0.html.

Hu, D., Wu, L., Cai, W., Gupta, A. Sen, Ganachaud, A., Qiu, B., et al. (2015). Pacific western boundary currents and their roles in climate. doi: 10.1038/nature14504.

Imbrie, J., and Kipp, N. (1971). A new micropaleontological method for quantitative paleoclimatology: Application to a Late Pleistocene Caribbean core, in The Late Cenozoic Glacial Ages. *Late Cenozoic Glacial Ages*, 71–181.

Isoguchi, O., Kawamura, H., and Oka, E. (2006). Quasi-stationary jets transporting surface warm waters across the transition zone between the subtropical and the subarctic gyres in the North Pacific. *J. Geophys. Res. Ocean.* 111, 1–17. doi: 10.1029/2005JC003402.

Jaccard, S. L., Galbraith, E. D., Sigman, D. M., and Haug, G. H. (2010). A pervasive link between Antarctic ice core and subarctic Pacific sediment records over the past 800 kyrs. *Quat. Sci. Rev.* 29, 206–212. doi: 10.1016/j.quascirev.2009.10.007.

Joh, Y., and Di Lorenzo, E. (2019). Interactions between Kuroshio Extension and Central Tropical Pacific lead to preferred decadal-timescale oscillations in Pacific climate. *Sci. Rep.* 9, 1–12. doi: 10.1038/s41598-019-49927-y.

Kucera, M., and Schönfeld, J. (2007). The origin of modern oceanic foraminiferal faunas and Neogene climate change. *Geol. Soc. Spec. Publ.*, 409–425. doi: 10.1144/tms002.18.

Kucera, M., Weinelt, M., Kiefer, T., Pflaumann, U., Hayes, A., Weinelt, M., et al. (2005). Reconstruction of sea-surface temperatures from assemblages of planktonic foraminifera: Multi-technique approach based on geographically constrained calibration data sets and its application to glacial Atlantic and Pacific Oceans. *Quat. Sci. Rev.* 24, 951–998. doi: 10.1016/j.quascirev.2004.07.014.

Lea, D. W., Mashiotta, T. A., and Spero, H. J. (1999). Controls on magnesium and strontium uptake in planktonic foraminifera determined by live culturing. *Geochim. Cosmochim. Acta* 63, 2369–2379. doi: 10.1016/S0016-7037(99)00197-0.

Lisiecki, L. E., and Raymo, M. E. (2005). A Pliocene-Pleistocene stack of 57 globally distributed benthic δ 18O records. *Paleoceanography* 20, 1–17. doi: 10.1029/2004PA001071.

Liu, H., Suzuki, K., and Saito, H. (2004). Community structure and dynamics of phytoplankton in the western subarctic Pacific Ocean: A synthesis. *J. Oceanogr.* 60, 119–137. doi: 10.1023/B:JOCE.0000038322.79644.36.

Mitnik, L. M., Khazanova, E. S., and Dubina, V. A. (2020). Mesoscale and synoptic scale dynamic phenomena in the Oyashio current region observed in SAR imagery. *Int. J. Remote Sens.* 41, 5861–5883. doi: 10.1080/01431161.2019.1701215.

Mulitza, S., Boltovskoy, D., Donner, B., Meggers, H., Paul, A., and Wefer, G. (2003). Temperature: δ18O relationships of planktonic foraminifera collected from surface waters. *Palaeogeogr. Palaeoclimatol. Palaeoecol.* 202, 143–152. doi: 10.1016/S0031-0182(03)00633-3.

Nürnberg (2018). RV SONNE Fahrtbericht/Cruise Report SO264 - SONNE-EMPEROR: The Plio/Pleistocene to Holocene development of the pelagic North Pacific from surface to depth – assessing its role for the global carbon budget and Earth´s climate, Suva (Fiji) – Yokohama (Japa. *GEOMAR Report, N. Ser. 046 . GEOMAR Helmholtz-Zentrum für Ozeanforschung, Kiel, Ger.*, 1–284. doi: 10.3289/GEOMAR_REP_NS_46_2018.

Nürnberg, D. (1995). Magnesium in tests of Neogloboquadrina pachyderma sinistral from high northern and southern latitudes. *J. Foraminifer. Res.* 25, 350–368. doi: 10.2113/gsjfr.25.4.350.

Nürnberg, D. (2000). Taking the temperature of past ocean surfaces. *Science (80-.).* 289, 1698–1699. doi: 10.1126/science.289.5485.1698.

Nürnberg, D., Bijma, J., and Hemleben, C. (1996). Assessing the reliability of magnesium in foraminiferal calcite as a proxy for water mass temperatures. *Geochim. Cosmochim. Acta* 60, 803–814. doi: 10.1016/0016-7037(95)00446-7.

Pachauri, R. K. ., Meyer, L. A. ., Van Ypersele, J. P. ., Brinkman, S. ., Van Kesteren, L. ., Leprince-Ringuet, N. ., et al. (2014). Climate Change 2014: Synthesis Report. Contribution of Working Groups I, II and III to the Fifth Assessment Report of the Intergovernmental Panel on Climate Change. *Ipcc*, 151.

Polovina, J. J., Mitchum, G. T., and Evans, G. T. (1995). Decadal and basin-scale variation in mixed layer depth and the impact on biological production in the Central and North Pacific, 1960-88. *Deep. Res. Part I* 42, 1701–1716. doi: 10.1016/0967-0637(95)00075-H.

Qiu, B. (2002). The Kuroshio Extension system: Its large-scale variability and role in the midlatitude ocean-atmosphere interaction. *J. Oceanogr.* 58, 57–75. doi: 10.1023/A:1015824717293.

Qiu, B. (2019). *Kuroshio and Oyashio currents*. 3rd ed. Elsevier Ltd. doi: 10.1016/B978-0-12-409548-9.11295-3.

Regenberg, M., Nürnberg, D., Steph, S., Groeneveld, J., Garbe-Schönberg, D., Tiedemann, R., et al. (2006). Assessing the effect of dissolution on planktonic foraminiferal Mg/Ca ratios: Evidence from Caribbean core tops. *Geochemistry, Geophys. Geosystems* 7. doi: 10.1029/2005GC001019.

Sasai, Y., Sasaoka, K., Sakaki, H., and Ishida, A. (2007). Seasonal and intra-seasonal variability of chlorophyll-a in the North Pacific: model and satellite data. *J. Earth Simulator* 8, 3–11.

Schiebel, R., and Hemleben, C. (2017). Planktic foraminifers in the modern ocean. *Planktic Foraminifers Mod. Ocean*, 1–358. doi: 10.1007/978-3-662-50297-6.

Schlitzer, R. (2019). Ocean Data View (Version 4.7.2.). *owa.awi.de*.

Shackleton, N. (1967). Oxygen isotope analyses and pleistocene temperatures re-assessed. *Nature* 215, 15–17. doi: 10.1038/215015a0.

Shimizu, Y., Yasuda, I., and Ito, S. I. (2001). Distribution and circulation of the coastal

Oyashio intrusion. *J. Phys. Oceanogr.* 31, 1561–1578. doi: 10.1175/1520-0485(2001)031<1561:DACOTC>2.0.CO;2.

Sigman, D. M., Hain, M. P., and Haug, G. H. (2010). The polar ocean and glacial cycles in atmospheric CO2 concentration. *Nature* 466, 47–55. doi: 10.1038/nature09149.

Sigman, D. M., Jaccard, S. L., and Haug, G. H. (2004). Polar ocean stratification in a cold climate. *Nature* 428, 59–63. doi: 10.1038/nature02378.1.

Takahashi, T., Sutherland, S. C., Wanninkhof, R., Sweeney, C., Feely, R. A., Chipman, D. W., et al. (2009). Climatological mean and decadal change in surface ocean pCO2, and net sea-air CO2 flux over the global oceans. *Deep. Res. Part II Top. Stud. Oceanogr.* 56, 554–577. doi: 10.1016/j.dsr2.2008.12.009.

Talley, L. D. (1995). Some advances in understanding of the general circulation of the Pacific Ocean, with emphasis on recent U.S. contributions. *Rev. Geophys.* 33, 1335–1352. doi: 10.1029/95RG00350.

Tanhua, T., Bates, N. R., and Körtzinger, A. (2013). The marine carbon cycle and ocean carbon inventories. *Int. Geophys.* 103, 787–815. doi: 10.1016/B978-0-12-391851-2.00030-1.

Vega, E. De, Cha, T. B., Wilson, P. A., Bysani, R. P., and Foster, G. L. (2020). Atmospheric CO 2 during the Mid-Piacenzian Warm Period and the M2 glaciation. 14–21. doi: 10.1038/s41598-020-67154-8.

Wang, J., Chang, F., Li, T., Sun, H., Cui, Y., and Liu, T. (2020). The evolution of the Kuroshio Current over the last 5 million years since the Pliocene: Evidence from planktonic foraminiferal faunas. *Sci. China Earth Sci.* 63, 1714–1729. doi: 10.1007/s11430-019-9641-9.

Warren, B. A. (1983). Why is no deep water formed in the North Pacific? *J. Mar. Res.* 41, 327–347. doi: 10.1357/002224083788520207.

Yasuda, I., Kouketsu, S., Katsumata, K., Ohiwa, M., Kawasaki, Y., and Kusaka, A. (2002). Influence of Okhotsk Sea intermediate water on the Oyashio and North Pacific intermediate water. *J. Geophys. Res. Ocean.* 107, 1–11. doi: 10.1029/2001jc001037.

Yasuda, I., Okuda, K., and Shimizu, Y. (1996). Distribution and modification of North Pacific Intermediate Water in the Kuroshio-Oyashio interfrontal zone. *J. Phys. Oceanogr.* 26, 448–465. doi: 10.1175/1520-0485(1996)026<0448:DAMONP>2.0.CO;2.

Yatsu, A., Chiba, S., Yamanaka, Y., Ito, S. I., Shimizu, Y., Kaeriyama, M., et al. (2013). Climate forcing and the Kuroshio/Oyashio ecosystem. *ICES J. Mar. Sci.* 70, 922–933. doi: 10.1093/icesjms/fst084.

2. Scientific Chapter I

ENSO vs glacial-interglacial-induced changes in the Kuroshio-Oyashio transition zone during the Pleistocene

Lara Jacobi[1*], Dirk Nürnberg[1], Weng-si Chao[2], Lester Lembke- Jene[2], Ralf Tiedemann[2]
[1]GEOMAR - Helmholtz Centre for Ocean Research Kiel, Kiel, Germany
[2]Alfred-Wegner-Institute - Helmholtz Centre for Polar and Marine Research, Bremerhaven, Germany

Submitted to Frontiers in Marine Science

Abstract

The subarctic front (SAF) in the pelagic North Pacific is the northernmost front of the Kuroshio-Oyashio transition zone separating the subpolar- and subtropical gyre and is marked by a strong sea surface temperature gradient. A complex, not yet entirely understood interplay of e.g. variations of currents, the wind system and other forcing mechanisms causes shifts of the SAF's position on timescales from interannual to glacial/interglacial. In this study, we present proxy data from the Emperor Seamount chain, which reveals a link between long-term ENSO (El Niño/Southern Oscillation) dynamics in the tropics and shifts of the SAF. Based on sediment core SO264-45-2 (46°33.792'N, 169°36.072'E), located close to the modern position of the SAF we reconstruct: changes in (sub)surface temperature ((sub)$SST_{Mg/Ca}$) and $\delta^{18}O_{sw-ivc}$ (approximating salinities) via combined Mg/Ca and $\delta^{18}O$ analyses of the shallow-dwelling foraminifera *Globigerina bulloides* and the near-thermocline-dwelling *Neogloboquadrina pachyderma*, biological productivity (XRF-based Ba/Ti ratios), and terrigenous input via dust (XRF-based Fe). From ~600 to ~280 ka BP we observe significantly higher $SST_{Mg/Ca}$ than after an abrupt change at 280 ka BP. We assume that during this time water from the Kuroshio-Oyashio transition zone reached the core site which would reflect a shift of the SAF from a position at or even north of our study site prior to 280 ka BP to a position south of our study site after 280 ka BP. We propose that such a northward displacement of the SAF between 600-280 ka BP was induced by sustained La Niña-like conditions, which led to increased transport of tropical ocean heat into the Kuroshio-Oyashio transition zone via the Kuroshio Current. After ~280 ka BP, the change to more El Niño-like conditions led to less heat transfer via the Kuroshio Current so that the SAF remained south of the core location. In contrast, our productivity record shows a clear glacial-interglacial pattern that is common in the North Pacific. We assume that this pattern is connected to changes in nutrient supply or utilization which are not primarily driven by changes of the Kuroshio and Oyashio Currents or the SAF.

2.1. Introduction

The North Pacific plays a key role in shaping Earth's climate, as it can either function as a sink or a source of atmospheric CO_2 depending on the effectiveness of the so-called 'biological carbon pump'. Yet the complex interplay of atmosphere and ocean, and their respective circulation patterns, as well as their influences on productivity over longer timescales, is not yet entirely understood. Proxy records for productivity and upper ocean temperature are sparse in the pelagic North Pacific, especially over longer time scales, beyond the last glacial. One of the main reasons is that the open North Pacific is rather deep, thus the availability of carbonate-bearing sediment records is restricted to e.g. seamount areas, where the water depth does not exceed the depth of the calcite compensation depth which lies at about ~4000 m in the open North Pacific (Chen et al., 2021). This constrains not only the use of foraminiferal calcite as temperature proxy, but also marks an obstacle for stratigraphy, because foraminiferal calcite is an important and well-established signal carrier ($\delta^{18}O$, $AMS^{14}C$) for the development of age models. Moreover, the few available sea surface temperature (SST) records are based on a variety of different proxies, which in turn may lead to inconsistent temperature estimates, since the recording of each proxy is related to a certain water depth and often shows a seasonal bias (Max et al., 2012). Jimmu Seamount is located right beneath the complex frontal system separating the tropical Kuroshio Extension and the Oyashio/Subarctic Current. Shifts of these currents and their relative mixing zones have significantly affected oceanographic conditions in the North Pacific on various timescales (Thompson and Shackleton, 1980; Hovan et al., 1991; Kawahata et al., 2000; Yamane, 2003; Chiyonobu et al., 2012). Yet both the timing and the causes of such shifts in the frontal system are still a matter of debate. Some authors suggest a connection between shifts of oceanic fronts in the North Pacific and climate changes related to glacial-interglacial cycles (Thompson and Shackleton, 1980; Kawahata and Ohshima, 2002; Harada et al., 2004; Yasudomi et al., 2014; Gallagher et al., 2015), others draw a connection between El Niño-Southern Oscillation (ENSO), the Kuroshio strength and the positioning of the front system (Yamane, 2003; Chen et al., 2007). ENSO oscillates interannually between "El Niño" and "La Niña" phases. The surface water temperature gradient between the WPWP and the Eastern Equatorial Pacific (EEP) ($\Delta T_{WPWP-EEP}$) is an indicator for ENSO. During El Niño phases there is a weak temperature gradient with a generally deep thermocline across the equatorial Pacific, whereas during La Niña phases there is an amplified $\Delta T_{WPWP-EEP}$ and a shoaling of the thermocline in the eastern equatorial Pacific (Picaut et al., 1996). Several authors suggest that there are not only decadal changes between El Niño and La Niña, but that there are also changes from more La Niña-like to more El Niño-like conditions on larger timescales (de Garidel-Thoron et al., 2005; Wara et al., 2005; Zheng et al., 2016; Jia et al., 2018). Moreover, a change in the wind system, e.g., the westerlies, which is a driver of subtropical and subarctic gyre circulation, or the Asian monsoon, which is supposedly linked to ENSO (Zhang et al., 2007), may have affected the path and strength of both the Kuroshio and Oyashio Current (Yatsu et al., 2013). Further there is the Pacific Decadal Oscillation (PDO), which represents not a single phenomenon but is the result of a combination of different physical processes, including both remote tropical forcing and local North Pacific atmosphere–ocean interactions, which operate on different time scales. The PDO, however is not seen as a forcing function of non-oceanic processes but a result of physical forcing mechanisms (Newman et al., 2016).

In contrast to the upper ocean temperature, primary productivity in the North Pacific is mainly described to be linked to glacial-interglacial cycles with higher productivity during interglacials and lower productivity during glacials (Narita et al., 2002; Gorbarenko et al., 2004; Kienast et al., 2004; Jaccard et al., 2005; Brunelle et al., 2007; Shigemitsu et al., 2007; Galbraith et al., 2008; Gebhardt et al., 2008; Jaccard et al., 2010; Riethdorf et al., 2013). Yet it is still under debate to what extent temperature change, sea ice formation, light limitation, wind strength, nutrient supply, and stratification changes did influence the productivity (Kawahata et al., 2000; Matsumoto et al., 2002; Brunelle et al., 2007; Shigemitsu et al., 2007; Jaccard et al., 2010; Nishioka et al., 2011; Costa et al., 2018; Sigman et al., 2021). Thus, our new dataset on upper ocean temperatures (based on foraminiferal Mg/Ca), marine productivity (XRF-based Ba/Ti), and terrigenous input via wind (XRF-based Fe) from the pelagic North Pacific provide a unique opportunity to gain further insights into upper ocean dynamics, especially spatial and temporal shifts of the Kuroshio-Oyashio frontal systems and a possible link to productivity over the past 650 ka.

2.1.1. Oceanographic setting

The North Pacific is characterized by two large-scale wind-driven gyre systems: the cyclonic Subarctic Gyre in the north and the anticyclonic Subtropical Gyre in the south (Huang, 2015). The Subarctic Gyre has a strong western boundary current. The Oyashio Current originates from the East Kamchatka Current and is further fed by cold, low saline nutrient-rich water from the Sea of Okhotsk. Close to the coast of northern Japan the Oyashio Current has an annual mean temperature of ~5°C and a salinity of ~33 (Locarnini et al., 2018; Zweng et al., 2019). At ~42°N the Oyashio Current splits and one path continues as the northeastward flowing Subarctic Current (SAC) (Qiu, 2019). The western limb of the North Pacific Subtropical Gyre is also formed by a strong western boundary current. The Kuroshio Current originates from the warm, saline North Equatorial Current (NEC) and transports oceanic heat from the West Pacific Warm Pool (WPWP) to the northern regions (Figure 2.1). The location where the North Equatorial Current (NEC) bifurcates into the Kuroshio Current and the Mindanao Current (Metzger & Hurlburt, 1996; Qiu & Lukas, 1996; Ujiié et al., 2003) is located at ~15.5°N for the annual average, but varies with time and depth. The meridional migration of the NEC bifurcation is strongly influenced by ENSO (Kim et al., 2004), which is the main driver of upper ocean circulation in the tropical Pacific, (Joh & Di Lorenzo, 2019; Hu et al., 2015). In El Niño years the NEC's bifurcation point migrates to the north and the Kuroshio velocity and volume transport decrease. During La Niña years, in contrast, the NEC's bifurcation migrates to the south and the Kuroshio velocity and volume transport increase (Qiu and Lukas, 1996; Yuan et al., 2001; Kim et al., 2004) (Figure 2.6). Close to the coast of southern Japan, the Kuroshio Current has an annual mean temperature of ~19°C and a salinity of ~35 (Locarnini et al., 2018; Zweng et al., 2019). After separating from the Japanese coast at ~35°N, the Kuroshio Current enters the open basin of the North Pacific and continues as Kuroshio Extension (Qiu, 2002). At Shatsky Rise (~159°E), the Kuroshio Extension bifurcates, where the main body of the Kuroshio Extension continues eastward. A secondary branch, the Kuroshio Bifurcation Front (KBF), extends northwards (Qiu, 2002).

Along the northern boundary of the Kuroshio Extension/Kuroshio Bifurcation Front, numerous meanders and mesoscale eddies occur (Figure 2.1) due to the dia- and isopycnal mixing between Kuroshio and Oyashio water with vertically different temperature, salinity and velocity structures (Yasuda et al., 1996, 2002; Shimizu et al., 2001; Isoguchi et al., 2006; Mitnik et al., 2020). This mixing zone of water originating from the Kuroshio and Oyashio currents is termed the Kuroshio-Oyashio transition zone or mixed water region and is characterized by a pronounced latitudinal sea surface temperature, salinity, and nutrient gradient (Science, 2003; Garcia et al., 2018; Locarnini et al., 2018; Zweng et al., 2019) (Figure 2.1). The northern end of the transitional zone is marked by the Subarctic Front (SAF) or Oyashio Front, which is defined as the 4°C isotherm at 100 m depth (Favorite, 1976). Subarctic surface water may drift southward across the SAF, and may cover the surface in the transition zone between the SAF and the Subarctic Boundary (SAB). The SAB is a near surface salinity front south of the SAF (Science, 2003). East of 180°W/E the distinction between the Kuroshio Extension and the Subarctic Current is no longer clear and together they form the broad eastward-moving North Pacific Current (Qiu, 2019). During La Niña years, an increased amount of tropical surface water enters the Kuroshio-Oyashio transition zone via the Kuroshio Current/Kuroshio

Extension and causes northward shifts of the frontal system, while during El Niño years, the front system migrates southwards (Chen et al., 2007).

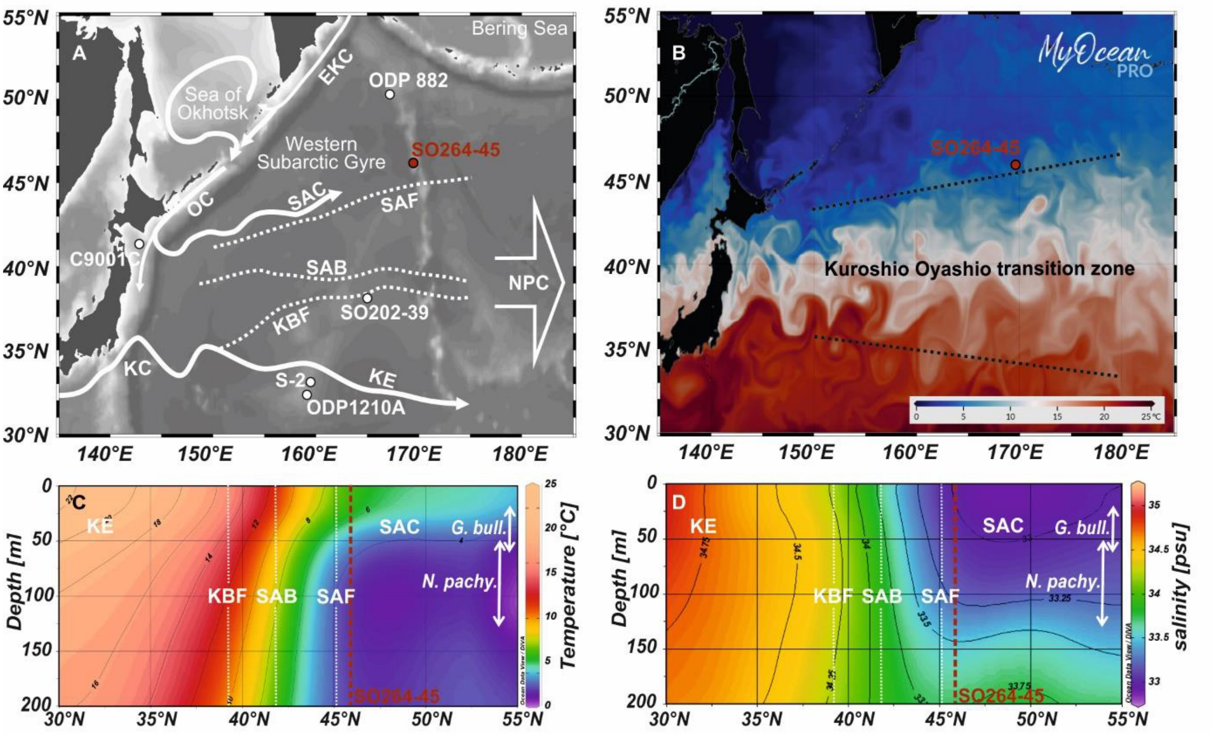

Figure 2.1: Sea surface and subsurface hydrology of the North West Pacific. **A**: Bathymetric map indicating the locations of the study site SO264-45 and reference cores ODP Site 882 (Jaccard et al., 2010), SO202-39 (Korff et al., 2016), ODP Site 1210A (Chiyonobu et al. 2012), S-2 (Yamame, 2003), and C9001C (Matsuzaki et al., 2014). The surface current and water-mass structure in the Kuroshio-Oyashio transition area is schematically illustrated: EKC = East Kamchatka Current, KC = Kuroshio Current, KE= Kuroshio Extension, NPC = North Pacific Current, OC = Oyashio Current, SAC = Subarctic Current; KBF = Kuroshio Bifurcation Front, SAB = Subarctic Boundary, SAF = Subarctic Front. The position of the currents and boundaries are based on Yasuda et al. (2003) **B:** Potential sea surface temperature of the North West Pacific from early summer 2021. The Oyashio-Kuroshio transition zone is characterized by large eddies. This figure was generated using EU Copernicus Marine Service Information with data from GLOBAL_ANALYSIS_FORECAST_PHY_001_024 (Zammit-Mangion and Wikle, 2020). **C&D**: North-south-oriented temperature and salinity transects along 170°E illustrated with Ocean Data View (Schlitzer and Ocean Data View, 2019) based on data from the World Ocean Atlas 2018 (Locarnini et al., 2018; Zweng et al., 2019). The position of fronts are marked by white dotted lines; the core position by a red dotted line and depth habitats of *G. bulloides* and *N. pachyderma* by white arrows.

Intermediate water masses (~400-900 m) in the Subtropical Gyre as well as in the mixed water region are dominated by North Pacific Intermediate Water (NPIW) (Talley, 1993). It is formed in the northern part of the mixed water region and is mainly fed by Gulf of Alaska Intermediate Water (GAIW), Okhotsk Sea Intermediate Water (OSIW) and water from the Kuroshio-Oyashio transition zone (Talley, 1993; You et al., 2000). Underneath the surface of the subarctic gyre there is the Pacific Subpolar Intermediate Water (PSIW) which is a mix of altered GAIW and NPIW (Emery, 2001; Fuhr et al., 2021).

2.2. Material and methods

The 8.35 m long gravity core SO264-45-2 was recovered from Jimmu Seamount at 46°33.792'N and 169°36.072'E from a water depth of 2425 m during R/V SONNE cruise SO264 (SONNE-EMPEROR) in August 2018 (Nürnberg, 2018). Additionally, the sediment surface was sampled with a Multi Corer (MUC: SO264-45-1, core length: 0.15 m; 46°33.795'N and 169°36.072'E). The core site selection was based on a systematic bathymetric survey, as well as sediment echosounder profiling. The upper 4.7 m of the core presented in this study consist of foraminifera-bearing sandy silt to foraminifera-bearing calcareous ooze, in some parts containing IRD (Nürnberg, 2018) and intercalated by five tephra layers (Figure 2.2).

2.2.1. XRF scanning

To determine the sedimentary elemental composition, the archive half of each core segment was scanned using an Avaatech X-ray Fluorescence (XRF) core scanner at the Alfred-Wegener-Institute (AWI) Bremerhaven. For preparation, the uppermost sediment layer was removed to provide a fresh and undisturbed surface, which was then covered with SPEXCerti Prep Ultralene foil. Each core segment was triple scanned at a one-centimeter resolution with a current of 0.15, 0.175 and 1 mA, tube voltages of 10, 30, and 50 kV, and acquisition times of 10, 15, and 20 sec, respectively. Element intensities were determined with the proprietory Aavatech WinAxil (Batch) software covering elements from aluminum to barium and are reported as counts per second (cps). We use the barium/titanium ratio (Ba/Ti) record as proxy for changes in paleoproductivity (biogenic barium reflecting diatom productivity) and the iron (Fe) record as proxy for relative changes in terrigenous Fe input. Based on the assumption that the aluminum (Al) and Ti content of terrigenous material remained constant in space and time (Galbraith et al., 2007), the XRF-derived barium counts normalized against terrigenous background elements like Al or Ti are well-established paleoproductivity proxies in the North Pacific (Nürnberg et al., 2004; Jaccard et al., 2010; Korff et al., 2016). Al and Ti are both exclusively of detrital origin and correlate well at our study site (Supplementary Figure 2.12). Yet the detection of light elements like Al during XRF scanning shows a higher risk to be influenced by water trapped between the sediment and the scanning foil than heavier elements (Tjallingii et al., 2007). Thus, we use Ti for normalizing our Ba record. Fe, like Ti, has been widely used to document variations in terrigenous sediment delivery and often relates to aeolian dust flux and thus wind strength (Jahn et al., 2003, 2005; Nürnberg et al., 2004; Mohtadi et al., 2007; Helmke et al., 2008; Kaiser et al., 2008). The very good correlation of our Fe and Ti records ($R^2=0.98$) (Supplementary Figure 2.12) indicates that a potential diagenetic imprint on Fe is negligible (Croudace and Rothwell, 2015). We follow the suggestion to present the natural logarithms of XRF element counts and ratios to account for the problem, that raw intensities or peak integrals cannot be interpreted in terms of sediment composition (Weltje and Tjallingii, 2008).

2.2.2. Foraminiferal geochemistry

For geochemical studies, we use the most abundant planktic foraminiferal species *G. bulloides* and *N. pachyderma* (sinistral-coiling, Darling et al., 2006). In the Northwest Pacific, *G. bulloides* is a near-surface dweller and mainly found above the thermocline (Iwasaki et al., 2017; Schiebel et al., 2017; Taylor et al., 2018), which occurs at ~40-50 m at the study site (Locarnini et al., 2018) (Figure 2.1, Supplementary Figure 2.7). In the study region, *G. bulloides* calcifies throughout the year (Kuroyanagi et al., 2008; Sagawa et al., 2013; Taylor et al., 2018). In the North Pacific, *N. pachyderma* is mainly found at thermocline depth (Sarnthein et al., 2004; Riethdorf, 2013; Taylor et al., 2018) thus, we assume a depth habitat of 50-130 m for our study site (Locarnini et al., 2018). *N. pachyderma* is a subpolar species and prefers water temperatures below 7°C (Reynolds and Thunell, 1986), thus in modern settings it mainly occurs from autumn to spring at our study site, which is shown by sediment trap studies from the North Pacific (Kuroyanagi et al., 2008; Sagawa et al., 2013; Taylor et al., 2018). For a detailed discussion about seasonality and habitat depth, see Supplement (2.7.1).

2.2.2.1. Magnesium and calcium element ratios

Mostly, ~50 visually well-preserved specimens of *G. bulloides and* ~120 of *N. pachyderma* were selected from core SO264-45-2 at 2 cm sample spacing. Due to insufficient sample material in most of the samples, specimens were selected from a rather wide size range (*G. bulloides*: 250 – 400 µm; *N. pachyderma:* 125-315 µm; potential size effects on Mg/Ca ratios are discussed in the Supplement 2.7.1). Tests were gently crushed between cleaned glass plates to open the test chambers for efficient cleaning. Chamber fillings e.g. sediment or pyrite particles were removed. The fragmented and homogenized samples were divided into one-third for stable isotope analyses and two-thirds for trace element measurements.

Cleaning of foraminiferal fragments prior to trace element analyses followed the procedures of Boyle & Keigwin (1985) and Boyle & Rosenthal (1996). These include oxidative and reductive (with hydrazine) cleaning steps. Samples were measured at GEOMAR - Helmholtz Centre for Ocean Research, on a VARIAN 720 ES axial ICP-OES coupled with a VARIAN SPS3 sample preparation system. The measurement strategy included regular analyses of standards and blanks to ensure analytical quality control. The data was drift-corrected and standardized to the internal consistency standard BCS-DRM 393 (ECRM 752-1) with an Mg/Ca reference value of 3.761 mmol/mol (Greaves et al., 2008). The long-term external reproducibility for the ECRM standard for Mg/Ca is ± 0.1 mmol/mol (2σ). When Mg/Ca values were considerable higher or lower than expected, measurements were repeated.

To monitor contamination and insufficient removal of siliciclastic material during the cleaning procedure, Al/Ca, Mn/Ca and Fe/Ca ratios were measured alongside the Mg/Ca. By assessing this data, we could not find any evidence of an influence of contamination on our Mg/Ca ratios. A detailed discussion can be found in the supporting information (Supplement 2.7.3).

In addition, statistical Mg/Ca outliers were identified by applying the 1.5 interquartile method after Tukey (1977) (Supplement 2.7.3).

2.2.2.2. Stable oxygen and carbon isotopes

In addition to the planktic foraminiferal species (*G. bulloides*: 250 – 400 µm; *N. pachyderma:* 125-315 µm), 3-5 tests of the benthic foraminiferal species *Uvigerina* spp. and *Cibicidoides wuellerstorfi* were selected from the size fraction 315-400 µm for oxygen and carbon isotope measurements. Planktic and benthic specimen were measured on a Thermo Fischer Scientific MAT 253 mass spectrometer equipped with an automated Kiel IV carbonate preparation device. Isotope values were calibrated to NBS-19 (National Bureau of Standards) and reported relative to the Vienna Pee Dee Belemnite (VPDB) standard. The long-term external reproducibility (n = <3,000) was monitored by the in-house Bremen standard (Solnhofen Limestone) with an analytic precision of 0.06 ‰ for $\delta^{18}O$ and 0.03 ‰ for $\delta^{13}C$. Applying the 1.5 interquartile method after Tukey (1977) the Mg/Ca and $\delta^{18}O$ records of both the planktic and benthic foraminifera were checked for outliers (Supplement 2.7.3).

In order to combine the $\delta^{18}O$-values of both benthic species, we follow the conventional assumption that *Uvigerina spp*. calcifies in equilibrium with surrounding seawater $\delta^{18}O$ (Shackleton, 1974; Shackleton and Hall, 1984; Labeyrie et al., 1999; Fontanier et al., 2006) and that *C. wuellerstorfi* deviates by ~0.64 ‰ from *Uvigerina* values (Shackleton and Opdyke, 1973; Labeyrie et al., 1999; Waddell et al., 2009). We hence corrected $\delta^{18}O_{C.\ wuellerstorfi}$ by adding 0.64 ‰.

2.2.3. Upper ocean temperature and ice volume corrected $\delta^{18}O$ seawater assessment based on foraminiferal Mg/Ca and $\delta^{18}O$

For converting Mg/Ca of foraminiferal calcite into water temperature we used well-established species-specific equations from Elderfield & Ganssen (2000) for *G. bulloides* ($Mg/Ca=0.56e^{(0.10*T)}$) and from Kozdon et al. (2009) for *N. pachyderma* ($Mg/Ca=0.13*T+0.35$) (Supplement 2.7.2). The temperature derived from *G. bulloides* is referred to as annual sea surface temperature ($SST_{Mg/Ca}$: ~20-60 m) and the temperature from *N. pachyderma* as sub surface temperature ($subSST_{Mg/Ca}$: ~50-130 m). Late Holocene temperatures of both species match the modern annual mean temperatures in the defined depth habitats (Locarnini et al., 2018; Supplementary Figure 2.7). For our interpretations, we assume that the foraminiferal species did not significantly change their habitat depth over time.

We are aware that changes in pH and salinity of the surrounding seawater, calcite dissolution and diagenetic effects can influence foraminiferal Mg/Ca, and hence the reconstructed absolute temperature values. Yet, we assume that these effects are either neglectable for our interpretation or lie within the assigned error range. A detailed discussion can be found in the Supplement 2.7.2, 2.7.3 and 2.7.4.

Via the combined $\delta^{18}O$ and Mg/Ca measurement of the foraminiferal calcite, we calculate the $\delta^{18}O$ of seawater ($\delta^{18}O_{sw}$) by removing the temperature effect from the initial foraminiferal $\delta^{18}O$ signal. For *G. bulloides* we use the equation from Shackleton (1974) ($T=16.9-4.38*(\delta^{18}O_{calcite}-\delta^{18}O_{sw})+0.1*(\delta^{18}O_{calcite}-\delta^{18}O_{sw})^2$) and for *N. pachyderma* the species-specific equation from Mulitza et al. (2003) ($T=3.55*(\delta^{18}O_{calcite}-\delta^{18}O_{sw})+12.69$). The $\delta^{18}O_{sw}$ data is further corrected for changes in global ice volume ($\delta^{18}O_{sw-ivc}$ reported in ‰ versus SMOW; ivc = ice-volume corrected) by using a data set from De Boer et al. (2014). This was calculated based on the global LR04 stack (Lisiecki and Raymo, 2005) and simulations of continental ice sheets (De Boer et al., 2014). Modern $\delta^{18}O_{sw}$ is positively correlated to salinity (e.g. $\delta^{18}O_{sw} = 0.44*S-15.13$; LeGrande & Schmidt, 2006), yet previous studies have shown, that this relationship can vary over time e.g. through changes in regional freshwater budgets, ocean circulation, and sea ice regimes (Caley and Roche, 2015; Holloway et al., 2016). Therefore, we refrain from further converting the calculated $\delta^{18}O_{sw-ivc}$ into absolute salinity units. However, we interpret high values in terms of relative high saline conditions and low values in terms of relative freshening. We present $\delta^{18}O_{sw-ivc}$ as relative changes deviating from the calculated modern value.

2.2.4. Chronostratigraphy

Accelerated mass spectrometer radiocarbon (AMS^{14}C) dating provides an age estimation for the sediment surface (0–1 cm) from station SO264-45-1 (MUC). We chose the undisturbed surface sample of the MUC for this measurement, because the surface of gravity cores is often disturbed during core recovery. Approximately 90 µg C of the planktic species *G. bulloides* and the benthic species *Uvigerina peregrina* were measured at the MICADAS (Mini Carbon Dating System) facility at the AWI in Bremerhaven, Germany (AWI sample nr. 3976.1.1 & 3976.2.1). The raw ^{14}C age was converted into calendar age, using the Calib8.20 software (Stuiver et al., 2020) along with the marine calibration dataset MARINE20 (Heaton et al., 2020) and a regional reservoir age correction of ΔR = 273 +- 70 years. In this case, ΔR is the mean reservoir age of six sites from the North Pacific published by Kuzmin et al. (2001, 2007) and Yoneda et al. (2007). The generated AMS^{14}C age range (2 sigma) for *U. peregrina* is 263-745 a BP and 1871-1301 a BP for *G. bulloides*. This age difference lies within the age range for one sample (~1500 years/sample) as discussed below.

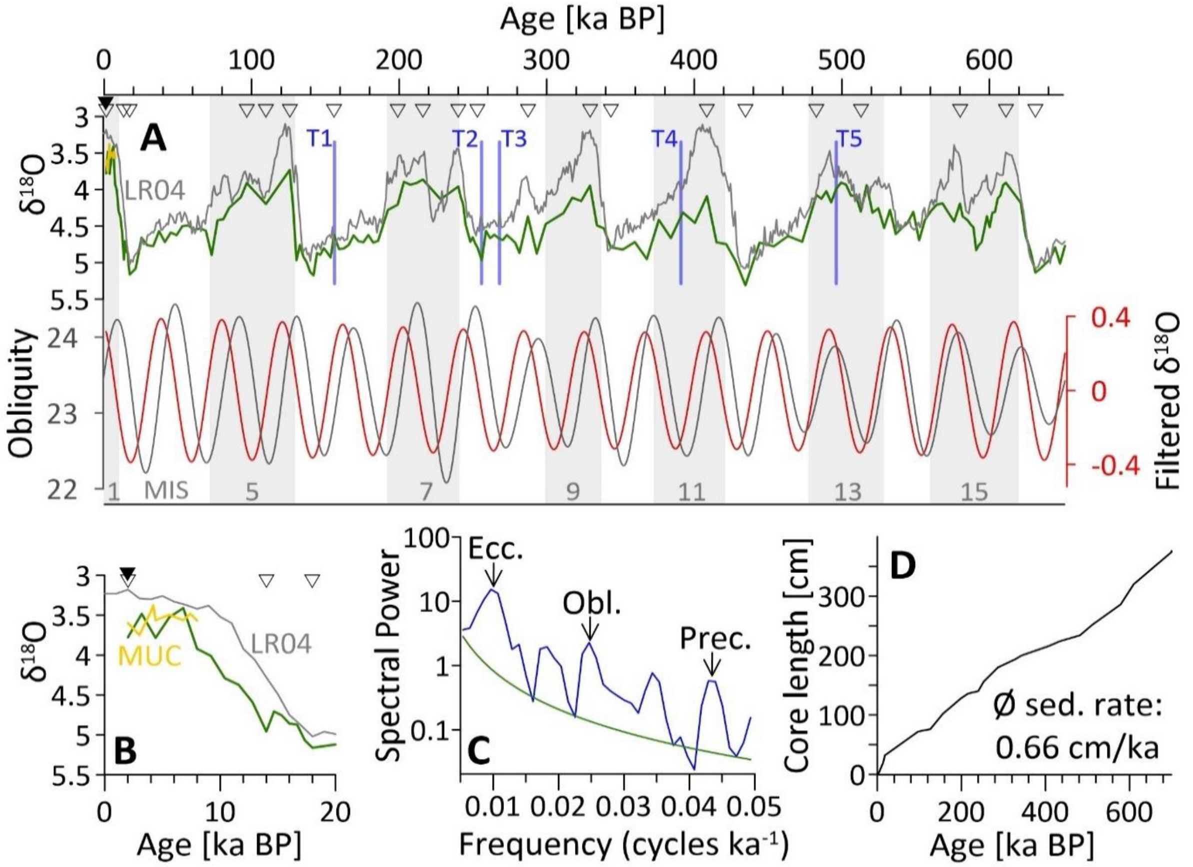

Figure 2.2: Chronostratigraphy of core SO264-45 from Jimmu Seamount (Emperor Seamount Chain). **A**: Top: Benthic δ^{18}O stack of core SO264-45 (green line = gravity core; yellow line = multicorer) in comparison to the global benthic LR04 δ^{18}O reference stack from Lisiecki and Raymo (2005). White triangles = tie lines used for tuning the core SO264-45 δ18O to LR04. Black triangle = AMS14C dating. Bottom: The filtered 41 kyr component of the benthic δ^{18}O stack of SO264-45 (red) in comparison to the orbital obliquity. Gray shadings and numbers mark Marine Isotope Stages (MIS 1-17). Tephra layers identified in core SO264-45 are indicated as blue vertical lines. **B**: The first 20 ka of A as a close up to better indicate the MUCs δ^{18}O in correlation with the gravity core and LR04. **C**: The frequency spectrum of the benthic δ^{18}O stack (green = 95% significance line) indicates dominant cyclicities of 100, 41 and 23 kyr as a response to cyclic fluctuations in the Earth's orbital parameters eccentricity, obliquity and precession. **D**: Age-depth diagram for core SO264-45; the sedimentation rate is given by the curve's slope.

As benthic foraminiferal $\delta^{18}O$ values from the MUC SO264-45-1 fit rather well to those of the uppermost centimeters of the gravity core SO264-45-2 (Figure 2.2), it is likely that both have similar surface ages. Thus, based on the ^{14}C ages from the MUC's surface we assume that the gravity core top sediments are of late Holocene age.

The stacked benthic $\delta^{18}O$ isotope record of SO264-45-2 was visually correlated to the global benthic isotope stack LR04 (Lisiecki and Raymo, 2005) by using QAnalySeries v1.5.0 (Kotov et al., 2018). Our benthic record shows smaller amplitudes than LR04, which is most likely caused by low sedimentation rates, which mute extreme values. By applying 21 tie lines and linear interpolation between the tie lines, a correlation coefficient of r = 0.82 was achieved. Further support for the age model is provided by the spectral analysis of the benthic $\delta^{18}O$ stack that reveals dominant cyclicities with a frequency of 0.01 and 0.025 as a response to the cyclic fluctuations in the Earth's orbital parameters eccentricity and obliquity (Figure 2.2). The spectral analysis reveals that all obliquity cycles of the past 650 ka are reflected in our benthic $\delta^{18}O$ stack. The calculated sedimentation rates are rather low with an average of 0.66 cm/ka for the discussed interval, thus one sample of 1 cm width reflects on average ~1500 years. Yet due to the observed bioturbation of the sediment (Nürnberg, 2018) the absolute age range of foraminifera in one sample might be higher.

The ages of five tephra layers mentioned in the core description (Nürnberg, 2018) are shown in Figure 2.2. We assume that T4 might be the prominent Pauzhetka ash found in several records from the Northwest Pacific and Okhotsk Sea and dated to 421.2 ± 6.6 ka BP (Ponomareva et al., 2018). Yet according to our age model, the depth of T4 refers to an age of ~390 ka BP, which is likely within the range of dating uncertainty.

2.3. Results

2.3.1. Reconstruction (sub)$SST_{Mg/Ca}$ and $\delta^{18}O_{sw-ivc}$

Over the last ~650 ka BP, $\delta^{18}O$ values of *G. bulloides* fluctuate between 1.5 and 4 ‰, and those of *N. pachyderma* between 2.4 and 3.8 ‰ (Figure 2.3). With only few exceptions in MIS 6-8 the $\delta^{18}O$ of *N. pachyderma* are heavier than those of *G. bulloides*. The $\delta^{18}O$ fluctuations of both species follow the glacial-interglacial pattern of the LR04 reference record (Lisiecki and Raymo, 2005) with heavy $\delta^{18}O$ values during glacials and light $\delta^{18}O$ values during interglacials (Figure 2.3). In MIS 11, however, *G. bulloides* shows lighter $\delta^{18}O$ values than in the adjacent interglacials. In MIS 7 the $\delta^{18}O$ are not light throughout the entire interglacial, yet decrease steadily. $\delta^{18}O$ of *G. bulloides* is lightest in MIS 15 and 13 compared to the other interglacials in our record, while the $\delta^{18}O$ of LR04 is heavier in MIS 15 and 13 compared to the other interglacials.

Mg/Ca ratios from *G. bulloides* vary between 0.82 and 2 mmol/mol, which leads to $SST_{Mg/Ca}$ estimates between 3.8 and 12.7°C. The $SST_{Mg/Ca}$ development of *G. bulloides* can be divided into two phases (Figures 2.3, 2.4). Between ~600 and 280 ka BP (phase B), the surface ocean temporally reached $SST_{Mg/Ca}$ of up to ~12°C (with a mean of 8.7°C), thereby being up to ~6.5°C warmer than modern annual mean SST at 30 m (Figure 2.3). Within this time interval, the $SST_{Mg/Ca}$ broadly follow glacial-interglacial cycles except for MIS 10, during which the $SST_{Mg/Ca}$ is high (~10°C) throughout the glacial and MIS 11 where temperatures are ~2°C lower

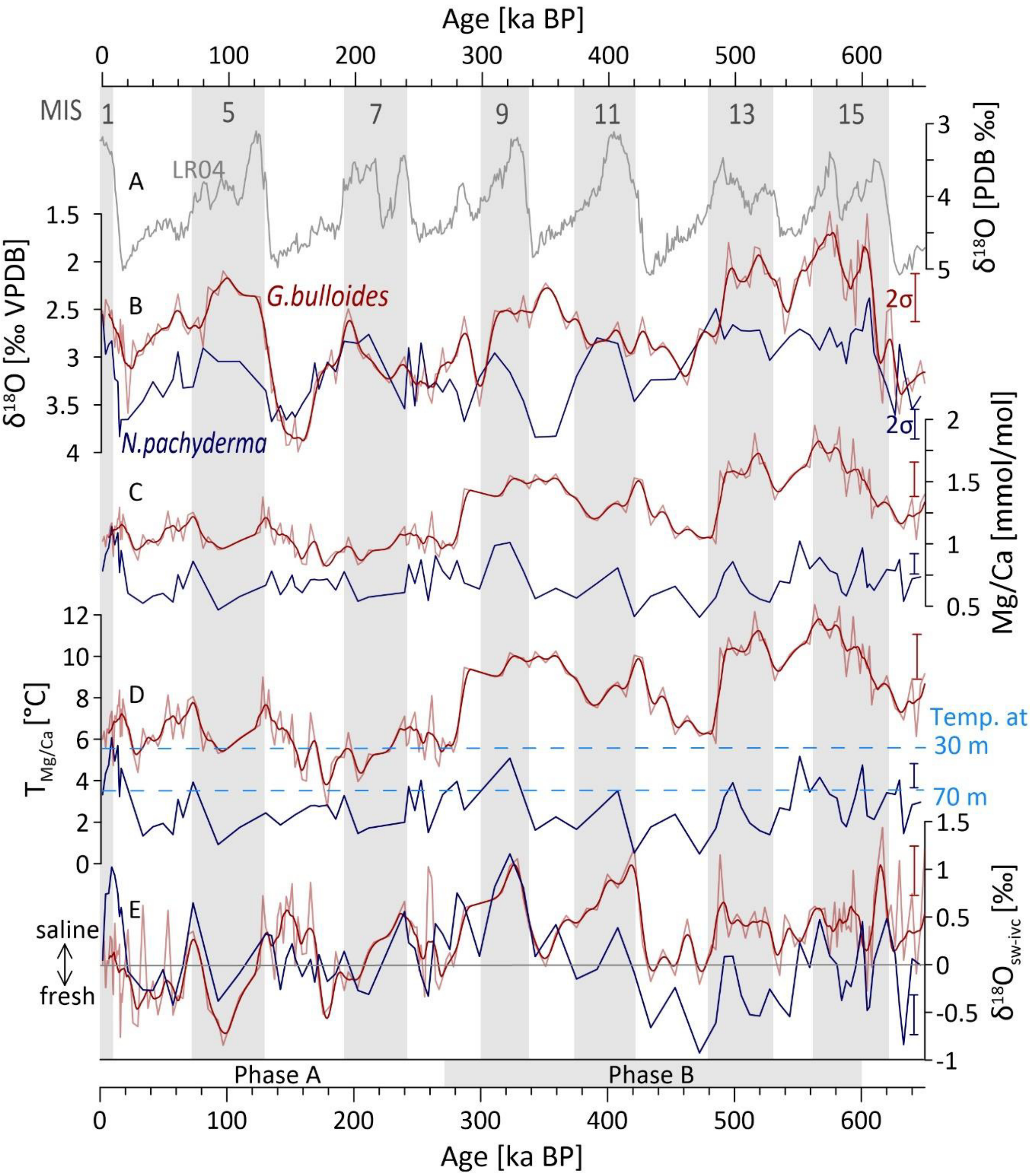

Figure 2.3: Foraminiferal sea surface (red = *G. bulloides*, all data (thin line) overlain by a 10 ka unweighted smooth (thick line)) and sub sea surface (dark blue = *N. pachyderma*) proxy data of core SO264-45 versus age. **A**: global benthic LR04 $\delta^{18}O$ climate record (Lisiecki and Raymo, 2005) for reference. **B:** foraminiferal $\delta^{18}O$; **C**: foraminiferal Mg/Ca; **D**: reconstructed sea surface ($SST_{Mg/Ca}$) and subsurface ($subSST_{Mg/Ca}$) temperatures; dashed blue lines = modern annual mean water temperatures at the defined living depths of *G. bulloides* (~30 m) and *N. pachyderma* (~70 m) (Locarini et al., 2018). **E**: Relative changes in Ice-volume corrected $\delta^{18}O_{sw}$ deviating from the calculated modern value (gray line). Gray shadings and numbers mark Marine Isotope Stages (MIS 1-17). Error bars mark the 95% standard deviation (2σ). Phase A (0-270 ka) & B (270-600 ka) are indicated by gray boxes.

than in the adjacent glacials. In contrast to the cold MIS 16 (min ~ 7°C), MIS 14 remains rather warm with minimum temperatures of ~9.5°C. At 480 ka BP, the $SST_{Mg/Ca}$ abruptly decreases by ~4°C (calculated as the temperature difference between three data points prior and after the decrease; the decrease itself occurs between two data points) coming close to the modern-day SST value (Figure 2.3). This decrease is followed by an overall increasing $SST_{Mg/Ca}$ trend for the next 200 ka. Phase B ends at ~ 280 ka BP after a second abrupt $SST_{Mg/Ca}$ decrease of ~3.5°C (calculated as the temperature difference between three data points prior and after the decrease; the decrease itself occurs between two data points). From here on (phase A) $SST_{Mg/Ca}$ remain rather low with an average of ~ 6.1°C and show only minor variations (max ±2°C) around the modern annual mean temperature at 30 m of ~5.5°C (Locarnini et al., 2018). The warmest $SST_{Mg/Ca}$ during this time interval occurs at the beginning and end of MIS 5 and in MIS 2 while in the middle of MIS 7 and 6 the $SST_{Mg/Ca}$ is coldest.

N. pachyderma shows consistently lower Mg/Ca ratios than *G. bulloides*, which vary between 0.41 and 1.14 mmol/mol with $subSST_{Mg/Ca}$ estimates between 0.5 and 6.1°C (Figure 2.3). Throughout the entire record, the $subSST_{Mg/Ca}$ show amplitude variations of ±3°C around an average of ~2.9°C. This average matches the modern annual temperature at thermocline depth of ~3°C (Locarnini et al., 2018). The highest $subSST_{Mg/Ca}$ of up to ~6°C is reached at the transition to the Holocene and the lowest with ~0.5°C during MIS 12. In contrast to the $SST_{Mg/Ca}$ the $subSST_{Mg/Ca}$ do not show a shift towards warmer temperatures prior to 280 ka BP, yet rather cold subsurface conditions between MIS 13 and MIS 10. From MIS 5 to MIS 1 $subSST_{Mg/Ca}$ and $SST_{Mg/Ca}$ follow a similar low-amplitude pattern.

The $\delta^{18}O_{sw-ivc}$ records reveal a different pattern than the $SST_{Mg/Ca}$ and $subSST_{Mg/Ca}$ records (Figure 2.3). Both, the seasurface and subsurface $\delta^{18}O_{sw-ivc}$ records have rather similar amplitudes and fluctuations. Between 650- 350 ka BP *G. bulloides* shows constantly higher $\delta^{18}O_{sw-ivc}$ values than *N. pachyderma*. Between 0 and ~350 ka BP, however, both records lie within error range of each other and alternately show higher values. Prior to 280 ka BP the $\delta^{18}O_{sw-ivc}$ records of both species tend to be higher in interglacials and lower in glacials.

2.3.2. Productivity and terrigenous input

The XRF-based Ba/Ti record and thus the reflection of marine productivity shows a clear glacial-interglacial cyclicity. Ba/Ti values start to increase during the deglaciations and reach their maxima during the early interglacials (Figure 2.4). During the late interglacials and the subsequent early glacials low Ba/Ti values predominate. This pattern even holds for the period MIS 15-14, although the Ba/Ti ratios remain on an exceptionally high level during glacial MIS 14, which even exceeds typical deglacial to early interglacial values. The deglaciation towards MIS 13 is again characterized by a continuous increase in Ba/Ti. In the late interglacial MIS 13 (~500-480 ka BP), we observe a rapid and significant decrease in Ba/Ti to typical glacial values, synchronous to significant changes in Fe and $SST_{Mg/Ca}$ (Figure 2.4).

The XRF-based Fe record, which is used as a proxy for terrigenous input commonly increases at the transitions from late interglacials to early glacials and decreases during the glacials. Prior to MIS 12, no distinct glacial-interglacial pattern is recognizable. Between ~560 and ~500 ka BP, Fe values are exceptionally low, which is followed by a sudden increase from ~500-480 ka BP (Figure 2.4). Ba/Ti and Fe appear to be anticorrelated with low Fe values in times of high Ba/Ti and vice versa. Thus, between MIS 13 and 5 Ba/Ti maxima occur on average ~30 ka earlier than Fe maxima.

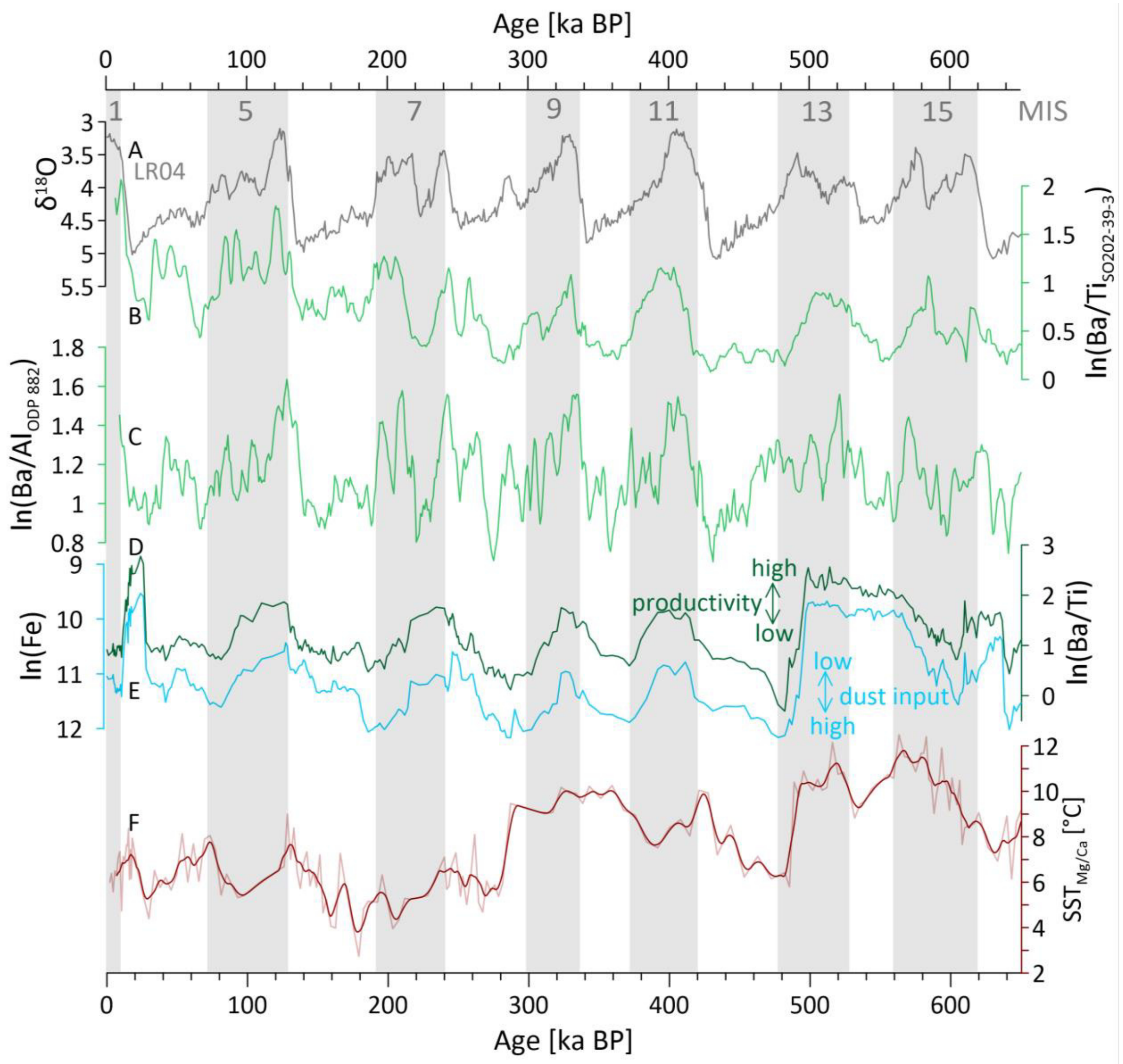

Figure 2.4: Marine productivity and eolian flux in comparison to the $SST_{Mg/Ca}$ development**:** **A**: LR04 δ18O benthic isotope stack from Lisiecki and Raymo (2005). **B-D**: XRF-based productivity records from the North Pacific displayed as natural logarithm; high Ba/Al and Ba/Ti values point to a high marine productivity. **B:** Ba/Ti record of SO202-39-3 (Korff et al., 2016). **C:** Ba/Al record of ODP 882 (Jaccard et al., 2010). **D:** Ba/Ti record SO264-45 (this study). **E**: XRF-based Fe record as indicator for eolian dust supply to core SO264-45 (this study); note the descending y-axis. **F**: $SST_{Mg/Ca}$ record SO264-45 (thin line = raw data; thick line = 10 ka unweighted smooth). Gray shadings and numbers mark Marine Isotope Stages (MIS1-16).

2.4. Discussion

2.4.1. Influence of changes in the Kuroshio/Oyashio Current System on upper ocean temperatures at Jimmu Seamount

At the study site, glacial-interglacial changes are well documented in the benthic and planktic $\delta^{18}O$ records of all species with high $\delta^{18}O$ values during glacials and low $\delta^{18}O$ values during interglacials. This indicates that climate variations did have an effect on both the upper and deep ocean. Yet in our $SST_{Mg/Ca}$ and $subSST_{Mg/Ca}$ records changes between glacial and interglacial periods are neither particularly dominant nor continuously reflected. Thus, the observed temperature variations and especially the mode shift between phases A and B, recorded in the $SST_{Mg/Ca}$ record must have been caused by different forcing mechanisms. A shift from higher SSTs prior to 280 ka BP to colder SSTs in more recent times, as reflected in our proxy data, does occur in few records from certain areas in the North Pacific (*cf.* 2.4.1.1) but it is neither a global phenomenon nor significant in the whole Pacific region (Morley and Heusser, 1997; Herbert et al., 2001; Lang and Wolff, 2011; Bordiga et al., 2013). Thus, our observed $SST_{Mg/Ca}$ shift cannot be explained by a general cooling of the (North) Pacific climate after 280 ka BP yet must be linked to changes in local hydrography, most likely the complex interplay of the Kuroshio and Oyashio Current.

2.4.1.1. ENSO-induced changes of the Kuroshio Current

Today the volume transport of the Kuroshio Current is linked to ENSO and the induced changes of the location of the NEC's bifurcation point (*cf.* 2.1.1). This way the Kuroshio velocity and volume transport is increased during La Niña years and reduced during El Niño years (Qiu and Lukas, 1996; Yuan et al., 2001; Kim et al., 2004). It is likely that such changes do not only appear on decadal timescales, but also over longer time periods. This is indicated by a study from the Ryukyu Arc region (north of the NECs bifurcation point) based on planktic foraminiferal assemblages. It shows that during the last 21 ka BP lower rates of surface transport in the Kuroshio Current occurred when more El Niño-like conditions prevailed in the Equatorial Pacific (Ujiié et al., 2003). Assuming that these mechanisms did not significantly change over the past 650 ka BP, they would also have affected the upper ocean dynamic at our study site.

To test this hypothesis, we compare our $SST_{Mg/Ca}$ record to proxy records from De Garidel-Thoron et al. (2005) and Jia et al. (2018) (Figure 2.5). Both studies reconstructed mean states of more La Niña-like and more El Niño-like conditions in the WPWP on millennial timescales. De Garidel-Thoron et al. (2005) used records from the WPWP (MD97-2140: SSTs generated via Mg/Ca from planktic foraminifera) and the EEP (ODP846: SSTs generated from alkenones) to calculate the temperature difference between the WPWP and the EEP ($\Delta T_{WPWP\text{-}EEP}$). Jia et al. (2018) calculated the $\Delta T_{WPWP\text{-}EEP}$ by using four Mg/Ca-based SST records from the WPWP as well as three SST records from the EEP generated from Mg/Ca and UK_{37}. The records from Jia et al. (2018) and De Garidel-Thoron et al. (2005) are not entirely concordant (Figure 2.5). This is likely a result of local influences on the temperature development besides ENSO which reflects the highly dynamic development of the WPWP and EEP and uncertainties in age models. Yet, the general trends of both records are rather similar and thus we assume that they are a reliable indicator for major changes of ENSO dynamics on long time scales. Thus, in our approach to compare our $SST_{Mg/Ca}$ record to these paleo-ENSO records we concentrate on longer-term trends rather than short-term variations.

In phase B (650-280 ka BP) we observe up to 6.5°C higher $SSTs_{Mg/Ca}$ than modern values. During this phase, the records from Jia et al., (2018) and De Garidel-Thoron et al. (2005) show several intervals of very large temperature gradients between the WPWP and the EEP pointing to prevailing La Niña-like conditions (Figure 2.5). From MIS 16 to MIS 15 we observe a strong increase of $SST_{Mg/Ca}$ from ~7.5 to >11°C, while both ENSO records indicate a shift from El Niño-like to a 'extreme' La Niña-like conditions. This coherent shift to higher SSTs and La Niña-like conditions implies an increased Kuroshio Current and thus through the increased amount of Kuroshio water in the Kuroshio-Oyashio transition zone a northward shift of the SAF. From the modern surface temperature distribution we infer that the SAF was shifted at least 5° northwards, so that it reached a position north of our study site (Figure 2.1, 2.6). This way surface water from the mixed water region would have reached the study site, thereby causing SSTs that are significantly higher than during times where the SAF is located south of the study site and the surface water is dominated by water from the Subarctic Current (Figures 2.1, 2.6).

Around 480 ka BP we observe an abrupt $SST_{Mg/Ca}$ decrease of ~4°C, which is accompanied by an abrupt and pronounced change from very strong La Niña-like to the strongest El Niño-like phase in the record from Jia et al. (2018). This change is also reflected in the record from De Garidel-Thoron et al. (2005) yet less pronounced (Figure 2.5). This change has most likely reduced the volume and velocity transport of the Kuroshio Current so immensely, that it triggered a southward displacement of the SAF to a position south of our study site (Figure 2.6). Between ~470-440 ka BP both tropical ENSO records show another increase of $\Delta T_{WPWP-EEP}$ and thus La Niña-like conditions. Similar to before, this change will have increased the Kuroshio Current's volume and velocity transport and thus caused another northwards shift of the SAF. From here until 280 ka BP La Niña-like conditions are dominant, especially in the record from De Garidel-Thoron et al. (2005). Minor decreases of the $\Delta T_{WPWP-EEP}$ between 600-480 ka BP and 440-280 ka BP do not seem to have had enough influence on the Kuroshio Current strength to induce a shift of the SAF to a position south of the study site. This suggests that there might be a tipping point in Kuroshio Current strength that needs to be reached in order to induce a shift of the SAF to a position north of the study site.

At ~280 ka BP we observe a second abrupt $SST_{Mg/Ca}$ decrease (~3.5°C) (Figure 2.5), while the ENSO records from De Garidel-Thoron et al. (2005) and Jia et al. (2018) indicate a change from extreme La Niña-like to more El Niño-like conditions. Thus, we assume that there was another southward displacement of the SAF to a position south of the study site. From here on (phase A: 280-0 ka BP) the $SST_{Mg/Ca}$ is on average 3.6°C lower than in phase B and shows minor variations (~±2°C) around the modern annual mean temperature at 30 m of ~5.5°C (Figure 2.5). During this period both tropical records indicate that El Niño-like conditions prevailed in the tropical Pacific, with almost no strong La Niña-like phases (except for 20-5 ka BP in the record from Jia et al., (2018)). Variations between El Niño-like and La Niña-like conditions within phase A are not corresponding to $SST_{Mg/Ca}$ changes, which further implies that tropical surface water entering the Kuroshio-Oyashio transition zone via the Kuroshio

Current/Kuroshio Extension did no longer have an influence on the $SST_{Mg/Ca}$ development at the study site. Therefore, the SAF likely stayed south of the study site between 280-0 ka BP. The assumption of the intensification and northward migration of the Kuroshio Current/Extension in times of more La Niña-like conditions in the tropics is further supported by a study from Yamane (2003) from the Shatsky Rise (core S-2; Figure 2.1). Shatsky Rise is located about 13° south of our core location, were the surface water is dominated by the Kuroshio Current.

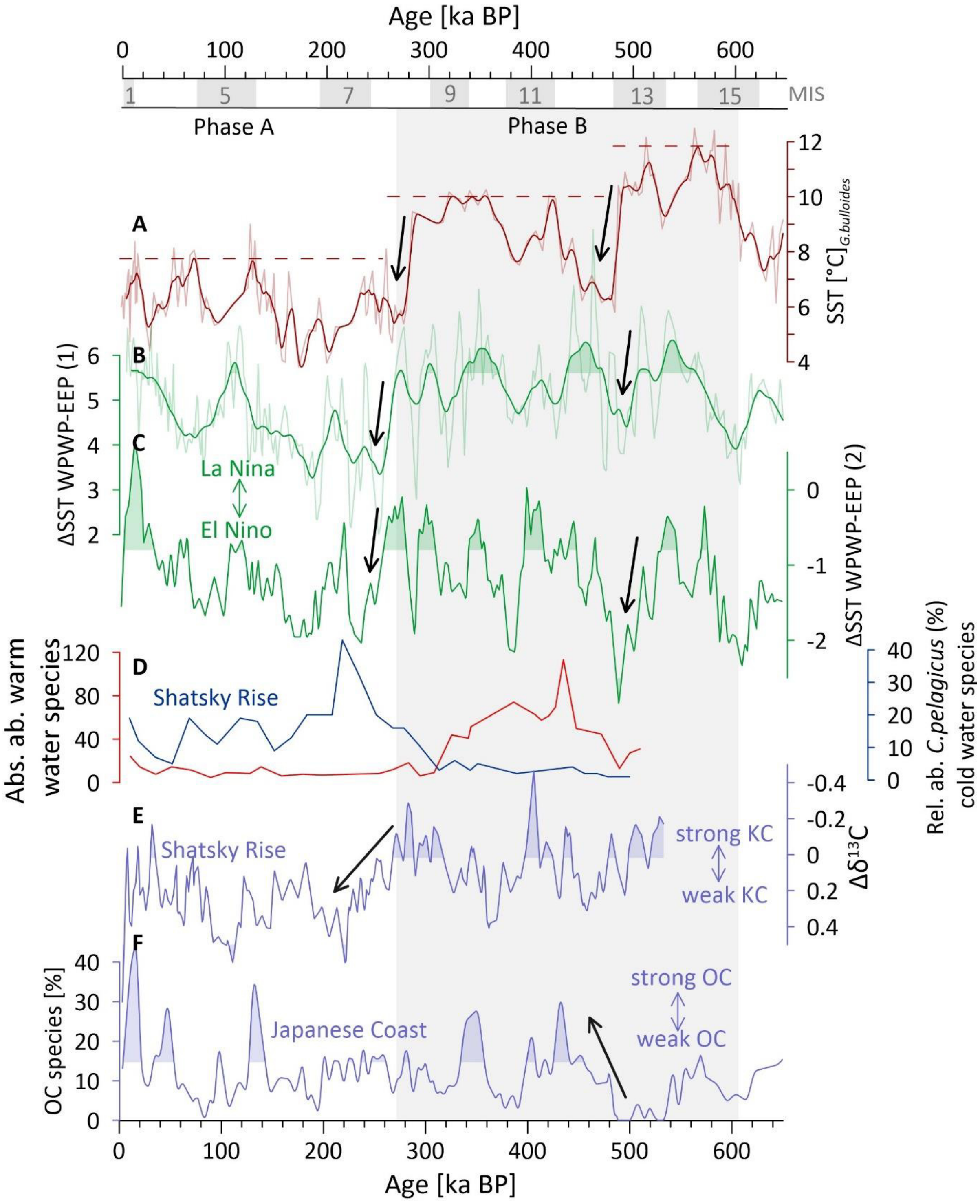

Figure 2.5: ENSO effect on the N Pacific oceanography. **A:** $SST_{Mg/Ca}$ record (thin line = raw data overlain by a 10 ka unweighted smooth (thick line) at core location SO264-45. Maximum $SST_{Mg/Ca}$ divided into different time periods are marked as dotted lines. **B&C:** Proxy records of ENSO variability from De Garidel-Thoron et al. (2005; thin green line = complete record overlain by a 10 ka unweighted smooth = thick green line; B) and Jia et al. (2018; green; C). High $\Delta SST_{WPWP-EEP}$ values point to more La Niña-like conditions in the tropical W Pacific. **D**: Relative abundance of cold water species (blue) and absolute abundances of warm water species (red) reflecting a significant change in Kuroshio influence at Shatsky Rise (Chiyonobu et al., 2012). **E**: $\delta^{13}C$ gradient between shallow- and deep-dwelling planktonic foraminifera revealing Kuroshio Current strength variations at Shatsky Rise (Yamane 2003). **F**: Oyashio Current strength off the Japanese coast approximated from the abundance of radiolarian fauna typical for the OC (Matsuzaki et al., 2014). Curve fillings (B, C, E & F) mark the upper 25% of the data. Phase A and B denote two phases of different ocean settings characterized by a mode shift between a phase of extreme La Niña-like conditions (~240-650 ka) to a phase of less strong La Niña-like and more El Niño-like like conditions (~260 ka - present). Marine Isotope Stages (MIS1-17) are marked. Black arrows mark prominent transitions between phases. Phase A (0-270 ka) & B (270-600 ka) are indicated by gray boxes.

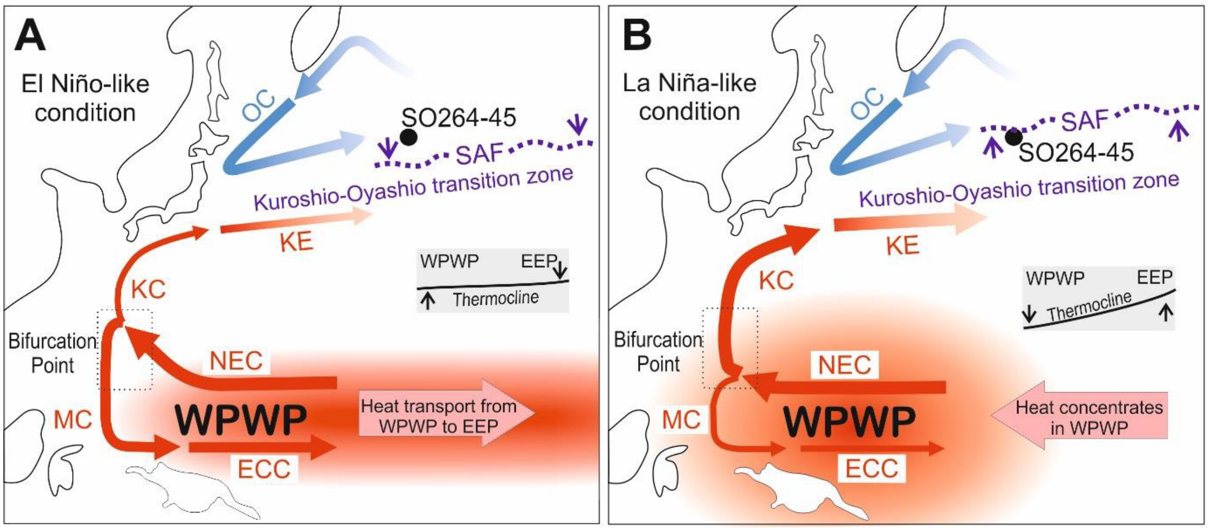

Figure 2.6: Schematic scenarios to explain the SST development and SAF positioning in the study region in terms of more La Niña-like (**B**) and more El Niño-like (**A**) climate conditions. The heat distribution and flux between the Western Pacific Warm Pool (WPWP) and the Eastern equatorial Pacific (EEP) are indicated by arrows and color shading in. Thicker (thinner) arrows indicate stronger (weaker) currents. ECC = Equatorial Counter Current, KC = Kuroshio Current, KE = Kuroshio Extension, MC =Mindanao Current, NEC = North Equatorial Current, OC = Oyashio Current, SAC = Subarctic Current, SAF = Subarctic Front. Gray boxes display thermocline variations in the tropical region.

Yamane (2003) compared $\delta^{13}C$ values of shallow and deep-dwelling planktonic foraminifera and interpreted small $\Delta\delta^{13}C$ values as sustained influence of Kuroshio (Extension) water (Figure 2.5). This record implies that in phase B, where we observe a high $SST_{Mg/Ca}$ there was a greater influence of the subtropical Kuroshio water at Shatsky Rise than in phase A or modern days, where we observe lower a $SST_{Mg/Ca}$ (Figure 2.5). Moreover, the abrupt $SST_{Mg/Ca}$ decrease at 280 ka BP (this study) goes along with Yamane's observation of a reduced influence of the Kuroshio Current at Shatsky Rise. Another study from the Shatsky Rise (ODP 1210A) by Chiyonobu et al. (2012) indicates a decrease of warm-water species of calcareous nannofossils from $5x10^9$ specimens/m²/ka to $2x10^9$ specimens/m²/ka at ~300 ka BP, while the relative abundance of the cold-water species *Coccolithus pelagicus* increased. Notably, the time difference between the abundance change and our $SST_{Mg/Ca}$ decrease could be a feature of the different resolution of time models in the study of Chiyonobu et al. (2012) and our own study and is not necessarily an indicator of a different timing between Shatsky Rise and our core location.

Thus, we assume that during very strong La Niña-like conditions in the tropical Pacific, as observed temporally in phase B, the high velocity transport of the Kuroshio Current and thus the enhanced amount of tropical water in the Kuroshio-Oyashio transition zone caused a northward shift of the SAF. During times of more El Niño-like conditions, like in phase A, the SAF stayed south of the core location, which is reflected by the temporally cooler $SST_{Mg/Ca}$. Yet the temperature variations within phase A and B can not exclusively be explained by variations in the SAF position but must have had additional influencing factors (*cf.* 2.4.1.2).

2.4.1.2. Variations of the Oyashio/Subarctic Current

Aside from changes of the Kuroshio Current/Extension, changes of the Oyashio/Subarctic Current are of major importance for the surface temperature development at our study site. This becomes apparent when comparing our $SST_{Mg/Ca}$ record to the proxy record of Matsuzaki et al. (2014) (Figure 2.5). They investigated the radiolarian fauna east of Japan, where the Oyashio Current deviates from the coast and enters the open Pacific as Subarctic Current (core C9001C) (Figure 2.1, 2.6). Although there is no peak-to-peak correlation between increased abundances of species typical for the Oyashio Current and thus an intensification of the Oyashio and lower $SST_{Mg/Ca}$ at our study site, some parallels are apparent.

Between 600 and 480 ka BP, there are events of strong La Niña-like conditions in the tropics, and our $SST_{Mg/Ca}$ record shows its highest values while Matsuzaki et al. (2014) observes a weak Oyashio Current. At ~480 ka BP, where we observe a sudden temperature decrease at our study site there is not only a change from strong La Niña-like to strong El Niño-like conditions yet also an intensified Oyashio Current. Thus, the combination of an intensified Oyashio Current in line with the change towards strong El Niño-like conditions (and thus a weak Kuroshio Current) could have caused the a southward displacement of the SAF. Through such a southward shift of the SAF more cold subarctic water would reach our study site and could cause the observed sudden temperature decrease at ~480 ka BP.

After 480 ka BP, $SST_{Mg/Ca}$ increases again, which we link to several phases of strong La Niña-like conditions. Yet, even though the La Niña-like phases are similarly pronounced and long, as before 480 ka BP, the maximum $SST_{Mg/Ca}$ remains lower (Figure 2.5). We assume that this observed $SST_{Mg/Ca}$ difference is linked to the Oyashio Current. Between 480-390 ka BP and 360-340 ka BP the Oyashio Current is transiently enhanced (Figure 2.5; Matsuzaki et al., 2014). As both Currents contribute to the water of the Kuroshio-Oyashio transition zone it is likely that this enhanced influence of the Oyashio Current caused an overall lowered SST-level in the Kuroshio-Oyashio transition zone. Thus, the enhancement of the Oyashio/Subarctic Current system after 480 ka BP muted the SST-effect of the La Niña-like induced enhancement of the Kuroshio Current at our study site.

Between ~20-5 ka BP the record of Jia et al. (2018) shows another phase of very strong La Niña-like conditions in the tropical Pacific. Similar $\Delta T_{WPWP\text{-}EEP}$ values have caused a shift of the SAF in phase B. Yet, between ~20-5 ka BP our $SST_{Mg/Ca}$ record does not show any significant rise (Figure 2.5). In contrast to previous northward migrations of the SAF in phase B, the Oyashio Current is very strong between ~20-5 ka. We hence assume that the strong Oyashio/Subarctic Current prevented a significant northwards shift of the SAF between ~20-5 ka BP.

2.4.1.3. Glacial-interglacial shifts of the SAF

It has been suggested that the frontal zones in the Kuroshio-Oyashio transition area migrated northwards during interglacials and southwards during glacials at least during the last two glacial-interglacial cycles (Thompson and Shackleton, 1980; Kawahata and Ohshima, 2002; Harada et al., 2004; Yasudomi et al., 2014; Gallagher et al., 2015). Assuming that the described changes occurred throughout our entire studied time interval, such shifts could have contributed to changes in $SST_{Mg/Ca}$ and $\delta^{18}O_{sw-ivc}$ at our study site. On modern timescales and throughout the last 280 ka BP (phase A), our study site was located north of the SAF and thus dominated by subarctic water (Figure 2.6), which is indicated by the rather cold $SST_{Mg/Ca}$. During this time interval our $SST_{Mg/Ca}$ record does not show changes that would fit to glacial-interglacial variation. Therefore, we conclude that if there had been a northward migration of the SAF during interglacials it can only have migrated to a position still south of our study site. In phase B, we assume our study site to be located south of the SAF (Figure 2.6). This is indicated by the rather warm $SST_{Mg/Ca}$. Within this time interval, the $SST_{Mg/Ca}$ and $\delta^{18}O_{sw-ivc}$ broadly follow glacial-interglacial cycles except for MIS 11-10. So if the SAF migrated further north during interglacials it could have caused warmer, more saline water from the Kuroshio-Oyahio transition to reach the study site, whereas southwards shift during glacials could have brought the SAF closer to the core location and thereby caused an increase of colder, less saline water from the Subarctic Current. Thus it is likely that glacial/interglacial induced shifts of the SAF contributed to our observed $SST_{Mg/Ca}$ pattern.

2.4.1.4. The $subSST_{Mg/Ca}$ record from *N. pachyderma*

The $subSST_{Mg/Ca}$ record derived from *N. pachyderma* is consistently lower than the $SST_{Mg/Ca}$ record derived from *G. bulloides* (Figure 2.3). This difference reflects firstly the deeper habitat depth of *N. pachyderma* in comparison to *G. bulloides,* where the latter inhabits water depths above the thermocline, whereas the former occurs at and below the thermocline. Thus the temperature difference between the two species indicates a stable and pronounced thermocline stratification. Secondly the seasonal bias is expressed, as *G. bulloides* reflects annual $SST_{Mg/Ca,}$ whereas *N. pachyderma* reflects $subSST_{Mg/Ca,}$ derived from the colder seasons from autumn to spring. In phase A (280-0 ka BP) our $SST_{Mg/Ca}$ and $subSST_{Mg/Ca}$ records show similar variations in amplitude in MIS 7 and 5-1, yet with an average offset of 3.5°C, while in MIS 6 the $SST_{Mg/Ca}$ and $subSST_{Mg/Ca}$ records show opposing trends.

In phase B (600-280 ka BP) the $SST_{Mg/Ca}$ record yields significantly (up to ~6.5°C) higher values than in phase A, while the $subSST_{Mg/Ca}$ record does not reflect this trend. This indicates that the dispersal of Kuroshio-Oyahio transition water in phase B was either a pure surface phenomenon, or was linked to the different temperature tolerance of both species. In the first case, water from the Kuroshio-Oyahio transition would have migrated northwards in form of a warm surface water lens, while the subsurface would have still been dominated by water from the Subarctic Current. Thus, there would have been a very pronounced shallow thermocline, as indicated in Supplementary Figure 2.7. However, we consider it more likely that the different temperature trends of *N. pachyderma* and *G. bulloides* are not only a phenomenon of significantly different surface and subsurface temperature evolution, but an ecological phenomenon. *N. pachyderma* is less tolerant to warmer temperatures and prefers values below 7°C (*cf.* 2.2.2 and Supplement 2.7.1). Therefore, it occurs less during warmer seasons than *G. bulloides*. We assume that in phase B, with an increased influence of Kuroshio-Oyashio transition water at the study site, temperatures in the preferred depth habitat of *N. pachyderma* exceeded optimal temperatures even in spring and autumn. Thus, in times of a northward displacement of the SAF *N. pachyderma* would most likely reflect a pure winter signal, which is significantly colder than the annual signal from *G. bulloides*. This change in seasonality is in accordance with plankton tow studies from the North Pacific that suggest that in modern days, *N. pachyderma* occurs from autumn to spring at colder sites (~50°N, ~165°E) while their abundance stays low until December at warmer sites (~40°N, ~165°E) (Taylor et al., 2018; Supplememt 2.7.1).

2.4.2. Marine productivity changes

Higher marine productivity during deglaciations and interglacials and lower productivity during glacials as observed in our Ba/Ti record is common in the North Pacific and its marginal seas (Narita et al., 2002; Gorbarenko et al., 2004; Kienast et al., 2004; Nürnberg and Tiedemann, 2004; Jaccard et al., 2005, 2010; Brunelle et al., 2007; Shigemitsu et al., 2007; Galbraith et al., 2008; Gebhardt et al., 2008; Riethdorf et al., 2013). In our record we further observe, that the productivity already starts to increase during the deglaciations and decreases during the late interglacials. This is similar to observations at ODP Site 882 (Jaccard et al., 2010) located north of our site (Figure 2.1) which also shows productivity increases during deglaciations and its highest values in the early interglacials (Figure 2.4). A similar feature is observed for site SO202-39-3 (Korff et al., 2016) located south of our study site in the area of the Kuroshio Extension (Figure 2.1, 2.4). The forcing mechanisms for these productivity patterns, however, are still a matter of debate (Jaccard et al., 2010; Knudson and Ravelo, 2015; Korff et al., 2016). For the North Pacific, most authors suggest a change of nutrient supply, and in the subarctic marginal seas light limitation through sea ice cover and changes in stratification as main drivers for productivity changes (Narita et al., 2002; Gorbarenko et al., 2004; Kienast et al., 2004; Jaccard et al., 2005, 2010; Brunelle et al., 2007; Shigemitsu et al., 2007; Galbraith et al., 2008; Gebhardt et al., 2008; Riethdorf et al., 2013; Davis et al., 2020). As our site is located south of the area where sea ice would have a direct influence on productivity, we exclude it as a forcing mechanism. Therefore we conclude that the availability of nutrients or their utilization causes the observed glacial-interglacial productivity pattern.

Iron fertilization has been invoked as an important driver for nutrient sequestration efficiency and thus, an enhanced supply of the micronutrient Fe could increase productivity (Boyd et al., 2004; Harrison et al., 2004; Tsuda et al., 2003). One of the sources of Fe is aeolian transport (Boyd et al., 2007; Hovan et al., 1991; Kawahata et al., 2000; Shigemitsu et al., 2007). To test whether the Fe input via dust caused our observed productivity pattern, we compared our XRF-Fe record of core SO264-45, used as a proxy for terrigenous input via wind to our Ba/Ti record (Figure 2.4). The proxy records are apparently anticorrelated suggesting that Fe fertilization via dust is not the (principal) driver of marine productivity at our study site, although, we cannot say to what extent it still contributed to the observed pattern.

The amount of nutrient transport via water masses could have contributed to changes in productivity (Jaccard et al., 2005; Galbraith et al., 2007; Nishioka et al., 2011; Costa et al., 2018; Gray et al., 2018). Today, nutrient-rich water from the Oyashio/Subarctic Current dominates the upper ocean at our study site. The transported nutrients reach the mixed layer through vertical wintertime mixing (Nishioka et al., 2011). Our $SST_{Mg/Ca}$ record, which is linked to changes in the Kuroshio-Oyashio transition zone does not show the same fluctuations as our productivity record. Thus, although it could have contributed to changes in productivity we assume that the interplay of the Kuroshio and Oyashio Current is not the main driver for the observed productivity pattern at our study site. We do, however, consider that the amount of transported nutrients might have changed on glacial-interglacial timescales. Lembke-Jene et al. (2017) show that the export of nutrients from the Okhotsk Sea increased at the beginning of the deglacial warm phases Allerød and Preboreal, because of an enhanced input of iron and nutrient-rich terrestrial material from the Siberian hinterland via the Amur River caused by melting processes. They argue that such an increased export of nutrients from the Okhotsk Sea could have caused temporary nutrient-replete conditions in the Subarctic North Pacific. Riethdorf et al. (2013) also observe an enhanced input of terrestrial-derived organic matter from flooded shelf areas during early deglacial phases. As water from the Bering and Okhotsk Sea feeds the Oyashio/Subarctic Current, these nutrients could have reached the study site and caused an increase in productivity. Assuming that an enhanced terrestrial sourced nutrient supply from marginal seas like the Sea of Okhotsk and the Bering Sea via subsurface water did not only occur on millennial- but also on glacial-interglacial timescales, this could contribute to our observed productivity pattern. Yet to further clarify on this additional proxy records on longer time scales and in the open North Pacific would be needed.

Further it has been proposed for subarctic and Antarctic sites that strong stratification during glacials limits nutrient availability at the surface while weak stratification in interglacials enables upwelling of nutrients-rich deep water thereby enhancing productivity (Jaccard et al., 2005; Brunelle et al., 2007; Galbraith et al., 2008). Yet this topic alongside the efficiency of nutrient uptake is still a matter of debate (e.g. Knudson and Ravelo, 2015) for which further studies with detailed nutrient records and very reliable control would be needed.

2.5. Conclusion

Through the reconstruction of Mg/Ca and $\delta^{18}O$ based (sub)surface temperature and $\delta^{18}O_{sw-ivc}$ in the open Northwest Pacific and a comparison of XRF-based Ba/Ti and iron records we draw the following conclusions regarding the hydrological and productivity variations at the northern boundary of the Kuroshio-Oyashio transition zone:

- The $SST_{Mg/Ca}$ development at our study site is strongly related to changes in the velocity transport of the tropical Kuroshio Current induced by ENSO. In phases of very strong La Niña-like conditions in the tropics, the NEC bifurcation point migrates southward which enhances the velocity transport of the Kuroshio Current/Extension. This way more tropical water enters the transition zone, which causes a northward displacement of the SAF to a position north of our study site, thus a relocation of at least 5°. This way more transition water reaches our core position, which we observe as higher $SST_{Mg/Ca}$ in the time interval 280-600 ka BP. Further, we show that shifts of the SAF cause very abrupt strong temperature changes at our core position e.g. at 480 and 280 ka BP. Such shifts of the SAF have been proposed on shorter timescales and for areas closer to the cost, yet our $SST_{Mg/Ca}$ record makes it possible to track these shifts on longer time scales and into the open Pacific.

- The $SST_{Mg/Ca}$ development at our study site is further influenced by changes in the strength of the Oyashio/Subarctic Current. Both, the Kuroshio Current/Extension and the Oyashio/Subarctic Current contribute to the water in the Kuroshio-Oyashio transition zone so that an enhancement of the Oyashio Current can mute the effect of an enhancement of Kuroshio Current. We observe such an effect a) between 480-280 ka BP, where the enhanced influence of the Subarctic Current at our study site causes temperatures to stay lower than in the time interval 480-600 ka BP, even though there are similarly strong and long La Niña-like phases in both intervals and b) between ~20-5 ka BP, where a strong Oyashio Current seems to prevent a shift of the SAF up to a position north of our study site.
- Glacial-interglacial variations in the Kuroshio-Oyashio transition zone also influence the $SST_{Mg/Ca}$ development at our study site, yet they are less pronounced in our data than the mode shift between phases A and B. In phase B, where the SAF is located north of our study we observe an increase of warmer, more saline water in interglacials and colder, less saline water during glacials. We link these shifts to general glacial-interglacial variations of the Kuroshio-Oyashio transition zone and the front system.
- The productivity at our study site follows glacial-interglacial patterns with high values during the deglaciations/early interglacials and low values during glacials. Thus, we conclude that productivity is not primarily linked to the changing influences of Kuroshio/Oyashio water at our study site.
- Our Fe and Ba/Ti records are anticorrelated, thus we conclude that Fe fertilization via dust is not the (principal) driver of marine productivity at our study site. We further hypothesize that the observed productivity pattern might be linked to (a) glacial/interglacial variations in the subpolar marginal seas and the induced nutrient supply via the subarctic water masses in deglaciations because of melting processes and (b) changes in stratification that have an influence on nitrate availability and utilization.

2.6. Acknowledgements

We thank the German Ministry of Education and Research (BMBF), which provided funding for cruise SO264 (SONNE-Emperor) with R/V SONNE in 2018 through project 03G0264A and for the funding of the NOPAWAC (The North Pacific in Warming Climates) project: 03F0784A. This work was further supported by initial studies within the research programs “PACES-II” and “Changing Earth – Sustaining Our Future” funded through institutional funds from AWI and GEOMAR. We thank the captain, crew, and shipboard scientific crew of R/V

SONNE for their support. We are grateful to our lab technicians N. Gehre and S. Fessler for their great support, G. Mollenhauer from AWI Bremerhaven for AMS^{14}C measurements. We are thankful to the reviewers, whose comments considerably helped to improve the manuscript.

2.7. Supplement

Presented data is available online at the Data Publisher for Earth and Environmental Science, PANGEA under:

- https://doi.org/10.1594/PANGAEA.949795
- https://doi.org/10.1594/PANGAEA.949771

2.7.1. Ecology and distribution of *G. bulloides* and *N. pachyderma* in the North Pacific

Globigerina bulloides is a spinose morphospecies that occurs in high abundances in transitional to subpolar regions (Bé et al., 1977; Coulbourn et al., 1980; Schiebel and Hemleben, 2017; Schiebel et al., 2017). Different genotypes have been recognized within the morphospecies *G. bulloides*, which inhabit different habitats (Darling and Wade, 2008; Seears et al., 2012; Morard et al., 2013). *G. bulloides* from Type II (Types IIa-IIe and IIg) occur in cooler transitional and high latitude regions (Darling et al., 2000; Darling and Wade, 2008) and thus, most likely at our study site. In the North Pacific, *G. bulloides* mainly dwells near the surface above the thermocline (Field, 2004; Kuroyanagi and Kawahata, 2004; Taylor et al., 2018). As the thermocline at the study site lies at ~ 40-60 m (Locarnini et al., 2018) (figure 2.7) we assume the main habitat depth at 20-60 m. This fits well with observations from multi net studies from the North Pacific (Taylor et al., 2018), where the highest standing stock of *G. bulloides* is found above 50 m in most areas. Yet the distribution of *G. bulloides* within the surface water column may change over time depending on hydrological conditions, and the availability of prey (Schiebel et al., 2017).

In the North Pacific, *G. bulloides* calcifies throughout the year (Kuroyanagi et al., 2008; Sagawa et al., 2013; Taylor et al., 2018 Malevich 2019). Seasonal flux data of *G. bulloides* is sparse in the open North Pacific. In the Bering Sea, *G. bulloides'* abundance increases with the increase of light and productivity during spring and summer while it is very low in winter (Asahi and Takahashi, 2007). Yet closer to the study site at ~50°N (~165°E) the abundance of *G. bulloides* is steadier throughout the year. At the onset of the phytoplankton bloom in spring there is an abundance-peak while the abundance in summer is relatively low (Kuroyanagi et al., 2008; Taylor et al., 2018). Further south at ~40°N (165°E) the flux of *G. bulloides* is more variable than at the site at ~50°N. Additional to the common spring abundance peak there is a peak of abundance in late autumn/winter (Kuroyanagi et al., 2008; Taylor et al., 2018). Taylor et al. (2018) link this variability to the location of the sediment trap at the interface between the Oyashio and the Kuroshio Current and the variable influence of these different systems that might also change throughout the seasons and years. This shows that abundance peaks of *G. bulloides* are closely linked to the changing seasonal hydrography and food availability in the western North Pacific. As our study site is at ~46°N, we expect a seasonal distribution of *G. bulloides* that is rather a combination of those observed at ~40°N and ~50°N. To account for how much a seasonal bias could influence the observed temperature signal we combined the data from the station at 40°N and 50°N (data from Taylor et al., 2018 and references therein). We calculated that ~32% of total shell flux occurred between April and June. Thus, a bias toward spring values is neglectable for our interpretation, as it does not exceed the error range of SST$_{Mg/Ca}$. We hence assume that our Mg/Ca$_{G.bulloides}$-derived temperature estimate reflects an annual signal.

There is an ongoing debate on whether shell size does influence both Mg/Ca and stable isotope values of *G. bulloides* (Spero and Lea, 1996; Elderfield et al., 2002; Martínez-Botí et al., 2011; Friedrich et al., 2012). From each sample in our study, we randomly collected specimens from a wide size range (250 – 400 µm) due to insufficient abundances in narrower size ranges. We assume that this way small and large tests contribute equally to the sample and that possible size effects will therefore, be negligible.

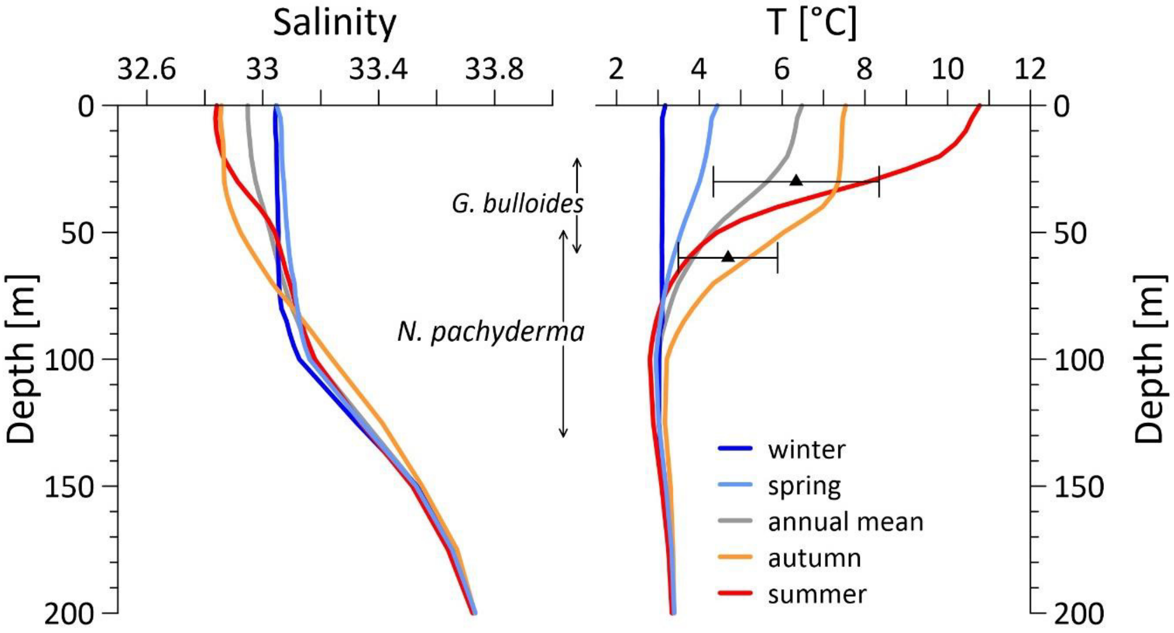

Figure 2.7: Seasonal and annual mean temperate (left) and salinity (right) profiles at 46°30'N 169°30'E (Locarini et al., 2018) and calculated late Holocene (black triangles) temperatures of core site SO264-45 from *G. bulloides* (SST$_{Mg/Ca}$) and *N. pachyderma* (subSST$_{Mg/Ca)}$in the respective depth habitats (marked with black arrows at the site). Error bars mark the 95% standard deviation (2σ).

Neogloboquadrina pachyderma is a sinistral coiling, non-spinose, sub-surface-dwelling species, which does not sequester symbionts and can be divided into several cryptic genotypes that show clear ecological differences (Darling et al., 2004, 2017; Darling and Wade, 2008; André et al., 2014). The distinction from the dextral coiling *Neogloboquadrina incompta* was exclusively done by coiling direction. *N. pachyderma* strongly dominates foraminiferal assemblages in polar high latitudes, but also inhabits subpolar regions (Bé et al., 1977; Schiebel and Hemleben, 2017). At the end of its life cycle, this species can add a secondary layer of calcite usually at depths of the main pycnocline (Kohfeld et al., 1996). This crust has lower Mg/Ca ratios than the rest of the shell (Davis et al., 2017) and would therefore cause lower Mg/Ca temperatures. Yet we did not observe encrusted specimens and therefore refrain from correcting Mg/Ca values for encrustation as proposed by e.g Davis et al. (2017).

The vertical distribution of *N. pachyderma* varies with regional hydrography and is mainly controlled by temperature and food availability (Kuroyanagi and Kawahata, 2004; Taylor et al., 2018). Several studies conducted in the North Pacific state that calcification of *N. pachyderma* mostly occurs at or close to thermocline depth (Riethdorf, 2013; Sarnthein et al., 2004; Taylor et al., 2018). Based on these studies the authors assumed depth ranges between 30 and 300 m. Further, plankton tow samples from the NW Pacific showed that the main habitat of *N. pachyderma* lies below the pycnocline at ~30 m and above ~150 m (Kuroyanagi and Kawahata, 2004; Taylor et al., 2018). According to WOA data (Locarnini et al., 2018) (Figure 2.7) the thermocline lies at ~40-60 m at our study site and does not significantly change its depth throughout the year. We, therefore, assume a depth habitat of 50-130 m for our study site. This assumption is further supported by the comparison of the early Holocene Mg/Ca temperature estimate to the temperature right below the thermocline (Figure 2.7).

According to several studies, *N. pachyderma* is abundant throughout the year at latitudes close to our study site (e.g. Kuroyanagi et al., 2008, 2011; Sagawa et al., 2013; Taylor et al., 2018). However, there have been varying observations regarding the seasons of peak appearances. Sarnthein (2006) interpret their *N. pachyderma* temperature from a station at 51°N (~ 167°E) as (late) spring and early fall signal. Sediment trap data from the North West Pacific at ~40°N and ~50°N (both ~165°E) also show that *N. pachyderma* peaks predominantly during the spring phytoplankton bloom between April and May when organic matter flux is high (Kuroyanagi et al., 2008; Taylor et al., 2018). The abundance in summer is low at both sites. Yet, while the abundance starts to increase again in September at 50°N it stays low at the site at 40°N until December. As *N. pachyderma* is a subpolar species it prefers water temperatures below 7°C (Reynolds and Thunell, 1986). The observed differences in seasonality is most likely related to the warmer temperatures at site 40°N compared to site 50°N. For our site at ~46°N, we therefore, conclude that *N. pachyderma*, mainly occurs from autumn to spring at our study site in modern days. Yet might change its seasonality if temperature exceeds its preferred range.

2.7.2. Foraminiferal Mg/Ca paleo thermometry and pH effect

Foraminiferal Mg/Ca is highly sensitive to temperature and thus one of the most widely applied proxies to reconstruct paleo sea (surface) temperature (Nürnberg, 1995, 2000; Nürnberg et al., 1996; Lea et al., 1999; Elderfield and Ganssen, 2000). The Mg incorporation, however, is not only a function of temperature but also of salinity and carbonate chemistry (pH, calcite dissolution) of the surrounding seawater (e.g. Gray & Evans, 2019; Lea et al., 1999; Nürnberg et al., 1996; Regenberg et al., 2006). A recent study by Gray & Evans (2019) argues, that the influence of pH on species like *G. bulloides* might be higher than previously considered. Thus, they suggest considering pH changes overtime when calculating paleo SSTs. For this they created a software tool (MgCaRB) that iteratively solves Mg/Ca and atmospheric CO_2 (using ice core data) for temperature and pH, while regional salinity is treated as a known, accounting for glacial-interglacial sea-level changes. We compared temperatures calculated via this tool to the ones derived from "traditional" calibrations for *G. bulloides*. As shown in Figure 2.8 the temperature amplitudes of all "traditional" calibrations are rather equal yet the absolute temperatures deviate by ~9°C. The MgCaRB temperatures, however, show higher amplitudes than the ones of the "traditional" calibrations. Notably, both the equation from Jonkers et al.

(2013) and the *G. bulloides* specific MgCaRB approach provide unrealisticly low temperatures (in some time intervals way below 0°C). The MgCaRB multispecies approach provides Holocene temperatures consistent with the modern temperature, yet the total amplitude is higher than the ones from traditional equations. Although we cannot finally clarify this topic, we assume that higher amplitudes are less likely and that the MgCaRB tool might overcorrect the data. Further, it is remarkable that the MgCaRB multispecies approach provides more realistic temperatures than the *G. bulloides* specific approach. Therefore, although we acknowledge the proposition of correcting Mg/Ca based temperatures for pH, we prefer to use a "traditional" equation for our study and consider the influence of pH within our error range. We choose the species-specific equation from Elderfield & Ganssen (2000) because it provides Holocene temperatures that are consistent with the modern temperature at the study site and it is based on core top samples. Notably, the temperatures deviated via the multispecies MgCaRB approach lie within the assigned error range of the temperatures deviated from the Elderfield & Ganssen (2000) calibration. For *N. pachyderma* we decided to use the species-specific equation from Kozdon et al. (2009). It provides Holocene subSSTs consistent with the modern annual subsurface temperature and is based on core top samples that were taken in a region without sea ice cover Figure 2.8.

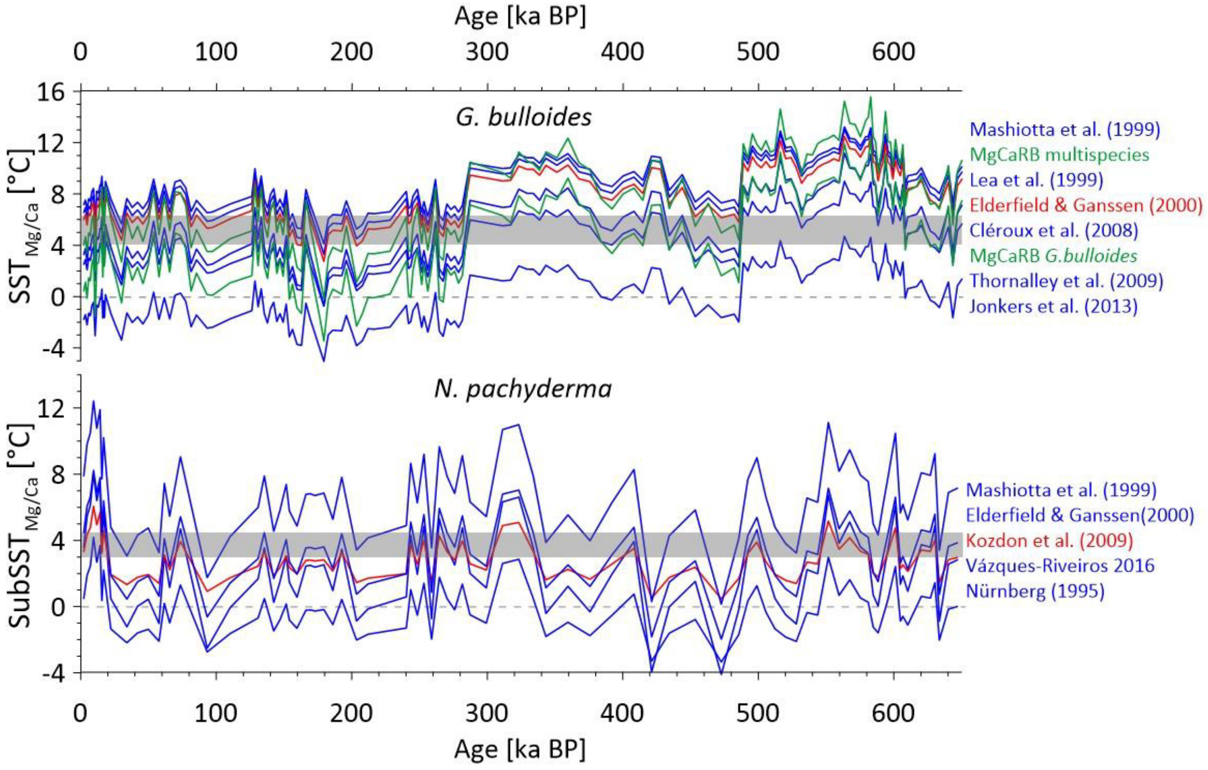

Figure 2.8: Comparison of $SST_{Mg/Ca}$ and $subSST_{Mg/Ca}$ calculated via different species-specific calibrations for *G. bulloides* (top) and *N. pachyderma* (bottom). The red calibrations are used in this study, because reconstructed late Holocene values fit best to the modern annual temperature ranges (Locarnini et al., 2018) in the respective depth habitats (marked as gray boxes). The green temperature curves for *G. bulloides* were derived with the MgCaRB tool from Taylor et al. (2018) and explicitly corrected SST values for local changes in salinity and pH.

2.7.3. Contamination effects and outliers

During the cleaning procedure described in chapter 2.2.1 siliciclastic material and Mn/Fe oxide rich coatings should have been removed from the foraminiferal sample material. Yet as both can have a significant influence on the Mg/Ca values (Barker et al., 2003; Hasenfratz 2017) it is crucial to check for cleaning efficiency. According to Barker et al. (2003) typical values of Al/Ca and Fe/Ca lie below 0.1 mmol/mol after cleaning, which is lower than average values we found in our data (Fe/Ca: *G. bulloides* mean: 0.09 mmol/mol, n = 186; *N. pachyderma* mean: 0.07 mmol/mol, n =71 / Al/Ca: *G. bulloides* mean: 0.23 mmol/mol, n = 186; *N. pachyderma* mean: 0.01 mmol/mol, n = 71). To check for a correlation between high Al/Ca, Fe/Ca, and high Mg/Ca values these values are plotted against each other and the coefficient of determination (r^2) is calculated (Figure 2.9). Based on r^2, there is no significant correlation between high Al and Fe contamination and high Mg/Ca values in our data (Figure 2.9 & 2.10) and thus we consider our data free from the influence of Al and Fe contamination.

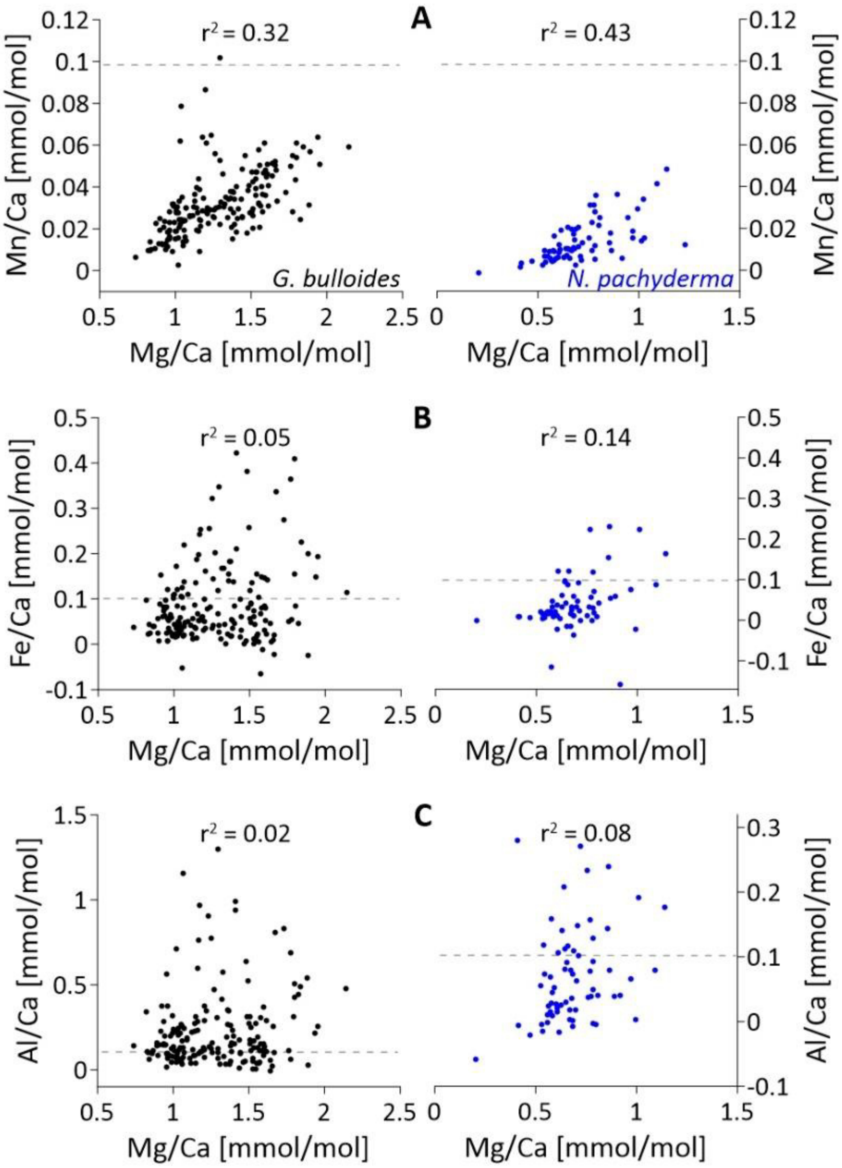

Figure 2.9: Foraminiferal Mg/Ca of *G. bulloides* (black) and *N. pachyderma* (blue) vs. **A**: Mn/Ca, **B**: Fe/Ca, **C**: Al/Ca. For both species, some Fe/Ca and Al/Ca values exceed the proposed threshold of 0.1 mmol/mol (dotted lines) by (Barker et al., 2003), yet the coefficient of correlation (r^2) is low therefore implying no correlation between higher Mg/Ca values and higher contamination.

Manganese-rich coatings on foraminifera can also have a significant effect on Mg/Ca ratios thereby biasing seawater temperature reconstructions (Hasenfratz et al 2017). Yet we assume that manganese was sufficiently eliminated during the cleaning procedure as our Mn/Ca values are very low (*G. bulloides* mean: 0.03 mmol/mol, n = 186; *N. pachyderma* mean: 0.01 mmol/mol, n =71) (Figure 2.9 & 2.10).

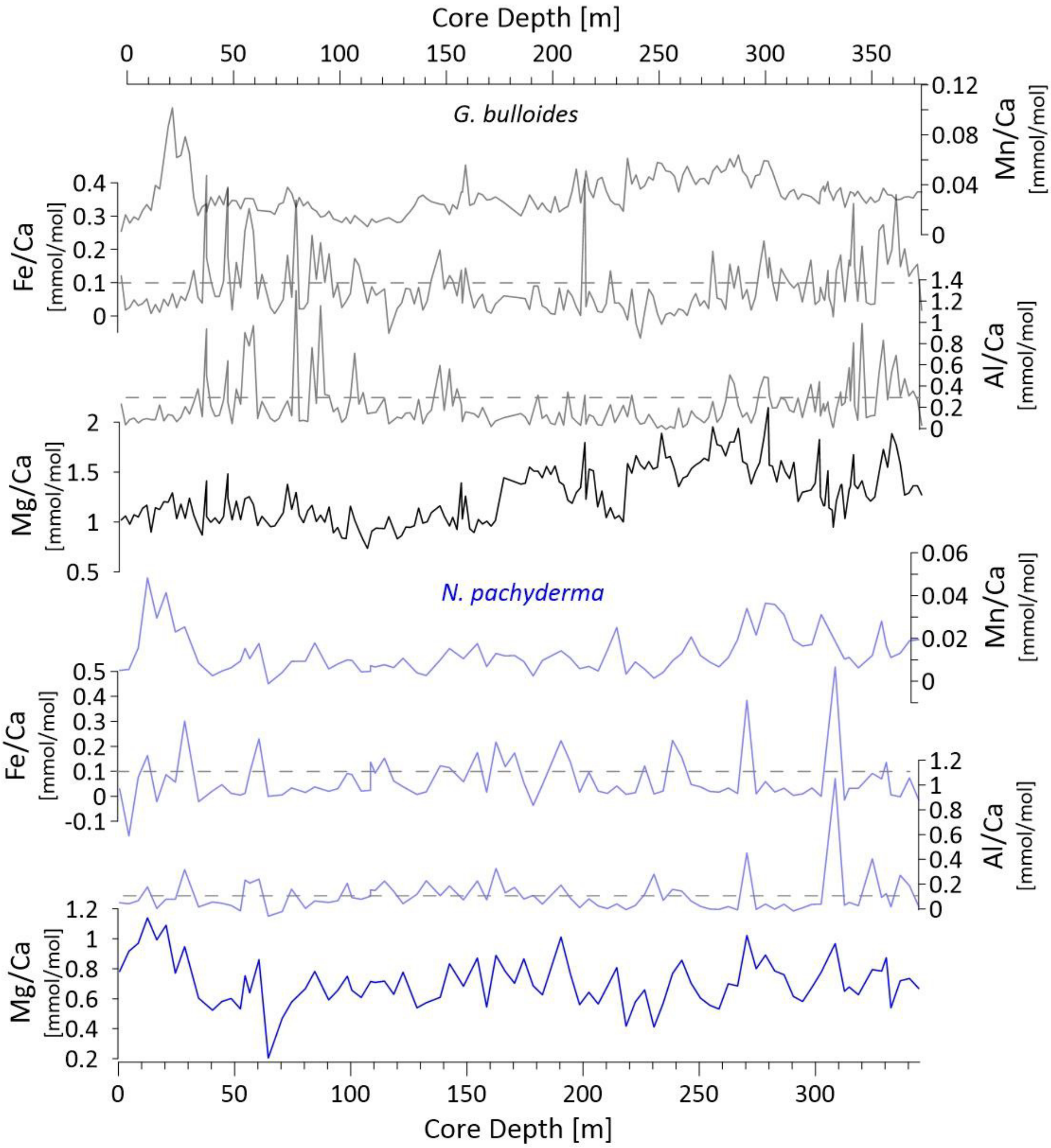

Figure 2.10: Foraminiferal Mg/Ca and contaminant elemental ratios Mn/Ca, Fe/Ca and Al/Ca of *G. bulloides* (black) and *N. pachyderma* (blue) vs core depth. Threshold values of contamination of 0.1 mmol/mol (dotted lines) as proposed by (Barker et al., 2003) are exceeded in some core depths. Yet there is no distinct correlation of high (low) contamination and high (low) Mg/Ca, thus no Mg/Ca values needed to be removed due to contamination.

Despite contamination, other factors might cause unexplainably high or low values. Applying the 1.5 interquartile method after Tukey (1977) the Mg/Ca and $\delta^{18}O$ records of both the planktic and benthic foraminifera were checked for outliers. Critical samples were remeasured where possible. This way only two Mg/Ca values and one $\delta^{18}O$ value needed to be removed from the dataset, due to insufficient material for resampling.

2.7.4. Dissolution effects on foraminiferal Mg/Ca

When planktic foraminifera are deposited in areas where the calcite saturation of the bottom water is lower than a critical threshold of 21.3 ± 6.6 µmol/kg (Regenberg et al., 2006, 2014) a selective ion removal of Mg^{2+} from foraminiferal calcite decreases the initial Mg/Ca values of these foraminifera (Brown and Elderfield, 1996). The calcite saturation state of the water is dependent on the carbonate ion concentration in the water column and decreases with increasing depth. According to Regenberg et al. (2014) the onset of foraminiferal Mg/Ca dissolution occurs in the North Pacific at water depth shallower than 500 m. Taking the influence of Mg/Ca dissolution into account thus seems crucial when referring to water temperatures calculated via the Mg/Ca ratios of foraminifera that were deposited at 2425 m water depth.
The modern calcite saturation state $\Delta[CO_3^{2-}]$ at the core site SO264-45 can be calculated via the difference between the *in situ* carbonate ion concentration ($\Delta[CO_3^{2-}]_{in\,situ}$) and the carbonate ion concentration at saturation ($\Delta[CO_3^{2-}]_{sat}$) (Brown and Elderfield, 1996). For our study site, we calculated $\Delta[CO_3^{2-}]_{sat}$ after Jansen et al. (2002) and $\Delta[CO_3^{2-}]_{in\,situ}$ using the CO2SYS Macro for MS Excel (Pierrot et al., 2006) applying constants K1 and K2 from Millero (2010), KSO4 from Dickson (1990), and [B]I value from Lee et al. (2010). Necessary input data of total alkalinity (TA) and total CO_2 (TCO_2) are obtained from the world ocean circulation experiment (WOCE) from a total of 14 Stations closest to the core location (GEOSECS Station 221; P13_3220CGC92_1 Stations 24, 26, 29, 32 and P14N_325023_1 Stations 27, 31, 35, 37, 38, 39, 40, 41, 43). According to this, our results would indicate, that $\Delta[CO_3^{2-}]$ at the core site SO264-45 reached the critical value of 21.3 µmol/kg (±6.6 µmol/kg) in water depths between 50 and 500 m and the calcite-saturation horizon would lie at 200-700 m (Figure 2.11). At the depth where our core was taken, the average $\Delta[CO_3^{2-}]$ would be -10 µmol/kg ($\pm$6.6 µmol/kg) (Figure 2.11). Thus, the foraminifera used in this study where most likely deposited in calcite undersaturated water, which would cause calcite dissolution (selective removal of Mg^{2+} ions) and therefore would lead to an underestimation of temperature. Regenberg et al. (2014) stated that Mg/Ca decreases by 0.054 ± 0.019 mmol/mol per µmol/kg decline. Thus the presented Mg/Ca values would be ~1.7 mmol/mol lower than the initially preserved Mg/Ca values, which would lead to a theoretical underestimation of temperature by up to ~12°C (when applying the abovementioned Mg/Ca vs. temp. equations) compared to the initial temperature recorded within the planktonic foraminiferal habitat.

Yet such a high underestimation of temperature at the study site is very unlikely, because it is not consistent with present-day observations and temperatures would lie outside of the species' livable temperature range. Although likely situated in unsaturated waters, our Holocene $SST_{Mg/Ca}$ and $subSST_{Mg/Ca}$ calculated via the calibrations of Elderfield & Ganssen (2000) and Kozdon et al. (2009), appear close to modern temperatures at the respective habitat depths (Figure 2.7 & 2.8). This could suggest that the influence of dissolution on calculated Mg/Ca temperature is smaller than assumed via the dissolution correction by Regenberg et al. (2014)

and/or that the calibrations of Elderfield & Ganssen (2000) and Kozdon et al. (2009) might be based on foraminifera that were exposed to a similar degree of dissolution. Moreover, the proposed dissolution correction attempts do not consider changes in dissolution through time (e.g. glacial/interglacial cycles). Thus, we can not determine to what exact degree our samples were affected by dissolution. Therefore, we refrain from correcting our absolute Mg/Ca temperature data for dissolution. As observed while picking and cracking the preservation state of the foraminiferal tests does not seem to vary throughout the core. Thus, we assume that relative changes in dissolution over time and interspecies differences in preferential dissolution are minimal and lie within the assigned error range.

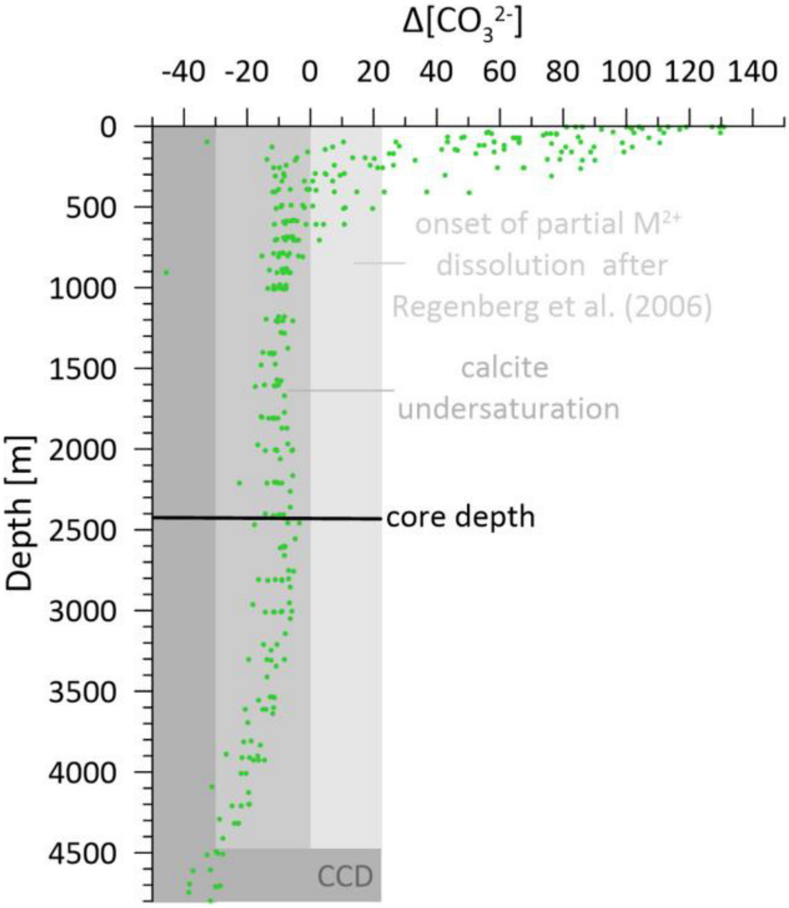

Figure 2.11: $\Delta[\mathrm{CO}_3^{2-}]$ in the North West Pacific, defined as the difference between the in situ carbonate ion concentration ($\Delta[CO_3^{2-}]_{in\ situ}$) and the carbonate ion concentration at saturation ($\Delta[CO_3^{2-}]_{sat}$), versus water depth. Total alkalinity (TA) and total CO_2 (TCO_2) data necessary to calculate the in $\Delta[CO_3^{2-}]_{in\ situ}$ were obtained from the World Ocean Circulation Experiment (WOCE) from a total of 14 stations closest to our core location (GEOSECS Station 221; P13_3220CGC92_1 Stations 24, 26, 29, 32 and P14N_325023_1 Stations 27, 31, 35, 37, 38, 39, 40, 41, 43. The $\Delta[CO_3^{2-}]_{in\ situ}$ was calculated using CO2SYS Macro for MS Excel (Pierrot et al., 2006). $\Delta[CO_3^{2-}]_{sat}$ was calculated after (Jansen et al., 2002).The horizons of selective Mg^{2+} dissolution and calcite dissolution are marked in gray. The CCD lies at ~4500 m.

2.7.5 Additional figures

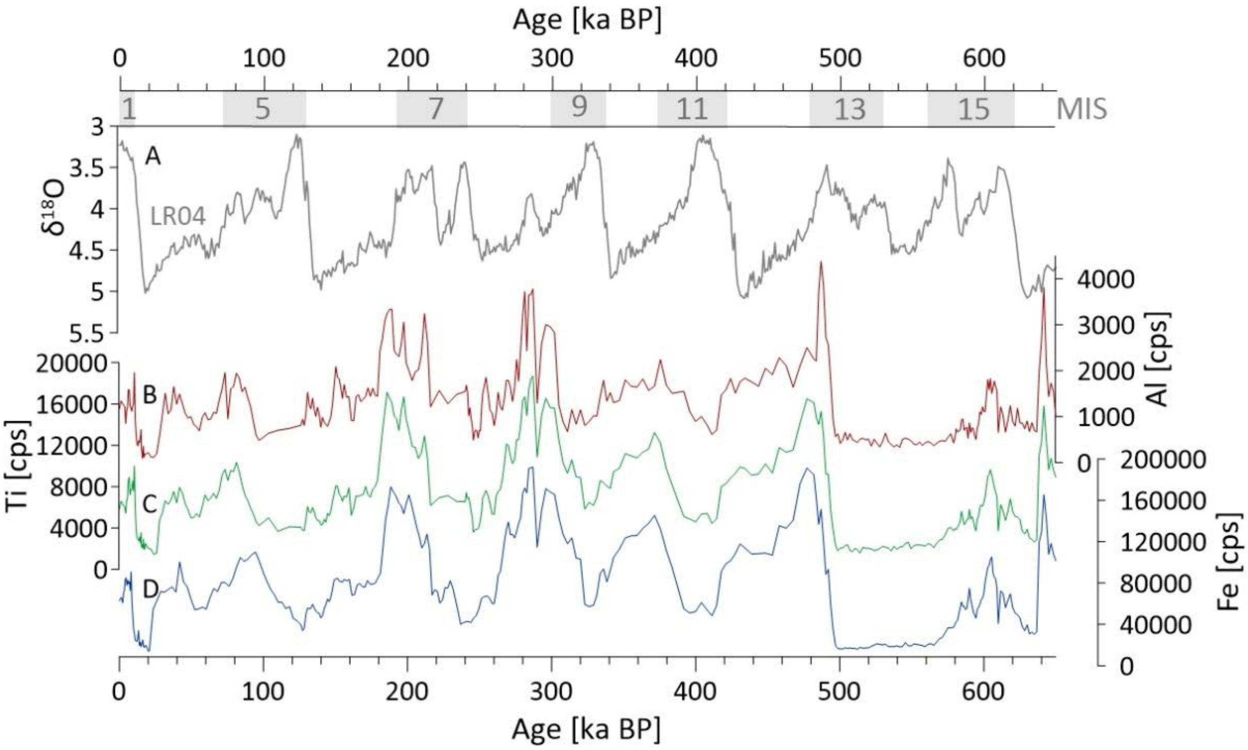

Figure 2.12: **A**: LR04 δ18O benthic isotope stack from Lisiecki and Raymo (2005). **B-D**: XRF-based aluminum (B) titanium and iron (C) records of SO264-45.

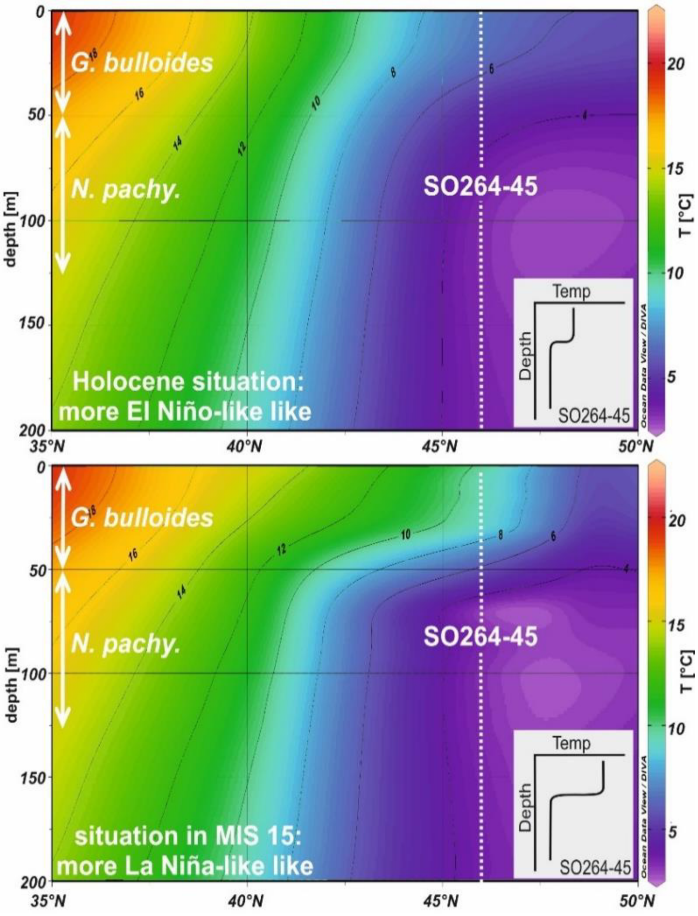

Figure 2.13: Modeled ocean temperature profiles (~170° W) for a possible surface dominated spreading of the Kuroshio-Oyashio transition water during times of more El Niño-like phases e.g. the Holocene (A) and more La Niña-like phases e.g. MIS 15 (B). White arrows indicate the average depth habitats of *G .bulloides* and *N. pachyderma*. This model is based on annual mean water temperature data from the WOA 2018 (Locarnini et al., 2018) and calculated $\mathrm{SSTs_{Mg/Ca}}$ and $\mathrm{subSSTs_{Mg/Ca}}$ from this study. Gray boxes exemplify thermocline variations at the study site. White lines indicate the core location of SO264-45. The temperature model of the figure was illustrated with Ocean Data View (Schlitzer and Ocean Data View, 2019).

2.8. References

André, A., Quillévéré, F., Morard, R., Ujiié, Y., Escarguel, G., De Vargas, C., et al. (2014). SSU rDNA divergence in planktonic foraminifera: Molecular taxonomy and biogeographic implications. *PLoS One* 9. doi: 10.1371/journal.pone.0104641.

Asahi, H., and Takahashi, K. (2007). A 9-year time-series of planktonic foraminifer fluxes and environmental change in the Bering sea and the central subarctic Pacific Ocean, 1990-1999. *Prog. Oceanogr.* 72, 343–363. doi: 10.1016/j.pocean.2006.03.021.

Barker, S., Greaves, M., and Elderfield, H. (2003). A study of cleaning procedures used for foraminiferal Mg/Ca paleothermometry. *Geochemistry, Geophys. Geosystems* 4, 1–20. doi: 10.1029/2003GC000559.

Bé, A. W. H., Hutson, W. H., and Be, A. W. H. (1977). Ecology of Planktonic Foraminifera and Biogeographic Patterns of Life and Fossil Assemblages in the Indian Ocean. *Micropaleontology* 23, 369. doi: 10.2307/1485406.

Bordiga, M., Beaufort, L., Cobianchi, M., Lupi, C., Mancin, N., Luciani, V., et al. (2013). Calcareous plankton and geochemistry from the ODP site 1209B in the NW Pacific Ocean (Shatsky Rise): New data to interpret calcite dissolution and paleoproductivity changes of the last 450ka. *Palaeogeogr. Palaeoclimatol. Palaeoecol.* 371, 93–108. doi: 10.1016/j.palaeo.2012.12.021.

Boyle, E. A., and Keigwin, L. D. (1985). Comparison of Atlantic and Pacific paleochemical records for the last 215,000 years: changes in deep ocean circulation and chemical inventories. *Earth Planet. Sci. Lett.* 76, 135–150. doi: 10.1016/0012-821X(85)90154-2.

Boyle, E., and Rosenthal, Y. (1996). Chemical Hydrography of the South Atlantic During the Last Glacial Maximum: Cd vs. δ13C. *South Atl.*, 423–443. doi: 10.1007/978-3-642-80353-6_23.

Brown, S. J., and Elderfield, H. (1996). Variations in Mg/Ca and Sr/Ca ratios of planktonic foraminifera caused by postdepositional dissolution: Evidence of shallow Mg-dependent dissolution. *Paleoceanography* 11, 543–551. doi: 10.1029/96PA01491.

Brunelle, B. G., Sigman, D. M., Cook, M. S., Keigwin, L. D., Haug, G. H., Plessen, B., et al. (2007). Evidence from diatom-bound nitrogen isotopes for subarctic Pacific stratification during the last ice age and a link to North Pacific denitrification changes. *Paleoceanography* 22, 1–17. doi: 10.1029/2005PA001205.

Caley, T., and Roche, D. M. (2015). Modeling water isotopologues during the last glacial: Implications for quantitative paleosalinity reconstruction. *Paleoceanography* 30, 739–750. doi: 10.1002/2014PA002720.

Chen, J., Zou, J., Zhu, A., Shi, X., Nürnberg, D., Lembke-Jene, L., et al. (2021). Geochemistry of Surface Sediments From the Emperor Seamount Chain, North Pacific. *Front. Earth Sci.* 9, 1–15. doi: 10.3389/feart.2021.674842.

Chen, Zhao, X. H., and Chen, Y. (2007). Influence of El Niño/La Niña on the western winter-spring cohort of neon flying squid (Ommastrephes bartramii) in the northwestern Pacific Ocean. *ICES J. Mar. Sci.* 64, 1152–1160. doi: 10.1093/icesjms/fsm103.

Chiyonobu, S., Mori, Y., and Oda, M. (2012). Reconstruction of paleoceanographic conditions in the northwestern Pacific Ocean over the last 500kyr based on calcareous nannofossil and planktic foraminiferal assemblages. *Mar. Micropaleontol.* 96–97, 29–37. doi: 10.1016/j.marmicro.2012.07.002.

Costa, K. M., McManus, J. F., and Anderson, R. F. (2018). Paleoproductivity and Stratification Across the Subarctic Pacific Over Glacial-Interglacial Cycles. *Paleoceanogr. Paleoclimatology* 33, 914–933. doi: 10.1029/2018PA003363.

Coulbourn, W. T., Parker, F. L., and Berger, W. H. (1980). Faunal and solution patterns of planktonic foraminifera in surface sediments of the North Pacific. *Mar. Micropaleontol.* 5, 329–399. doi: 10.1016/0377-8398(80)90019-5.

Croudace, I. W., and Rothwell, R. G. (2015). *Micro-XRF Studies of Sediment Cores*. Spinger doi: 10.1007/978-94-017-9849-5.

Darling, K. F., Kucera, M., Kroon, D., and Wade, C. M. (2006). A resolution for the coiling direction paradox in Neogloboquadrina pachyderma. *Paleoceanography* 21, 1–14. doi: 10.1029/2005PA001189.

Darling, K. F., Kucera, M., Pudsey, C. J., and Wade, C. M. (2004). Molecular evidence links cryptic diversification in polar planktonic protists to Quaternary climate dynamics. *Proc. Natl. Acad. Sci. U. S. A.* 101, 7657–7662. doi: 10.1073/pnas.0402401101.

Darling, K. F., and Wade, C. M. (2008). The genetic diversity of planktic foraminifera and the global distribution of ribosomal RNA genotypes. *Mar. Micropaleontol.* 67, 216–238. doi: 10.1016/j.marmicro.2008.01.009.

Darling, K. F., Wade, C. M., Siccha, M., Trommer, G., Schulz, H., Abdolalipour, S., et al. (2017). Genetic diversity and ecology of the planktonic foraminifers Globigerina bulloides, Turborotalita quinqueloba and Neogloboquadrina pachyderma off the Oman margin during the late SW Monsoon. *Mar. Micropaleontol.* 137, 64–77. doi: 10.1016/j.marmicro.2017.10.006.

Darling, K. F., Wade, C. M., Stewart, I. A., Kroon, D., Dingle, R., and Leigh Brown, A. J. (2000). Molecular evidence for genetic mixing of Arctic and Antarctic subpolar populations of planktonic foraminifers. *Nature* 405, 43–47. doi: 10.1038/35011002.

Davis, C. V., Fehrenbacher, J. S., Hill, T. M., Russell, A. D., and Spero, H. J. (2017). Relationships Between Temperature, pH, and Crusting on Mg/Ca Ratios in Laboratory-Grown Neogloboquadrina Foraminifera. *Paleoceanography* 32, 1137–1152. doi: 10.1002/2017PA003111.

Davis, C. V., Myhre, S. E., Deutsch, C., Caissie, B., Praetorius, S., Borreggine, M., et al. (2020). Sea surface temperature across the Subarctic North Pacific and marginal seas through the past 20,000 years: A paleoceanographic synthesis. *Quat. Sci. Rev.* 246, 106519. doi: 10.1016/j.quascirev.2020.106519.

De Boer, B., Lourens, L. J., and Van De Wal, R. S. W. (2014). Persistent 400,000-year variability of Antarctic ice volume and the carbon cycle is revealed throughout the Plio-Pleistocene. *Nat. Commun.* 5, 1–8. doi: 10.1038/ncomms3999.

de Garidel-Thoron, T., Rosenthal, Y., Bassinot, F., and Beaufort, L. (2005). Stable sea surface temperatures in the western Pacific warm pool over the past 1.75 million years. *Nature* 433, 294–298. doi: 10.1038/nature03189.

Dickson, A. G. (1990). Thermodynamics of the dissociation of boric acid in synthetic seawater from 273.15 to 318.15 K. *Deep Sea Res. Part A, Oceanogr. Res. Pap.* 37, 755–

766. doi: 10.1016/0198-0149(90)90004-F.

Elderfield, H., and Ganssen, G. (2000). Past temperature and δ18O of surface ocean waters inferred from foraminiferal Mg/Ca ratios. *Nature* 405, 442–445. doi: 10.1038/35013033.

Elderfield, H., Vautravers, M., and Cooper, M. (2002). The relationship between shell size and Mg/Ca, Sr/Ca, δ 18 O, and δ 13 C of species of planktonic foraminifera . *Geochemistry, Geophys. Geosystems* 3, 1–13. doi: 10.1029/2001gc000194.

Emery, W. J. (2001). Water Types And Water Masses. *Encycl. Ocean Sci.*, 3179–3187. doi: 10.1006/rwos.2001.0108.

Favorite, F. (1976). Oceanography of the subarctic Pacific region, 1960-71. *Bull Int North Pac Fish Comm* 33, 1–187. Available at: http://ci.nii.ac.jp/naid/10015636766/.

Field, D. B. (2004). Variability in vertical distributions of planktonic foraminifera in the California current: Relationships to vertical ocean structure. *Paleoceanography* 19. doi: 10.1029/2003PA000970.

Fontanier, C., MacKensen, A., Jorissen, F. J., Anschutz, P., Licari, L., and Griveaud, C. (2006). Stable oxygen and carbon isotopes of live benthic foraminifera from the Bay of Biscay: Microhabitat impact and seasonal variability. *Mar. Micropaleontol.* 58, 159–183. doi: 10.1016/j.marmicro.2005.09.004.

Friedrich, O., Schiebel, R., Wilson, P. A., Weldeab, S., Beer, C. J., Cooper, M. J., et al. (2012). Influence of test size, water depth, and ecology on Mg/Ca, Sr/Ca, δ 18O and δ 13C in nine modern species of planktic foraminifers. *Earth Planet. Sci. Lett.* 319–320, 133–145. doi: 10.1016/j.epsl.2011.12.002.

Fuhr, M., Laukert, G., Yu, Y., Nürnberg, D., and Frank, M. (2021). Tracing Water Mass Mixing From the Equatorial to the North Pacific Ocean With Dissolved Neodymium Isotopes and Concentrations. *Front. Mar. Sci.* 7, 1–18. doi: 10.3389/fmars.2020.603761.

Galbraith, E. D., Jaccard, S. L., Pedersen, T. F., Sigman, D. M., Haug, G. H., Cook, M., et al. (2007). Carbon dioxide release from the North Pacific abyss during the last deglaciation. *Nature* 449, 890–893. doi: 10.1038/nature06227.

Galbraith, E. D., Kienast, M., Jaccard, S. L., Pedersen, T. F., Brunelle, B. D., Sigman, D. M., et al. (2008). Consistent relationship between global climate and surface nitrate utilization in the western subarctic Pacific throughout the last 500 ka. *Paleoceanography* 23, 1–11. doi: 10.1029/2007PA001518.

Gallagher, S. J., Kitamura, A., Iryu, Y., Itaki, T., Koizumi, I., and Hoiles, P. W. (2015). The Pliocene to recent history of the Kuroshio and Tsushima Currents: a multi-proxy approach. *Prog. Earth Planet. Sci.* 2, 1–23. doi: 10.1186/s40645-015-0045-6.

Garcia, H., Weathers, K. W., Paver, C. R., Smolyar, I., Boyer, T. P., Locarnini, R. A., et al. (2018). World Ocean Atlas 2018. Volume 4: Dissolved Inorganic Nutrients (phosphate, nitrate and nitrate+nitrite, silicate). *NOAA Atlas NESDIS 84* 84, 35.

Gebhardt, H., Sarnthein, M., Grootes, P. M., Kiefer, T., Kuehn, H., Schmieder, F., et al. (2008). Paleonutrient and productivity records from the subarctic North Pacific for Pleistocene glacial terminations I to V. *Paleoceanography* 23, 1–21. doi: 10.1029/2007PA001513.

Gorbarenko, Southon, J. R., Keigwin, L. D., Cherepanova, M. V., and Gvozdeva, I. G. (2004). Late Pleistocene-Holocene oceanographic variability in the Okhotsk Sea:

Geochemical, lithological and paleontological evidence. *Palaeogeogr. Palaeoclimatol. Palaeoecol.* 209, 281–301. doi: 10.1016/j.palaeo.2004.02.013.

Gray, W. R., and Evans, D. (2019). Nonthermal Influences on Mg/Ca in Planktonic Foraminifera: A Review of Culture Studies and Application to the Last Glacial Maximum. *Paleoceanogr. Paleoclimatology* 34, 306–315. doi: 10.1029/2018PA003517.

Gray, W. R., Rae, J. W. B., Wills, R. C. J., Shevenell, A. E., Taylor, B., Burke, A., et al. (2018). Deglacial upwelling, productivity and CO2 outgassing in the North Pacific Ocean. *Nat. Geosci.* 11, 340–344. doi: 10.1038/s41561-018-0108-6.

Greaves, M., Caillon, N., Rebaubier, H., Bartoli, G., Bohaty, S., Cacho, I., et al. (2008). Interlaboratory comparison study of calibration standards for foraminiferal Mg/Ca thermometry. *Geochemistry, Geophys. Geosystems* 9, 1–27. doi: 10.1029/2008GC001974.

Harada, N., Ahagon, N., Uchida, M., and Murayama, M. (2004). Northward and southward migrations of frontal zones during the past 40 kyr in the Kuroshio-Oyashio transition area. *Geochemistry, Geophys. Geosystems* 5, 1–16. doi: 10.1029/2004GC000740.

Heaton, T. J., Köhler, P., Butzin, M., Bard, E., Reimer, R. W., Austin, W. E. N., et al. (2020). Marine20—The Marine Radiocarbon Age Calibration Curve (0–55,000 cal BP). *Radiocarbon* 62, 779–820. doi: 10.1017/rdc.2020.68.

Helmke, J. P., Bauch, H. A., Röhl, U., and Kandiano, E. S. (2008). Uniform climate development between the subtropical and subpolar Northeast Atlantic across marine isotope stage 11. *Clim. Past* 4, 181–190. doi: 10.5194/cp-4-181-2008.

Herbert, T. D., Schuffert, J. D., Andreasen, D., Heusser, L., Lyle, M., Mix, A., et al. (2001). Collapse of the California current during glacial maxima linked to climate change on land. *Science (80-.).* 293, 71–76. doi: 10.1126/science.1059209.

Holloway, M. D., Sime, L. C., Singarayer, J. S., Tindall, J. C., and Valdes, P. J. (2016). Reconstructing paleosalinity from δ18O: Coupled model simulations of the Last Glacial Maximum, Last Interglacial and Late Holocene. *Quat. Sci. Rev.* 131, 350–364. doi: 10.1016/j.quascirev.2015.07.007.

Hovan, S. A., Rea, D. K., and Pisias, N. G. (1991). Late Pleistocene Continental Climate and Oceanic Variability Recorded in Northwest Pacific Sediments. *Paleoceanography* 6, 349–370. doi: 10.1029/91PA00559.

Hu, D., Wu, L., Cai, W., Gupta, A. Sen, Ganachaud, A., Qiu, B., et al. (2015). Pacific western boundary currents and their roles in climate. *Nature* 522, 299–308. doi: 10.1038/nature14504.

Huang, R. X. (2015). *Oceanographic Topics: Surface/Wind Driven Circulation*. Second Edi. Elsevier doi: 10.1016/B978-0-12-382225-3.00280-2.

Isoguchi, O., Kawamura, H., and Oka, E. (2006). Quasi-stationary jets transporting surface warm waters across the transition zone between the subtropical and the subarctic gyres in the North Pacific. *J. Geophys. Res. Ocean.* 111, 1–17. doi: 10.1029/2005JC003402.

Iwasaki, S., Kimoto, K., Kuroyanagi, A., and Kawahata, H. (2017). Horizontal and vertical distributions of planktic foraminifera in the subarctic Pacific. *Mar. Micropaleontol.* 130, 1–14. doi: 10.1016/j.marmicro.2016.12.001.

Jaccard, S. L., Galbraith, E. D., Sigman, D. M., and Haug, G. H. (2010). A pervasive link between Antarctic ice core and subarctic Pacific sediment records over the past 800 kyrs. *Quat. Sci. Rev.* 29, 206–212. doi: 10.1016/j.quascirev.2009.10.007.

Jaccard, S. L., Haug, G. H., Sigman, D. M., Pedersen, T. F., Thierstein, H. R., and Röhl, U. (2005). Glacial/interglacial changes in subarctic North Pacific stratification. *Science (80- .).* 308, 1003–1006. doi: 10.1126/science.1108696.

Jahn, B., Donner, B., Müller, P. J., Röhl, U., Schneider, R. R., and Wefer, G. (2003). Pleistocene variations in dust input and marine productivity in the northern Benguela Current: Evidence of evolution of global glacial-interglacial cycles. *Palaeogeogr. Palaeoclimatol. Palaeoecol.* 193, 515–533. doi: 10.1016/S0031-0182(03)00264-5.

Jahn, Schneider, R. R., Müller, P. J., Donner, B., and Röhl, U. (2005). Response of tropical African and East Atlantic climates to orbital forcing over the last 1.7 Ma. *Geol. Soc. Spec. Publ.* 247, 65–84. doi: 10.1144/GSL.SP.2005.247.01.04.

Jansen, H., Zeebe, R. E., and Wolf-Gladrow, D. A. (2002). Modeling the dissolution of settling CaCO 3 in the ocean. *Global Biogeochem. Cycles* 16, 11-1-11–16. doi: 10.1029/2000gb001279.

Jia, Q., Li, T., Xiong, Z., Steinke, S., Jiang, F., Chang, F., et al. (2018). Hydrological variability in the western tropical Pacific over the past 700 kyr and its linkage to Northern Hemisphere climatic change. *Palaeogeogr. Palaeoclimatol. Palaeoecol.* 493, 44–54. doi: 10.1016/j.palaeo.2017.12.039.

Joh, Y., and Di Lorenzo, E. (2019). Interactions between Kuroshio Extension and Central Tropical Pacific lead to preferred decadal-timescale oscillations in Pacific climate. *Sci. Rep.* 9, 1–12. doi: 10.1038/s41598-019-49927-y.

Jonkers, L., Jiménez-Amat, P., Mortyn, P. G., and Brummer, G. J. A. (2013). Seasonal Mg/Ca variability of N. pachyderma (s) and G. bulloides: Implications for seawater temperature reconstruction. *Earth Planet. Sci. Lett.* 376, 137–144. doi: 10.1016/j.epsl.2013.06.019.

Kaiser, J., Schefuß, E., Lamy, F., Mohtadi, M., and Hebbeln, D. (2008). Glacial to Holocene changes in sea surface temperature and coastal vegetation in north central Chile: high versus low latitude forcing. *Quat. Sci. Rev.* 27, 2064–2075. doi: 10.1016/j.quascirev.2008.08.025.

Kawahata, H., and Ohshima, H. (2002). Small latitudinal shift in the Kuroshio Extension (Central Pacific) during glacial times: Evidence from pollen transport. *Quat. Sci. Rev.* 21, 1705–1717. doi: 10.1016/S0277-3791(01)00150-0.

Kawahata, H., Okamoto, T., Matsumoto, E., and Ujiie, H. (2000). Fluctuations of eolian flux and ocean productivity in the mid-latitude North Pacific during the last 200 kyr. *Quat. Sci. Rev.* 19, 1279–1291. doi: 10.1016/S0277-3791(99)00096-7.

Kienast, S. S., Hendy, I. L., Crusius, J., Pedersen, T. F., and Calvert, S. E. (2004). Export production in the subarctic North Pacific over the last 800 kyrs: No evidence for iron fertilization? *J. Oceanogr.* 60, 189–203. doi: 10.1023/B:JOCE.0000038326.73943.aa.

Kim, Y. Y., Qu, T., Jensen, T., Miyama, T., Mitsudera, H., Kang, H. W., et al. (2004). Seasonal and interannual variations of the North Equatorial current bifurcation in a high-resolution OGCM. *J. Geophys. Res. Ocean.* 109, 1–19. doi: 10.1029/2003jc002013.

Knudson, K. P., and Ravelo, A. C. (2015). Enhanced subarctic Pacific stratification and nutrient utilization during glacials over the last 1.2 Myr. *Geophys. Res. Lett.* 42, 9870–

9879. doi: 10.1002/2015GL066317.

Kohfeld, K. E., Fairbanks, R. G., Smith, S. L., and Walsh, I. D. (1996). Neogloboquadrina pachyderma (sinistral coiling) as paleoceanographic tracers in polar oceans: Evidence from Northeast Water Polynya plankton tows, sediment traps, and surface sediments. *Paleoceanography* 11, 679–699. doi: 10.1029/96PA02617.

Korff, L., von Dobeneck, T., Frederichs, T., Kasten, S., Kuhn, G., Gersonde, R., et al. (2016). Cyclic magnetite dissolution in Pleistocene sediments of the abyssal northwest Pacific Ocean: Evidence for glacial oxygen depletion and carbon trapping. *Paleoceanography* 31, 600–624. doi: 10.1002/2015PA002882.

Kotov, S., Paelike, H., Kotov, S., and Paelike, H. (2018). QAnalySeries - a cross-platform time series tuning and analysis tool. *AGUFM* 2018, PP53D-1230. Available at: https://ui.adsabs.harvard.edu/abs/2018AGUFMPP53D1230K/abstract [Accessed April 12, 2021].

Kozdon, R., Eisenhauer, A., Weinelt, M., Meland, M. Y., and Nürnberg, D. (2009). Reassessing Mg/Ca temperature calibrations of Neogloboquadrina pachyderma (sinistral) using paired δ44/40Ca and Mg/Ca measurements. *Geochemistry, Geophys. Geosystems* 10, 1–14. doi: 10.1029/2008GC002169.

Kuroyanagi, A., and Kawahata, H. (2004). Vertical distribution of living planktonic foraminifera in the seas around Japan. *Mar. Micropaleontol.* 53, 173–196. doi: 10.1016/j.marmicro.2004.06.001.

Kuroyanagi, A., Kawahata, H., and Nishi, H. (2011). Seasonal variation in the oxygen isotopic composition of different-sized planktonic foraminifer Neogloboquadrina pachyderma (sinistral) in the northwestern North Pacific and implications for reconstruction of the paleoenvironment. *Paleoceanography* 26, 1–10. doi: 10.1029/2011PA002153.

Kuroyanagi, A., Kawahata, H., Nishi, H., and Honda, M. C. (2008). Seasonal to interannual changes in planktonic foraminiferal assemblages in the northwestern North Pacific: Sediment trap results encompassing a warm period related to El Niño. *Palaeogeogr. Palaeoclimatol. Palaeoecol.* 262, 107–127. doi: 10.1016/j.palaeo.2008.02.012.

Kuzmin, Y. V, Burr, G. S., Gorbunov, S. V, Rakov, V. A., and Razjigaeva, N. G. (2007). A tale of two seas: Reservoir age correction values (R, ΔR) for the Sakhalin Island (Sea of Japan and Okhotsk Sea). *Nucl. Instruments Methods Phys. Res. Sect. B Beam Interact. with Mater. Atoms* 259, 460–462. doi: https://doi.org/10.1016/j.nimb.2007.01.308.

Kuzmin, Y. V, Burr, G. S., and Jull, A. J. (2001). Radiocarbon Reservoir Correction Ages in the Peter the Great Gulf, Sea of Japan, and Eastern Coast of the Kunashir, Southern Kuriles (Northwestern Pacific). *Radiocarbon* 43, 477–481. doi: 10.1017/S0033822200038364.

Labeyrie, L., Leclaire, H., Waelbroeck, C., Cortijo, E., Duplessy, J. C., Vidal, L., et al. (1999). Temporal variability of the surface and deep waters of the northwest atlantic ocean at orbital and millennial scales. *Geophys. Monogr. Ser.* 112, 77–98. doi: 10.1029/GM112p0077.

Lang, N., and Wolff, E. W. (2011). Interglacial and glacial variability from the last 800 ka in marine, ice and terrestrial archives. *Clim. Past* 7, 361–380. doi: 10.5194/cp-7-361-2011.

Lea, D. W., Mashiotta, T. A., and Spero, H. J. (1999). Controls on magnesium and strontium uptake in planktonic foraminifera determined by live culturing. *Geochim. Cosmochim. Acta* 63, 2369–2379. doi: 10.1016/S0016-7037(99)00197-0.

Lee, K., Kim, T. W., Byrne, R. H., Millero, F. J., Feely, R. A., and Liu, Y. M. (2010). The universal ratio of boron to chlorinity for the North Pacific and North Atlantic oceans. *Geochim. Cosmochim. Acta* 74, 1801–1811. doi: 10.1016/j.gca.2009.12.027.

LeGrande, A. N., and Schmidt, G. A. (2006). Global gridded data set of the oxygen isotopic composition in seawater. *Geophys. Res. Lett.* 33, 1–5. doi: 10.1029/2006GL026011.

Lembke-Jene, L., Tiedemann, R., Nürnberg, D., Kokfelt, U., Kozdon, R., Max, L., et al. (2017). Deglacial variability in Okhotsk Sea Intermediate Water ventilation and biogeochemistry: Implications for North Pacific nutrient supply and productivity. *Quat. Sci. Rev.* 160, 116–137. doi: 10.1016/j.quascirev.2017.01.016.

Lisiecki, L. E., and Raymo, M. E. (2005). A Pliocene-Pleistocene stack of 57 globally distributed benthic δ 18O records. *Paleoceanography* 20, 1–17. doi: 10.1029/2004PA001071.

Locarnini, R. A., Mishonov, A. V., Baranova, O. K., Boyer, T. P., Zweng, M. M., Garcia, H. E., et al. (2018). World Ocean Atlas 2018, Volume 1: Temperature. A. Mishonov, Technical Editor. *NOAA Atlas NESDIS* 1, 52pp.

Martínez-Botí, M. A., Mortyn, P. G., Schmidt, D. N., Vance, D., and Field, D. B. (2011). Mg/Ca in foraminifera from plankton tows: Evaluation of proxy controls and comparison with core tops. *Earth Planet. Sci. Lett.* 307, 113–125. doi: 10.1016/j.epsl.2011.04.019.

Matsumoto, K., Oba, T., Lynch-Stieglitz, J., and Yamamoto, H. (2002). Interior hydrography and circulation of the glacial Pacific Ocean. *Quat. Sci. Rev.* 21, 1693–1704. doi: 10.1016/S0277-3791(01)00142-1.

Matsuzaki, K. M., Nishi, H., Suzuki, N., Cortese, G., Eynaud, F., Takashima, R., et al. (2014). Paleoceanographic history of the Northwest Pacific Ocean over the past 740kyr, discerned from radiolarian fauna. *Palaeogeogr. Palaeoclimatol. Palaeoecol.* 396, 26–40. doi: 10.1016/j.palaeo.2013.12.036.

Max, L., Riethdorf, J. R., Tiedemann, R., Smirnova, M., Lembke-Jene, L., Fahl, K., et al. (2012). Sea surface temperature variability and sea-ice extent in the subarctic northwest Pacific during the past 15,000 years. *Paleoceanography* 27, 1–20. doi: 10.1029/2012PA002292.

Millero, F. J. (2010). History of the equation of state of seawater. *Oceanography* 23, 18–33. doi: 10.5670/oceanog.2010.21.

Mitnik, L. M., Khazanova, E. S., and Dubina, V. A. (2020). Mesoscale and synoptic scale dynamic phenomena in the Oyashio current region observed in SAR imagery. *Int. J. Remote Sens.* 41, 5861–5883. doi: 10.1080/01431161.2019.1701215.

Mohtadi, M., Romero, O. E., Kaiser, J., and Hebbeln, D. (2007). Cooling of the southern high latitudes during the Medieval Period and its effect on ENSO. *Quat. Sci. Rev.* 26, 1055–1066. doi: 10.1016/j.quascirev.2006.12.008.

Morard, R., Quillévéré, F., Escarguel, G., de Garidel-Thoron, T., de Vargas, C., and Kucera, M. (2013). Ecological modeling of the temperature dependence of cryptic species of planktonic Foraminifera in the Southern Hemisphere. *Palaeogeogr. Palaeoclimatol. Palaeoecol.* 391, 13–33. doi: 10.1016/j.palaeo.2013.05.011.

Morley, J. J., and Heusser, L. E. (1997). Role of orbital forcing in east Asian monsoon climates during the last 350 kyr: Evidence from terrestrial and marine climate proxies from core RC14-99. *Paleoceanography* 12, 483–493. doi: 10.1029/97PA00213.

Mulitza, S., Boltovskoy, D., Donner, B., Meggers, H., Paul, A., and Wefer, G. (2003). Temperature: δ18O relationships of planktonic foraminifera collected from surface waters. *Palaeogeogr. Palaeoclimatol. Palaeoecol.* 202, 143–152. doi: 10.1016/S0031-0182(03)00633-3.

Narita, H., Sato, M., Tsunogai, S., Murayama, M., Ikehara, M., Nakatsuka, T., et al. (2002). Biogenic opal indicating less productive northwestern North Pacific during the glacial ages. *Geophys. Res. Lett.* 29, 2–5. doi: 10.1029/2001GL014320.

Newman, M., Alexander, M. A., Ault, T. R., Cobb, K. M., Deser, C., Di Lorenzo, E., et al. (2016). The Pacific decadal oscillation, revisited. *J. Clim.* 29, 4399–4427. doi: 10.1175/JCLI-D-15-0508.1.

Nishioka, J., Ono, T., Saito, H., Sakaoka, K., and Yoshimura, T. (2011). Oceanic iron supply mechanisms which support the spring diatom bloom in the Oyashio region, western subarctic Pacific. *J. Geophys. Res. Ocean.* 116, 1–17. doi: 10.1029/2010JC006321.

Nürnberg (2018). RV SONNE Fahrtbericht/Cruise Report SO264 - SONNE-EMPEROR: The Plio/Pleistocene to Holocene development of the pelagic North Pacific from surface to depth – assessing its role for the global carbon budget and Earth´s climate, Suva (Fiji) – Yokohama (Japa. *GEOMAR Report, N. Ser. 046 . GEOMAR Helmholtz-Zentrum für Ozeanforschung, Kiel, Ger.*, 1–284. doi: 10.3289/GEOMAR_REP_NS_46_2018.

Nürnberg, D. (1995). Magnesium in tests of Neogloboquadrina pachyderma sinistral from high northern and southern latitudes. *J. Foraminifer. Res.* 25, 350–368. doi: 10.2113/gsjfr.25.4.350.

Nürnberg, D. (2000). Taking the temperature of past ocean surfaces. *Science (80-.).* 289, 1698–1699. doi: 10.1126/science.289.5485.1698.

Nürnberg, D., Bijma, J., and Hemleben, C. (1996). Assessing the reliability of magnesium in foraminiferal calcite as a proxy for water mass temperatures. *Geochim. Cosmochim. Acta* 60, 803–814. doi: 10.1016/0016-7037(95)00446-7.

Nürnberg, D., Brughmans, N., Schönfeld, J., Ninnemann, U., and Dullo, C. (2004). Paleo-export production, terrigenous flux and sea surface temperatures around tasmania-implications for glacial/interglacial changes in the subtropical convergence zone. *Geophys. Monogr. Ser.* 151, 291–318. doi: 10.1029/151GM17.

Nürnberg, D., and Tiedemann, R. (2004). Environmental change in the Sea of Okhotsk during the last 1.1 million years. *Paleoceanography* 19, 1–23. doi: 10.1029/2004PA001023.

Picaut, J., Loualalen, M., Menkes, C., Delcroix, T., and McPhaden, M. J. (1996). Mechanism of the zonal displacements of the Pacific warm pool: Implications for ENSO. *Science (80-.).* 274, 1486–1489. doi: 10.1126/science.274.5292.1486.

Pierrot, D., Lewis, E., and Wallace, D. W. . (2006). MS Excel Program Developed for CO2 System CalculationsProgram developed for CO2 system calculations. ORNL/CDIAC-105a.

Ponomareva, V., Bubenshchikova, N., Portnyagin, M., Zelenin, E., Derkachev, A., Gorbarenko, S., et al. (2018). Large-magnitude Pauzhetka caldera-forming eruption in

Kamchatka: Astrochronologic age, composition and tephra dispersal. *J. Volcanol. Geotherm. Res.* 366, 1–12. doi: 10.1016/j.jvolgeores.2018.10.006.

Qiu, B. (2002). The Kuroshio Extension system: Its large-scale variability and role in the midlatitude ocean-atmosphere interaction. *J. Oceanogr.* 58, 57–75. doi: 10.1023/A:1015824717293.

Qiu, B. (2019). *Kuroshio and oyashio currents. In: Cochran SJK, Bokuniewicz HJ, Yager PL (eds) Encyclopedia of Ocean Sciences*. 3rd ed. London: Elsevier Ltd. doi: 10.1016/B978-0-12-409548-9.11295-3.

Qiu, B., and Lukas, R. (1996). Seasonal and interannual variability of the North Equatorial Current, the Mindanao Current, and the Kuroshio along the Pacific western boundary. *J. Geophys. Res. C Ocean.* 101, 12315–12330. doi: 10.1029/95JC03204.

Regenberg, M., Nürnberg, D., Steph, S., Groeneveld, J., Garbe-Schönberg, D., Tiedemann, R., et al. (2006). Assessing the effect of dissolution on planktonic foraminiferal Mg/Ca ratios: Evidence from Caribbean core tops. *Geochemistry, Geophys. Geosystems* 7. doi: 10.1029/2005GC001019.

Regenberg, M., Regenberg, A., Garbe-schönberg, D., and Lea, D. W. (2014). Global dissolution effects on planktonic foraminiferal Mg/Ca ratios controlled by the calcite-saturation state of bottom waters. doi: 10.1002/2013PA002492.Received.

Reynolds, L. A., and Thunell, R. C. (1986). Seasonal Production and Morphologic Variation of Neogloboquadrina pachyderma (Ehrenberg) in the Northeast Pacific. *Micropaleontology* 32, 1. doi: 10.2307/1485696.

Riethdorf, J. R. (2013). Appendix: Deglacial development of (sub) sea surface temperature and salinity in the subarctic northwest Pacific.

Riethdorf, J. R., Nürnberg, D., Max, L., Tiedemann, R., Gorbarenko, S. A., and Malakhov, M. I. (2013). Millennial-scale variability of marine productivity and terrigenous matter supply in the western Bering Sea over the past 180 kyr. *Clim. Past* 9, 1345–1373. doi: 10.1002/aur.1919.

Sagawa, T., Kuroyanagi, A., Irino, T., Kuwae, M., and Kawahata, H. (2013). Seasonal variations in planktonic foraminiferal flux and oxygen isotopic composition in the western North Pacific: Implications for paleoceanographic reconstruction. *Mar. Micropaleontol.* 100, 11–20. doi: 10.1016/j.marmicro.2013.03.013.

Sarnthein, M. (2006). Warmings in the far northwestern Pacific promoted pre-Clovis immigration to America during Heinrich event 1. 141–144. doi: 10.1130/G22200.1.

Sarnthein, M., Gebhardt, H., Kiefer, T., Kucera, M., Cook, M., and Erlenkeuser, H. (2004). Mid Holocene origin of the sea-surface salinity low in the subarctic North Pacific. *Quat. Sci. Rev.* 23, 2089–2099. doi: 10.1016/j.quascirev.2004.08.008.

Schiebel, R., and Hemleben, C. (2017). Planktic foraminifers in the modern ocean. *Planktic Foraminifers Mod. Ocean*, 1–358. doi: 10.1007/978-3-662-50297-6.

Schiebel, R., Spielhagen, R. F., Garnier, J., Hagemann, J., Howa, H., Jentzen, A., et al. (2017). Modern planktic foraminifers in the high-latitude ocean. *Mar. Micropaleontol.* 136, 1–13. doi: 10.1016/j.marmicro.2017.08.004.

Schlitzer, R., and Ocean Data View (2019). Ocean Data View. *Https://Odv.Awi.De*.

Science, P. (2003). Hydrographic Structure and Variability in the Kuroshio- Oyashio Transition Area. *J. Oceanogr.* 59, 389–402.

Seears, H. A., Darling, K. F., and Wade, C. M. (2012). Ecological partitioning and diversity in tropical planktonic foraminifera. *BMC Evol. Biol.* 12. doi: 10.1186/1471-2148-12-54.

Shackleton, N. J. (1974). Attainment of isotopic equilibrium between ocean water and the benthonic foraminifera geuns *Uvigerina*: Isotopic changes in the ocean during the last glacial. *Colloq. Int. du C.N.R.S.* 219, 203–210.

Shackleton, N. J., and Hall, M. A. (1984). Oxygen and carbon isotope stratigraphy of Deep Sea Drilling Project Hole 552A: Plio-Pleistocene glacial history. *Initial reports DSDP, Leg 81, Southampt. to Azores*, 599–609. doi: 10.2973/dsdp.proc.81.116.1984.

Shackleton, N. J., and Opdyke, N. D. (1973). Oxygen isotope and palaeomagnetic stratigraphy of Equatorial Pacific core V28-238: Oxygen isotope temperatures and ice volumes on a 105 year and 106 year scale. *Quat. Res.* 3, 39–55. doi: 10.1016/0033-5894(73)90052-5.

Shigemitsu, M., Narita, H., Watanabe, Y. W., Harada, N., and Tsunogai, S. (2007). Ba, Si, U, Al, Sc, La, Th, C and 13C/12C in a sediment core in the western subarctic Pacific as proxies of past biological production. *Mar. Chem.* 106, 442–455. doi: 10.1016/j.marchem.2007.04.004.

Shimizu, Y., Yasuda, I., and Ito, S. I. (2001). Distribution and circulation of the coastal Oyashio intrusion. *J. Phys. Oceanogr.* 31, 1561–1578. doi: 10.1175/1520-0485(2001)031<1561:DACOTC>2.0.CO;2.

Sigman, D. M., Fripiat, F., Studer, A. S., Kemeny, P. C., Martínez-García, A., Hain, M. P., et al. (2021). The Southern Ocean during the ice ages: A review of the Antarctic surface isolation hypothesis, with comparison to the North Pacific. *Quat. Sci. Rev.* 254. doi: 10.1016/j.quascirev.2020.106732.

Spero, H. J., and Lea, D. W. (1996). Experimental determination of stable isotope variability in Globigerina bulloides: Implications for paleoceanographic reconstructions. *Mar. Micropaleontol.* 28, 231–246. doi: 10.1016/0377-8398(96)00003-5.

Stuiver, M., Reimer, P. J., and Reimer, R. W. (2020). CALIB 8.2 [WWW program] at http://calib.org, accessed 2020-10-9.

Talley, L. D. (1993). Distribution and formation of North Pacific Intermediate Water. *J. Phys. Oceanogr.* 23, 517–537. doi: 10.1175/1520-0485(1993)023<0517:DAFONP>2.0.CO;2.

Taylor, B. J., Rae, J. W. B., Gray, W. R., Darling, K. F., Burke, A., Gersonde, R., et al. (2018). Distribution and ecology of planktic foraminifera in the North Pacific: Implications for paleo-reconstructions. *Quat. Sci. Rev.* 191, 256–274. doi: 10.1016/j.quascirev.2018.05.006.

Thompson, P. R., and Shackleton, N. J. (1980). North Pacific palaeoceanography: Late quaternary coiling variations of planktonic foraminifer neogloboquadrina pachyderma. *Nature* 287, 829–833. doi: 10.1038/287829a0.

Tjallingii, R., Röhl, U., Kölling, M., and Bickert, T. (2007). Influence of the water content on X-ray fluorescence corescanning measurements in soft marine sediments. *Geochemistry, Geophys. Geosystems* 8, 1–12. doi: 10.1029/2006GC001393.

Tukey, J. W. (1977). *Exploratory Data Analysis.* Reading, MA: Addison-Wesley.

Ujiié, Y., Ujiié, H., Taira, A., Nakamura, T., and Oguri, K. (2003). Spatial and temporal variability of surface water in the Kuroshio source region, Pacific Ocean, over the past 21,000 years: Evidence from planktonic foraminifera. *Mar. Micropaleontol.* 49, 335–364. doi: 10.1016/S0377-8398(03)00062-8.

Waddell, L. M., Hendy, I. L., Moore, T. C., and Lyle, M. W. (2009). Ventilation of the abyssal Southern Ocean during the late Neogene: A new perspective from the subantarctic Pacific. *Paleoceanography* 24. doi: 10.1029/2008PA001661.

Wara, M. W., Ravelo, A. C., and Delaney, M. L. (2005). Climate change: Permanent El Niño-like conditions during the Pliocene warm period. *Science (80-.).* 309, 758–761. doi: 10.1126/science.1112596.

Weltje, G. J., and Tjallingii, R. (2008). Calibration of XRF core scanners for quantitative geochemical logging of sediment cores: Theory and application. *Earth Planet. Sci. Lett.* 274, 423–438. doi: 10.1016/j.epsl.2008.07.054.

Yamane, M. (2003). Late quaternary variations in water mass in the Shatsky Rise area, northwest Pacific Ocean. *Mar. Micropaleontol.* 48, 205–223. doi: 10.1016/S0377-8398(03)00017-3.

Yasuda, I., Kouketsu, S., Katsumata, K., Ohiwa, M., Kawasaki, Y., and Kusaka, A. (2002). Influence of Okhotsk Sea intermediate water on the Oyashio and North Pacific intermediate water. *J. Geophys. Res. Ocean.* 107, 1–11. doi: 10.1029/2001jc001037.

Yasuda, I., Okuda, K., and Shimizu, Y. (1996). Distribution and modification of North Pacific Intermediate Water in the Kuroshio-Oyashio interfrontal zone. *J. Phys. Oceanogr.* 26, 448–465. doi: 10.1175/1520-0485(1996)026<0448:DAMONP>2.0.CO;2.

Yasudomi, Y., Motoyama, I., Oba, T., and Anma, R. (2014). Environmental fluctuations in the northwestern Pacific Ocean during the last interglacial period: Evidence from radiolarian assemblages. *Mar. Micropaleontol.* 108, 1–12. doi: 10.1016/j.marmicro.2014.02.001.

Yatsu, A., Chiba, S., Yamanaka, Y., Ito, S. I., Shimizu, Y., Kaeriyama, M., et al. (2013). Climate forcing and the Kuroshio/Oyashio ecosystem. *ICES J. Mar. Sci.* 70, 922–933. doi: 10.1093/icesjms/fst084.

Yoneda, M., Uno, H., Shibata, Y., Suzuki, R., Kumamoto, Y., Yoshida, K., et al. (2007). Radiocarbon marine reservoir ages in the western Pacific estimated by pre-bomb molluscan shells. *Nucl. Instruments Methods Phys. Res. Sect. B Beam Interact. with Mater. Atoms* 259, 432–437. doi: https://doi.org/10.1016/j.nimb.2007.01.184.

You, Y., Suginohara, N., Fukasawa, M., Yasuda, I., Kaneko, I., Yoritaka, H., et al. (2000). Roles of the Okhotsk Sea and Gulf of Alaska in forming the North Pacific Intermediate Water. *J. Geophys. Res. Ocean.* 105, 3253–3280. doi: 10.1029/1999jc900304.

Yuan, Y. C., Liu, Y. G., and Su, J. L. (2001). Variability of the Kuroshio in the East China Sea during El-Niño to La Niña phenomenon of 1997 and 1998. *Acta Geophys. Sin.* 44, 199–210. doi: 10.1002/cjg2.132.

Zammit-Mangion, A. ., and Wikle, C. K. (2020). Deep integro-difference equation models for spatio-temporal forecasting, Spatial Statistics, 37, 100408. Available at: https://doi.org/10.1016/j.spasta.2020.100408.

Zhang, J., Wang, P., Li, Q., Cheng, X., Jin, H., and Zhang, S. (2007). Western equatorial

Pacific productivity and carbonate dissolution over the last 550 kyr: Foraminiferal and nannofossil evidence from ODP Hole 807A. *Mar. Micropaleontol.* 64, 121–140. doi: 10.1016/j.marmicro.2007.03.003.

Zheng, X., Li, A., Kao, S. J., Gong, X., Frank, M., Kuhn, G., et al. (2016). Synchronicity of Kuroshio Current and climate system variability since the Last Glacial Maximum. *Earth Planet. Sci. Lett.* 452, 247–257. doi: 10.1016/j.epsl.2016.07.028.

Zweng, M. M., Reagan, J. R., Seidov, D., Boyer, T. P., Antonov, J. I., Locarnini, R. A., et al. (2019). World Ocean Atlas 2018, Volume 2: Salinity. *NOAA Atlas NESDIS* 2, 50.

3. Scientific Chapter II

Glacial-interglacial variations of productivity and carbonate deposition in the Northwest Pacific during the last 500,000 years

Chao, Weng-Si[1*], Jacobi, Lara[2], Niederbockstruck, Bryan[1,3], Langemann, Linda[1], Kuhn, Gerhard[1], Zou, Jian-Jun[4], Shi, Xue-Fa[4], Nürnberg, Dirk[2], Tiedemann, Ralf[1], Lembke-Jene, Lester[1]

[1] Alfred-Wegener-Institut Helmholtz-Zentrum für Polar- und Meeresforschung, Bremerhaven, Germany
[2] GEOMAR Helmholtz-Zentrum für Ozeanforschung, Kiel, Germany
[3] Now at MARUM, Bremen, Germany
[4] First Institute of Oceanography, Ministry for Natural Resources, Qingdao, China

In preparation for submission in Frontiers in Earth Science

Abstract

The modern North Pacific constitutes one of the main marine natural carbon sinks and thus helps regulate atmospheric CO_2 concentrations. However, the relationship between biological export production (biological carbon pump), deep sea carbonate deposition, and meridional overturning circulation in shaping this marine carbon reservoir remains poorly understood on geological timescales. In particular, the combination of these processes beyond the last glacial cycle and across the dynamic subarctic and subtropical gyre regions with their dominant Western Boundary Current systems (Kuroshio/Oyashio) has been proven to be dynamic and highly regionalized. We here present a suite of new sediment records along a meridional transect from the subpolar Northwest (NW) Pacific, retrieved from the Emperor Seamount Chain and Hess Rise, in order to reconstruct changes in the export production and its relation to carbonate deposition and dissolution on suborbital timescales for the last 500,000 years before present (500 ka BP). We used X-ray fluorescence (XRF)-scanning records to correlate prominent patterns between sediment cores, supported by high-resolution oxygen isotope time series of epibenthic foraminifera *Cibicidoides wuellerstorfi* to develop a coherent stratigraphic framework for the study area. Our sediment records show southward decreasing productivity variations, as evidenced in XRF-ln Ba/Ti ratios, and dust supply, based on XRF-Fe intensities, from 52 to 37° N. Higher export production occurred during peak interglacials, but an out-of-phase pattern exists in carbonate deposition below 40°N. We assume that regional shifts in the subpolar and subtropical gyre circulation and upper ocean stratification exerted a major control on the macro-nutrient supply, rather than solely changing amount of micronutrient input through aeolian transport. On the other hand, the productivity in the subpolar region had a more direct influence and depositional contribution on the carbonate system supported by coherent increases in biogenic barium, carbonate flux, alkenone concentration, sand fraction and opal content during interglacials. The Hess Rise carbonate preservation, however, showed weak correlation to the productivity signals but matched to the deep Pacific carbonate chemistry changes which relate to variations in carbonate dissolution. The inconsistency between these productivity and carbonate records also implied the boundary shifting between the subpolar and subtropical gyre which provide different nutrient regime to the NW Pacific region.

3.1. Introduction

Today, the North Pacific plays an important role in the oceanic carbon cycle and global climate, due to its vast size, its high biological export production and potential for deep carbon storage in the form of dissolved inorganic carbon (DIC). It also comprises one of the three major high-nutrient low-chlorophyll (HNLC) regions of the global ocean, which are characterized by upwelling of nutrient-rich deep waters into the photic zone and remain partially unutilized due to micronutrient or light limitation (Falkowski et al., 1998). Hence, the biological carbon pump is not working efficiently in fixing carbon into sinking organic matter, in comparison to the co-occurring release of carbon from deep water masses. The macro-nutrient supply is constrained by the strength of the permanent salinity-driven density gradient (halocline) in the North Pacific.

On glacial-interglacial timescales, a number of subarctic Northwest (NW) Pacific reconstructions show lower export production (e.g., biogenic opal, biogenic barium) during glacials, with a remarkable correlation to Antarctic climatic and greenhouse gas changes preserved in ice cores (e.g. Jaccard et al., 2005, 2010; Narita et al., 2002; Nürnberg and Tiedemann, 2004; Shigemitsu et al., 2007). Evidence based nutrient utilization proxies indicates low export production. Hence, nitrate consumption in the North Pacific was more complete during glacials, contributing to lowered surface ocean nutrient content including carbon (e.g. Brunelle et al., 2007; Galbraith et al., 2008; Knudson and Ravelo, 2015a). Causes were most likely decreased vertical exchange through strengthened surface ocean stratification and increased surface isolation during glacials, suggesting less nutrient supply from nutrient-rich deep waters (Brunelle et al., 2007; Galbraith et al., 2008; Gebhardt et al., 2008; Jaccard et al., 2005, 2009, 2010; Kienast et al., 2004; Narita et al., 2002; Shigemitsu et al., 2007). The decrease of this physical transfer of deeply sequestered DIC to the surface ocean also potentially contributed to lower glacial atmospheric CO_2 concentrations. In combination with enhanced supply of dust-derived, or marine-transported, iron (Fe) as essential micronutrient, these processes set the upper NW Pacific as an efficient driver of glacial atmospheric CO_2 drawdown.

However, differing nutrient preferences for siliceous and carbonate planktic organisms in biological primary production, their relative contributions towards export production (i.e., the biological carbon pump), and the resulting deep-sea carbonate deposition, i.e., the role of carbonate counter-pump remain poorly understood in this region. In particular, whether the calcium carbonate ($CaCO_3$) content of deep-sea sediments in the North Pacific is mainly controlled by either surface biological production or changes in carbonate preservation related to the paleo-chemical configuration of deep-water masses, has consequences for the deep oceanic carbon storage capacity and its relationship with climate change.

Deep-sea carbonate deposition has been studied for a long time and the patterns of Atlantic and Pacific $CaCO_3$ preservation are known for their anti-correlation, at least for the last ca. 500 ka BP (Sexton and Barker, 2012). They are most clearly expressed in significant changes in the carbonate compensation depth (CCD), the upper limit of the zone where less than 5-10 weight % (wt %) of $CaCO_3$ accumulates on the seafloor. The glacial Atlantic $CaCO_3$ content is generally lower in comparison to interglacials, the so-called “Atlantic-type” (Bé et al. 1976; Berger, 1973; Crowley, 1985; Curry and Lohmann, 1990; Damuth, 1977; Gardner, 1975; Hodell et al., 2001; deMenocal et al., 1997; Verardo and McIntyre, 1994; Volat et al., 1980). On the contrary, the “Pacific-type” generally exhibits higher $CaCO_3$ contents during glacials (Anderson et al., 2008; Arrhenius, 1952; Berger, 1973; Farrell and Prell, 1991, 1989; Hays et al., 1969; Karlin et al., 1992; LaMontagne et al., 1996; Le and Shackleton, 1992; Thompson and Saito, 1974; Zahn et al., 1991). The causes of these opposed $CaCO_3$ cycles have been discussed controversially, with controlling factors ascribed to various reasons, such as carbonate production from surface waters, dilution by non-carbonate materials (e.g. opal), or dissolution driven by changes in carbonate ion concentration $[CO_3^{2-}]$ of the deep-water masses. In particular the latter process has been in turn linked to the supply of bathyal to abyssal southern-sourced Circumpolar Deep Water for the last ca. 1 Ma BP (Sexton and Barker, 2012). In that case, better ventilated and hence less carbonate-corrosive deep waters, sourced mainly from the South Pacific and Ross Sea sector of the Southern Ocean, would have led to better carbonate preservation in the Pacific during glacials, relative to the Atlantic.

In this study, we present four proxy-based carbonate and biological export production time series from sediment cores along a meridional transect from the NW Pacific covering the last 500 ka BP. The records are mainly based on high-resolution XRF-derived Ba, Ca, $CaCO_3$ contents and accumulation rates, supplemented by discrete measurements of alkenone concentrations and coarse fraction percent (>63 µm, sand %) on select time intervals. We investigate the relation between the carbonate deposition and productivity in the NW Pacific over the last five glacial cycles and assess the potential causes of the subarctic NW Pacific carbonate system.

3.2. Study area and oceanographic setting

The North Pacific constitutes one of the largest ocean basins, crossing several climatic zones from the tropical to the polar domain. Water depths range mostly in the abyssal zone below 4000 m, with only a few shallower locations along seamounts and ridge systems. Due to the extensive geographical range, the North Pacific is influenced by (sub-)tropical climates from the West Pacific Warm Pool, the El Niño – Southern Oscillation (ENSO) as well as East Asian Monsoon dynamics. No deep-water formation occurs in the North Pacific due to the presence of a permanent halocline (Warren, 1983). This halocline stratification is controlled by high precipitation rates and limited meridional flow of salty subtropical water (Emile-Geay et al., 2003). This comparably strong stratification today leads to the area acting as a net sink of atmospheric CO_2 (Takahashi et al., 2002). The intermediate depths in the NW Pacific are mainly occupied by North Pacific Intermediate Water (NPIW) sourced from the Okhotsk Sea (Shcherbina et al., 2003; Talley, 1993). Below 2000 m depth, the North Pacific Deep Water (NPDW) is the dominant water mass, sourced from Lower Circumpolar Deep Water (LCDW) from the Southern Hemisphere by northward transport (Reid and Losdale, 1974).

The upper ocean water masses are characterized by a clockwise subtropical circulation and a counterclockwise subarctic circulation. Warm water masses from the equatorial Pacific are transported along the eastern coast of Japan and flow eastward as the Kuroshio Extension into the NW Pacific (Figure 3.1A). This relatively warm water flows until it diverges on the American west coast and part of it is transported north and westwards into the Alaskan Stream along the Aleutian Islands. After flowing southward as the East Kamchatka Current, the cold and nutrient-rich Oyashio Current forms East of the Kurile Island Chain. The deflection point of the Oyashio eastwards into the open Pacific defines the North Pacific Subarctic Front. Today, the western North Pacific Subarctic Front is located around 38 to 41°N, and identified by changes of the meridional temperature and salinity gradient (Yuan and Talley, 1992).

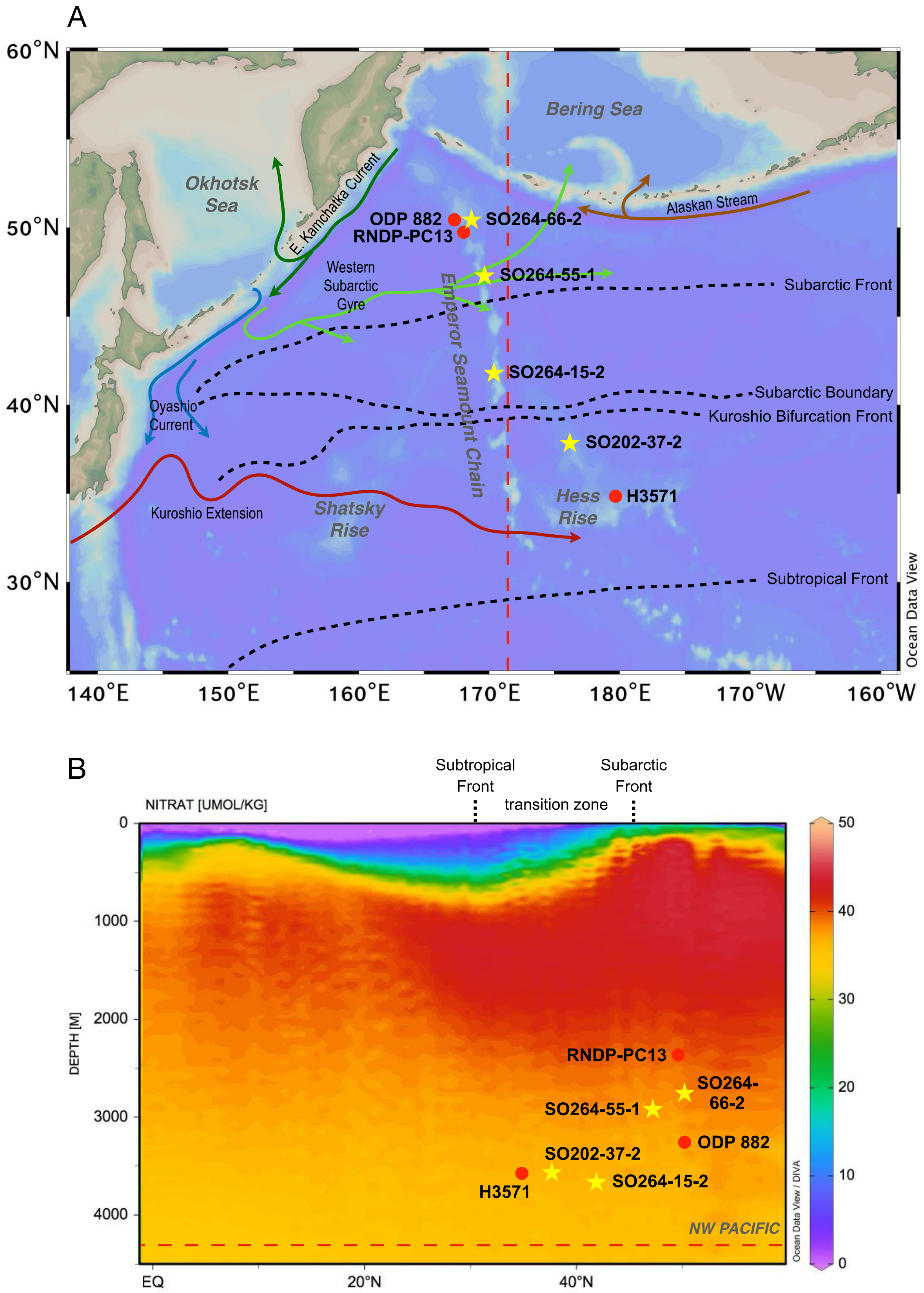

Figure 3.1: (A) Map of the research region. The study cores are marked by yellow stars and the Northwest Pacific reference cores are marked by red dots. The major surface ocean currents and fronts are marked by arrows and black dashed lines, based on Yasuda (2003). SO264-51-2 is a twin core of SO264-55-1 which both have the same

coring location and water depth. (B) Nitrate concentration alone a zonal section indicated by the red dashed line in (A), with positions of the study and reference cores in water depth.

Compared to the near-absence of macro-nutrients in the Subtropical Gyre (STG), the Subarctic Gyre (SAG) is highly enriched in nitrate. Overall productivity is higher in the SAG, but less effective due to a lack of micronutrients, in particular iron. For the STG, the water is oligotrophic due to a deep permanent thermocline, preventing the upwelling of nutrients into the photic zone (Figure 3.1B). The transition zone, or Mixed Water Region is defined as the area between the Subarctic Front and the Subtropical Front (Figure 3.1B). The northern end of this transition zone constitutes the Subarctic Front, acting as the boundary to the SAG. The Subarctic Front in the North Pacific is characterized by changes in the physical characteristics. The Mixed Water Region has been shown to change on geological timescales in the past (Gray et al., 2020; Isono et al., 2009; Oba and Murayama, 2004; Yasudomi et al., 2014), and is projected to change under future global warming (Yang et al., 2016, 2020), thereby affecting heat and nutrient transport throughout the entire North Pacific. The Mixed Water Region and both gyre systems are of importance regarding the CO_2 uptake from the atmosphere into the ocean. On an annual basis, the North Pacific acts as a net sink for CO_2, with the most effective area of CO_2 sequestration in the North Pacific occurring around 30 to 40° (Takahashi et al., 2002, 2009).

3.3. Material and methods

The investigated meridional transect ranges from 37 to 49°N latitude along the Emperor Seamount Chain in the subarctic NW Pacific, crossing the Subarctic Front, the Subarctic Boundary and the Kuroshio Bifurcation Front, which is defined by the inflow of the two NW Pacific coastal currents, the cold subarctic Oyashio Current and the warm subtropical Kuroshio Current Extension (Figure 3.1A). We selected four sediment cores along this transect: three cores were recovered during expedition SO264 of R/V SONNE in 2018, while one was taken from Hess Rise during a previous expedition SO202 INOPEX in 2009 also with R/V SONNE (Figure 3.1A and Table 3.1).

The sedimentary facies of the area from the Minnetonka Seamount to the northern Detroit Seamounts features dark olive green silty clays, which are mainly intercalated with brown to yellowish-brown diatom oozes and terrigenous components. In contrast, the southern area from Ninigi Seamount to Hess Rise is dominated by gray to light brown foraminifera-bearing silty calcareous oozes, interbedded with light gray to greenish-gray clayey calcareous oozes (Nürnberg, 2018). Several tephra layers were found in most of the cores.

Table 3.1: Core locations of the study and reference cores in the Northwest Pacific.

	Core ID	Area/Seamount	Latitude	Longitude	Water depth (m)	Reference
Cores in this study	SO264-66-2	south of Detroit	50°15.064'N	168°17.818'E	2751	
	SO264-55-1	Minnetonka	47°10.553'N	169°25.291'E	2936	
	SO264-51-2	Minnetonka	47°10.553'N	169°25.291'E	2936	
	SO264-15-2	east of Ninigi	41°36.917'N	170°25.340'E	3662	
	SO202-37-2	north of Hess Rise	37°46.07'N	176°16.13'E	3568	
Reference cores	ODP 882	Detroit	50°21.798'N	167°35.9879'E	3255	*Jaccard et al.,* 2010
	RNDP-PC13	open western subarctic Pacific	49°43.0859'N	168°18.1139'E	2393	*Brunelle et al.,* 2010
	H3571	Hess Rise	34°54.25'N	179°42.18'E	3571	*Kawahata et al.,* 2000

3.3.1. X-ray fluorescence (XRF) core scanning

XRF core scanning provides a rapid and nondestructive analytical approach for obtaining semi-quantitative, high-resolution downcore variations of major and minor elements. XRF-scanning measurements were carried out on the split archive halves of all cores with an Avaatech XRF core scanner at the Alfred-Wegener-Institut Helmholtz-Zentrum für Polar- und Meeresforschung (AWI) in Bremerhaven, Germany. The X-ray excitation scanning settings of the cores were 10 kV at 150 µA with no filter for a count time of 10 s, 30 kV at 175 µA with thick-Pb filter for 15 s, and 50 kV at 1000 µA with Cu filter for 20 s. Sample distance was 10 mm, with a 10x12 mm slit size.

3.3.2. Bulk sample processing and physical properties

For the determination of bulk sediment parameters and physical properties, immediately after opening the sediment cores on board, we took syringe samples of 10 cubic centimeters in 10 cm intervals from the working halves into pre-weighed glass vials. All samples were stored at 4°C until further shore-based processing. Samples were weighed before and after freeze-drying, homogenized and measured for density calculations on four AccuPyc II 1340 Gas Pycnometer units in the AWI Marine Geology Laboratory in Bremerhaven.

Dry bulk density (DBD) for the calculation of mass accumulation rates (MAR) was carried out according to Dadey et al. (1992).

(1) $\rho_d = M_s/V$

In which ρ_d = DBD, M_S = the weight of the dry sample and V = the total volume of the wet sample.

The carbonate content, expressed as weight percent (wt. %), was obtained from freeze-dried and homogenized samples. For SO264 cores, around 40 samples per core were selected based on the initial XRF scanning Ca data and measured, while ca. 240 samples were measured from core SO202-37-2 with 10 cm sample spacing. Total carbon (TC) content was measured with an Elementar Vario EL III CNS-analyzer and total organic carbon (TOC) content was determined from decalcified samples with an Eltra CS-800 carbon/sulfur analyzer at the AWI in Bremerhaven. The carbonate content was then calculated from the difference between TC and TOC as follows:

(2) $$CaCO_3 \text{ wt\%} = (\text{TC} - \text{TOC}) \times 8.333 \times 100\%$$

Mass accumulation rates were calculated as follows:

(3) $$MAR = DBD \times sedi.rate$$

Mass accumulation rates of carbonate (CAR) were calculated as the product of dry bulk density, sedimentation rate and carbonate percentage:

(4) $$CAR = \text{DBD} \times \text{sedi. rate} \times CaCO_3 \text{ wt\%}$$

3.3.3. Coarse fraction processing and stable isotopes measurements

For stable isotope measurements and foraminifera counts, we continuously sampled all cores in 1 cm-thick sediment slices from the working half rounds. Samples were freeze-dried and washed through a 63-µm sieve. The coarse fractions were dried in an oven at 50°C and dry sieved into four size fractions of 63-125 µm, 125-250 µm, 250-500 µm and >500 µm.

While processing those samples, sediments were weighed both before and after wet sieving to obtain the sediment sand (>63-µm) weight fraction as a carbonate dissolution parameter. Every second 1 cm slice was processed for isotope measurements and foraminifera counting. Most of the stable oxygen isotope ratios ($\delta^{18}O$) of core SO264-55-1 have been presented in a MSc. thesis and were largely measured on the endobenthic foraminifera *Uvigerina peregrina* and *Uvigerina senticosa* from the 250-500 µm size fraction (Langemann, 2021). For core SO202-37-2, two specimen of the epibenthic foraminifera *Cibicidoides wuellerstorfi* were picked from the same size fraction for $\delta^{18}O$ and were measured at the AWI in Bremerhaven, using a Thermo Finnigan MAT 253 isotope ratio mass-spectrometer coupled to an automated KIEL IV CARBO preparation device. Long-time reproducibility based on NIST-19 and an in-house carbonate standard is 0.06 ‰ for $\delta^{18}O$.

3.3.4. AMS ^{14}C ages

AMS ^{14}C ages of core SO202-37-2 were measured on the planktonic foraminifera *Globigerina bulloides* (*G. bulloides*) from the 250-500 µm size fraction and were obtained from the accelerator mass spectrometer Mini Carbon Dating System (MICADAS) at AWI. All radiocarbon ages were converted into calibrated 2-sigma calendar age ranges using the radiocarbon calibration tool CALIB Execute Version 8.20 (http://calib.org/calib/) with the MARINE20 calibration curve (Table S1).

3.3.5. Alkenone content

We used 1 cm-thick freeze-dried sediment slices and applied selective accelerated solvent extraction (ASE; Auderset et al., 2020) for the extraction of n-alkanes, alkenones and GDGTs used a Dionex ASE350 system. This system is equipped with 10 mL stainless steel extraction cells, filled with 3-5 g of dry silica gel (60 Å, 70-230 mesh), previously deactivated by 5% milli-Q water, soaked with 3-5 g of hexane. Muffled glass fiber filters were added between the silica gel and the sediment (0.5-1.5 g) and on the top of the sample Internal standards for alkanes, alkenones and GDGT's (squalene, C_{36} n-alkane, nC_{46}-GDGT) were added prior to extraction to quantify the sample recovery and the concentration of the biomarker within the sediment. During the extraction and separation, the cell was preheated to 100 °C, filled with 10 ml of hexane, heated for 5 min and held in a static cycle for 2 min. Hexane was flushed through the cells into the first collecting vial. After the hexane flush, 10 ml of DCM was injected three times heated for 5 min and held in a static cycle for 2 min before the first flush and without static cycle in the 2nd and 3rd flushes.

3.4. Age model

The non-destructive high-resolution XRF core scanner has been often used in reconstructions of paleoenvironmental and paleoceanographic changes via various elemental ratios. In NW Pacific sediment records, e.g. XRF-derived Barium (Ba) and Calcium (Ca) counts normalized against terrigenous background elements like Aluminum (Al), Potassium (K) or Titanium (Ti) have served as proxies for paleo-productivity (biogenic barium), while Ca (calcium carbonate content) has been used for assessing carbonate production vs. bottom water corrosivity and hence of alkalinity (Gebhardt et al., 2008; Jaccard et al., 2005, 2010). Jaccard et al. (2005) amended the existing stratigraphy by an XRF-based high-resolution record on Ocean Drilling Program (ODP) Site 882 (50°21'N, 167°35'E, 3244 m water depth). The biogenic Barium (indicated by Ba/Al) showed a strong resemblance with the EDC CO_2, in conjunction with transient $CaCO_3$ (indicated by Ca/Al) maxima during peak interglacials in the otherwise carbonate-free sediments. In our study, Site 882 serves as the regional reference record for comparisons of the productivity records from our Emperor Seamount Chain and Hess Rise sediment cores.

Although Al and Ti are both exclusively of detrital origin and normally can be used for XRF-ratio normalization, we preferred to normalize against Ti in this study, because its variations are more clearly expressed, and also elemental intensities of light elements like Al can be strongly influenced by the increase of water content, which is trapped between the sediment and the scanning foil (Tjallingii et al., 2007). In addition, previous calibration studies (e.g.Weltje and Tjallingii, 2008) , indicated that in order to provide the most reliable signals in relative changes of down-core elements, the natural logarithmic ratios of XRF core scanner raw data should be adopted. Therefore, we present our XRF elemental variations in the ln-element/Ti format.

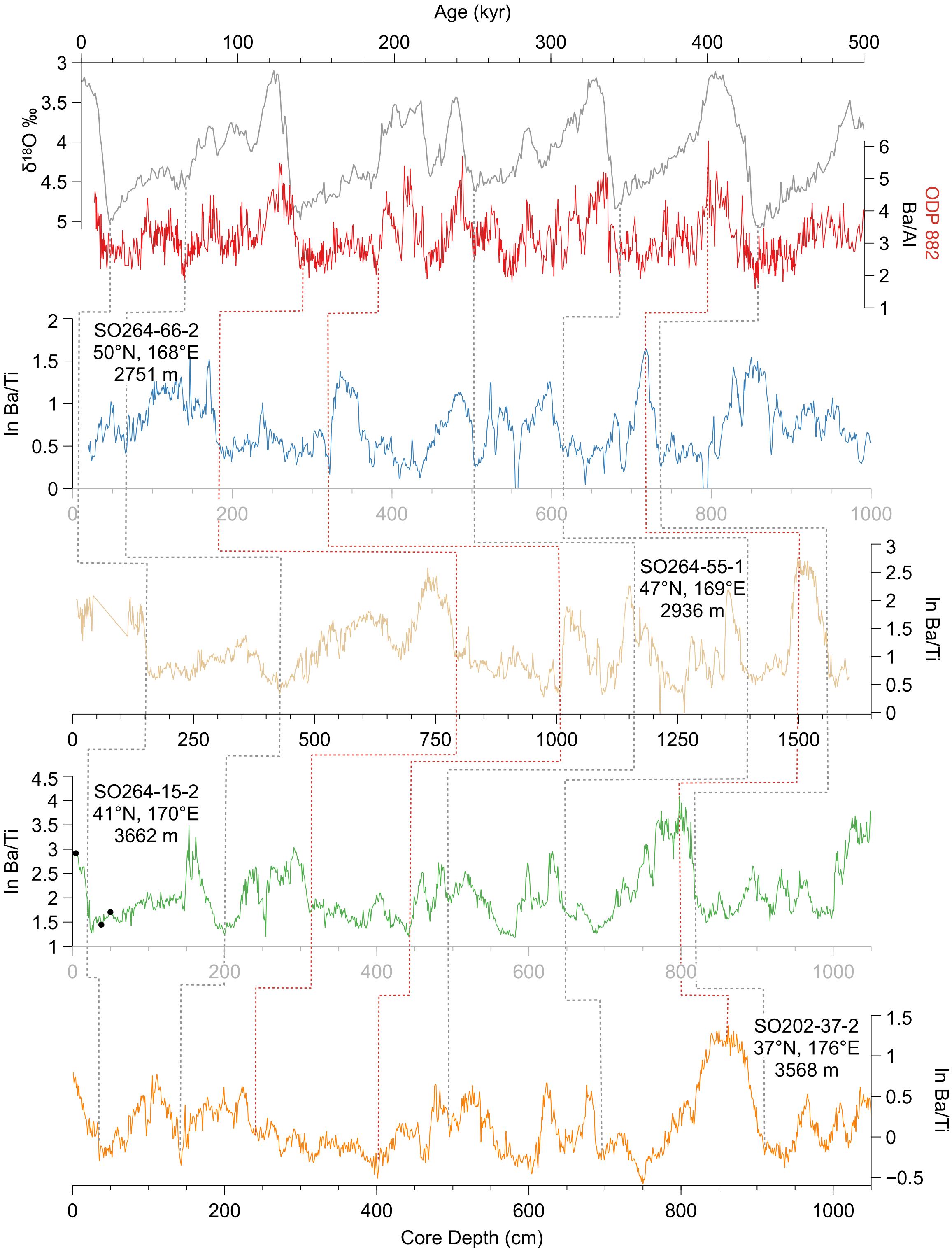

Figure 3.2: Stratigraphic framework of sediment cores from the Northwest Pacific and correlation with high-resolution XRF data to the benthic $\delta^{18}O$ stack of Lisiecki and Raymo (2005) and the stratigraphic established record site 882. The stratigraphy is based on the comparison between the benthic $\delta^{18}O$ stack and XRF Ba-normalized ratio. Gray stippled lines indicate correlation points to the benthic $\delta^{18}O$ stack and the sediment cores. Red stippled lines indicate correlation points to the site 882 record and the sediment cores. Blank spots mark the AMS ^{14}C dating control points for core SO202-37-2.

To establish a coherent chronostratigraphic framework for all cores along our meridional transect, we used an iterative approach combining various XRF-based chemostratigraphic correlation patterns indicative of orbital-scale primary production and dust transport changes, anchored by oxygen isotope stratigraphy, AMS ^{14}C ages, tephra identification and supported by information from paleomagnetic measurements on neighboring abyssal cores (Wang et al., 2021).

Our ln-Ba/Ti records show a pronounced characteristic following glacial-interglacial changes, as known from ODP Site 882, piston core MD01-2416 and other regional records (Gebhardt et al., 2008; Nürnberg and Tiedemann, 2004; Wang et al., 2021). We correlated our ln-Ba/Ti records to both the global benthic $\delta^{18}O$ stack of Lisiecki and Raymo (2005) and ODP site 882 Ba/Al (Jaccard et al., 2010) to establish an initial age model for the studied cores, with the assumption that higher values represent interglacials and lower values glacials (Figure 3.2). While this correlation pattern is less clear towards the south, especially during MIS 5, we refined the age model by correlating well-defined interglacial Ca peaks to Site 882 (Figure S1).

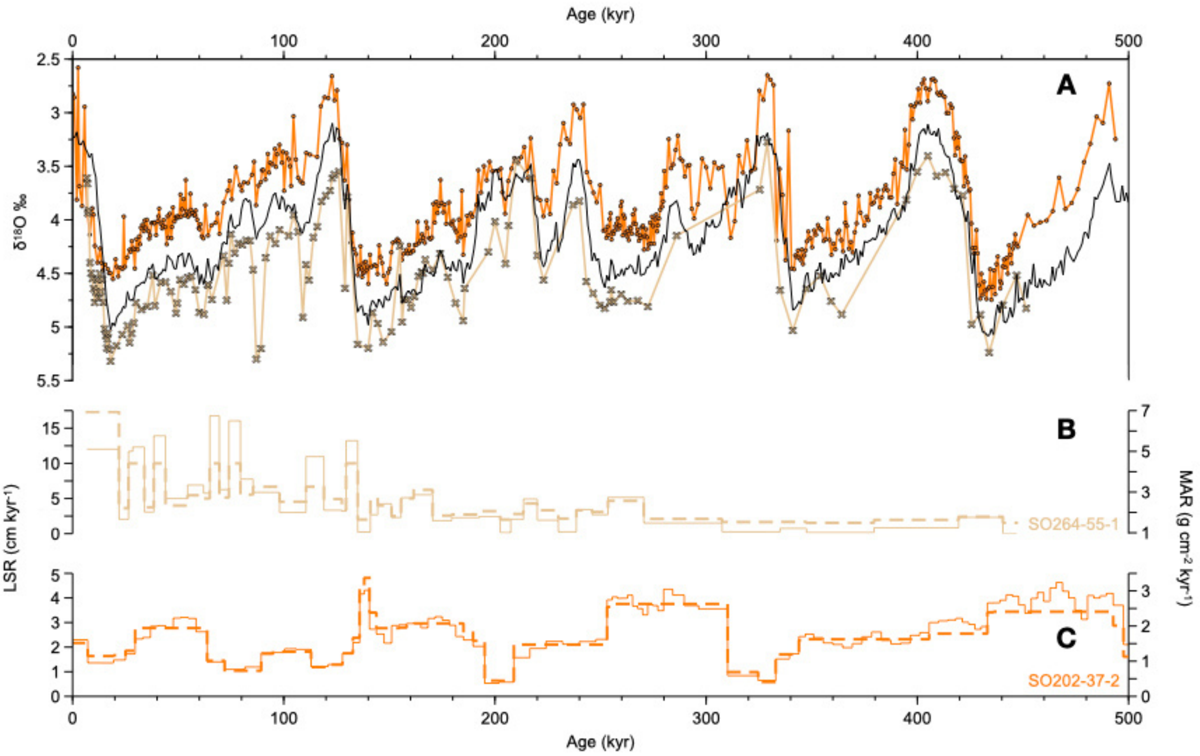

Figure 3.3: (A) Benthic $\delta^{18}O$ records from the Northwest Pacific cores SO264-55-1 (light brown line) and SO202-37-2 (orange line, measured on C. wuellerstorfi) compared to the global benthic $\delta^{18}O$ stack (Lisiecki and Raymo, 2005) in black line. (B) Linear sedimentation rates (LSR, dashed lines) and mass accumulation rates (MAR, solid lines) of core SO264-55-1 and SO202-37-2 plotted against age.

To develop independence from this initial XRF-based age model, we correlated the benthic *C. wuellerstorfi* $\delta^{18}O$ of SO202-37-2 and composite benthic $\delta^{18}O$ of SO264-55-1 to the benthic $\delta^{18}O$ stack (Figure 3.3A). The results provide an excellent agreement between the isotope stratigraphy and the initial XRF-based age models of these two cores (Figure S1), with maximum offsets never exceeding ~2 ka between our isotope stratigraphy and the XRF-based age model.

All age-depth tie points were primarily selected at climatic transitions (Table S2), the resulting calculated linear sedimentation rates (LSR) and MAR (Figure 3.3B and C) show variations starting from Termination II, in particular in core SO264-55-2 , while core SO202-37-2 shows relativity high values during glacials. Overall, LSRs and MARs are higher above the Subarctic Front (SO264-55-2) than below (SO202-37-2).

3.5. Results and discussion

In the following, we examine biological export production (ln-Ba/Ti), carbonate content and accumulation rates, and dust-related (XRF-Fe) variations of four sediment cores from the western subarctic Pacific during the last 500 ka BP, with the aim of better understanding productivity variations in the Pacific and its relation to the marine carbonate and carbon cycle.

3.5.1. NW Pacific glacial-interglacial productivity variations and their forcing factors over the last 500 ka

As corroborated from the adjacent ODP Site 882, XRF-based Ba-normalized ratios have an excellent correlation with biogenic barite (Jaccard et al., 2009) and therefore, we took ln-Ba/Ti as an indicator for past changes in biological export production. The ln-Ba/Ti ratios from all four sediment cores show strong orbital-scale variations, with generally higher productivity during interglacials and lower during glacials, though some maxima occur also during glacial MIS 8 and 12 (Figure 3.4C to F), notably as well in ODP Site 882 . The amplitude of variations between glacials and interglacials decreases towards the south, and according values differ from ca. 4 down to less than 1 in ln(Ba/Ti) (Figure 3.4C to F). Notably, MIS 11 as the longest interglacial interval of the last 500 ka is well characterized in all records by a broad-scale productivity peak (also in ln-Ca/Ti, see Figure S1). However, the similarly warmer-than-present interglacial MIS 5 does not yield a similarly distinct peak feature. Fe counts, considered mostly as an indicator of dust input (e.g. Martínez-Garcia et al., 2011), generally show an anti-correlation with the other proxies, with higher values during glacials and lower during interglacials (Figure 3.4G). The amplitude also decreases towards the south from ca. 3×10^5 to 0.9×10^5 counts per second (cps) in respective maxima.

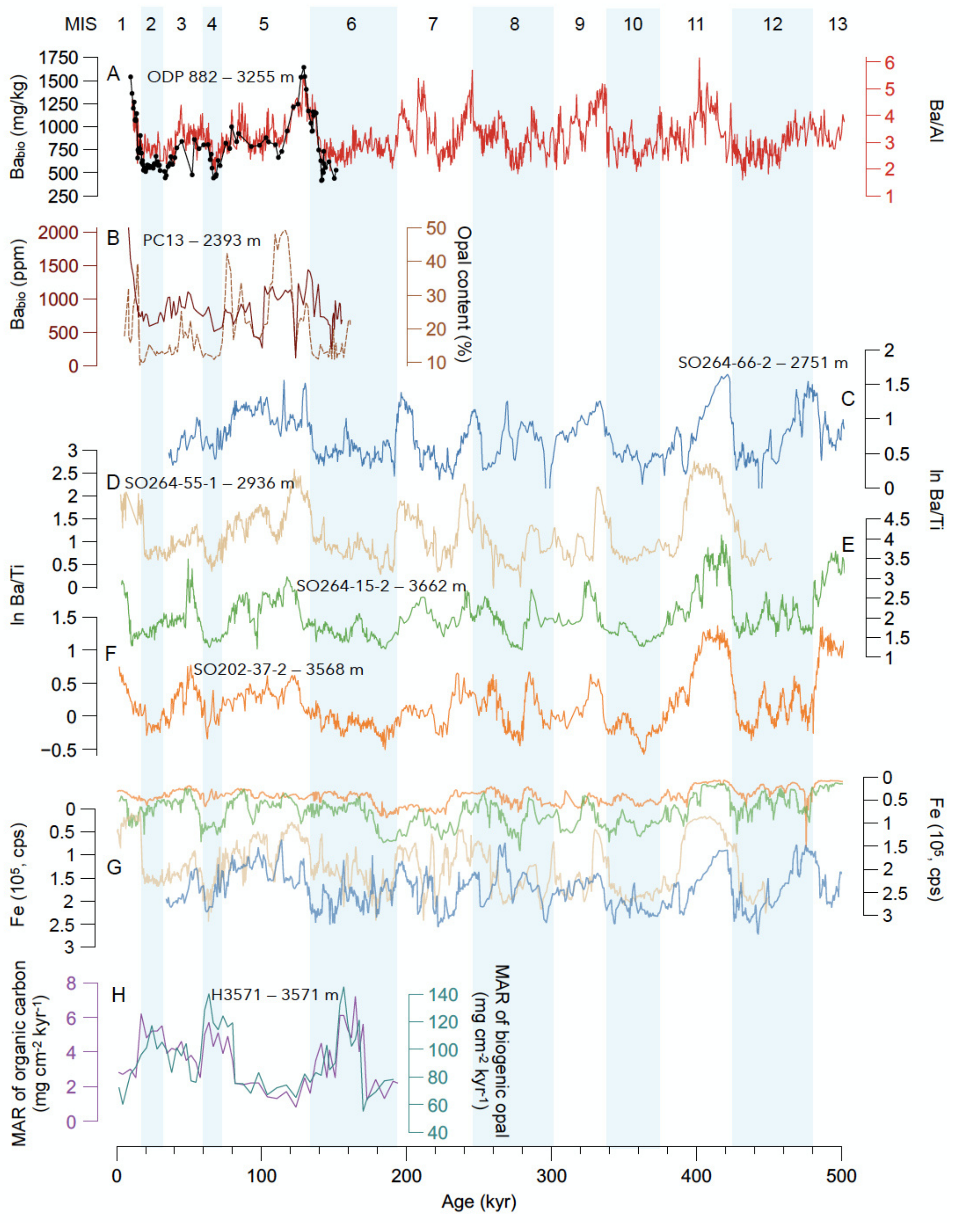

Figure 3.4: Multiproxy productivity records from the Northwest Pacific in order from north to south. (A) Biogenic barium (Ba_{Bio}) (black) and XRF Ba/Al (red) from ODP site 882 (Jaccard et al., 2009, 2010). (B) Ba_{Bio} (reddish brown) and opal content (brown) from PC13 (Brunelle et al., 2010). (C)-(F) XRF ln-Ba/Ti of the study cores (this study). (G) XRF Fe counts of the study cores plotted with inverted y-axis (this study). (H) fluxes of organic carbon (purple) and biogenic opal (dark-cyan) from H3571 (Kawahata et al., 2000).

The productivity pattern observed in our ln-Ba/Ti results aligns with previous studies in the subarctic NW Pacific (Costa et al., 2018; Galbraith et al., 2008; Iwasaki et al., 2012; Jaccard et al., 2010; Kohfeld and Chase, 2011; Shigemitsu et al., 2007). However, our records extend the southern boundary of this glacial-interglacial pattern first identified in the subarctic domain (Galbraith et al., 2008; Jaccard et al., 2010) further south, across the Subarctic Boundary and the Kuroshio Bifurcation Front into the Mixed Water Region. In the following, we evaluate potential control mechanisms that lead to the observed distribution of export production patterns in the NW Pacific and their underlying forcing.

3.5.1.1. Iron micronutrient supply by aeolian or marine lateral transport

Today, iron supply – as a key micronutrient for phytoplankton growth – limits primary production in the modern subarctic Pacific, parts of the equatorial Pacific, and the Southern Ocean (Boyd et al., 2007). A higher iron-containing dust flux can thus promote nitrogen fixation and therefore increase the nitrate pool, thereby increasing biological export production. Numerous records have shown a higher aeolian flux, sourced from East Asian desert regions, into the North Pacific during glacials (Hovan et al., 1991; Jacobel et al., 2017; Kawahata et al., 2000; Serno et al., 2017; Shigemitsu et al., 2007). An additional possible micronutrient source would be dust-borne iron accumulating on sea ice and icebergs, which would have been subsequently transported along the main current trajectories, ultimately delivered to the surface ocean while melting. Enhanced flux of Ice-rafted debris (IRD) occurred near the onset of terminations in the NW Pacific (Gebhardt et al., 2008) and IRD were found from further south at the Shatsky Rise (McCarron et al., 2021) and also in our N-S transect records. However, this type of supply would be likely more episodical, and quickly removed from surface waters instead of being maintained over several thousand years.

However, recent studies from the Equatorial Pacific have demonstrated that there is no significant relationship between the efficiency of the biological pump and dust input (Costa et al., 2016; Jacobel et al., 2019; Kienast et al., 2004; Shigemitsu et al., 2007; Winckler et al., 2016). Although the subtropical to subpolar NW Pacific exhibits a different nutrient regime, the observed higher interglacial productivity signal throughout our NW Pacific N-S transect shows an anti-correlation to higher dust supply during glacials (Figure 3.4C to G). Thus, increased aeolian iron delivery during glacials alone does not seem to constitute the major influence on controlling North Pacific productivity.

3.5.1.2. Influence of ocean gyre circulation – high vs. low-latitude forcing

In comparison with records north of the Subarctic Front including ODP Site 882, the amplitudes of ln-Ba/Ti variations in our southern studied cores are apparently much lower and look less similar to global climate change patterns, as e.g., expressed in the benthic δ^{18}O stack (Figure 3.4C to F and Figure S1). One possibility to explain the increasingly subdued glacial-interglacial productivity pattern towards the south could be a regionally pronounced, meridional shift between the subarctic and subtropical gyres. This would also relocate both the Mixed Water Region and its boundary between the Subarctic and the Subtropical Front, driven by the respective current energy and strength of the Kuroshio Extension and the Oyashio Current. At present, the primary productivity in the transition zone is strongly influenced by the relative positions of these two currents (Kawahata and Ohshima, 2002). Pollen and benthic foraminiferal fauna studies have shown that a small southward shift of the Kuroshio Extension and/or the Subarctic Front during glacials (Kawahata and Ohshima, 2002; Ohkushi et al., 2018), supported by the decreasing amplitude of iron dust-related records from north to south in our records (Figure 3.4G).

However, the neighboring core H3571 from Hess Rise suggests higher productivity during glacial periods (Figure 3.4H), indicated by higher biogenic opal and organic carbon burial in the sediments (Kawahata et al., 2000). Also, foraminiferal abundance records from Shatsky Rise reflect high productivity during glacial periods, correlating to biogenic opal and organic carbon (Ohkushi et al., 2018). These opposite productivity signals might also simply be showing that preservation is not necessarily equivalent to initial component fluxes, as e.g., organic carbon is sensitive to oxygenation of bottom and pore waters. Its preservation also decreases along with increasing oxygen exposure time (Hartnett et al., 1998). Compiled data from the North Pacific showed that organic carbon flux was generally lower during the Last Glacial Maximum in comparison to the Holocene (Kohfeld and Chase, 2011). Additionally, an inverse glacial-interglacial productivity condition occurred in latitudes below 40°N (Rae et al., 2020). These observed opposite productivity signals at Hess Rise might also support that gyre shifts of the cold nutrient-rich Oyashio Current and the warm nutrient-poor Kuroshio Current, as a transition zone, provided different nutrient regimes to the transitional region in our study area. Although it has been discussed and proposed previously that export production peaked during or towards glacial terminations in the subarctic Pacific (Crusius et al., 2004; Gebhardt et al., 2008; Kawahata et al., 2000; Ohkushi et al., 2018), we suggest the maximum export production persisted during the peak interglacial periods reflected by maximum in biogenic Ba records from the Emperor Seamount Chain and the Hess Rise. Based on our result, this condition extended further south to the Hess Rise at 37°N as the end member of the northern-dominated nutrient regime in the NW Pacific.

3.5.1.3. Macronutrient supply and limitation through upper ocean stratification changes

Export production is generally higher during interglacials and lower in glacials (Figure 3.4). However, sedimentary, foraminifera- and diatom-bound nitrogen isotopes ($\delta^{15}N$) as proxy for the nutrient utilization efficiency revealed that the nutrient utilization enhanced during glacial periods in the subarctic Pacific (Brunelle et al., 2007; Galbraith et al., 2008; Knudson and Ravelo, 2015a; Ren et al., 2015). A common physical mechanism has been proposed to modulate the nutrient supply: by increasing stratification during glacials, the nutrient-rich deep water was then more isolated from surface waters, thereby leading to nearly complete nutrient utilization (Brunelle et al., 2007, 2010; Costa et al., 2018; Gebhardt et al., 2008; Jaccard et al., 2005, 2010; Kienast et al., 2004; Knudson and Ravelo, 2015a; Sigman et al., 2004). IRD has been found in the NW Pacific sediments and recently published studies extended the lateral coverage further south to the northern Shatsky Rise at 38°N (Kotilainen and Shackleton, 1995; McCarron et al., 2021). We have also qualitatively observed IRD grains in the coarse fractions in all four sites during glacial intervals. Evidence for increased glacial sea ice formation in the subpolar NW Pacific (e.g. Max et al., 2012; Méheust et al., 2016, 2018), which is mechanistically connected to the closure of the Bering Sea acting as positive feedback mechanism (Knudson and Ravelo, 2015b), further supports this scenario by freshening surface waters and decreasing salinity. As a result, upper ocean stratification during glacials was likely enhanced (Costa et al., 2018). Therefore, when vertical water mass mixing increased during interglacials, nutrients would be more vigorously upwelled into the surface ocean and result in enhanced productivity.

This pattern would be in line with previous suggestions that invoked a differential nutrient signature in mid-depth waters both on instrumental time scales (Nishioka et al., 2014; Nishioka et al., 2020; Wong et al., 2022), and on glacial-interglacial changes and glacial terminations (Lembke-Jene et al., 2017; Max et al., 2014; Ovsepyan et al., 2017). Under these assumptions, a more extensive glacial NPIW is better ventilated and occupies an increased depth domain down to ca. 1500-2000 m water depth (Gong et al., 2019; Herguera et al., 2010; Jaccard and Galbraith, 2013). These mid-depth waters were nutrient poorer then their modern equivalents, while a more isolated glacial NPDW was enriched in nutrients, thus leading to a lower preformed nutrient pool that is subjected to winter upwelling and thermocline replenishment (Gong et al., 2019; Lembke-Jene et al., 2017). These macro-nutrient supply changes via surface ocean stratification combined with different configurations of the deep preformed nutrient pool could hence constitute one of the primary controls on export production changes in the NW Pacific.

3.5.2. NW Pacific variations in carbonate production and preservation

3.5.2.1. Quantification of XRF-derived calcium data for high-resolution carbonate time-series

In order to obtain records of sufficiently high temporal resolution, we used XRF-scanning-derived Ca data which has been proposed to reflect the $CaCO_3$ variations in marine sediments. Many studies have used and provided evidences that XRF-based Ca-normalized ratios can be used as indicator of the carbonate saturation state of the deep ocean (e.g., Gottschalk et al., 2018; Jaccard et al., 2010). We compared the XRF-Ca counts and the $CaCO_3$ content and it presented high correlation coefficients in all four studied cores (SO264-66-2: $Y = 7358.3X + 40105$, $r^2 = 0.8742$, SO264-55-1: $Y = 8312.7X + 28955$, $r^2 = 0.8171$, SO264-15-2: $Y = 15154X – 138732$, $r^2 = 0.8293$, SO202-37-2: $Y = 11080X – 137077$, $r^2 = 0.8986$; Figure 3.5), indicating that our XRF-Ca ratio data faithfully represents $CaCO_3$ content variations in the study area.

On the basis of $CaCO_3$ content being potentially affected by dilution with biogenic material such as opal, and terrigenous components such as tephra, ice-rafted detritus and dust, we then calculated carbonate accumulation rates (CAR, g/cm^2ka^{-1}) to mitigate these effects to some extent. The converted CAR records thus provide a more comprehensive picture of the carbonate sedimentation regime than solely $CaCO_3$ content.

For the northern Emperor Seamount Chain cores SO264-66-2 and SO264-55-2, the CARs track the patterns of $CaCO_3$ content very closely, indicating better carbonate preservation during interglacials and higher dissolution in glacials (Figure 3.6B and C). As recorded in the regional reference core ODP site 882 (Jaccard et al., 2010), one prominent feature are interglacial carbonate peaks followed by carbonate-free sediments in the northern sites (Figure 3.6A). The cores SO264-66-2 and SO264-55-2 clearly repeat this feature; the $CaCO_3$ content maxima appeared during interglacial MIS 1, 3, 5, 7, 9 and 11 up to 95-40 % and then dropped to 10-0 % during most of the glacials and even in some of the late interglacials, such as MIS 9 and 11 (Figure 3.6B and C).

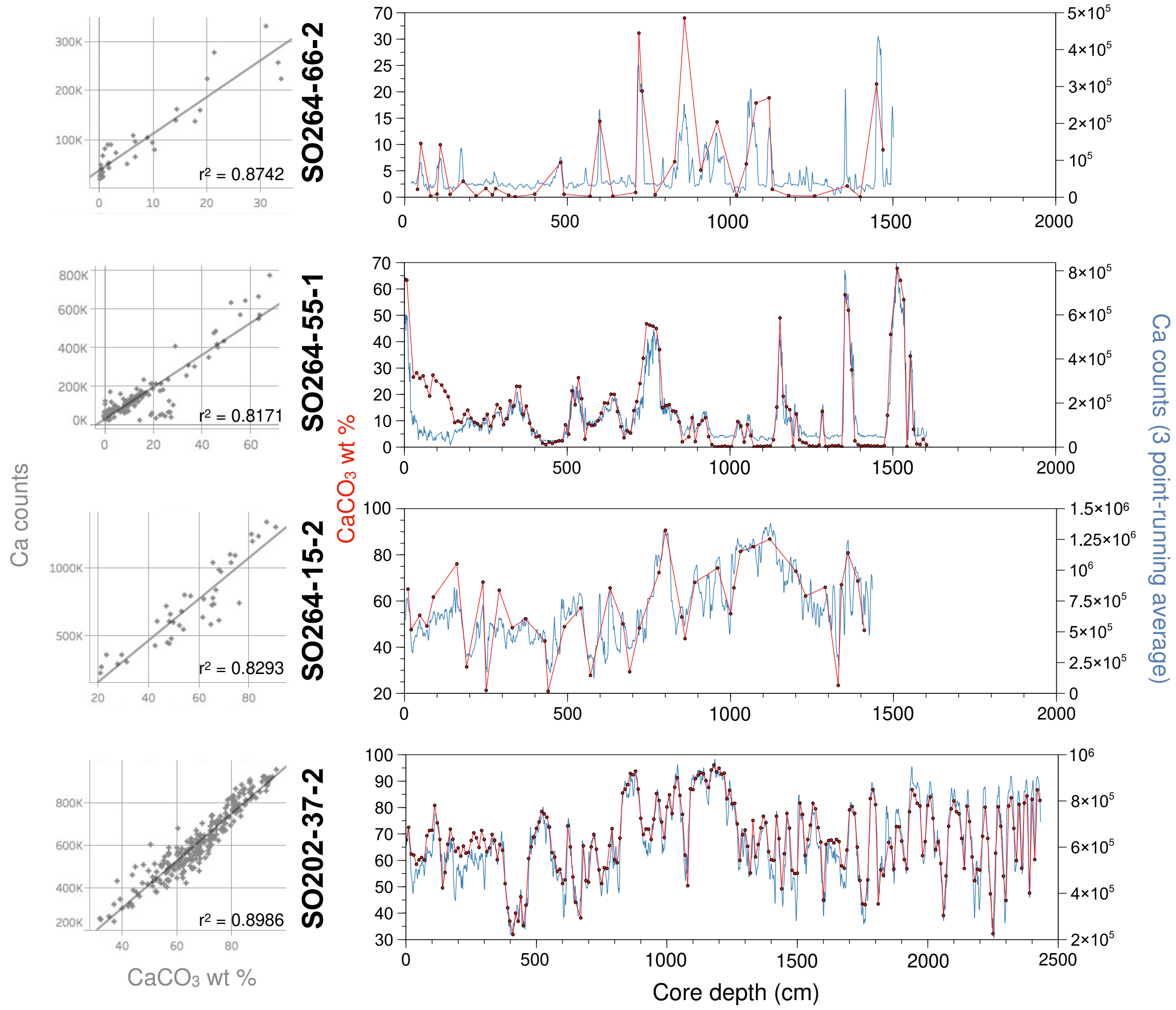

Figure 3.5: Comparison of downcore variations of carbonate content in weight percent (red lines) and smoothed (3 point-running average) XRF-Ca counts (blue lines) of four cores from the Northwest Pacific (right panels), shown against individual core depths (noted scale change in the lower most right panel). The four left panels show correlation between $CaCO_3$ content and XRF-Ca counts and the corresponding linear regression lines with the resulting correlation coefficient r^2.

The southern Emperor Seamount Chain cores SO264-15-2 and SO202-37-2, however, do not record similar carbonate peak structures. The $CaCO_3$ contents of these two cores are nearly identical and show significant variations (Figure 3.6D and E). $CaCO_3$ contents rise in glacial periods, except the sustained preservation during MIS 5 and the early MIS 11 and 9. In addition, a continued period of carbonate dissolution began roughly 500 ka BP and lasted around 200 ka. While the two southern sites SO264-15-2 and SO202-37-2 show some comparable trends between CAR and $CaCO_3$ content, they yield differences, most notably during MIS 5, early MIS 7 and MIS 9 (Figure 3.6D and E). CAR variations reveal a clearer pattern than $CaCO_3$ content does, e.g., throughout the CAR profile of SO202-37-2, a ~100 ka cyclic pattern, indicative of orbital forcing-induced changes in carbonate production or preservation, emerges with higher values during glacial, and relatively lower values in interglacial periods, except the last 60 ka BP, where this relationship switches.

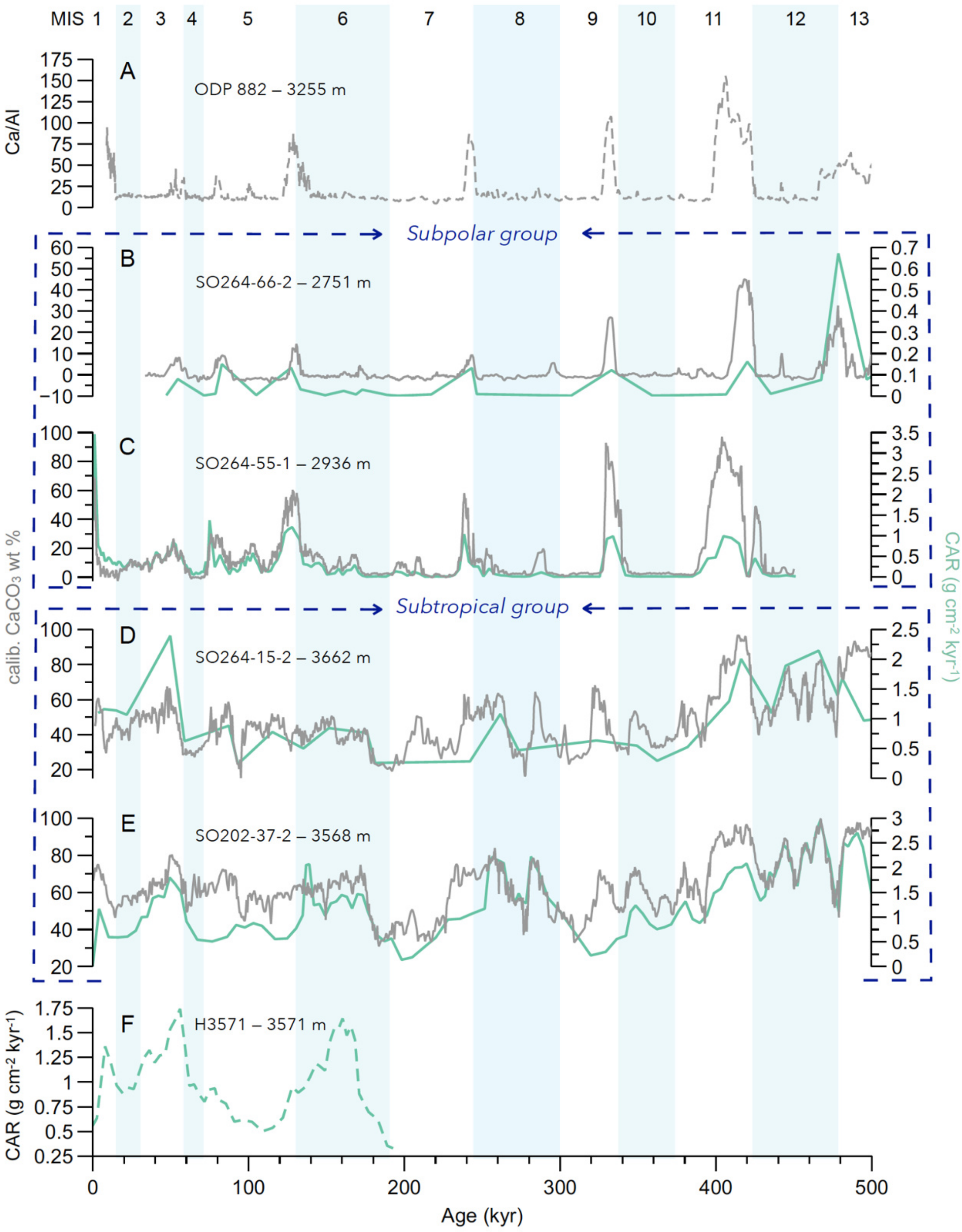

Figure 3.6: Comparison of carbonate variations along the NW Pacific transect, based on XRF-derived Ca/Al, calibrated carbonate content (gray, in wt. %) and carbonate accumulation rate (light green, in g/cm^{2}ka^{-1}) from (A) ODP site 882 (Jaccard et al., 2010), (B) SO264-66-2 (this study), (C) SO264-55-1 (this study), (D) SO264-15-2 (this study), (E) SO202-37-2 (this study) and (F) H3571 (Kawahata et al., 2000). Due to the differences of the carbonate patterns, the studied cores (B) and (C) are grouped as “Subpolar group”, while (D) and (E) as “Subtropical group”.

Due to the observed $CaCO_3$ content and CAR differences, we grouped and named the NW Pacific cores from the northern Emperor Seamount Chain SO264-64-1 and SO264-55-1 as

"Subpolar group", and the southern cores SO264-15-2 and SO202-37-2 as "Subtropical group" (Figure 3.6). We determined SO264-55-1 as representative core for the Subpolar group and SO202-37-2 for the Subtropical group due to their higher resolutions.

3.5.2.2. Latitudinal dynamics between export production and carbonate depositional patterns

In our Subtropical Group, the relation between paleo-export production, as represented in ln-Ba/Ti ratios, and $CaCO_3$ content and/or accumulation rates is not straightforward. Maxima between the two proxies are most significant between late MIS 13 to MIS 9, but their respective amplitude expressions are different (Figure 3.7-Subtropical group). This period of broad CAR decline roughly fits into the period of the so-called Mid-Brunhes Dissolution Interval (MBDI), which has been identified throughout individual sites in different regions of the world ocean (Sexton and Barker, 2012). The MBDI was hypothesized to be due to a global proliferation of the *Gephyrocapsa* coccolithophore, causing the increase of ocean surface carbonate production and driving enhanced deep-sea carbonate dissolution (Barker et al., 2006). From MIS 8 onward, CAR patterns changed to a more pronounced glacial-interglacial timing, less consistent with $CaCO_3$ content variations (Figure 3.7-Subtropical Group). An earlier study of calcareous nannofossils on Shatsky Rise also showed a significant shift between MIS 8 and 7, and the bulk $CaCO_3$ content switching from coccolith calcite to foraminifera with co-occurring biogenic opal, which could have been favored by iron fertilization via aeolian dust increase (Bordiga et al., 2014). This might explain the mismatch between the $CaCO_3$ content and CAR being due to dilution by biogenic opal.

Overall, the carbonate records in the Subtropical Group are evidently recording a pattern reminiscent of the "Pacific-type" with enhanced $CaCO_3$ preservation during glacials, similar to NE and equatorial Pacific records (Figure 3.5D to F; e.g., Farrell and Prell, 1989; Karlin et al., 1992; Wu et al., 1991). Earlier studies based on data of Equatorial Pacific sediment cores suggested that Pacific glacial-interglacial carbonate preservation cycles are mainly controlled by dissolution through calcite lysocline fluctuations (Farrell and Prell, 1989; Wu et al., 1991). It is mostly assumed that the underlying forcing of these lysocline and CCD adjustments reflect a buffering of the deep-sea $[CO_3^{2-}]$, which controls the Pacific carbonate accumulation patterns (Anderson et al., 2008; Farrell and Prell, 1989; Hodell et al., 2001; Zhang et al., 2007). Sexton and Barker (2012) attributed the cause of the glacial Pacific $CaCO_3$ dissolution minimum to a consistently strengthened ventilation within the Pacific sector of the Southern Ocean, referred to as "glacial Pacific ventilation hypothesis". In addition, in the primary productivity-related "rain ratio hypothesis" (Archer and Maier-Reimer, 1994), changes in the relative ratio of organic carbon vs. $CaCO_3$ are thought to indicate change in ocean pH $[CO_3^{2-}]$ due to the degradation of organic carbon, which promotes carbonate dissolution in the sediments.

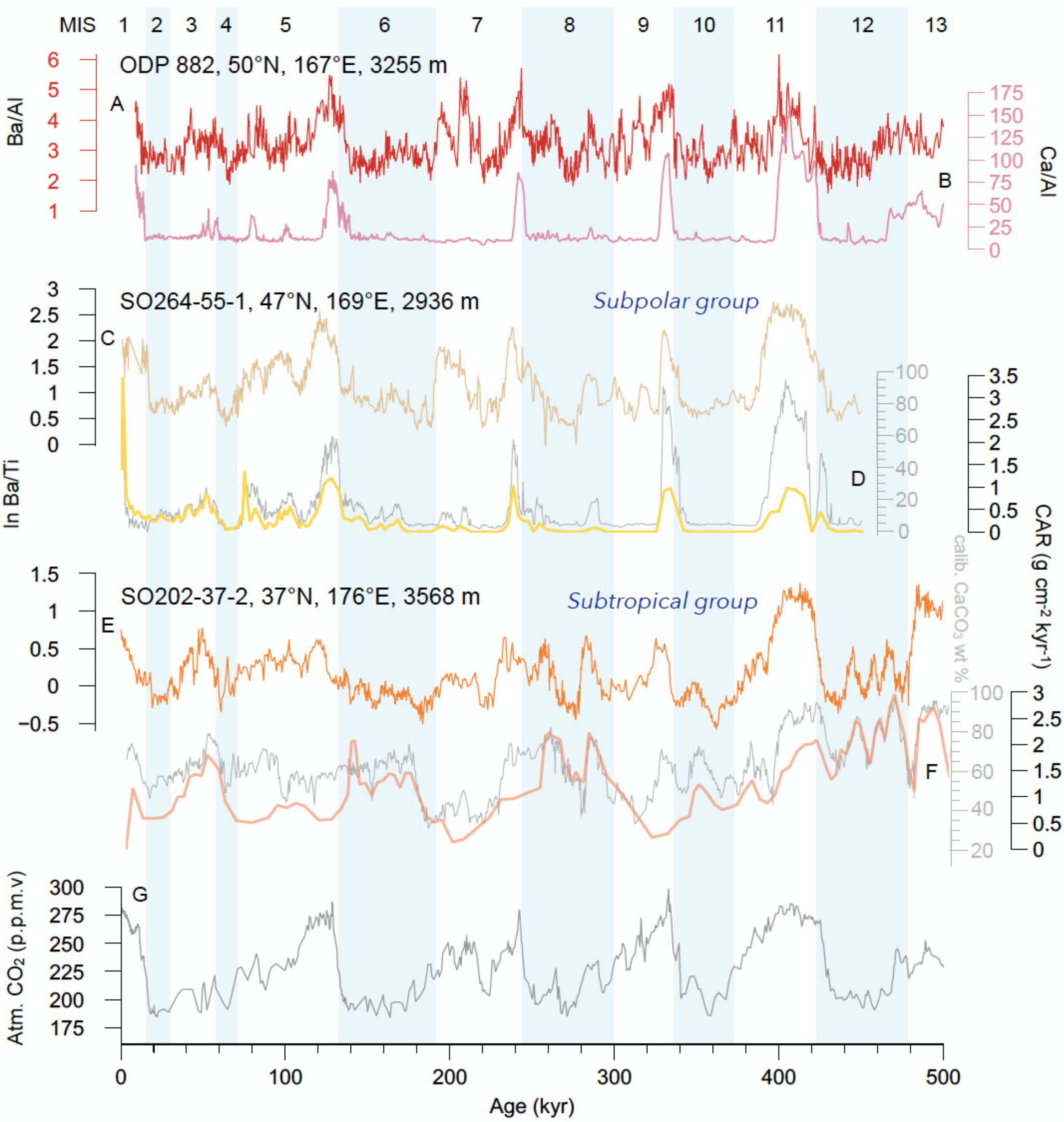

Figure 3.7: Comparison of productivity and carbonate records from the study region along the latitudinal transect for the last 500,000 years. (A)-(B) XRF Ba/Al and Ca/Al ratios from ODP Site 882. (C)-(D) XRF ln-Ba/Ti, CAR and ln-Ca/Ti (in gray) from SO264-55-1 as a representative core from the "Subpolar group". (E)-(F) XRF ln-Ba/Ti, CAR and ln-Ca/Ti (in gray) from SO202-37-2 as a representative core from the "Subtropical group". (G) Atmospheric CO_2 concentration from Antarctic ice core EPICA Dome C (EDC Lüthi et al., 2008; Monnin et al., 2001; Siegenthaler et al., 2005).

In contrast, in the Subpolar group, severe carbonate dissolution dominates throughout all glacials during the last 500 ka BP. Nearly no carbonate was preserved, even extending into to some mid- and late-interglacials. However, the interglacial productivity and carbonate signals are relatively straightforward (Figure 3.7-Subpolar group). In almost all interglacials, i.e., MIS 11, 9, 7e, 5e, 5c and 5a, corresponding $CaCO_3$ content and CAR peaks correlate with productivity maxima. Thus, in the Subpolar group, no "Pacific-type" $CaCO_3$ can be observed, instead an overall carbonate-corrosive, but distinct "Atlantic-type", featuring severe $CaCO_3$

dissolution during glacials seems to prevail throughout the investigated 500 ka BP. The "Atlantic-type" $CaCO_3$ preservation originally mainly results from changes in the strength of the Atlantic Meridional Overturning Circulation (AMOC), and the extent and distribution of well-ventilated North Atlantic Deep Water (NADW; Broecker and Clark, 2001; Hodell et al., 2001). However, the higher $[CO_3^{2-}]$ in NADW causes the CCD to be located relatively deeper (~5000 m) in the Atlantic basin relative to the Pacific (~3500 - 4500 m).

Transient carbonate peaks as seen in the Subpolar group have also been observed in the biogenic carbonate (indicated by Ca/Al ratios) of neighboring site ODP Site 882 (Jaccard et al., 2010). Notably, even relatively shallow mesopelagic records from the marginal seas also show similar $CaCO_3$ pattern with rapid interglacial peaks and nearly absent $CaCO_3$ content during glacial periods (Brunelle et al., 2010; Iwasaki et al., 2012). The $CaCO_3$ content disparity between the glacial and the interglacial sediments from the Subarctic group is substantial (Figure 3.6B and C). The peak-interglacial carbonate peaks, followed by near absence of carbonate in the glacial sediments suggest that the Subpolar group sites were always bathed in waters below the CCD during most of the glacials and even part of the late interglacial periods, with intermittent rapid shallowing. The rapid decline of $CaCO_3$ content in the Subpolar group indicates a fast shallowing of the lysocline which leads to an increased alkalinity and therefore reduced pCO_2 in the surface ocean.

In the "carbonate compensation hypothesis", the deep ocean carbonate chemistry called for changes in increasing $[CO_3^{2-}]$ and following increasing alkalinity, when CO_2 was released back to the surface ocean (and the atmosphere) at the end of glacials. Such ventilation changes and CO_2 outgassing cause a transient carbonate compensation in order to buffer and balance the saturation state, leading to preservation of $CaCO_3$ in response to the deep ocean carbon storage changes (Boyle, 1988; Broecker and Peng, 1989; Marchitto et al., 2005). Other studies also suggested these interglacial carbonate peaks could imply high loading of regenerated dissolved inorganic carbon and therefore a short-term of major CO_2 release from the deep subarctic North Pacific, due to ventilation from the south and/or local bottom water ventilation (Gebhardt et al., 2008; Jaccard et al., 2010).

We finally added to our datasets a further examination of the relation between productivity and carbonate preservation on a shorter time scale, covering the last 200 ka BP. By adding alkenone concentrations and coarse fraction percent (>63µm, sand %) data to our data set (Figure 3.8), we attempted to qualitatively assess whether carbonate preservation changes in both or either the Subpolar and Subtropical groups are mostly associated with carbonate (coccolithophore) production or carbonate dissolution.

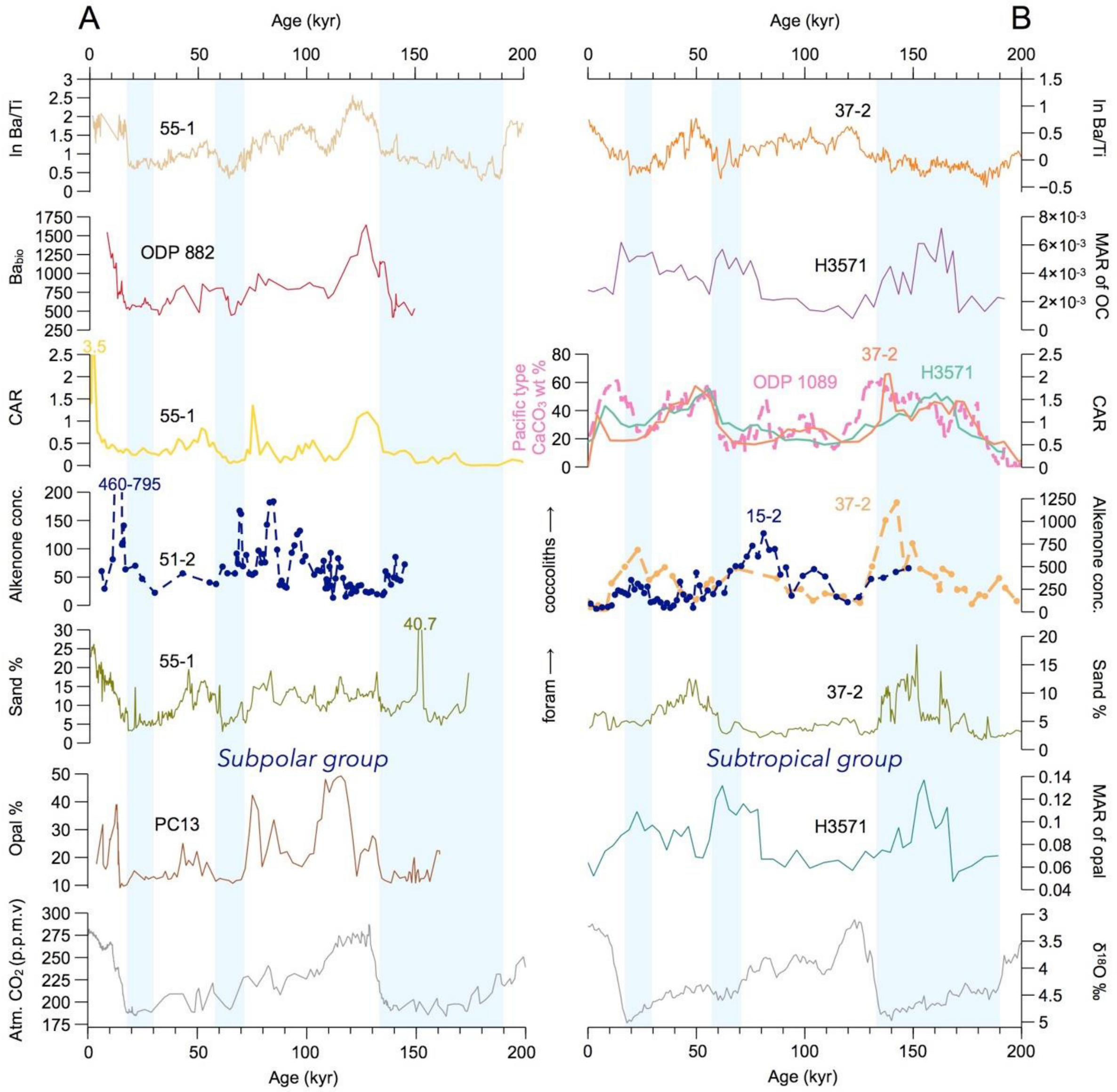

Figure 3.8: Comparison of multiproxy records from Subpolar group (column A) and Subtropical group (column B) for the last 200,000 years. The lowest panels show the EDC CO_2 concentration (EDC Lüthi et al., 2008; Monnin et al., 2001; Siegenthaler et al., 2005) and the benthic $\delta^{18}O$ stack (Lisiecki and Raymo, 2005).

In the Subpolar group, the coherent increase in biogenic Ba and other biogenic proxies across the region suggests enhances organic carbon export, which led to an increase in carbonate production and according carbonate flux maxima during interglacials (Jaccard et al., 2009; Kohfeld and Chase, 2011). Alkenone concentration of SO264-51-2 (Figure 3.8A 51-2) shows a likewise increase in MIS 5, indicating higher coccolithophore production contributed to maximum carbonate accumulation. In addition, the high coarse fraction content shows a dominance of foraminifera and hence low dissolution intensity of coarse carbonate particles. The relative high values of the sand fraction (sand %) in interglacials further support a productivity-related rather than dissolution-dominated carbonate regime (Figure 3.8A). Unfortunately, our results cannot provide direct information about whether this interglacial inorganic carbon pattern was related to prior CO_2 release from the deep subarctic NW Pacific, which might be attributed to re-invigorated ventilation from the south and/or of local bottom water (Gebhardt et al., 2008; Jaccard et al., 2010). Clearly, further studies on benthic foraminiferal carbon isotopes and [CO_3^{2-}] from this region would be necessary to resolve this question.

Notably, in the Subtropical group the export production signal and carbonate flux, e.g., in SO202-37-2, pace largely out of phase for the last 300 ka BP, except for a few local maxima in MIS 3 and 8, where both productivity and carbonate flux increased (Figure 3.7-Subtropical group). Otherwise, the carbonate patterns are expressed as glacial-interglacial cycles, with higher preservation during glacials and dissolution during interglacials, while ln-Ba/Ti variations were relatively higher during interglacials. The poor correlation between productivity and $CaCO_3$ has also been known from some other sites from the equatorial Pacific (Anderson et al., 2008; Qin et al., 2017; Zhang et al., 2007). On the other hand, considering that the ODP site 1089 (40.94°S, 9.89°E; 4624 cm water depth) is bathed in the LCDW and reflects high-resolution [CO_3^{2-}] changes in deep Pacific, the good correlation to the carbonate records from the Hess Rise suggested that the typical "Pacific-type" $CaCO_3$ pattern prevails in particular for this period of the last 200-300 ka BP. Moreover, the sand% in the Subtropical group shows a clear indication for a dissolution signal during MIS 5 (Figure 3.8B, 37-2 olive green line), and while the alkenone concentration remained high (Figure 3.8B, 15-2), this can be explained by coccoliths being more resistant to dissolution than foraminifera (Chiu and Broecker, 2008). The mismatch between export production and carbonate records from the Hess Rise not only could be explained by the possibility of $CaCO_3$ production varying independently of organic carbon export, but also reveal the boundary shifts between the subarctic and subtropical gyre, which provide different nutrient regimes to the region. These large reorganizations of the carbonate depositional regime and underlying ecological changes or boundary conditions around 280-300 ka BP were ultimately possibly linked to changes in low-latitude climate forcing and long-term ENSO activity and Asian Monsoon changes (Beaufort et al., 2022; Bordiga et al., 2013).

3.6. Conclusion

Our sediment sites from the Emperor Seamount Chain and the Hess Rise showed a decreasing gradient in paleo-export production based on XRF-derived ln-Ba/Ti ratios and dust supply (XRF-Fe), reconstructed from records from the subarctic north at 52°N to the transitional-subtropical south at around 37°N. Maxima in biogenic Ba records suggested the maximum export production took place during the peak interglacial periods in the NW Pacific during the last 500 ka. We conclude that the local subarctic and subtropical gyre circulation shift and the upper ocean stratification had the major control on the nutrient regime, rather than dust supply. Additionally, a reverse pattern in carbonate content and preserved flux occurred along the Emperor Seamount Chain. In our subpolar group, the productivity had a more direct influence on the carbonate system in the western Subarctic Pacific. The coherent increases in biogenic Ba, CAR, alkenone concentration, sand% and opal% during interglacials indicating a regional surface biological production promoted these interglacial carbonate peaks in this carbonate-corrosive region. On the other hand, the Subtropical group carbonate deposition attributed to the dissolution which supported by the comparable patterns between sand% and CAR. The CAR semblance to the LCDW carbonate signal suggested this carbonate pattern is related to the deep Pacific [CO_3^{2-}] changes responding to the global ocean carbonate budget balance. The mismatch between export production and carbonate records from the Hess Rise also revealed the boundary of the shifting between the cold nutrient-rich Oyashio Current and the warm nutrient-poor Kuroshio Current which provide different nutrient regime to the region.

3.7. Acknowledgements

We thank the master, crew and the SO264 science party for their contributions to a successful expedition. We thank Valea Schumacher, Susanne Wiebe for technical support, and Lisa Schoenborn, and Dorothee Wilhelms-Dick for analytical support with the IRMS. We thank Tunde Gabriel for support in sample processing. We acknowledge financial support from the AWI institutional budget under the “PACES-II” (2018-20) and “Changing Earth – Sustaining our Future” (2020-2022), the German Federal Ministry for Education and Research (BMBF) through grants no. 03G0264B “SO264-EMPEROR” and 3F0785A “NOPAWAC”.

3.8. Data availability

The datasets used and analyzed during this study are available on Pangaea and/or from the corresponding author or project PI on reasonable request.

3.9. Supplement

Table S1: AMS ^{14}C ages of the SO202-37-2 with calibrated calendar ages.

AWI no.	Depth (cm)	Species	Radiocarbon age (yr)	Median calendar age (yr)	Calendar age ±2σ (yr)
3943.1.1	2.5	*G. bulloides*	3427±84	3121	2865 - 3361
3954.1.1	38.5	*G. bulloides*	18195±175	21071	20569 - 21622
3957.1.1	50.5	*G. bulloides*	24356±304	27678	27118 - 28381

Table S2: Age model of cores SO202-37-2 and SO264-55-1. C14: base on radiocarbon dating on planktonic foraminifera. δ^{18}O: benthic δ^{18}O correlation of cores to the benthic δ^{18}O stack of Lisiecki and Raymo (2005). Tiepoint-XRF: XRF correlation of elemental ratio records of cores to Ba/Al of ODP site 882 (Jaccard et al., 2010) and benthic δ^{18}O stack (Lisiecki and Raymo, 2005). Tephra: tephra identification during cruise (Nürnberg, 2018).

SO202-37-2		
Depth (cm)	Age (ka)	Comment
2.5	0.3	C14
38.5	21.1	C14
50.5	27.7	C14
144.5	61.9	Tiepoint-XRF, $\delta^{18}O$
170.6	87	Tiepoint-XRF, $\delta^{18}O$
210.9	109.2	Tiepoint-XRF, $\delta^{18}O$
226.6	122.9	Tiepoint-XRF, $\delta^{18}O$
238.5	130	Tiepoint-XRF, $\delta^{18}O$
250.6	135.1	Tiepoint-XRF, $\delta^{18}O$
274.4	140	Tiepoint-XRF
318.8	156.1	Tiepoint-XRF
404.5	185	Tiepoint-XRF, $\delta^{18}O$
420.6	192.1	Tiepoint-XRF, $\delta^{18}O$
439.7	204.9	Tiepoint-XRF, $\delta^{18}O$
463.7	223.1	Tiepoint-XRF, $\delta^{18}O$
500.4	252.1	Tiepoint-XRF, $\delta^{18}O$
617.7	280.2	Tiepoint-XRF, $\delta^{18}O$
643.7	294.1	Tiepoint-XRF, $\delta^{18}O$
661.7	319.9	Tiepoint-XRF
679.6	329.1	Tiepoint-XRF, $\delta^{18}O$
696.9	341.5	Tiepoint-XRF, $\delta^{18}O$
718.9	348.1	Tiepoint-XRF, $\delta^{18}O$
824.5	396.4	Tiepoint-XRF, $\delta^{18}O$
870.6	417	Tiepoint-XRF, $\delta^{18}O$
987.2	455.1	Tiepoint-XRF, $\delta^{18}O$
1063.9	479	Tiepoint-XRF
1119.6	491	Tiepoint-XRF, $\delta^{18}O$
1205.7	524.2	Tiepoint-XRF

SO264-55-1		
Depth (cm)	Age (ka)	Comment
5.5	6.8	C14
17.5	10.5	C14
29.5	13.2	C14
195.5	15.7	C14
215.5	18.5	C14
295.5	29.1	C14
315.5	30	C14
325.5	33.9	C14
335.5	39.8	C14
387.1	59.1	Tiepoint-XRF
431.4	64.6	Tiepoint-XRF
455.4	68.1	Tiepoint-XRF, $\delta^{18}O$
473.6	70.2	Tiepoint-XRF
483	72.8	Tiepoint-XRF
500	77	Tiepoint-XRF
503.9	78.6	Tiepoint-XRF
550.9	86.3	Tiepoint-XRF
574.3	90.8	Tiepoint-XRF
614.4	103.8	Tiepoint-XRF
649.6	108.5	Tiepoint-XRF
707.2	111.4	Tiepoint-XRF
761.8	123	$\delta^{18}O$
769.8	124.9	Tiepoint-XRF
777.5	130	$\delta^{18}O$
781.5	135.2	Tiepoint-XRF
797.8	140	$\delta^{18}O$
823.6	144	$\delta^{18}O$
1011.8	190.3	Tiepoint-XRF, $\delta^{18}O$
1029.2	197.6	Tiepoint-XRF, $\delta^{18}O$
1038.8	203.3	Tiepoint-XRF, $\delta^{18}O$
1084.3	217.5	Tiepoint-XRF, $\delta^{18}O$
1103.9	222.7	Tiepoint-XRF, $\delta^{18}O$
1164.8	244.2	Tiepoint-XRF, $\delta^{18}O$
1279.6	282.9	Tiepoint-XRF, $\delta^{18}O$
1297.6	299.5	Tiepoint-XRF, $\delta^{18}O$
1348.1	328.2	Tiepoint-XRF, $\delta^{18}O$
1410.8	350.4	Tiepoint-XRF, $\delta^{18}O$
1514.3	405.8	Tiepoint-XRF
1545.5	421.2	Tephra

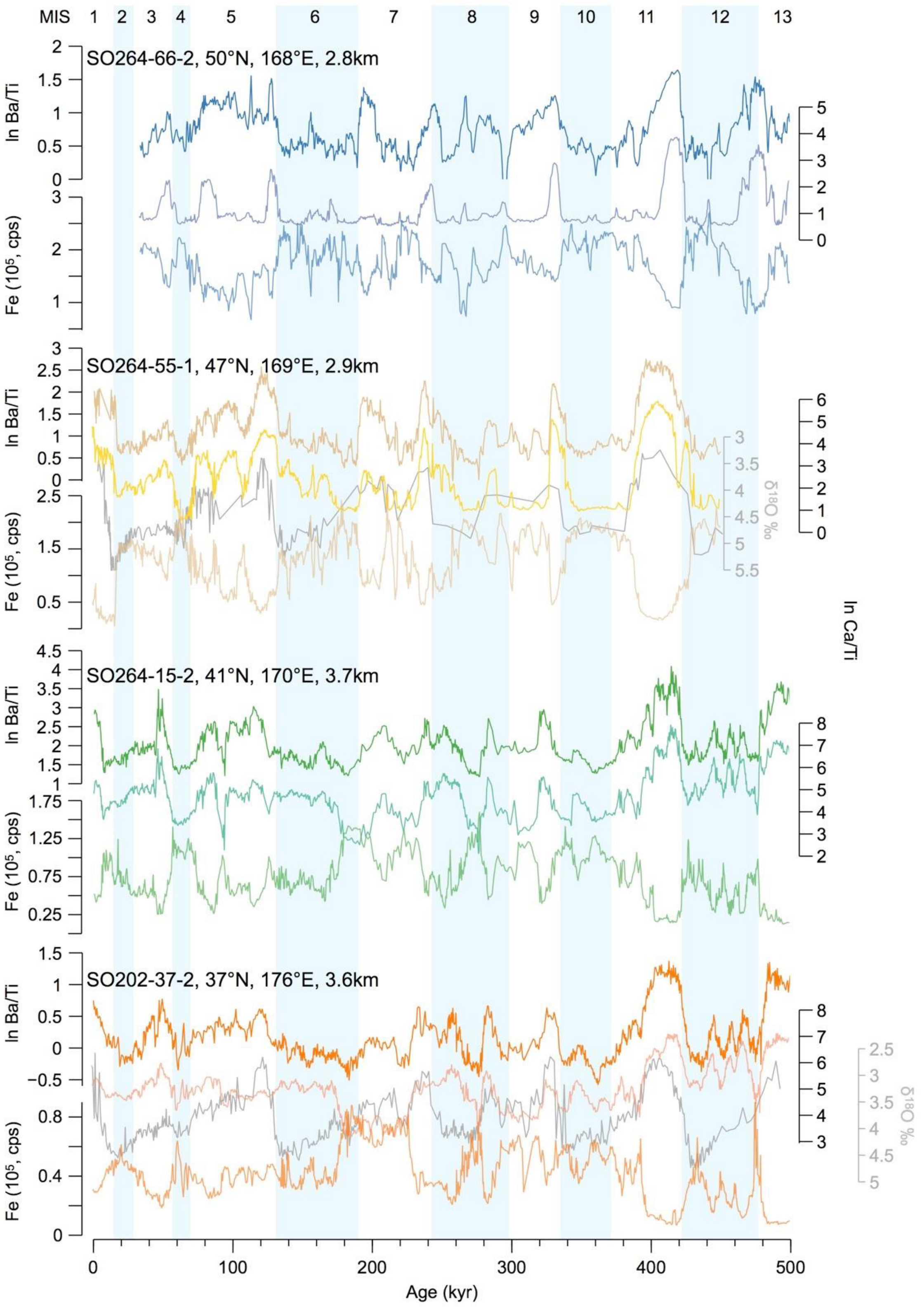

Figure S1: XRF ln-Ba/Ti (upper curve) and ln-Ca/Ti (lower curve) ratios of the Northwest Pacific cores plotted against age and the two benthic $\delta^{18}O$ records (SO264-55-1 and SO202-37-2) in gray line at the back as comparison. Marine Isotope Stages: MIS 1 to 13. Light blue shadings indicate glacial stages.

3.10. References

Anderson, R., Fleisher, M., Lao, Y. and Winckler, G., 2008. Modern CaCO3 preservation in equatorial Pacific sediments in the context of late-Pleistocene glacial cycles. Mar. Chem. 111, 30–46.

Archer, D. and Maier-Reimer, E., 1994. Effect of deep-sea sedimentary calcite preservation on atmospheric CO 2 concentration. Nature, 367, 260-263.

Arrhenius, G., 1952. Sediment cores from the East Pacific. Reports of the Swedish deep-sea expedition, 1947-1948, 5: 201.

Auderset, A., Schmitt, M. and Martínez-García, A., 2020. Simultaneous extraction and chromatographic separation of n-alkanes and alkenones from glycerol dialkyl glycerol tetraethers via selective Accelerated Solvent Extraction. Organic Geochemistry, 143: 103979.

Barker, S., Archer, D., Booth, L., Elderfield, H., Henderiks, J. and Rickaby, R.E., 2006. Globally increased pelagic carbonate production during the Mid-Brunhes dissolution interval and the CO2 paradox of MIS 11. Quaternary Science Reviews, 25(23-24): 3278-3293.

Bé, A.W.H., Damuth, J.E., Lott, L. and Free, R., 1976. Late Quaternary climatic record in western equatorial Atlantic sediment. Investigation of Late Quaternary Paleoceanography and Paleoclimatology, 145: 165.

Beaufort, L., Bolton, C.T., Sarr, A.-C., Suchéras-Marx, B., Rosenthal, Y., Donnadieu, Y., Barbarin, N., Bova, S., Cornuault, P. and Gally, Y., 2022. Cyclic evolution of phytoplankton forced by changes in tropical seasonality. Nature, 601(7891): 79-84.

Berger, W.H., 1973. Deep-sea carbonates; Pleistocene dissolution cycles. The Journal of Foraminiferal Research, 3(4): 187-195.

Bordiga, M., Beaufort, L., Cobianchi, M., Lupi, C., Mancin, N., Luciani, V., Pelosi, N. and Sprovieri, M., 2013. Calcareous plankton and geochemistry from the ODP site 1209B in the NW Pacific Ocean (Shatsky Rise): New data to interpret calcite dissolution and paleoproductivity changes of the last 450 ka. Palaeogeography, Palaeoclimatology, Palaeoecology, 371: 93-108.

Bordiga, M., Cobianchi, M., Lupi, C., Pelosi, N., Venti, N.L. and Ziveri, P., 2014. Coccolithophore carbonate during the last 450 ka in the NW Pacific Ocean (ODP site 1209B, Shatsky Rise). Journal of Quaternary Science, 29(1): 57-69.

Boyd, P.W., Jickells, T., Law, C., Blain, S., Boyle, E., Buesseler, K., Coale, K., Cullen, J., De Baar, H.J. and Follows, M., 2007. Mesoscale iron enrichment experiments 1993-2005: synthesis and future directions. Science, 315(5812): 612-617.

Boyle, E.A., 1988. The role of vertical chemical fractionation in controlling late Quaternary atmospheric carbon dioxide. Journal of Geophysical Research: Oceans, 93(C12): 15701-15714.

Broecker, W.S. and Clark, E., 2001. Glacial-to-Holocene redistribution of carbonate ion in the deep sea. Science, 294(5549): 2152-2155.

Broecker, W.S. and Peng, T.H., 1989. The cause of the glacial to interglacial atmospheric CO2 change: A polar alkalinity hypothesis. Global Biogeochemical Cycles, 3(3): 215-239.

Brunelle, B.G., Sigman, D.M., Cook, M.S., Keigwin, L.D., Haug, G.H., Plessen, B., Schettler, G. and Jaccard, S.L., 2007. Evidence from diatom-bound nitrogen isotopes for subarctic Pacific stratification during the last ice age and a link to North Pacific denitrification changes. Paleoceanography, 22:1-17.

Brunelle, B.G., Sigman, D.M., Jaccard, S.L., Keigwin, L.D., Plessen, B., Schettler, G., Cook, M.S. and Haug, G.H., 2010. Glacial/interglacial changes in nutrient supply and stratification in the western subarctic North Pacific since the penultimate glacial maximum. Quaternary Science Reviews, 29(19-20): 2579-2590.

Chiu, T.C. and Broecker, W.S., 2008. Toward better paleocarbonate ion reconstructions: New insights regarding the CaCO3 size index. Paleoceanography, 23(2).

Costa, K.M., McManus, J.F. and Anderson, R.F., 2018. Paleoproductivity and Stratification Across the Subarctic Pacific Over Glacial-Interglacial Cycles. Paleoceanography and Paleoclimatology, 33(9): 914-933.

Costa, K.M., McManus, J.F., Anderson, R.F., Ren, H., Sigman, D.M., Winckler, G., Fleisher, M.Q., Marcantonio, F. and Ravelo, A.C., 2016. No iron fertilization in the equatorial Pacific Ocean during the last ice age. Nature, 529(7587): 519-522.

Crowley, T.J., 1985. Late Quaternary carbonate changes in the North Atlantic and Atlantic/Pacific comparisons. The carbon cycle and atmospheric CO2: Natural variations Archean to present, 32: 271-284.

Crusius, J., Pedersen, T.F., Kienast, S., Keigwin, L. and Labeyrie, L., 2004. Influence of northwest Pacific productivity on North Pacific Intermediate Water oxygen concentrations during the Bølling-Allerød interval (14.7–12.9 ka). Geology, 32(7): 633-636.

Curry, W. and Lohmann, G., 1990. Reconstructing past particle fluxes in the tropical Atlantic Ocean. Paleoceanography, 5(4): 487-505.

Dadey, K.A., Janecek, T. and Klaus, A., 1992. Dry-bulk density: its use and determination, Proceedings of the Ocean Drilling Program, Scientific Results. College Station, TX, pp. 551-554.

Damuth, J.E., 1977. Late Quaternary sedimentation in the western equatorial Atlantic. Geological Society of America Bulletin, 88(5): 695-710.

deMenocal, P., Archer, D. and Leth, P., 1997. Pleistocene variations in deep Atlantic circulation and calcite burial between 1.2 and 0.6 Ma: a combined data-model approach, Proc. ODP, Sci. Results, pp. 285-298.

Emile-Geay, J., Cane, M.A., Naik, N., Seager, R., Clement, A.C. and van Geen, A., 2003. Warren revisited: Atmospheric freshwater fluxes and "Why is no deep water formed in the North Pacific". Journal of Geophysical Research: Oceans, 108(C6).

Falkowski, P.G., Barber, R.T. and Smetacek, V., 1998. Biogeochemical controls and feedbacks on ocean primary production. science, 281(5374): 200-206.

Farrell, J.W. and Prell, W.L., 1989. Climatic change and CaCO3 preservation: An 800,000 year bathymetric reconstruction from the central equatorial Pacific Ocean. Paleoceanography, 4(4): 447-466.

Farrell, J.W. and Prell, W.L., 1991. Pacific CaCO3 preservation and δ18O since 4 Ma: paleoceanic and paleoclimatic implications. Paleoceanography, 6(4): 485-498.

Galbraith, E.D., Kienast, M., Jaccard, S.L., Pedersen, T.F., Brunelle, B.G., Sigman, D.M. and Kiefer, T., 2008. Consistent relationship between global climate and surface nitrate utilization in the western subarctic Pacific throughout the last 500 ka. Paleoceanography, 23(2).

Gardner, J., 1975. Late Pleistocene carbonate dissolution cycles in the eastern equatorial Atlantic. In Sliter, W.V., Bé, A.W.H., and Berger, W.H. (Eds.), Dissolution of Deep-Sea Carbonates. Spec. Publ. Cushman Found. Foraminiferal Res., 13:129-141.

Gebhardt, H., Sarnthein, M., Grootes, P.M., Kiefer, T., Kuehn, H., Schmieder, F. and Röhl, U., 2008. Paleonutrient and productivity records from the subarctic North Pacific for Pleistocene glacial terminations I to V. Paleoceanography, 23:1-23.

Gong, X., Lembke-Jene, L., Lohmann, G., Knorr, G., Tiedemann, R., Zou, J. and Shi, X., 2019. Enhanced North Pacific deep-ocean stratification by stronger intermediate water formation during Heinrich Stadial 1. Nature communications, 10(1): 1-8.

Gottschalk, J., Hodell, D.A., Skinner, L.C., Crowhurst, S.J., Jaccard, S.L. and Charles, C., 2018. Past carbonate preservation events in the deep Southeast Atlantic Ocean (Cape Basin) and their implications for Atlantic overturning dynamics and marine carbon cycling. Paleoceanography and paleoclimatology, 33(6): 643-663.

Gray, W.R., Wills, R.C., Rae, J.W., Burke, A., Ivanovic, R.F., Roberts, W.H., Ferreira, D. and Valdes, P.J., 2020. Wind-driven evolution of the North Pacific subpolar gyre over the last deglaciation. Geophysical Research Letters, 47(6): e2019GL086328.

Hartnett, H.E., Keil, R.G., Hedges, J.I. and Devol, A.H., 1998. Influence of oxygen exposure time on organic carbon preservation in continental margin sediments. Nature, 391(6667): 572-575.

Hays, J.D., Saito, T., Opdyke, N.D. and Burckle, L.H., 1969. Pliocene-Pleistocene sediments of the equatorial Pacific: their paleomagnetic, biostratigraphic, and climatic record. Geological Society of America Bulletin, 80(8): 1481-1514.

Herguera, J., Herbert, T., Kashgarian, M. and Charles, C., 2010. Intermediate and deep water mass distribution in the Pacific during the Last Glacial Maximum inferred from oxygen and carbon stable isotopes. Quaternary Science Reviews, 29(9-10): 1228-1245.

Hodell, D., Charles, C. and Sierro, F., 2001. Late Pleistocene evolution of the ocean's carbonate system. Earth and Planetary Science Letters, 192(2): 109-124.

Hovan, S.A., Rea, D.K. and Pisias, N.G., 1991. Late Pleistocene continental climate and oceanic variability recorded in northwest Pacific sediments. Paleoceanography, 6(3): 349-370.

Isono, D., Yamamoto, M., Irino, T., Oba, T., Murayama, M., Nakamura, T. and Kawahata, H., 2009. The 1500-year climate oscillation in the midlatitude North Pacific during the Holocene. Geology, 37(7): 591-594.

Iwasaki, S., Takahashi, K., Maesawa, T., Sakamoto, T., Sakai, S. and Iijima, K., 2012. Paleoceanography of the last 500 kyrs in the central Okhotsk Sea based on geochemistry. Deep Sea Research Part II: Topical Studies in Oceanography, 61: 50-62.

Jaccard, S., Galbraith, E., Sigman, D.M. and Haug, G., 2010. A pervasive link between Antarctic ice core and subarctic Pacific sediment records over the past 800 kyrs. Quaternary Science Reviews, 29(1-2): 206-212.

Jaccard, S.L. and Galbraith, E.D., 2013. Direct ventilation of the North Pacific did not reach the deep ocean during the last deglaciation. Geophysical Research Letters, 40(1): 199-203.

Jaccard, S.L., Galbraith, E.D., Sigman, D.M., Haug, G.H., Francois, R., Pedersen, T.F., Dulski, P. and Thierstein, H.R., 2009. Subarctic Pacific evidence for a glacial deepening of the oceanic respired carbon pool. Earth and Planetary Science Letters, 277(1-2): 156-165.

Jaccard, S.L., Haug, G.H., Sigman, D.M., Pedersen, T.F., Thierstein, H.R. and Röhl, U., 2005. Glacial/interglacial changes in subarctic North Pacific stratification. Science, 308(5724): 1003-1006.

Jacobel, A., Anderson, R., Winckler, G., Costa, K., Gottschalk, J., Middleton, J., Pavia, F., Shoenfelt, E. and Zhou, Y., 2019. No evidence for equatorial Pacific dust fertilization. Nature Geoscience, 12(3): 154-155.

Jacobel, A., McManus, J., Anderson, R. and Winckler, G., 2017. Climate-related response of dust flux to the central equatorial Pacific over the past 150 kyr. Earth and Planetary Science Letters, 457: 160-172.

Karlin, R., Lyle, M. and Zahn, R., 1992. Carbonate variations in the Northeast Pacific during the late Quaternary. Paleoceanography, 7(1): 43-61.

Kawahata, H. and Ohshima, H., 2002. Small latitudinal shift in the Kuroshio Extension (Central Pacific) during glacial times: evidence from pollen transport. Quaternary Science Reviews, 21(14-15): 1705-1717.

Kawahata, H., Okamoto, T., Matsumoto, E. and Ujiie, H., 2000. Fluctuations of eolian flux and ocean productivity in the mid-latitude North Pacific during the last 200 kyr. Quaternary Science Reviews, 19(13): 1279-1291.

Kienast, S.S., Hendy, I.L., Crusius, J., Pedersen, T.F. and Calvert, S.E., 2004. Export production in the subarctic North Pacific over the last 800 kyrs: No evidence for iron fertilization? Journal of Oceanography, 60(1): 189-203.

Knudson, K.P. and Ravelo, A.C., 2015a. Enhanced subarctic Pacific stratification and nutrient utilization during glacials over the last 1.2 Myr. Geophysical Research Letters, 42(22): 9870-9879.

Knudson, K.P. and Ravelo, A.C., 2015b. North Pacific Intermediate Water circulation enhanced by the closure of the Bering Strait. Paleoceanography, 30(10): 1287-1304.

Kohfeld, K.E. and Chase, Z., 2011. Controls on deglacial changes in biogenic fluxes in the North Pacific Ocean. Quaternary Science Reviews, 30(23-24): 3350-3363.

Kotilainen, A. and Shackleton, N., 1995. Rapid climate variability in the North Pacific Ocean during the past 95,000 years. Nature, 377(6547): 323-326.

LaMontagne, R., Murray, R., Wei, K.Y., Leinen, M. and Wang, C.H., 1996. Decoupling of carbonate preservation, carbonate concentration, and biogenic accumulation: A 400-kyr record from the central equatorial Pacific Ocean. Paleoceanography, 11(5): 553-562.

Langemann, L., 2021. North Pacific Deep Water circulation during the last 160 ka - Implications for the marine carbon pool and atmospheric CO2 changes. Master Thesis, Universität Bremen.

Le, J. and Shackleton, N.J., 1992. Carbonate dissolution fluctuations in ther western Equatorial Pacific during the late Quaternary. Paleoceanpgrahpy, 7(1): 21-42.

Lembke-Jene, L., Tiedemann, R., Nürnberg, D., Kokfelt, U., Kozdon, R., Max, L., Röhl, U. and Gorbarenko, S.A., 2017. Deglacial variability in Okhotsk Sea Intermediate Water ventilation and biogeochemistry: Implications for North Pacific nutrient supply and productivity. Quaternary Science Reviews, 160: 116-137.

Lisiecki, L.E. and Raymo, M.E., 2005. A Pliocene-Pleistocene stack of 57 globally distributed benthic δ18O records. Paleoceanography, 20(1).

Lüthi, D., Le Floch, M., Bereiter, B., Blunier, T., Barnola, J.-M., Siegenthaler, U., Raynaud, D., Jouzel, J., Fischer, H. and Kawamura, K., 2008. High-resolution carbon dioxide concentration record 650,000–800,000 years before present. Nature, 453(7193): 379-382.

Marchitto, T.M., Lynch-Stieglitz, J. and Hemming, S.R., 2005. Deep Pacific CaCO3 compensation and glacial–interglacial atmospheric CO2. Earth and Planetary Science Letters, 231(3-4): 317-336.

Martínez-Garcia, A., Rosell-Melé, A., Jaccard, S.L., Geibert, W., Sigman, D.M. and Haug, G.H., 2011. Southern Ocean dust–climate coupling over the past four million years. Nature, 476(7360): 312-315.

Max, L., Lembke-Jene, L., Riethdorf, J.-R., Tiedemann, R., Nürnberg, D., Kühn, H. and Mackensen, A., 2014. Pulses of enhanced North Pacific Intermediate Water ventilation from the Okhotsk Sea and Bering Sea during the last deglaciation. Climate of the Past, 10(2): 591-605.

Max, L., Riethdorf, J.-R., Tiedemann, R., Smirnova, M., Lembke-Jene, L., Fahl, K., Nürnberg, D., Matul, A. and Mollenhauer, G., 2012. Sea surface temperature variability and sea-ice extent in the subarctic northwest Pacific during the past 15,000 years. Paleoceanography, 27(3).

McCarron, A., Bigg, G., Brooks, H., Leng, M., Marshall, J., Ponomareva, V., Portnyagin, M., Reimer, P. and Rogerson, M., 2021. Northwest Pacific ice-rafted debris at 38° N reveals episodic ice-sheet change in late Quaternary Northeast Siberia. Earth and Planetary Science Letters, 553: 116650.

Méheust, M., Stein, R., Fahl, K. and Gersonde, R., 2018. Sea-ice variability in the subarctic North Pacific and adjacent Bering Sea during the past 25 ka: new insights from IP 25 and U k′ 37 proxy records. arktos, 4(1): 8.

Méheust, M., Stein, R., Fahl, K., Max, L. and Riethdorf, J.-R., 2016. High-resolution IP25-based reconstruction of sea-ice variability in the western North Pacific and Bering Sea during the past 18,000 years. Geo-Marine Letters, 36(2): 101-111.

Monnin, E., Indermühle, A., Dällenbach, A., Flückiger, J., Stauffer, B., Stocker, T.F., Raynaud, D. and Barnola, J.-M., 2001. Atmospheric CO2 concentrations over the last glacial termination. Science, 291(5501): 112-114.

Narita, H., Sato, M., Tsunogai, S., Murayama, M., Ikehara, M., Nakatsuka, T., Wakatsuchi, M., Harada, N. and Ujiié, Y., 2002. Biogenic opal indicating less productive northwestern North Pacific during the glacial ages. Geophysical Research Letters, 29(15): 22-1-22-4.

Nishioka, J., Nakatsuka, T., Ono, K., Volkov, Y.N., Scherbinin, A. and Shiraiwa, T., 2014. Quantitative evaluation of iron transport processes in the Sea of Okhotsk. Progress in Oceanography, 126: 180-193.

Nishioka, J., Obata, H., Ogawa, H., Ono, K., Yamashita, Y., Lee, K., Takeda, S. and Yasuda, I., 2020. Subpolar marginal seas fuel the North Pacific through the intermediate water at the termination of the global ocean circulation. Proceedings of the National Academy of Sciences, 117(23): 12665-12673.

Nürnberg, D., 2018. RV SONNE Fahrtbericht / Cruise Report SO264 - SONNE-EMPEROR: The Plio/Pleistocene to Holocene development of the pelagic North Pacific from surface to depth – assessing its role for the global carbon budget and Earth´s climate, Suva (Fiji) – Yokohama (Japan), 30.6. – 24.8.2018, GEOMAR Helmholtz-Zentrum für Ozeanforschung, Kiel, Germany.

Nürnberg, D. and Tiedemann, R., 2004. Environmental change in the Sea of Okhotsk during the last 1.1 million years. Paleoceanography, 19(4).

Oba, T. and Murayama, M., 2004. Sea-surface temperature and salinity changes in the northwest Pacific since the Last Glacial Maximum. Journal of Quaternary Science, 19(4): 335-346.

Ohkushi, K.I., Hata, M. and Nemoto, N., 2018. Response of Deep-Sea Benthic Foraminifera to Paleoproductivity Changes on the Shatsky Rise in the Northwestern Pacific Ocean Over the Last 187 Kyr. Paleontological Research, 22(4): 326-351.

Ovsepyan, E.A., Ivanova, E.V., Lembke-Jene, L., Max, L., Tiedemann, R. and Nürnberg, D., 2017. Penultimate and last glacial oceanographic variations in the Bering Sea on millennial timescales: Links to North Atlantic climate. Quaternary Science Reviews, 163: 135-151.

Qin, B., Li, T., Xiong, Z., Algeo, T.J. and Chang, F., 2017. Deepwater carbonate ion concentrations in the western tropical Pacific since 250 ka: Evidence for oceanic carbon storage and global climate influence. Paleoceanography, 32(4): 351-370.

Rae, J.W.B., Gray, W.R., Wills, R.C.J., Eisenman, I., Fitzhugh, B., Fotheringham, M., Littley, E.F.M., Rafter, P.A., Rees-Owen, R., Ridgwell, A., Taylor, B. and Burke, A., 2020. Overturning circulation, nutrient limitation, and warming in the Glacial North Pacific. Science Advances, 6(50): eabd1654.

Reid, J.L. and Lonsdale, P.F., 1974. On the flow of water through the Samoan Passage. Journal of Physical Oceanography, 4(1): 58-73.

Ren, H., Studer, A.S., Serno, S., Sigman, D.M., Winckler, G., Anderson, R.F., Oleynik, S., Gersonde, R. and Haug, G.H., 2015. Glacial-to-interglacial changes in nitrate supply and consumption in the subarctic North Pacific from microfossil-bound N isotopes at two trophic levels. Paleoceanography, 30(9): 1217-1232.

Serno, S., Winckler, G., Anderson, R.F., Jaccard, S.L., Kienast, S.S. and Haug, G.H., 2017. Change in dust seasonality as the primary driver for orbital-scale dust storm variability in East Asia. Geophysical Research Letters, 44(8): 3796-3805.

Sexton, P.F. and Barker, S., 2012. Onset of ‘Pacific-style’deep-sea sedimentary carbonate cycles at the mid-Pleistocene transition. Earth and Planetary Science Letters, 321: 81-94.

Shcherbina, A.Y., Talley, L.D. and Rudnick, D.L., 2003. Direct observations of North Pacific ventilation: Brine rejection in the Okhotsk Sea. Science, 302(5652): 1952-1955.

Shigemitsu, M., Narita, H., Watanabe, Y.W., Harada, N. and Tsunogai, S., 2007. Ba, Si, U, Al, Sc, La, Th, C and 13C/12C in a sediment core in the western subarctic Pacific as proxies of past biological production. Marine Chemistry, 106(3-4): 442-455.

Siegenthaler, U., Stocker, T.F., Monnin, E., Lüthi, D., Schwander, J., Stauffer, B., Raynaud, D., Barnola, J.-M., Fischer, H. and Masson-Delmotte, V., 2005. Stable carbon cycle–climate relationship during the late Pleistocene. Science, 310(5752): 1313-1317.

Sigman, D.M., Jaccard, S.L. and Haug, G.H., 2004. Polar ocean stratification in a cold climate. Nature, 428(6978): 59-63.

Takahashi, T., Sutherland, S.C., Sweeney, C., Poisson, A., Metzl, N., Tilbrook, B., Bates, N., Wanninkhof, R., Feely, R.A. and Sabine, C., 2002. Global sea–air CO2 flux based on climatological surface ocean pCO2, and seasonal biological and temperature effects. Deep Sea Research Part II: Topical Studies in Oceanography, 49(9-10): 1601-1622.

Takahashi, T., Sutherland, S.C., Wanninkhof, R., Sweeney, C., Feely, R.A., Chipman, D.W., et al., 2009. Climatological mean and decadal change in surface ocean pCO2, and net sea–air CO2 flux over the global oceans. Deep Sea Research Part II: Topical Studies in Oceanography, 56(8-10): 554-577.

Talley, L.D., 1993. Distribution and formation of North Pacific intermediate water. Journal of Physical Oceanography, 23(3): 517-537.

Thompson, P.R. and Saito, T., 1974. Pacific Pleistocene sediments: Planktonic foraminifera dissolution cycles and geochronology. Geology, 2(7): 333-335.

Tjallingii, R., Röhl, U., Kölling, M. and Bickert, T., 2007. Influence of the water content on X-ray fluorescence core-scanning measurements in soft marine sediments. Geochemistry, Geophysics, Geosystems, 8(2).

Verardo, D.J. and McIntyre, A., 1994. Production and destruction: Control of biogenous sedimentation in the tropical Atlantic 0–300,000 years BP. Paleoceanography, 9(1): 63-86.

Volat, J.-L., Pastouret, L. and Vergnaud-Grazzini, C., 1980. Dissolution and carbonate fluctuations in Pleistocene deep-sea cores: a review. Marine Geology, 34(1-2): 1-28.

Wang, W., von Dobeneck, T., Frederichs, T., Zhang, Y., Lembke-Jene, L., Tiedemann, R., Winklhofer, M. and Nürnberg, D., 2021. Dating North Pacific Abyssal Sediments by Geomagnetic Paleointensity: Implications of Magnetization Carriers, Plio-Pleistocene Climate Change, and Benthic Redox Conditions. Frontiers in Earth Science: 577.

Warren, B.A., 1983. Why is no deep water formed in the North Pacific? Journal of Marine Research, 41(2): 327-347.

Weltje, G.J. and Tjallingii, R., 2008. Calibration of XRF core scanners for quantitative geochemical logging of sediment cores: Theory and application. Earth and Planetary Science Letters, 274(3-4): 423-438.

Winckler, G., Anderson, R.F., Jaccard, S.L. and Marcantonio, F., 2016. Ocean dynamics, not dust, have controlled equatorial Pacific productivity over the past 500,000 years. Proceedings of the National Academy of Sciences, 113(22): 6119-6124.

Wong, K.H., Obata, H., Nishioka, J., Yamashita, Y., Kondo, Y., Kim, T., Mashio, A. and Hasegawa, H., 2022. Subarctic Pacific Intermediate Water: An Oceanic Highway for the Transport of Trace Metals in the North Pacific. Limnology and Oceanography Bulletin, 31(2): 31-36.

Wu, G., Yasuda, M. and Berger, W., 1991. Late Pleistocene carbonate stratigraphy on Ontong-Java Plateau in the western equatorial Pacific. Marine Geology, 99(1-2): 135-150.

Yang, H., Lohmann, G., Krebs-Kanzow, U., Ionita, M., Shi, X., Sidorenko, D., Gong, X., Chen, X. and Gowan, E.J., 2020. Poleward shift of the major ocean gyres detected in a warming climate. Geophysical Research Letters, 47(5): e2019GL085868.

Yang, H., Lohmann, G., Wei, W., Dima, M., Ionita, M. and Liu, J., 2016. Intensification and poleward shift of subtropical western boundary currents in a warming climate. Journal of Geophysical Research: Oceans, 121(7): 4928-4945.

Yasudomi, Y., Motoyama, I., Oba, T. and Anma, R., 2014. Environmental fluctuations in the northwestern Pacific Ocean during the last interglacial period: evidence from radiolarian assemblages. Marine Micropaleontology, 108: 1-12.

Yuan, X. and Talley, L.D., 1992. Shallow salinity minima in the North Pacific. Journal of physical oceanography, 22(11): 1302-1316.

Zahn, R., Rushdi, A., Pisias, N.G., Bornhold, B.D., Blaise, B. and Karlin, R., 1991. Carbonate deposition and benthicδ13C in the subarctic Pacific: implications for changes of the oceanic carbonate system during the past 750,000 years. Earth and planetary science letters, 103(1-4): 116-132.

Zhang, J., Wang, P., Li, Q., Cheng, X., Jin, H. and Zhang, S., 2007. Western equatorial Pacific productivity and carbonate dissolution over the last 550 kyr: Foraminiferal and nannofossil evidence from ODP Hole 807A. Marine Micropaleontology, 64(3-4): 121-140.

4. Scientific Chapter III

Changes of upper ocean dynamics and productivity in the North West Pacific in a late Pliocene - late Pleistocene comparison

Abstract

Today, the North Pacific is a major sink for CO_2 controlled by the biological carbon pump, which is in close relation to the surface ocean stratification and circulation. It has been inferred that a change in this complex system contributed to the dramatic climate change at the onset of the northern hemisphere glaciation ~2.7 Ma years ago. Thus, a detailed investigation of this system is crucial to understand how the ongoing climate change could influence this region and affect the future global climate. However, sparse proxy records of sea surface temperature, salinity, and productivity especially over longer time scales (> Holocene) limit investigations. Here we aim to contribute to a more comprehensive understanding of the pelagic North Pacific and its role in climate change by investigating late Pliocene and late Pleistocene temperature, $\delta^{18}O_{sw\text{-}ivc}$ (approximating salinity), productivity and dust proxy data of two marine sediment cores from the Emperor Seamount Chain in the North West Pacific. To achieve this goal, we developed age models and reconstructed changes in (sub-) surface temperature and $\delta^{18}O_{sw\text{-}ivc}$ based on combined Mg/Ca and $\delta^{18}O$ analyses of the planktic foraminiferal species *Globigerina bulloides*, *Neogloboquadrina pachyderma* and *Neogloboquadrina incompta.* Additionally, we reconstructed past primary productivity and terrestrial dust input from XRF-derived Ba/Ti, Ca/Ti, Si/Ti, and XRF-derived Fe input, respectively. Our new records, which are located near the modern position of the Subarctic Front (SAF) indicate higher SSTs in the late Pliocene compared to the late Pleistocene. These were not caused by a significant northward displacement of the SAF but rather linked to a) general global warmer SSTs and b) less seasonality at the study sites due to the lack of permanent salinity-driven stratification in the North Pacific. Nevertheless, the SAF may have been located between our study sites during the late Pliocene or it was less pronounced, leading to a more gradual SST decrease with increasing latitude. With the onset of a permanent halocline at ~2.7 Ma, there was a decrease in SST and productivity. This dramatic decrease is linked to the onset of the salinity-driven stratification that hindered nutrients from reaching the surface layer. However, while there was no permanent halocline throughout the late Pliocene, there was a constant thermocline. At the same time, as productivity decreases, there is an abrupt increase in dust input via wind, associated with a general increase in dust availability in the source regions and an intensification of the westerlies. During the Pleistocene, the productivity was significantly lower while the dust input was significantly higher than during the Pliocene. The productivity increased between the

deglaciations and interglacials followed by decrease in late interglacials and early glacials. The dust input, shows an anticorrelated pattern to the productivity. This contrasting development of dust supply and productivity at our study sites indicates that dust fertilization neither caused the high primary productivity in the North Pacific during the late Pliocene nor limited the primary productivity during the late Pleistocene.

4.1. Introduction

The Pliocene (2.58 to 5.33 Ma) is the most recent epoch with atmospheric CO_2 concentrations comparable to modern post-industrial values. During the mid-Pliocene warm period (mPWP) the mean CO_2 concentration was ~367 parts per million (ppm) by volume, significantly higher than during the late-Pleistocene, where the mean CO_2 concentration is ~241 ppm (Bereiter et al., 2014; Chalk et al., 2017; de la Vega et al., 2020). These high atmospheric CO_2 concentrations in the Pliocene were accompanied by a global mean temperature ~2-3°C higher than the pre-industrial temperature (Dutton et al., 2015). The Pliocene is further associated with a sea level that was ~20 m higher than present, which is linked to smaller Greenland and Antarctic ice sheets and a water expansion due to higher temperatures (Dutton et al., 2015; Dumitru et al., 2019). The tectonic boundary conditions in the Pliocene are similar to modern ones. Thus comparing the Pliocene epoch and the late Pleistocene climate can help to understand how the climate change towards warmer global mean temperatures could change our world in the future.

The North Pacific functions as a CO_2 sink on a mean annual basis (Ayers and Lozier, 2012) by acting as a strong sink in winter and a weak source in summer (Ogawa et al., 2006; Takahashi et al., 2009). The strength and efficiency of the biological carbon pump that controls the uptake of CO_2 are linked to plankton composition and productivity, which change under changing ocean conditions. Under modern conditions, nutrient- and CO_2-rich waters reach the surface due to Ekman divergence (Gargett, 1991; Talley, 1995), which fuels phytoplankton growth and releases previously sequestered CO_2 into the atmosphere. However, during phytoplankton growth, nutrients are consumed and CO_2 is absorbed from the water masses and the resulting export of organic matter subsequently lowers the $p\text{CO}_2$ of surface waters, causing the surface layer to reabsorb a portion of the CO_2 that was initially released from the upwelled water (Jaccard et al., 2010). Under modern conditions and throughout the Pleistocene, the upwelling of nutrient-rich waters to the surface has, however, been dampened by the pronounced stratification in the North Pacific north of the Subarctic Front (SAF) (Warren, 1983; Gargett, 1991; Haug et al., 1999) (figure 4.1).

However, it has been suggested that the permanent salinity-driven stratification did not exist in the subarctic Pacific in the Pliocene but developed abruptly 2.73 Ma ago in relation to the iNHG (Haug et al., 1999; Sigman et al., 2004). Therefore, higher primary productivity in the Pliocene compared to the Pleistocene, as observed by Haug et al. (1999) was likely linked to the higher nutrient availability from deeper waters because of easier exchange in times without a strong halocline (Haug et al., 1999; Studer et al., 2012). However, which specific atmospheric or oceanic changes caused the sudden development of the permanent halocline and to what extent it contributed to the iNHG is still unknown (Haug et al., 1999). Similar to these North Pacific sites, the Southern Ocean (Sigman et al., 2004) and parts of the North Atlantic (Lawrence et al., 2009) show higher marine productivity before the intensification of the Northern Hemisphere glaciation. In other regions, however, productivity was not higher during the Pliocene than during the Pleistocene. For example, higher opal accumulation rates were observed after 2.7 Ma in the Bering sea (März et al., 2013; Iwasaki et al., 2016). Similarly, in the equatorial Pacific (Lawrence et al., 2006, 2013; Liu et al., 2008) and the South Atlantic (Cortese et al., 2004; Martínez-Garcia et al., 2010) the marine productivity was lower before the iNHG which is indicated by opal and alkenone proxy data.

During the Pleistocene, primary productivity in the North Pacific is lower during glacials in comparison to interglacials and deglaciations (Narita et al., 2002; Gorbarenko et al., 2004; Kienast et al., 2004; Jaccard et al., 2005; Brunelle et al., 2007; Shigemitsu et al., 2007; Galbraith et al., 2008; Gebhardt et al., 2008; Jaccard et al., 2010; Riethdorf et al., 2013). However, the mechanisms causing the observed productivity pattern, such as sea-ice formation, light limitation or changes in temperature, wind strength, nutrient supply as well as stratification, are still a matter of debate (Kawahata et al., 2000; Matsumoto et al., 2002; Brunelle et al., 2007; Shigemitsu et al., 2007; Jaccard et al., 2010; Nishioka et al., 2011; Costa et al., 2018; Sigman et al., 2021; scientific chapter I, II). Nevertheless, an increase in the efficiency of the biological pump during glacials may have contributed to reduced atmospheric CO_2 concentrations (Jaccard et al., 2010).

The surface ocean circulation in the Pacific is closely linked to atmospheric circulation, especially the mid-latitude westerly winds (Toggweiler et al., 2006). It has been suggested that the position and intensity of the Northern Hemisphere Westerlies change with glacial-interglacial cycles (Gray et al., 2020). However, modeling studies and studies based on (marine) proxy data that reconstruct the strength and position of the westerlies in the Pliocene are sparse (Lawrence et al., 2013; Abell et al., 2021). Nevertheless, a recent study from Abell et al. (2021) suggests that the westerlies were weaker and located more poleward during the Pliocene than in the Pleistocene. Moreover, they observe a significant increase in dust flux around 2.73 Ma and link it to the iNHG.

In this study, we aim to draw a more overarching picture of the Pliocene vs. Pleistocene history of the upper ocean dynamics in the poorly studied pelagic North Pacific. We combine proxy records of past surface and subsurface ocean temperature as well as $\delta^{18}O_{sw\text{-}ivc}$ (approximating salinity), carbonate and diatom productivity, as well as terrigenous input via wind. Our results will hence expand the knowledge of the Pliocene and Pleistocene oceanographic variability and the complex interaction between upper ocean stratification, productivity and the influence of the westerlies.

4.1.1. Regional setting

Two large-scale wind-driven gyre systems dominate the North Pacific. In the north, there is the cyclonic Subarctic Gyre and in the south the anticyclonic Subtropical Gyre (Huang, 2015;

figure 4.1). Between these gyres, there is a transition zone in which waters originating from the tropical western boundary current, the Kuroshio Current and the subarctic western boundary current, the Oyashio Current meet. The Kuroshio Current transports heat from the West Pacific Warm Pool (WPWP) to the northern regions and originates from the warm, saline North Equatorial Current (NEC) (figure 4.1). At ~35°N the Kuroshio Current separates from the Japanese coast and continues as Kuroshio Extension (Qiu, 2002). The Oyashio Current originates from the East Kamchatka Current and is further fed by cold, low saline, nutrient-rich water from the Sea of Okhotsk. The Oyashio Current splits at ~42°N, and one path continues as the northeastward-flowing Subarctic Current (SAC) (Qiu, 2019). The mixing zone between these currents is named the Kuroshio-Oyashio transition zone or mixed water region and is characterized by a pronounced latitudinal sea surface temperature, salinity, and nutrient gradient (Science, 2003; Garcia et al., 2018; Locarnini et al., 2018; Zweng et al., 2019) (figure 4.1). These gradients are marked by a set of fronts: the Subarctic Front (SAF) which marks the northern end of the transitional zone (Favorite, 1976); the Subarctic Boundary (SAB), a near-surface salinity front south of the SAF (Science, 2003) and the Kuroshio Bifurcation Front (KBF). Along the northern boundary of the Kuroshio-Oyashio transition zone, numerous meanders and mesoscale eddies occur (figure 4.1) due to the dia- and isopycnal mixing between Kuroshio and Oyashio water with vertically different temperature, salinity and velocity structures (Yasuda et al., 1996, 2002; Shimizu et al., 2001; Isoguchi et al., 2006; Mitnik et al., 2020). Because of mixing the distinction between the Kuroshio Extension and the Subarctic Current is no longer clear east of ~180°W/E, and together they form the broad eastward-moving North Pacific Current (Qiu, 2019).

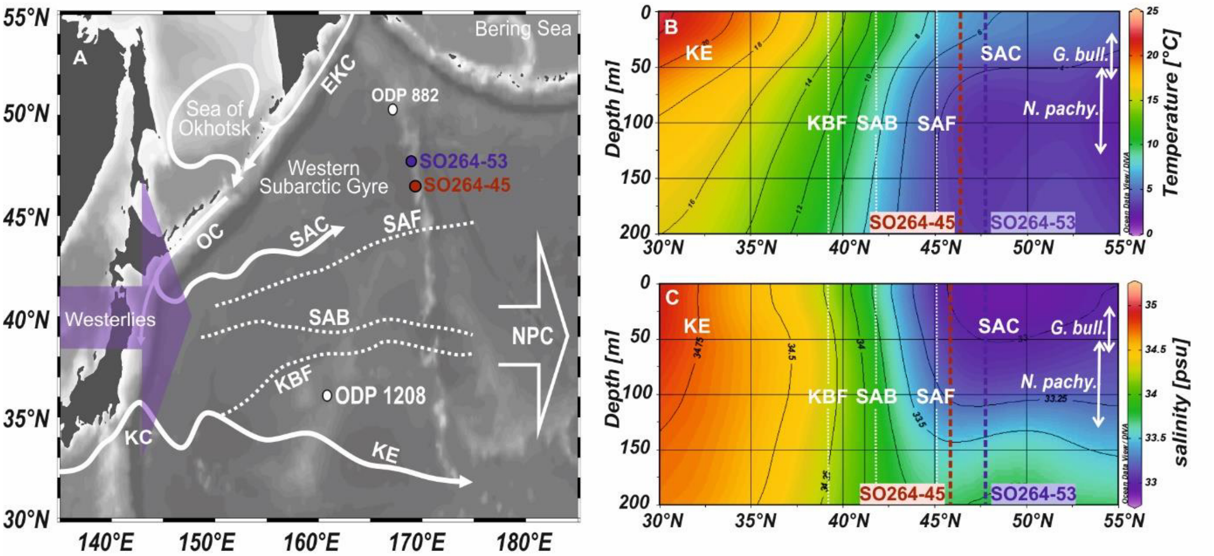

Figure 4.1: North West Pacific sea surface and subsurface hydrology. **A**: Bathymetric map illustrated with Ocean Data View (Schlitzer, 2019) with the surface current structure in the Kuroshio-Oyashio transition area: EKC = East Kamchatka Current, KC = Kuroshio Current, KE= Kuroshio Extension, NPC = North Pacific Current, OC = Oyashio Current, SAC = Subarctic Current; KBF = Kuroshio Bifurcation Front, SAB = Subarctic Boundary, SAF = Subarctic Front. The position of the currents and boundaries are based on Yasuda et al. (2003). The locations of the study sites SO264-45 (red dot) and -53 (blue dot) as well as reference cores ODP Site 882 (Jaccard et al., 2010) and ODP 1208 (Lariviere et al., 2012) (white dots). The modern position of the westerlies is indicated as purple arrow. **B&C**: North-south-oriented temperature and salinity transects along 170°E illustrated with Ocean Data View (Schlitzer and Ocean Data View, 2019) based on data from the World Ocean Atlas 2018 (Locarnini et al., 2018; Zweng et al., 2019). The positions of fronts are marked by white dotted lines; the core position by a red dotted line and the depth habitats of *G. bulloides* and *N. pachyderma* by white arrows.

4.2. Material and methods

The sediment cores presented in this study were recovered via gravity coring as part of a transect set of cores along the Emperor-Seamount Chain during R/V SONNE cruise SO264 (SONNE-EMPEROR) in August 2018. Core SO264-45 was retrieved from Jimmu Seamount at 46°33,792 'N, 169°36,072 'E and a water depth of 2425 m, while SO264-53 was retrieved from Minnetonka Seamount at 47°38,930 'N, 169°20,417 'E from a water depth of 2325 m. The data of the upper 3.74 m of core SO264-45-2 have already been presented in scientific chapter I. Both cores mainly consist of foraminifera-bearing sandy silt to foraminifera-bearing calcareous ooze, in some parts containing IRD and intercalated by several tephra layers (figure 4.2) (Nürnberg, 2018). At ~ 2.74 Ma, which translates to core depths of 6.43 m (SO264-45) and 6.61 m (SO264-53), both cores show a notable change from a relatively homogenous whitish color associated with the siliciclastic-carbonaceous facies to layers of different brown and green colors of a more siliciclastic-siliceous facies (supplementary figure 4.14) (Nürnberg, 2018). We present two periods with reliable chronostratigraphy, the late Pliocene and the late Pleistocene (further discussed in section 4.2.4). The records of the late Pliocene span from 3.3 Ma, the maximum age of core SO264-45, to 2.68 Ma. After 2.68 Ma, there are no more age control points and several hiatus. The records of the late Pleistocene span from 350 ka BP to 50 ka BP, which covers three glacial-interglacial cycles without hiatus.

4.2.1. XRF scanning

The relative sedimentary elemental composition of the cores was determined by scanning the archive half of each core segment with an Avaatech X-ray Fluorescence (XRF) core scanner at the Alfred-Wegener-Institute (AWI) in Bremerhaven, Germany. In order to have a fresh and undisturbed surface, the uppermost sediment layer was removed. Then the segments were covered with SPEXCerti Prep Ultalene foil. Each core segment was triple scanned with a down-core resolution of one centimeter at a current of 0.15, 0.175 and 1 mA, tube voltages of 10, 30, and 50 kV, and acquisition times of 10, 15, and 20 sec respectively, covering elements from aluminum to barium. Element intensities were determined with the proprietary Aavatech WinAxil (Batch) software and are reported as counts per second (cps). We follow the suggestion to present the natural logarithms of XRF element counts and ratios to account for the problem, that raw intensities or peak integrals cannot be interpreted in terms of sediment composition (Weltje and Tjallingii, 2008).

It is assumed that the aluminum (Al) and titanium (Ti) content of terrigenous material remained constant in space and time and can therefore be used to normalize XRF-derived barium (Ba) and calcium (Ca) counts against terrigenous input (Galbraith et al., 2007). During XRF scanning, the detection of light elements like Al shows a higher risk of being influenced by water trapped between the sediment and the scanning foil than heavier elements (Tjallingii et al., 2007). Therefore, we use Ti for normalizing Ba and Ca records and the rations as proxies for changes in paleoproductivity. Ba/Ti is well-established as a proxy in the North Pacific (Nürnberg and Tiedemann, 2004; Jaccard et al., 2010; Korff et al., 2016), reflecting the organic carbon export from the surface (Eagle et al., 2003; Jaccard et al., 2010). It may be influenced by dissolution in suboxic or under sulfate-depleted conditions. However, Jaccard et al. (2010) argue that sulfate repletion is mainly restricted to highly productive coastal areas and the equatorial Pacific upwelling system and that ~30% of precipitated Ba is still preserved in sediments under oxic/suboxic conditions in the North Pacific. As discussed in scientific chapter II the XRF-based Ca counts and the $CaCO_3$ calculated as the difference between total carbon (TC) and total organic carbon (TOC) show high correlation coefficients ($r^2 > 0.82$) at sites SO264-55 and -66 which are located close to our study sites. Therefore, the Ca/Ti faithfully reflects the $CaCO_3$ content variations in the study area. Yet dissolution can affect the carbon content of the sediment, therefore, this proxy only represents Ca-productivity in areas above the significantly undersaturated water. Otherwise, it rather reflects the carbonate saturation state of the bottom water (Jaccard et al., 2010; Gottschalk et al., 2018).

Terrigenous sediment delivery is also reflected in the Iron (Fe) record. As in the open North Pacific, there are no other sources for terrigenous material, XRF-based Fe can be used as a proxy for aeolian dust flux (Jahn et al., 2003, 2005; Nürnberg and Tiedemann, 2004; Mohtadi et al., 2007; Helmke et al., 2008; Kaiser et al., 2008). Fe and Ti correlate well in our records during the studied time intervals (R^2 core 45: 0.97; R^2 core 53: 0.96) (supplementary figure 4.16) therefore indicating that a potential diagenetic imprint on Fe is negligible (Croudace and Rothwell, 2015).

4.2.2. Foraminiferal geochemistry

In this study, we use Mg/Ca ratios of the planktic foraminiferal species *Globigerina bulloides*, *Neogloboquadrina pachyderma* and *Neogloboquadrina incompta* to reconstruct paleo upper ocean temperatures. In the North West Pacific, *G. bulloides* is a near-surface dweller and is mainly found above the thermocline (Iwasaki et al., 2017; Schiebel et al., 2017; Taylor et al., 2018), which lies at ~40-50 m at the study site (Locarnini et al., 2018) (supplementary figure 4.15). In the study region, *G. bulloides* likely calcifies throughout the year (Kuroyanagi et al., 2008; Sagawa et al., 2013; Taylor et al., 2018). In contrast, *N. pachyderma* are mainly found at thermocline depth (Sarnthein et al., 2004; Riethdorf et al., 2013; Taylor et al., 2018). Thus, we assume a depth habitat of 50-130 m (Locarnini et al., 2018), which might change with thermocline depth. *N. pachyderma* principally occurs in the subpolar regions as it prefers water temperatures below 7°C (Reynolds and Thunell, 1986). If the annual temperature is lower than 7°C, *N. pachyderma* occurs throughout the year. If the temperature exceeds its preferred habitat temperature of 7°C, *N. pachyderma* may change its seasonality and avoid the warmer seasons, which is likely to happen at our study site as shown by sediment trap studies (Kuroyanagi et al., 2008; Sagawa et al., 2013; Taylor et al., 2018). In contrast, *N. incompta* prefers warmer temperatures than *N. pachyderma* and is considered to inhabit a similar water depth in the North Pacific (Taylor et al., 2018). Similar to *G. bulloides* and *N. pachyderma* also *N. incompta* can occur annually in the North Pacific, while in the warmer regions, it is restricted to the winter months (Malevich et al., 2019). For a detailed discussion about seasonality and habitat depth, see chapters 2.7.1 and 4.2.1.

All cores were sampled equidistantly at 2 cm intervals. The samples were then freeze-dried, wet-sieved, and fractionated. From these samples, we picked the planktic species *G. bulloides*, *N. pachyderma* and *N. incompta*, as well as the benthic species *Cibicides wuellerstorfi, Melonis barleeanum* and *Uvigerina* spp. When possible, about 50 visually well-preserved specimens of *G. bulloides,* ~120 of *N. pachyderma* and ~120 of *N. incompta* were selected. Due to insufficient sample material in most samples, only the use of specimens from a relatively wide size range (*G. bulloides*: 250 – 400 µm; *N. pachyderma:* 125-315 µm) allowed to get enough sample material for analysis. Thus, size effects on Mg/Ca ratios can be excluded in this study. Notably, in the Pliocene sediments, *N. incompta* was considerably more abundant than *N. pachyderma*, which was in parts even absent. Therefore, we picked *N. incompta* in the late Pliocene records. In the late Pleistocene records, however, *N. pachyderma* was considerably more abundant and was therefore picked. Tests were cracked open between glass plates, and chamber fillings (e.g. pyrite) were removed. The fragmented and homogenized samples were divided into one-third for stable isotope analyses and two-thirds for trace element measurements. In addition, 3-5 tests of the benthic foraminiferal species *Uvigerina* spp. and *Cibicides wuellerstorfi* were selected from the size fraction 315-400 µm for stable isotope measurements.

For trace element analyses, foraminiferal fragments were prepared by oxidative and reductive (with hydrazine) cleaning after the protocols of Boyle and Keigwin (1985) as well as Boyle and Rosenthal (1996). We regularly measured standards and blanks alongside the samples to ensure analytical quality control. Samples were measured at GEOMAR - Helmholtz Centre for Ocean Research Kiel on a Varian 720 ES axial ICP-OES coupled with a VARIAN SPS3 sample preparation system. The internal consistency standard BCS-DRM 393 (ECRM 752-1 was used for drift correction and standardization. It has an Mg/Ca reference value of 3.761mmol/mol (Greaves et al., 2008), while the ECRM standard for Mg/Ca has a long-term external reproducibility of ± 0.1 mmol/mol (2σ). If necessary, the measurements were repeated to verify questionable Mg/Ca values. We show that an influence of contamination and incomplete removal of siliciclastic material during the cleaning procedure on our Mg/Ca ratios is unlikely. For this, we measured Al/Ca, Mn/Ca and Fe/Ca ratios alongside the Mg/Ca and checked for a correlation between high Mg/Ca values and high Al/Ca, Mn/Ca and Fe/Ca (supplementary chapter 4.6.3. including figures 4.10-4.14).

Stable isotopes of planktic and benthic samples were measured on a Thermo Fischer Scientific MAT 253 mass spectrometer equipped with an automated Kiel IV carbonate preparation device. The values were calibrated to NBS-19 (National Bureau of Standards) and reported relative to the Vienna Pee Dee Belemnite (VPDB) standard. The long-term external reproducibility (n = <3,000) was monitored by the in-house Bremen standard (Solnhofen Limestone) with an analytic precision of 0.06 ‰ for $\delta^{18}O$ and 0.03 ‰ for $\delta^{13}C$.

In order to check for outliers in the Mg/Ca and $\delta^{18}O$ records of the planktic and benthic foraminifera, we applied the 1.5 interquartile method after Tukey (1977) and checked values that strongly deviate from neighboring values individually. This way, we eliminated one value from the stable isotope (at 1.54 m) record from *N. pachyderma*, one from the Mg/Ca (at 6.88 m) record from *N. pachyderma* of core 53, and one from both the Mg/Ca as well as stable isotope records (at 6.72 m) from *N. incompta*.

4.2.3. Upper ocean temperature and ice volume corrected $\delta^{18}O$ seawater assessment based on foraminiferal Mg/Ca and $\delta^{18}O$

We used established species-specific equations for converting Mg/Ca ratios in foraminiferal calcite into water temperature: for *G. bulloides* the equation from Elderfield & Ganssen (2000) ($Mg/Ca=0.56e^{(0.10*T)}$), for *N.* pachyderma the equation from Kozdon et al. (2009) ($Mg/Ca=0.13*T+0.35$), and for *N. incompta* the equation from Morley et al. (2017) ($Mg/Ca=0.71e^{(0.08*T)}$) (supplementary chapter 4.6.2). We refer to the temperature derived from *G. bulloides* as sea surface temperature $SST_{G.bulloides}$ (~ 20-60 m water depth), and temperatures derived from *N. pachyderma* and *N. incompta* as subsurface temperatures: $subSST_{N.pachyderma}$ and $subSST_{N.incompta}$ (~ 50-130 m water depth). Notably, late Holocene temperatures obtained from *G. bulloides* and *N. pachyderma* align with the modern annual mean temperatures at the defined depth habitats (Locarnini et al., 2018; supplementary figure 4.14).

Several factors may impact foraminiferal Mg/Ca ratios and the resulting temperature reconstructions, including alterations in seawater pH, salinity, calcite dissolution, and diagenetic processes. A comprehensive discussion of these effects can be found in chapters 2.7.2, 2.7.4, and 4.6.2. We conclude that these effects either have a negligible influence on our interpretation or fall within the assigned error range.

The combined measurements of $\delta^{18}O$ and Mg/Ca of foraminiferal calcite, allow us to determine the $\delta^{18}O$ of seawater ($\delta^{18}O_{sw}$) by removing the temperature-related component from the initial foraminiferal $\delta^{18}O$ signal. For *G. bulloides*, we employ the equation from Shackleton (1974) ($T=16.9-4.38*(\delta^{18}O_{calcite}-\delta^{18}O_{sw})+0.1*(\delta^{18}O_{calcite}-\delta^{18}O_{sw})^2$), while for *N. pachyderma*, we use the species-specific equation from Mulitza et al. (2003) ($T=3.55*(\delta^{18}O_{calcite}-\delta^{18}O_{sw})+12.69$). As no species-specific equation exists for *N. incompta*, we compared $\delta^{18}O_{sw}$ derived from *N. incompta* data via both equations mentioned above (supplementary figure 4.9). Based on these results, we decide to use the equation from Mulitza et al. (2003) for *N. incompta*. Additionally, we corrected the $\delta^{18}O_{sw}$ for global ice volume changes by using a dataset from De Boer et al. (2014), which is based on the global LR04 stack (Lisiecki and Raymo, 2005), and simulations of continental ice sheets (De Boer et al., 2014). This data is represented as $\delta^{18}O_{sw\text{-}ivc}$ (ivc = ice-volume corrected) and is reported in ‰ versus SMOW, with higher values interpreted as relatively high salinity conditions and lower values as relatively fresh conditions.

4.2.4. Chronostratigraphy

Here we present two intervals of the cores SO264-45 and -53 (figure 4.2), discussed in more detail below. The age models of the cores belong to a set of stratigraphy that further includes the cores SO264-55 and -28. These age models are based on tephra-, bio- and magnetostratigraphy, AMS^{14}C dating, correlation to other cores of the region and the visual correlation of benthic $\delta^{18}O$ isotope records to the global benthic isotope stack LR04 (Lisiecki and Raymo, 2005).

To derive a continuous $\delta^{18}O$ record with a good signal-to-noise ratio over the entire core intervals, we calculated $\delta^{18}O$-stacks of the benthic species *C. wuellerstorfi, M. barleeanum* and *Uvigernia spp.* for both cores (supplementary figure 4.17). With this approach, we follow the conventional assumption that *Uvigerina spp.* calcify in equilibrium with surrounding seawater

$\delta^{18}O$ (Shackleton, 1974; Shackleton and Hall, 1984; Labeyrie et al., 1999; Fontanier et al., 2006). *M. barleeanum* deviates by ~0.4 ‰ (Labeyrie et al., 1999; Shackleton et al., 2000) from *Uvigerina* values and *C. wuellerstorfi* by ~0.64 ‰ (Shackleton and Opdyke, 1973; Labeyrie et al., 1999; Waddell et al., 2009). Hence, we corrected $\delta^{18}O_{M.barleeanum}$ by adding 0.4 ‰ and $\delta^{18}O_{C. wuellerstorfi}$ by adding 0.64 ‰. These stacked benthic $\delta^{18}O$ isotope records were visually correlated to the global benthic isotope stack LR04 (Lisiecki and Raymo, 2005) using QAnalySeries v1.5.0 (Kotov et al., 2018). The Pleistocene part of the age model of core SO264-45 is presented in scientific chapter I. The Pliocene part presented in this study is fixed by 5 tie lines and linear interpolation between tie lines. At ~7.42 m, a tephra layer (T3) was detected, which is geochemically correlated (EPMA (major elements) and LA-ICP-MS (major and trace elements) data obtained in GEOMAR and Kiel University) and thus of the same age as a tephra layer found at ODP site 884B and dated to ~3.039 Ma (Ponomareva et al., personal communication: 10/11.2022).

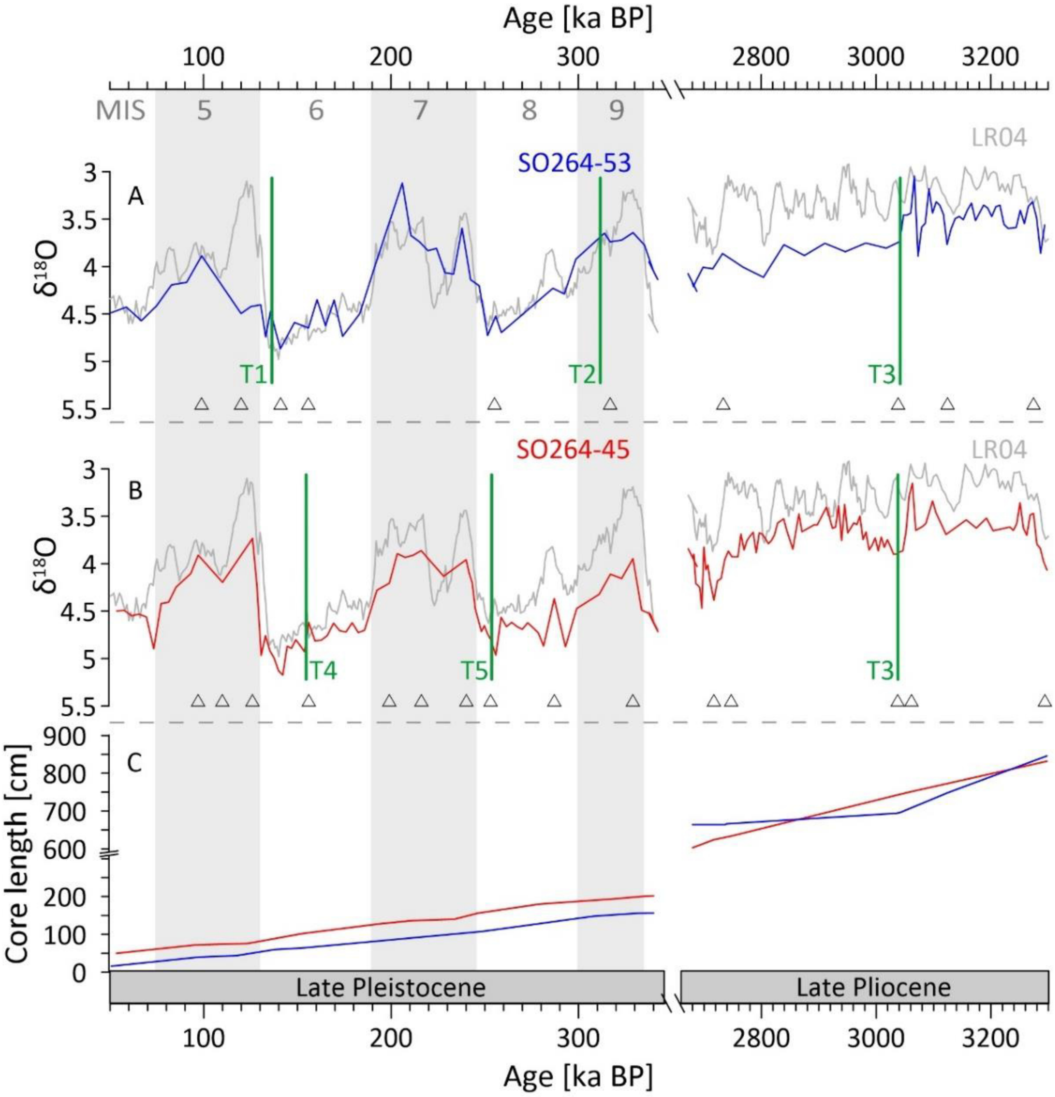

Figure 4.2: Chronostratigraphy of core SO264-45 and -53. Benthic $\delta^{18}O$ stack of core SO264-53 (**A**: blue line) and SO264-45 (**B**: red line) in comparison to the global benthic LR04 reference stack from Lisiecki and Raymo (2005). White triangles = tie lines used for tuning our $\delta^{18}O$-records to LR04. **C**: Sedimentation rates. Gray shadings and numbers mark Marine Isotope Stages (MIS 9-4). Tephra layers identified in the cores are indicated as green vertical lines.

Further, a lithological change from a relatively homogenous whitish color to layers of different brown and green colors at ~6.43 m occurs at ~2.74 Ma. This transition of colors fits well with core 882 in the subpolar North Pacific, where a similar change is observed at a similar age (Maslin et al., 1995). The Tephra layer and the lithological change have also been observed in SO264-53. Here the Tephra layer (T3) occurs at ~6.95 m and the lithological change at 6.61 m. Within this time interval, the $\delta^{18}O$ record of SO264-53 has been fixed by 4 tie lines to the reference record of Lisiecki & Raymo (2005). In between, the age is estimated by linear interpolation. Notably, the sedimentation rate before and after the tephra age control point at ~3.039 Ma varies from 0.6 cm/ka to 0.2 cm/ka. As the average sedimentation rate of both cores is ~0.5 cm/ka, a sedimentation rate of only 0.2 cm/ka is not very likely. This could either indicate a drastic change of sedimentation or, which is more likely, indicate there might have been a hiatus between the ~3.039 Ma and 2.73 Ma age control points. Hiatus have been observed in other parts of core SO264-53 and -45 as well as in several cores of the region (scientific chapters I & II; unpublished work on other cores of SO264). As our benthic $\delta^{18}O$ record does not have a resolution high enough to assess the exact timing of the hiatus, we refrain from appointing an exact age but present our data as a continuous record. However, this needs to be considered when interpreting the data and therefore, we do not discuss any specific event indicated in SO264-53 during this time interval.

The Pleistocene part of SO265-53 is based on 10 tie lines. This part contains two tephra layers (T4 and T5), one at ~0.56 m and one at ~1.43 m (Nürnberg, 2018), that correspond to ages of ~136 ka BP and 311 ka BP, respectively. The resulting sedimentation rates for our cores are relatively low with an average of 0.5 cm/ka for the late Pleistocene in SO264-53, 0.4 cm/ka for the Pliocene time interval of SO264-45 and 0.6 cm/ka for the Pleistocene time interval. Thus, one sample of 1 cm width reflects between ~1540 and ~2650 years. Due to the observed bioturbation of the sediment (Nürnberg, 2018), the absolute age range of foraminifera in one sample is likely to be higher. Because of the sampling resolution of 2 cm intervals for core 45 and 2-4 cm for core 53, there are at least ~3 ka for SO264-45 and up to 10.6 ka for SO264-53 between two data points, which should be taken into account for the uncertainty of the age models in this study. Moreover, several depth intervals contain too few foraminifera for reliable measurements.

4.3. Results

4.3.1. Upper ocean temperature and $\delta^{18}O_{sw\text{-}ivc}$ reconstructions from planktic foraminifera

4.3.1.1. Planktic $\delta^{18}O$

The planktic $\delta^{18}O$ records from cores SO264-45 and -53 range between 1 ‰ and 4 ‰ and correlate well with each other (figure 4.3). The $\delta^{18}O$ values of *G. bulloides* tend to be on average ~0.4 ‰ lighter, than the $\delta^{18}O$ values of *N. incompta* (late Pliocene) and *N. pachyderma* (late Pleistocene). All records show lighter values in the late Pliocene compared to the late Pleistocene. During the late Pleistocene, most records show lighter values in the interglacials than during the adjacent glacials. The only exception is the *G. bulloides* record of core SO264-53, which is lighter in MIS 8 than in MIS 7.

4.3.1.2. Mg/Ca derived temperature

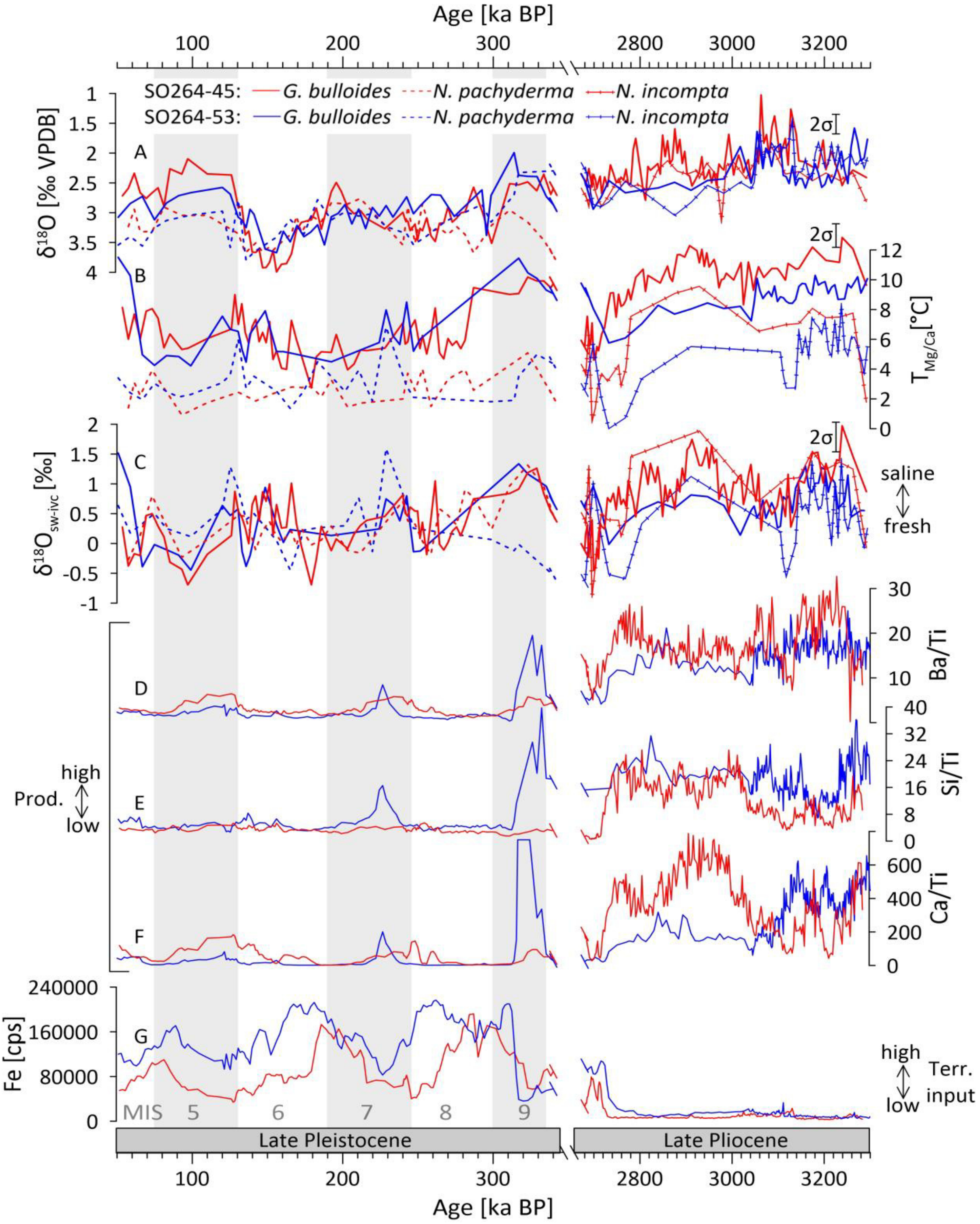

Figure 4.3: Proxy data of cores SO264-45 (red) and SO265-53 (blue). **A-C**: Results of foraminiferal analysis of *G. bulloides* (solid line), *N. pachyderma* (dotted line) and *N. incompta* (solid line with ticks). Error bars mark the 95% standard deviation (2σ). **A**: foraminiferal δ^{18}O; **B:** reconstructed upper ocean temperatures derived from Mg/Ca; **C:** relative changes in Ice-volume corrected δ^{18}O$_{\text{sw-ivc}}$. **D-G:** XRF derived proxy data for primary productivity (**D-E**) and terrigenous dust input via wind (**G**). Gray shadings and numbers mark Marine Isotope Stages (MIS 9-4).

In the late Pliocene (older than 2.7 Ma), the Mg/Ca derived temperature of *G. bulloides* ($SST_{Mg/Ca}$) from core SO264-45 fluctuates between 6.3°C and 12.8°C with an average of ~10.5°C (figure 4.3). The temperature derived from *G. bulloides* of core SO264-53 shows similar trends yet is on average 1.7°C colder. Between 2.74 Ma and 2.70 Ma, we observe a sudden temperature decrease of ~4.5°C (from 9.1°C at 2.74 Ma to 4.7°C at 2.70 Ma) in the record of SO264-45. A similar temperature decrease is also reflected in the *G. bulloides* record of core SO264-53 at ~ 2.77 Ma, followed by an increase up to average values of the late Pliocene record that is not observed in the SO264-45 record. Notably, part of the timing of this offset is induced by the lower sample resolution of core SO264-53.

In the late Pleistocene, the $SST_{Mg/Ca}$ of core SO264-45 is on average 4.1°C cooler than in the late Pliocene. It fluctuates between 2.7°C and 10.2°C with an average of 6.4°C. The record of core SO264-53 shows similar absolute values and amplitudes (temperature range: 4.2-11.5 °C; average temperature: 6.8°C). During the Pleistocene, the $SSTs_{Mg/Ca}$ records show more fluctuation with higher amplitudes than in the late Pliocene. These fluctuations, however, do not follow a distinct glacial-interglacial pattern. At 280 ka BP the $SST_{Mg/Ca}$ of core SO264-45 abruptly decreases by ~3.5°C (calculated as the temperature difference between three data points before and after the decrease). This decrease is also reflected in the record of core SO264-53, yet due to a lower sample resolution, the abruptness of the event cannot be displayed.
The temperature derived from *N. incompta* (late Pliocene) and *N. pachyderma* (late Pleistocene) of both cores is constantly lower than the accompanying *G. bulloides* SST records (figure 4.3). In the Pliocene, the records of *N. incompta* from both cores follow the same general pattern as the records from *G. bulloides,* including the decrease around 2.7/2.8 Ma (followed by an increase in the SO264-53 record back to average values before the drop), yet they are on average 4.4°C (SO264-45)/ 3.8°C (SO264-53) colder. The temperature derived from *N. incompta* is on average 3.4°C (SO264-45)/ 2°C (SO264-53) higher in the Pliocene than the temperature from *N. pachyderma* in the Pleistocene, which is similar to the observed SST difference between these time intervals in the *G. bulloides* records. In the late Pleistocene, the *N. pachyderma* temperature of both cores is on average 3.7°C lower than the *G. bulloides* SST records. Similar to *G. bulloides*, *N. pachyderma* also does not show glacial-interglacial behavior. The abrupt SST decrease at 280 ka BP is only reflected in the *N. pachyderma* record of SO264-45 yet less pronounced as in the *G. bulloides* record.

4.3.1.3. $\delta^{18}O_{sw-ivc}$

The *G. bulloides* $\delta^{18}O_{sw-ivc}$ record of core SO264-45 in the late Pliocene (older than 2.7 Ma) shows absolute values between -0.5 ‰ and 2.0 ‰ with an average of 0.9 ‰ (figure 4.3). The record of SO264-53 exhibits a similar trend but is on average 0.3 ‰ lower than the record of SO264-45. Similar to the temperature record, the $\delta^{18}O_{sw-ivc}$ record of core SO264-45 shows an abrupt decrease at ~2.7 Ma of about 1.1 ‰ (from 0.7 ‰ at 2.74 Ma to -0.4 ‰ at 2.70 Ma). A similar decrease is again also reflected in the SO264-53 record but appears ~ 30 ka earlier. The Pleistocene records of both cores are on average 0.6 ‰ (SO264-45) and 0.3 ‰ (SO264-53) lower than the Pliocene records. Like the temperature records, the $\delta^{18}O_{sw-ivc}$ fluctuations do not follow glacial-interglacial cycles. The abrupt decrease of the temperature records at 280 ka BP is also reflected in the *G. bulloides* $\delta^{18}O_{sw-ivc}$ records, yet less pronounced.

The *N. incompta* $\delta^{18}O_{sw\text{-}ivc}$ records of SO264-45 and SO264-53 show similar trends and absolute values as the *G. bulloides* $\delta^{18}O_{sw\text{-}ivc}$ records of the respective cores in the late Pliocene (figure 4.3). The decrease at ~2.7 Ma is even more pronounced in these records than in the *G. bulloides* records. The *N. incompta* $\delta^{18}O_{sw\text{-}ivc}$ records of the Pliocene are on average 0.4 ‰ (SO264-45) and 0.2 ‰ (SO264-53) higher than the $\delta^{18}O_{sw\text{-}ivc}$ records of *N. pachyderma* in the Pleistocene. The $\delta^{18}O_{sw\text{-}ivc}$ records of *N. pachyderma* of both cores follow the general pattern of the *G. bulloides* records in the Pleistocene.

4.3.2. Productivity and terrigenous input

The XRF-based Ba/Ti records reflect marine productivity. In the late Pliocene, Ba/Ti values of both cores are very high and generally follow a similar pattern (figure 4.3). At ~2.7 Ma, the Ba/Ti records of both cores exhibit a sudden decrease toward average values of the Pleistocene. In the late Pleistocene, even the Ba/Ti maximum values are mostly lower than the Pliocene minimum values prior to 2.7 Ma. The productivity during the late Pleistocene follows a glacial-interglacial pattern, where Ba/Ti values start to increase during the deglaciations and reach their maxima during the early interglacials. During the late interglacials and the subsequent early glacials, low Ba/Ti values predominate (figure 4.3).

A similar pattern is also observed in the Ca/Ti records, which reflect the productivity of carbonaceous microfossils like e.g. coccolithophores or foraminifera, and in the Si/Ti records, which reflect the productivity of siliceous microfossils like e.g. diatoms, radiolarian or silicoflagellates (figure 4.3). Both proxies at both core sites indicate up to 3.7 times higher values in the Pliocene than in the Pleistocene. Further, they show a decrease at ~2.7 Ma and a glacial-interglacial cyclicity in the Pleistocene. The Ca/Ti record of SO264-53 shows a significant decrease at ~3.04 Ma that is not reflected in the other proxies and is followed by values that stay considerably lower than in core SO264-45.

The XRF-based Fe records, which are used as a proxy for terrigenous input, show rather contrasting trends to the productivity records (figure 4.3). In the late Pliocene, the Fe records of both cores are very low yet suddenly increase by ~95% at ~2.7 Ma. In the late Pleistocene, however, the absolute values are significantly higher: even in phases of relatively low values within the late Pleistocene, Fe-values are still higher than before 2.7 Ma. The Fe records show significantly higher fluctuations in the Pleistocene than in the Pliocene. In both records, Fe values increase at the transitions from late interglacials to early glacials and decrease during the glacials. This pattern is rather anticorrelated to the Ba/Ti pattern. Notably, during the late Pleistocene, there is an offset in the Fe records of both cores. The record of SO264-53 indicates longer periods of high Fe values and decreases ~30 ka later than the record of SO264-45 in MIS 8 and 6.

4.4. Discussion

4.4.1. Temperature and $\delta^{18}O_{sw\text{-}ivc}$ development in the late Pliocene and late Pleistocene and their decrease in connection to the iNHG

Throughout the late Pliocene, the temperature records of both our study sites suggest a slowly decreasing temperature trend (figure 4.3). This trend represents well how the late Pliocene climate slowly migrated from a greenhouse world with a lack of large-scale Northern Hemisphere ice sheets towards the cooler Pleistocene with intense Northern Hemisphere Glaciation (e.g. Lisiecki and Raymo, 2005; Mudelsee and Raymo, 2005).

Our new records further show that there were significantly higher SST and subSST in the late Pliocene than in the late Pleistocene at both our studied sites, accompanied by more saline conditions in the Pliocene than in the Pleistocene (figure 4.4, 4.5).

This SSTs difference between the Pliocene and the Pleistocene could be attributed either to the cooler temperatures in the Pleistocene, in continuation of the cooling climate, or to a reorganization of the gyre circulation in the North Pacific, e.g. a significant northward shift of the SAF could cause more warm tropical water from the Kuroshio-Oyashio transition zone to reach our study sites. To test if the SST shift was rather a regional or a global phenomenon, we compare calculated average SSTs for both studied time intervals from our study sites to foraminiferal-based Mg/Ca and alkenone SSTs from tropic to subpolar regions, excluding Polar Regions (figure 4.5; Wara et al., 2005; Herbert et al., 2010; Lariviere et al., 2012).

While the correlation between latitude and average late Pliocene – late Pleistocene SSTs ($\Delta SST_{Plio\text{-}Plei}$) appears weak in our data set (figure 4.5; correlation coefficient R = 0.4) all sites show higher mean temperatures in the Pliocene than in the Pleistocene suggesting a global decrease in temperature. An exception to this general trend is ODP site 806 from the equatorial West Pacific, which shows similar temperatures in the late Pleistocene and the late Pliocene (figure 4.5).

The average late $\Delta SST_{Plio\text{-}Plei}$ is 2.4°C, which fits well with the $\Delta SST_{Plio\text{-}Plei}$ of core SO264-45 of 3.6°C and the $\Delta SST_{Plio\text{-}Plei}$ of SO264-53 of 2.1°C. Therefore, we assume that the observed higher temperatures in the late Pliocene are mainly linked to the generally warmer SSTs of this epoch rather than a reorganization of the gyre circulation. This is supported by our $\delta^{18}O_{sw\text{-}ivc}$ records, which indicate only slightly more saline conditions in the Pliocene than in the Pleistocene (figure 4.2). However, the water masses in the center of the Kuroshio-Oyashio transition zone are significantly more saline than the Oyashio-dominated water masses at our core sites (figure 4.1). Accordingly, a significant northward displacement of the SAF during the Pliocene should also be reflected by significantly more saline conditions at our core sites (figure 4.1) and is therefore unlikely.

Although we argue that the $\Delta SST_{Plio\text{-}Plei}$ was mainly induced by the generally warmer climate in the Pliocene and not by a significant northward displacement of the SAF, there might still have been a slight shift of this front. During the Pliocene, there is a temperature offset between our sites that is not observed during the late Pleistocene. SST and subSST at site SO264-45 were on average ~1.7°C and 1.1°C higher than at site SO264-53, which is located only 1° further north.

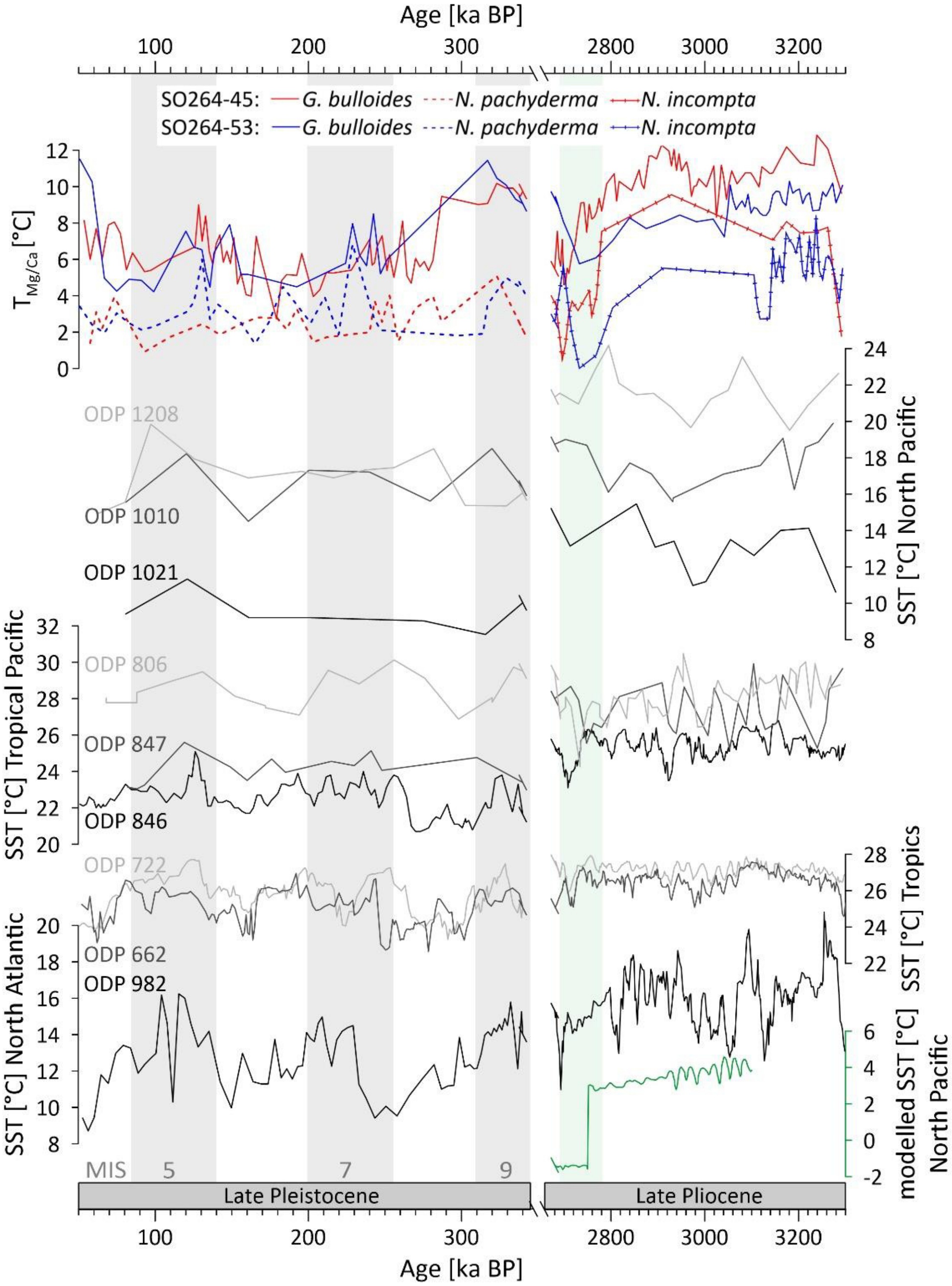

Figure 4.4: Foraminiferal sea surface (*G. bulloides = solid line)* and sub surface (*N. pachyderma* = dotted line*; N. incompta* = solid line with ticks) proxy data of cores SO264-45 (red) and SO265-53 (blue) in comparison to SST from other studies derived from alkenone paleothermometry (ODP sites 662, 722, 846, 982, 1010, 1021 and 1208) (Herbert et al., 2010; Lariviere et al., 2012) and foraminiferal Mg/Ca (ODP sites 806 and 847) (Wara et al., 2005) (black and gray solid lies). Site locations of these records are presented in table 4.1 and figure 4.5. The bottom green line indicates winter SST in the subarctic North West Pacific as simulated with the simple earth system model CLIMBER-2 (Haug et al., 2005). Gray shadings and numbers mark Marine Isotope Stages (MIS 9-4) while the green shading marks the time interval in which most records show an SST decrease associated with the intensification of the northern hemisphere glaciation.

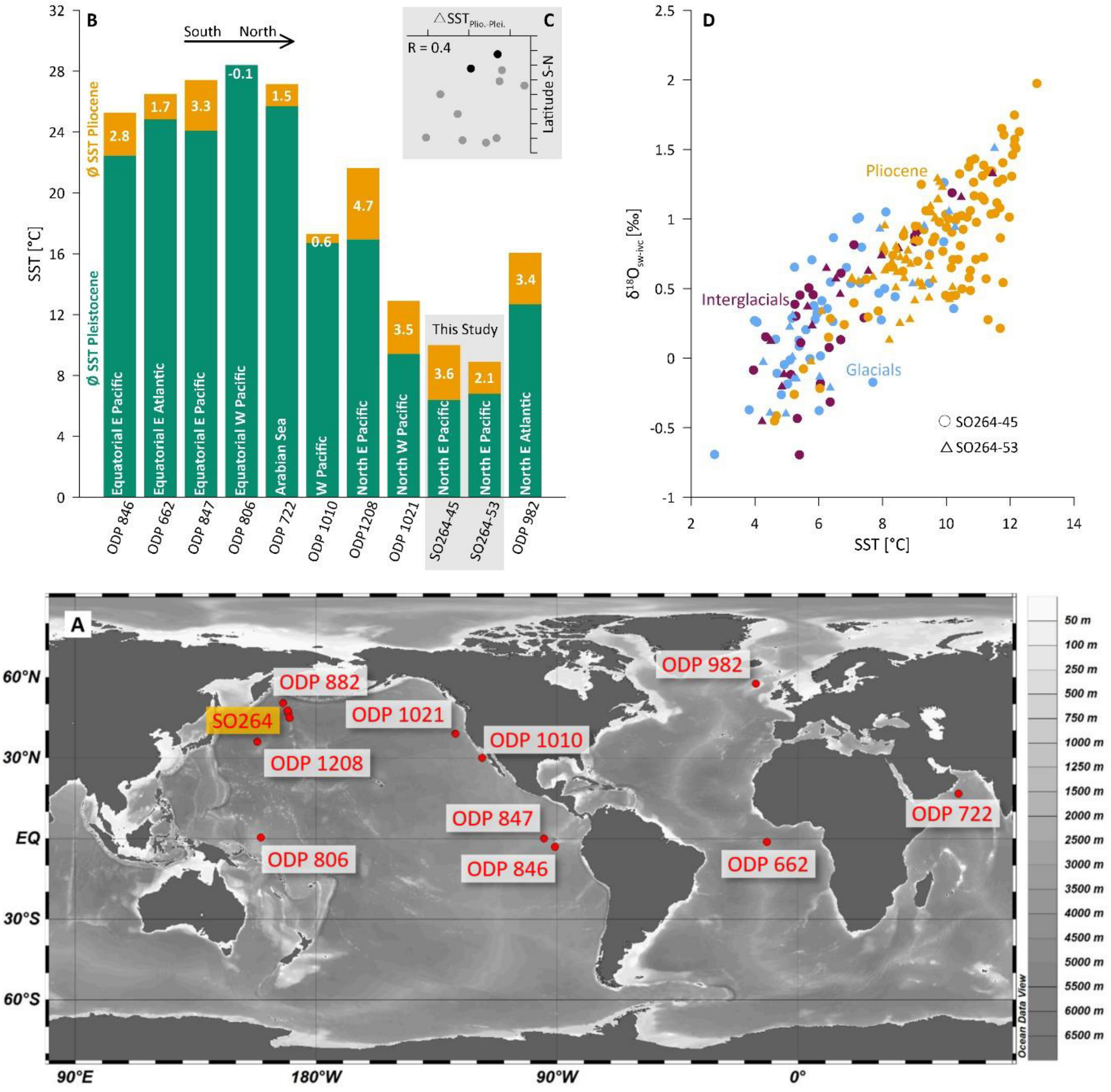

Figure 4.5: Comparison of late Pliocene and late Pleistocene SST records. **A**: Map showing the locations of cores used in the comparison. References and details of the cores can be found in table 1. **B**: Average SSTs of the late Pleistocene (350-50 ka) are indicated as green bars in comparison to average SSTs late Pliocene (3.3-2.68 Ma) indicated as yellow bars. The average SST difference between the time intervals is further presented as numbers in the yellow bars. The bars are sorted from south on the left to north on the right. Our cores are highlighted with a gray box. **C**: Correlation between $\Delta SST_{Plio.-Plei.}$ and latitude (correlation coefficient = 0.4) our cores are presented as black dots while reference cores are gray dots. **D**: $\delta^{18}O_{sw-ivc}$ and SST of the late Pliocene compared to glacial and interglacial values of the late Pleistocene. Data from core SO264-45 is presented as triangles, while data from core SO264-53 are presented as circles.

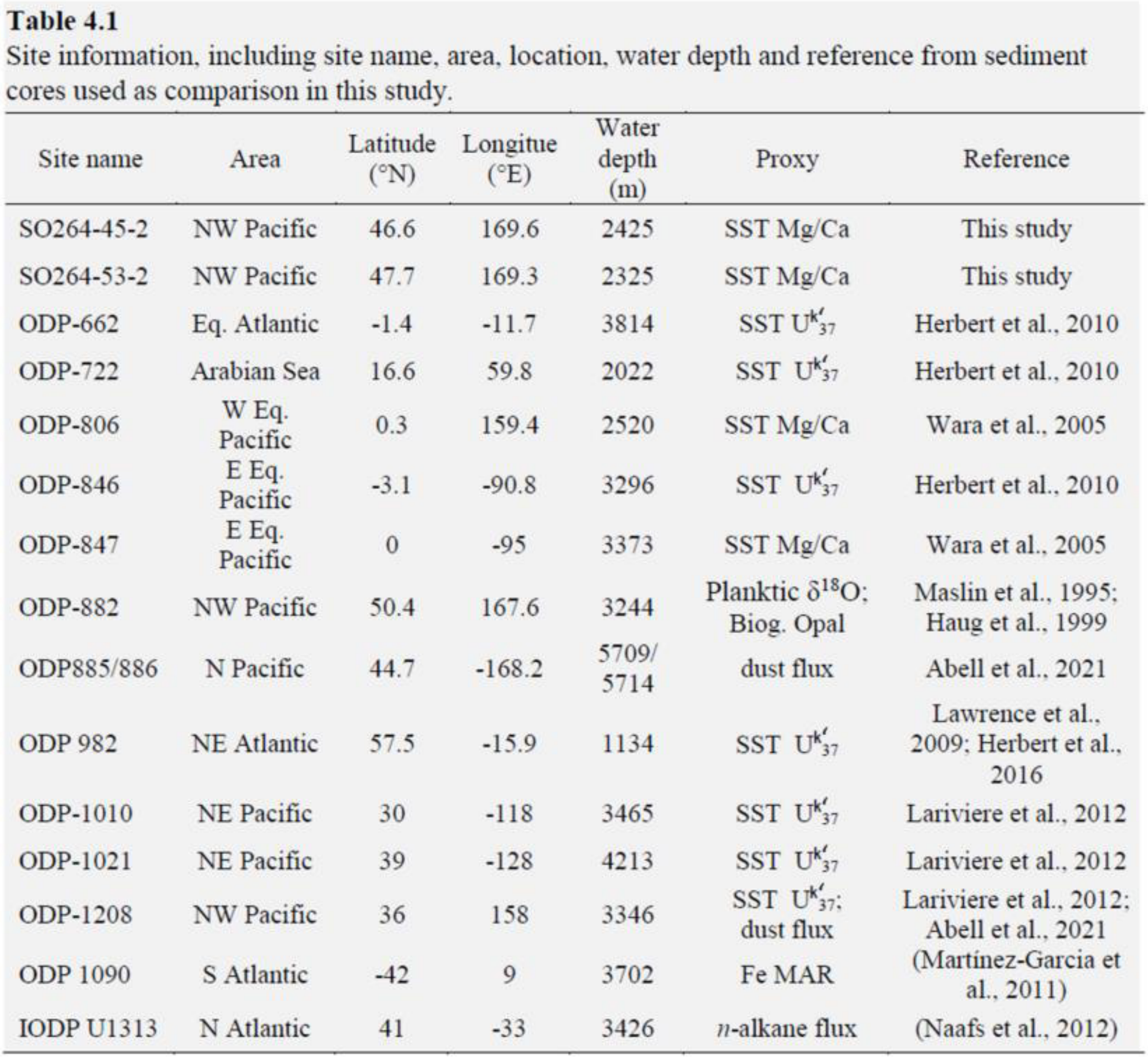

Table 4.1

Site information, including site name, area, location, water depth and reference from sediment cores used as comparison in this study.

Site name	Area	Latitude (°N)	Longitue (°E)	Water depth (m)	Proxy	Reference
SO264-45-2	NW Pacific	46.6	169.6	2425	SST Mg/Ca	This study
SO264-53-2	NW Pacific	47.7	169.3	2325	SST Mg/Ca	This study
ODP-662	Eq. Atlantic	-1.4	-11.7	3814	SST $U^{k'}_{37}$	Herbert et al., 2010
ODP-722	Arabian Sea	16.6	59.8	2022	SST $U^{k'}_{37}$	Herbert et al., 2010
ODP-806	W Eq. Pacific	0.3	159.4	2520	SST Mg/Ca	Wara et al., 2005
ODP-846	E Eq. Pacific	-3.1	-90.8	3296	SST $U^{k'}_{37}$	Herbert et al., 2010
ODP-847	E Eq. Pacific	0	-95	3373	SST Mg/Ca	Wara et al., 2005
ODP-882	NW Pacific	50.4	167.6	3244	Planktic $\delta^{18}O$; Biog. Opal	Maslin et al., 1995; Haug et al., 1999
ODP885/886	N Pacific	44.7	-168.2	5709/ 5714	dust flux	Abell et al., 2021
ODP 982	NE Atlantic	57.5	-15.9	1134	SST $U^{k'}_{37}$	Lawrence et al., 2009; Herbert et al., 2016
ODP-1010	NE Pacific	30	-118	3465	SST $U^{k'}_{37}$	Lariviere et al., 2012
ODP-1021	NE Pacific	39	-128	4213	SST $U^{k'}_{37}$	Lariviere et al., 2012
ODP-1208	NW Pacific	36	158	3346	SST $U^{k'}_{37}$; dust flux	Lariviere et al., 2012; Abell et al., 2021
ODP 1090	S Atlantic	-42	9	3702	Fe MAR	(Martínez-Garcia et al., 2011)
IODP U1313	N Atlantic	41	-33	3426	*n*-alkane flux	(Naafs et al., 2012)

Such a high temperature difference could indicate the presence of a front between the two study sites during the Pliocene that was at a different position during the Pleistocene. In the modern day the SAF, which is marked by a steep SST gradient, is located directly south of SO264-45 (figure 4.1). It has been suggested that during the Pleistocene there were shifts of the SAF, even towards a position north of site SO264-45 (scientific chapter I; Thompson and Shackleton, 1980; Kawahata and Ohshima, 2002; Harada et al., 2004; Yasudomi et al., 2014; Gallagher et al., 2015). Therefore, it is likely that there were also shifts in the position of the front system during the Pliocene. For example, if there was a shift of the SAF to a position between our two core sites, SO264-45 would have been under greater influence of warm water from the Kuroshio-Oyashio transition zone than SO264-53, thereby causing the steep temperature gradient between these sites. This could also explain why the $\Delta SST_{Plio\text{-}Plei}$ is higher at site SO264-45 than -53. Yet the temperature difference between our study sites could also be connected to the lack of a permanent halocline in the Pliocene. This weaker stratification may have weakened the sharpness of boundaries in the frontal system resulting in a more gradual decrease in temperature with increasing latitude.

At ~2.74 Ma (SO264-45)/ ~2.77 Ma (SO264-53) we observe a sudden and steep decrease in the temperature (~4.5°C) as well as the $\delta^{18}O_{sw\text{-}ivc}$ (1‰) records from *G. bulloides* and

N. incompta (figure 4.3). Notably, we assume that the time difference of this event between the two cores sites is partly induced by the lower sample resolution of core SO264-53. This, together with the limited accuracy of the age models, makes us consider the temperature decrease in the two cores as one event rather than speculate whether it occurred earlier at one of the sites.

A decrease in SST around this time has also been observed at many other sites. In the tropical Pacific, for example, records indicate an SST decrease of 2.5-3.8 °C between 2.8-2.72 Ma (Wara et al., 2005; Herbert et al., 2010). In the Arabian Sea and the tropical Atlantic, there is also an SST decrease around this time yet of only about 2°C (Herbert et al., 2010). In the North East Pacific, ODP sites 1010 and 1021 (Lariviere et al., 2012) show a similar decrease as the other sites. A precise dating of the change is not possible because of the low resolution of these cores.

This global decrease reflected in the SST records but also in a decrease of atmospheric CO_2 (Bereiter et al., 2014; de la Vega et al., 2020) is likely connected to the iNHG (figure 4.4; Wara et al., 2005; Herbert et al., 2010; Lariviere et al., 2012). However, the decrease at our study sites is more pronounced and persistent than in the other records (figure 4.4). Therefore, we propose that although being induced by the same mechanisms causing a global decrease in temperature, the decrease at our study site was further amplified by changes in the local hydrography.

Haug et al. (2005) and Maslin et al. (1995) proposed that around 2.7 Ma the upper ocean temperature dynamics changed in the subarctic North West Pacific most likely in connection to the onset of a permanent halocline. At site 882, Maslin et al. (1995) observed an increase in $\delta^{18}O$ of *G. bulloides*, *N. incompta* and *N. pachyderma* of >2 ‰ and associated it with a massive drop in SST of at least 7.5°C around 2.75 Ma (between 2.85-2.75 Ma). Haug et al. (2005), however, excluded a consistent SST drop throughout the seasons and argued that the actual drop might be smaller than predicted by Maslin et al. (1995). Haug et al. (2005) proposed that through the onset of a permanent halocline in the North Pacific at ~2.73 Ma, the interannual SST variability increased. A simulation with the simple earth system model CLIMBER-2 for the subarctic North West Pacific tested the links among subarctic Pacific stratification, SST and ice-sheet growth and showed that late summer temperatures increased by ~3°C through stratification compared to less stratified conditions which existed prior to 2.7 Ma. This has further been supported by alkenone data by Haug et al. (2005) and Studer et al. (2012). Contrasting the model also shows that SSTs are ~ 5°C colder in winter and spring after the onset of the permanent stratification of the North Pacific at 2.7 Ma. Therefore the overall decrease predicted by the model is ~2°C. Thus, it is likely that our observed temperature decrease around 2.7 Ma of ~4.5°C is partly induced by the global SST decrease event around this time and further amplified by the stratification change in the North Pacific and therefore more significant than SST decreases observed in other regions.

Most sites presented in figure 4.4 have in common, that the temperature decrease around ~2.7 Ma is only a short event that is followed by an increase up to previous values. In contrast, our records of site SO264-45, as well as ODP site 1208 (Lariviere et al., 2012) from Shatsky Rise, indicate that upper ocean temperatures stayed lower after this pronounced decrease at ~2.7 Ma than before during the Pliocene. This could indicate that the onset of the permanent halocline in the North Pacific hindered the SSTs from increasing to pre-event (~2,7 Ma) conditions. This would align with both the $\delta^{18}O$ values at North Pacific site ODP 882 (Maslin et al., 1995) and the simple earth system model CLIMBER-2 (Haug et al., 2005), which indicate that SST remained on average lower after the decrease at ~2.7 Ma than prior to 2.7 Ma (figure 4.4). However, the upper ocean temperature records of site SO264-53 show a different picture. As all records are only presented until 2.68 Ma, in this study, it cannot be excluded that the SO264-45 records and the record of ODP site 1208 also increased again after 2.68. Therefore, records spanning through the mid-Pleistocene transition would be needed to further clarify this topic.

Our so far unique data of both SST and subSST indicates a relatively sustained thermocline during the Pliocene similar to the setting in the Pleistocene (figure 4.3). This is shown at both our study sites by a rather constant offset between our SST and subSST of ~4°C. In contrast, there has been no halocline within the shallow habitat depths of *G. bulloides* and *N. pachyderma* (max ~130 m) as indicated by rather similar $\delta^{18}O_{sw\text{-}ivc}$ records of both species. This would support the theory of Haug et al. (1999) of a lacking halocline in the Pliocene. However, as the habitat depths of both species lie above the depth of the modern-day halocline (~150-200 m) we cannot exclude a deeper halocline.

In the late Pleistocene, the upper ocean dynamics in the study region did not primarily follow a glacial-interglacial development: neither the temperature nor the $\delta^{18}O_{sw}$ records of *G. bulloides* and *N. pachyderma* at both sites follow a clear glacial-interglacial pattern (figure 4.3). Yet they are linked to a complex interplay of the Oyashio/subarctic current and the Kuroshio Current/Extension in relation to the development of stronger or weaker SST gradients between the West Pacific warm pool and the Eastern Equatorial Pacific that is discussed in detail in scientific chapter I.

4.4.2. Changes in primary productivity

Our XRF-based Ca/Ti, Si/Ti and Ba/Ti records displayed as natural logarithm indicate overall substantially higher productivity during the late Pliocene in comparison to the late Pleistocene (figure 4.6). This indicates a drastic change in the productivity regime, which is even documented in a change in sediment color at both sites (supplementary figure 4.14). This difference in the productivity between the Pliocene and Pleistocene is closely linked to global climate as shown by a correlation of general trends in our productivity proxies and atmospheric CO_2 (figure 4.6; Bereiter et al., 2014; Vega et al., 2020). Higher productivity in the Pliocene than Pleistocene has also been reported from ODP site 882 (Haug et al., 1999) (figure 4.6). At this site, high opal accumulation rates are observed prior to 2.73 (2–6 g $cm^{-2}ka^{-1}$), followed by low opal accumulation rates during the past 2.73 Ma (0.1–1.2 g $cm^{-2}ka^{-1}$). Thus, the silica-dominated productivity that is reflected in the subarctic record by Haug et al. (1999) and the mainly carbonate-dominated productivity pattern at our North Pacific study sites could have had the same trigger that enhanced productivity in the Pliocene.

Increased primary productivity in the Pliocene is neither a global phenomenon nor present in the entire North Pacific: for example, the diatom productivity in the Bering Sea and the Gulf of

Alaska as well as primary productivity in costal upwelling regions like the California Margin and the Benguela upwelling system increased upon the iNHG (Janecek, 2000; Pérez et al., 2001; Cortese et al., 2004; März et al., 2013; Sánchez-Montes et al., 2020). This indicates that the observed productivity pattern in the pelagic North Pacific must be linked to a rather local phenomenon. A drop in (opal) productivity on the other hand has also been observed in the Southern Ocean indicating that similar processes might have influenced the productivity in the subarctic North Pacific and the southern Ocean (Hillenbrand and Cortese, 2006).

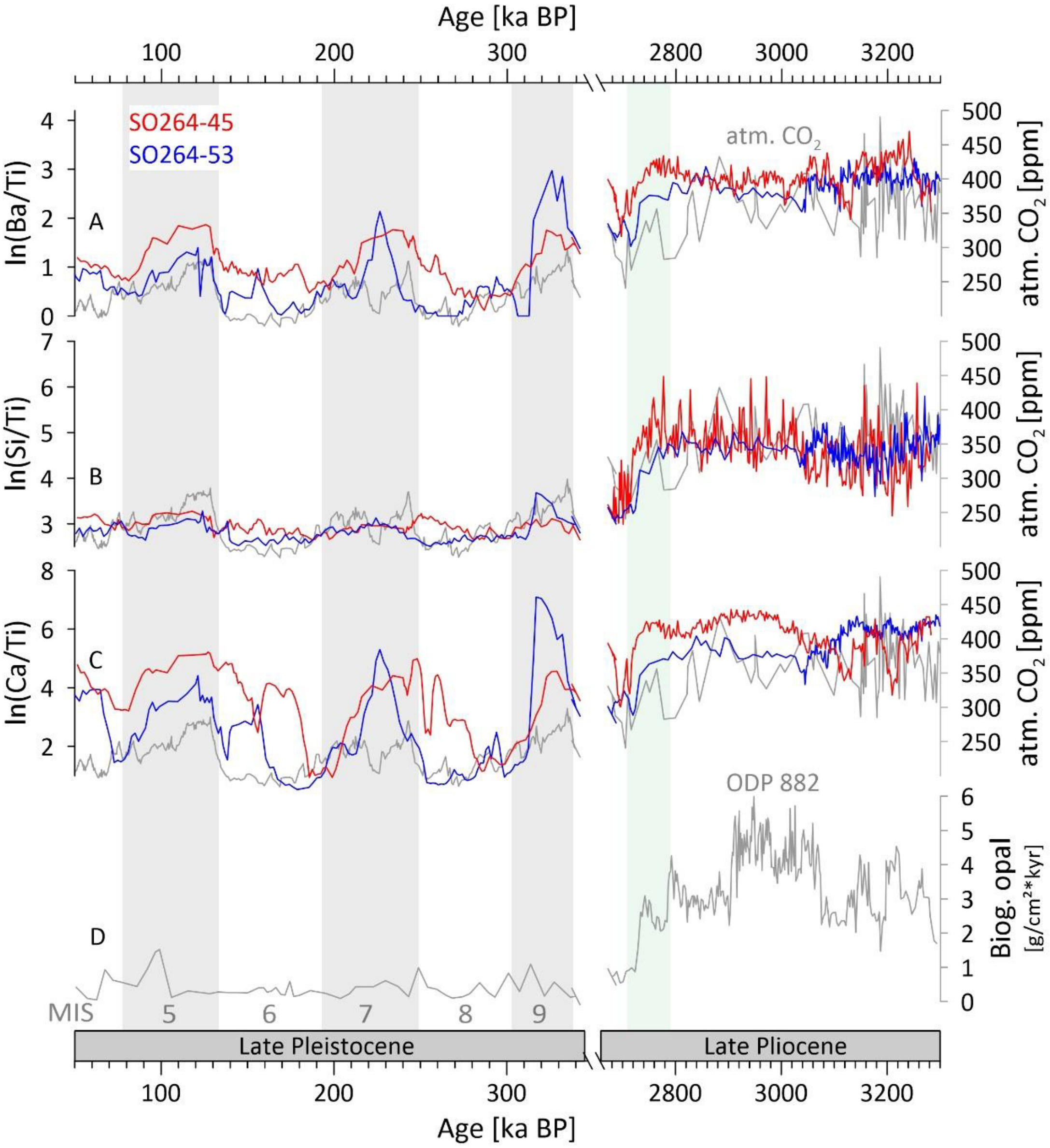

Figure 4.6: Productivity proxy data of cores SO264-45 (red) and SO265-53 (blue) (**A-C**), displayed as natural logarithm in comparison to atmospheric CO_2 (Bereiter et al., 2014; de la Vega et al., 2020) and the opal accumulation rate of site 882 (Haug et al., 1999) (**D**). **A**: Barium/titanium, **B**: Silicon/titanium and **C**: Calcium/titanium. Gray shadings and numbers mark Marine Isotope Stages (MIS 9-4) while the green shading marks the time interval in which SST records in figure 4 mark the iNHG.

Haug et al. (1999) suggested that the drastic productivity change at site 882 in the pelagic subarctic Pacific is caused by the onset of the permanent halocline at ~2.7 Ma. They argue that in the Pliocene, the lack of salinity-driven stratification enabled exchange between nutrient-rich deep water and the surface, which resulted in high primary productivity, while a permanent halocline after 2.7 Ma prevented the upwelling of nutrients and dampened productivity. We assume that this change in stratification also caused the observed productivity pattern at our sites. From our $\delta^{18}O_{sw-ivc}$ records from the shallow dwelling species *G. bulloides* and the deeper dwelling *N. incompta,* we can confirm that there has been no halocline within the upper ~130 m. Further, the temperature offset between *G. bulloides* and the *N. incompta* indicates that there was a persistent thermocline throughout the late Pliocene. This indicates that a change in salinity-driven stratification and not a change in temperature-driven stratification or combination of the two caused the change in nutrient availability.

Moreover, the decrease in SST and subSST at site SO264-45 and the decrease in productivity occur simultaneously, thereby indicating that not one caused the other to decrease, yet that their decrease was closely coupled. This might also hold true for site SO264-53, yet because of lower sample resolution or a possible hiatus, it is not as apparent as in SO264-45.

We assume that a decrease in Ca/Ti around 3 Ma at site SO264-53 that is not reflected in SO264-45 (figure 4.6) could indicate either dissolution, a change in fauna of the upper water column, or be an artifact of the age model of SO264-53. While the record of SO264-45 follows the general trends of atmospheric CO_2 and productivity at ODP Site 882 during the late Pliocene, the record of SO264-53 shows a significant decrease at ~3.04 Ma, followed by values that stay considerably lower than in core SO264-45. Our other productivity proxies do not show this different behavior of core SO264-45 and -53. This is unexpected as both our sites are located relatively close to each other and are from a similar water depth. Both study sites are located above the CCD throughout the studied time interval, yet in calcite-undersaturated conditions. North of our study site, there is a steep shallowing of the CCD (Emelyanov, 2005). So, if there had been a slight southward shift of this system, site SO264-53 could have been more affected by dissolution than site -45. Yet we consider this unlikely to have caused the Ca decrease in SO264-53 for several reasons. Firstly, SO264-45 and -53 are only 1° apart and secondly, sediments of core -53 have been deposited 100 m shallower than at site -45. Therefore, there would have had to be an unlikely steep gradient between these cores. Thirdly, Ca reflects mainly coccolithophores and foraminifera. Coccolithophores are more resistant to dissolution than foraminifera (Chiu and Broecker, 2008). If there had been strong dissolution, it should also be reflected as rather dissolved foraminifera. However, we did not observe signs of strong dissolution in our foraminifera samples, which should affect Mg/Ca-derived SSTs. As both SO264-45 and SO264-53 show rather similar trends in temperature and there is no sudden SST increase in SO264-53, it is unlikely that one site was distinctly more influenced by dissolution than the other site. To verify that no dissolution took place, a dissolution index could be investigated. Alternatively, the different patterns could be related to a change in fauna. As our cores are from the transition zone between the calcareous-dominated environment of the North Pacific and the diatom-dominated environment of the subarctic North Pacific (Nürnberg, 2018), there could have been a shift between these different productivity regimes at ~3.04 Ma that caused Ca productivity to decrease. Such a shift between environments should be mirrored in the temperature and salinity values. Accordingly, while the $\delta^{18}O_{sw-ivc}$ records, indicating salinity, are rather similar in both cores prior to 3.04 Ma, the values show an offset of ~0.4 ‰

after 3.04 Ma with site SO264-45 being more saline than SO264-53. Similarly, the SST record of site SO264-53 shows a sudden decrease of ~3°C at ~3.04 Ma, and afterward remaining ~1.5°C cooler compared to before 3.04 Ma. This cooling in SST was likely caused by either an increased influence of subarctic water or a decrease of transitional waters at site SO264-53. Overall, this shift in salinity and SST could have been induced by a general change in ocean dynamics that finally resulted in the onset of permanent stratification in the North Pacific at 2.7 Ma (Haug et al., 1999). However, a shift of the primary productivity regime does not align with the stronger increase in Si at site SO265-53 than at site -45 at the time of the Ca decrease. Lastly, it should be kept in mind that the lower Ca/Ti concentration of SO264-53 might also be an artifact of a possible hiatus between~3.039 Ma and 2.73 Ma. If there was a hiatus, as discussed in chapter 2.4, it could have cut out a part that showed a higher Ca/Ti ratio. This is, however, unlikely as it is not reflected in the other productivity patterns. Further, lower productivity of calcareous organisms could have lowered the overall sedimentation rates, which could explain the change of sedimentation rate at ~3 Ma in SO264-53. To solve this contradiction, more data would be needed, including reliable (proxy) data for calcite dissolution, quantitative primary productivity data and high-resolution data of the upper ocean dynamics in the Pliocene as well as better age control for SO264-53.

During the Pleistocene, all productivity proxies indicate an increase in productivity between the deglaciations and interglacials followed by a decrease in late interglacials and early glacials (figure 4.6). This pattern fits well with the dominant pattern of primary productivity in the North Pacific (Narita et al., 2002; Gorbarenko et al., 2004; Kienast et al., 2004; Jaccard et al., 2005, 2010; Brunelle et al., 2007; Shigemitsu et al., 2007; Galbraith et al., 2008; Gebhardt et al., 2008; Riethdorf et al., 2013). The driving mechanisms of this pattern are still a matter of debate. However, a change in nutrient availability linked to enhanced transport of nutrients form the subpolar marginal seas and changes in stratification appear to be important (see scientific chapter I).

4.4.3. Changes in dust supply via the westerlies and its influence on primary productivity

The distinct difference between the late Pliocene and the late Pleistocene is also reflected in the XRF-based Fe records that we use as a proxy for terrigenous input via wind, mainly the westerlies (figure 4.7). It shows very low values in the late Pliocene, thereby indicating only a little transport of terrigenous matter to the core locations during this time, while the primary productivity was high (figure 4.6). This appears to end at ~2.7 Ma when the Fe records show a sudden and strong increase toward average values of the late Pleistocene, while primary productivity decreases significantly. This indicates that dust fertilization did neither cause the high primary productivity in the North Pacific during the late Pliocene nor limited the primary productivity during the late Pleistocene.

It is likely that the increase in Fe observed at our sites around ~2.7 Ma, reflects a global change in the wind pattern or dust supply rather than a local change. This is indicated as records from the North and South Atlantic (Martínez-Garcia et al., 2011; Naafs et al., 2012), as well as two other records from the Pacific (Abell et al., 2021), show a similar trend: lower dust fluxes in the Pliocene followed by a sudden change towards higher values at the iNHG (figure 4.7). The abrupt change in dust supply to the pelagic oceans could either be caused by a change in the amount of transported material or a change in the strength and/or position of the westerlies at the time of the iNHG.

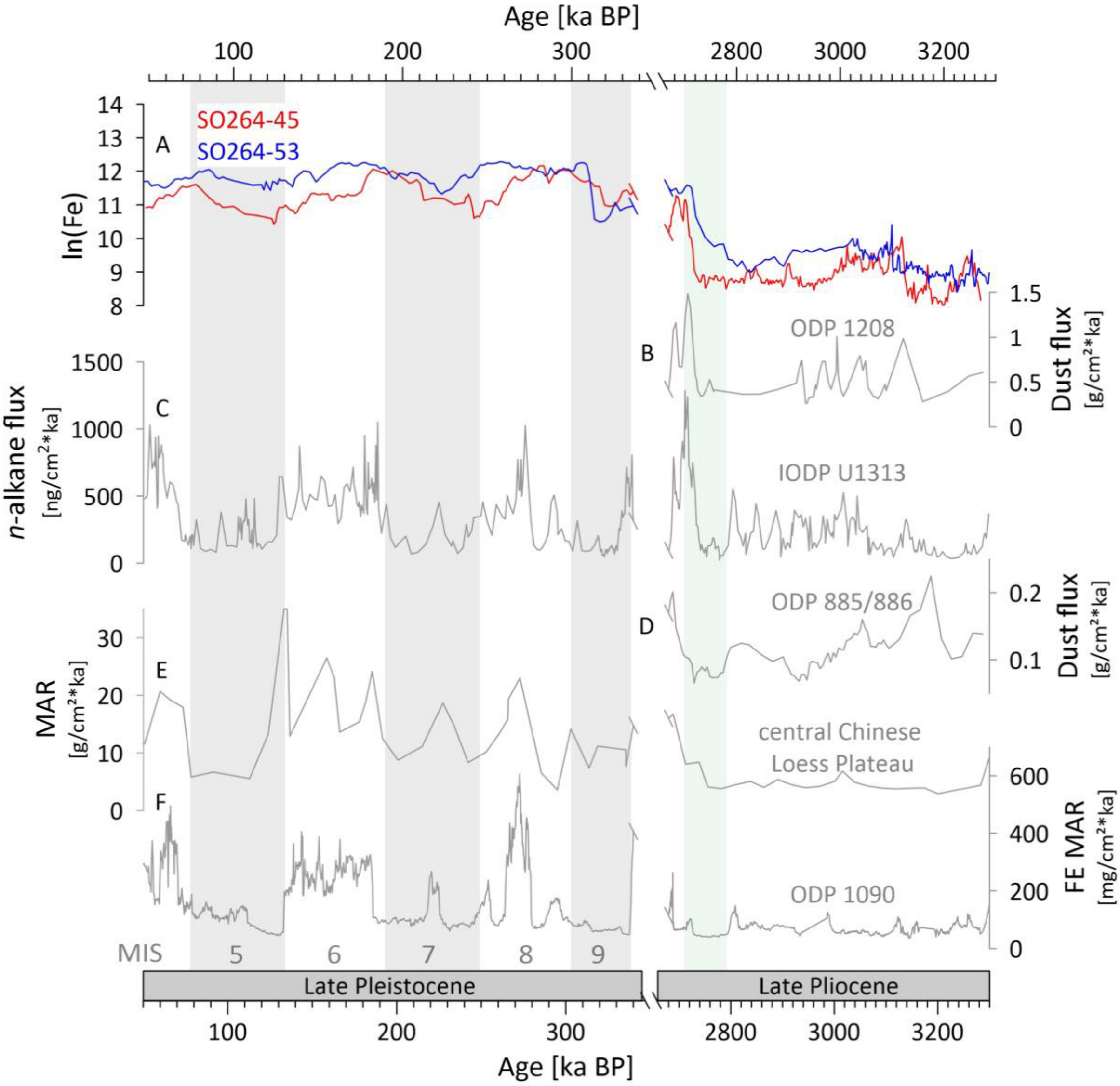

Figure 4.7: Proxy data of terrigenous dust input via wind (XRF-derived Fe displayed as natural logarithm) of cores SO264-45 (red line) and SO264-53 (blue line) (A), in comparison to dust flux proxies of: B) ODP 1208 from Shatsky Rise (Th and $^3He_{ET}$: Abell et al., 2021), C) IODP U1313 from the North Atlantic (accumulation rate of long-chain n-alkane: Naafs et al., 2012), D) ODP885/886 from the North Pacific (Th and $^3He_{ET}$: Abell et al., 2021), E) the central Chinese Loess Plateau (mean MAR of Lingtai and Zhaojiachuan: (Sun and An, 2005), F) ODP 1090 from the South Atlantic (Fe MAR: Martínez-Garcia et al., 2011). Gray shadings and numbers mark Marine Isotope Stages (MIS 9-4) while the green shading marks the time interval in which SST records in figure 4 mark the iNHG.

At the same time of the sudden increase in our Fe-records, the Mass Accumulation Rate (MAR) of the Chinese Loess Plateau, increased (Sun and An, 2005). Such an increasing amount of dust could be the result of aridification in the source area of the dust, mainly Eastern Asia (Mahowald et al., 2006; McGee et al., 2010). However, Abell et al. (2021) tried to link the different source regions of the North Pacific dust and found that aridification started earlier than the iNHG. Therefore, it cannot have been the main driver for the observed dust increase at the iNHG. Nevertheless, it is still a matter of debate to what extent the aridification attributed to the changes in weathering or vegetation that can also influence the dust availability (Abell et al., 2021). Another hypothesis is that the observed increase in dust supply in the North Pacific at the iNHG was driven by a southward shift and intensification of the westerlies (Li et al., 2015; Abell et al., 2021). Abell et al. (2021) suppose that such a shift may have been driven by a change in thermal gradients and ice volume and were connected to a generally weakened and expanded Hedley circulation as proposed by Brierley et al. (2009). Such a change in westerlies is likely to have occurred globally synchronously and could, therefore, also explain the changes that have been observed at the Atlantic sites (Martínez-Garcia et al., 2011; Naafs et al., 2012; Abell et al., 2021).

Our sites are located at the northern boundary of the westerlies. Thus, a major shift to the south would reduce the dust supply, while a strengthening alone would increase the dust supply. Therefore, we assume that a possible southward shift in the position of the westerlies at 2.7 Ma is unlikely. However, if the strengthening of the westerlies would have broadened the area that is under the influence of the westerlies a simultaneous strengthening and southward displacement of the westerlies as proposed by Abell et al. (2021) could have cause our observed increase in dust supply at ~2.7 Ma. From this, we conclude that either an increase in available dust from the source regions or a strengthening of the westerlies or a combination of the two caused our observed increase in the terrigenous matter at ~2.7 Ma, while we cannot constrain if there has also been a southward displacement of the westerlies.

During the Pleistocene, the dust supply at the study sites generally increases at the transitions from late interglacials to early glacials and decreases during the glacials (figure 4.7). This pattern fits well with globally observed patterns of dust-climate feedbacks that consider e.g. wind gustiness, sea level, glaciogenic sediment supply, vegetation and aridity as possible drivers for glacial-interglacial dust flux changes (Sun and An, 2005; McGee et al., 2010; Lamy et al., 2014; Shaffer and Lambert, 2018). Further, a southward displacement of the westerly winds during the glacials, as proposed by e.g. Gray et al. (2020) or Toggweiler et al. (2006) may have contributed to our observed wind pattern. Such a displacement would move the center of the westerlies further away from our study sites resulting in less terrigenous input at our study sites. Notably, we observe an offset in the Fe records of SO264-45 and -53. The record of SO264-53 indicates longer periods of high Fe values and decreases ~30 ka later than the record of SO264-45 in MIS 8 and 6. This could indicate that the westerlies had, because of unknown effects, a stronger and prolonged influence at site SO264-53 than 45 during this time, which would be rather the opposite of what we expect from the documented southward shifts of the westerlies at the transition from interglacials to glacials (e.g. Gray et al., 2020) with regard to our core locations. Alternatively, it could be an artifact of using Fe cps as a wind proxy, which could be influenced by other changes in the element composition in the sediment or changes in sedimentation rate (Croudace and Rothwell, 2015). A possibility to check for such an artifact would be to investigate a quantitative dust deposition proxy such as focusing-corrected ^{232}Th fluxes, which is, however, beyond the scope of this study. Lastly, this offset may point to an unlikely problem of in the age model of one or both of our studied cores that we cannot resolve with available methods.

4.5. Summary and Conclusion

Our comprehensive proxy data for upper ocean paleotemperature, $\delta^{18}O_{sw\text{-}ivc}$, productivity and dust input via wind suggests that the North Pacific underwent a drastic reorganization between the late Pliocene and late Pleistocene in connection to the iNHG:

- We show that the onset of a permanent halocline in connection to the iNHG and the thereby reduced availability of nutrients (Haug et al., 1999, 2005) caused a major decrease in primary productivity at our study sites. Thus, the onset of a permanent halocline did not only affect the diatom-dominated productivity regime in the subarctic North Pacific, but also the carbonate-dominated productivity regime at the transition zone between the subarctic and subtropical gyre.
- Our data of the shallow dwelling planktic foraminifer of *G. bulloides* and the deeper dwelling *N. incompta* (max ~130 m) supports the theory Haug et al. (1999), that there has been no permanent halocline during the late Pliocene at least in the habitat depth of these species (~130 m). Yet we do show that there has been a constant thermocline. From this, we conclude that the temperature-driven stratification did not have a major influence on the nutrient availability prior to the iNHG, yet that it really was a change in the salinity-driven stratification that caused the change in nutrient availability.
- Further, we discuss a decrease in carbonate productivity at site SO264-53 at ~3.04 Ma that might indicate a shift of the border between the calcareous-dominated environment of the North Pacific and the diatom dominated environment of the subarctic North Pacific. However, we cannot exclude that it might also be caused by dissolution or be an artifact of uncertainties in the age model (possible hiatus).
- We link an increase in dust supply at our study sites during the iNHG to a rather widespread phenomenon of either an increased availability of dust from the source regions, a strengthening of the westerlies, or a combination of the two. This rather contrasting development of dust supply and productivity at our study sites indicates that dust fertilization neither caused the high primary productivity in the North Pacific during the late Pliocene nor limited the primary productivity during the late Pleistocene.
- Further, we link high upper ocean temperatures in the Pliocene to the general higher temperatures of this epoch, and less seasonality at our study sites due to the lack of a permanent halocline. The steep temperature decrease at the iNHG is also partly induced by a global SST decrease and might have further been amplified by the aforementioned increased seasonality (Haug et al., 2005). Whether the upper ocean temperatures stayed low after the decrease as suggested for the subarctic Pacific and by SO264-45 or increased to pre-event values (~2.7 Ma) as suggested by SO264-53 cannot be finally resolved. Yet we assume that the onset of a permanent halocline in the North Pacific would have had the potential to hinder the SSTs from increasing again after the iNHG.
- Moreover, from a steep temperature gradient between our study sites in the Pliocene, we hypothesize that there was increased influence of water from the Kuroshio/Oyashio transition at SO264-45, which is located 1° south of SO264-53. This could either be linked to a position of the SAF between our sites or a weakened sharpness of boundaries

in the frontal system of the Kuroshio/Oyashio transition zone induced by the lack of a permanent halocline in the Pliocene.

- Moreover, we hypothesize that a steep temperature gradient between our study sites in the Pliocene could indicate increased influence of water from the Kuroshio/Oyashio transition at SO264-45 which is located 1° south of SO264-53. This could either be linked to a position of the SAF between our sites or a weakened sharpness of boundaries in the frontal system of the Kuroshio/Oyashio transition zone induced by the lack of salinity-driven stratification in the Pliocene.

4.6. Supplement

4.6.1. Ecology and distribution of *N. incompta* in the North Pacific

Neogloboquadrina incompta is the mainly right-coiling (dextral) relative of the mainly left-coiling (sinistral) *N. pachyderma* (Schiebel and Hemleben, 2017). Before it was shown that *N. incompta* is a genetically distinct species, it was often referred to as *N. pachyderma* dextral (Darling et al., 2006). *N. incompta* is a nonspinose planktic species mainly occurring in temperate, subpolar, and transitional water masses. Compared to *N. pachyderma,* which prefers water temperatures below ~7°C (Reynolds and Thunell, 1986), *N. incompta* prefers warmer water masses of ~12-17°C. It is represented by two genotypes: while type I inhabits the north and south Atlantic, type II is abundant in the North Pacific (Darling et al., 2006). In the middle to higher latitudes, *N. incompta* is found from the surface to ~200 m yet mainly below 50 m and above 80 m and migrates throughout its lifecycle (Kuroyanagi and Kawahata, 2004; Iwasaki et al., 2016; Kretschmer et al., 2018). According to plankton tow studies off the coast of Japan, it has a shallower habitat than *N. pachyderma,* most likely linked to its preference for warmer water temperatures (Sagawa et al., 2013; Iwasaki et al., 2016). If water temperatures do not exceed or fall below its preferred range, e.g., in higher latitudes (>23°; <55°), *N. incompta* occurs throughout the year (Sagawa et al., 2013; Malevich et al., 2019).

4.6.2. Foraminiferal Mg/Ca paleo thermometry and $\delta^{18}O_{sw\text{-}ivc}$

The ratio of incorporation of magnesium and calcium into the shells of foraminifera is closely related to the temperature of surrounding seawater. Therefore, Mg/Ca of foraminiferal tests is a widely applied proxy for reconstructing paleo sea (surface) temperature (Nürnberg, 1995, 2000; Nürnberg et al., 1996; Lea et al., 1999; Elderfield and Ganssen, 2000). Additional influencing factors on the Mg/Ca ratio that need to be considered for temperature reconstructions are salinity and carbonate chemistry (pH, calcite dissolution) of the surrounding seawater (e.g., Gray & Evans, 2019; Lea et al., 1999; Nürnberg et al., 1996; Regenberg et al., 2006). A detailed discussion about dissolution effects of foraminiferal Mg/Ca at site SO264-45 and why we consider the influence of dissolution insignificantly small for our site is found in chapter 2.7.4: For the calculation of the calcite saturation state $\Delta[CO_3^{2-}]$ in the core regions, data for total alkalinity (TA) and total CO_2 (TCO_2) is needed. Yet so far there is no data with high-spatial-resolution available in the region of cores SO264-45 and -53 which are located in proximity and thus the same data would be used for a calculation for both cores. Therefore we refer to the results of the calculation for SO264-45 in chapter 2.7.4 for site SO264-53.

Various calibrations are available to reconstruct paleo temperatures from *G. bulloides* and *N. pachyderma*. Some of these are based on culturing studies, while others are based on foraminifera from the water column or sediment tops (e.g., Lea et al., 1999; Mashiotta et al., 1999; Elderfield and Ganssen, 2000; Thornalley et al., 2009; Jonkers et al., 2013; Davis et al., 2017). The attempt from Gray & Evans (2019) even goes one step further by additionally considering pH changes over time when calculating paleo SSTs (discussed in detail in chapter 2.7.2). As shown exemplarily for core SO264-45 in figure 4.8, these equations lead to a range of paleo temperatures with an absolute deviation of up to ~9°C for *G. bulloides*. Although we acknowledge the proposition of correcting Mg/Ca-based temperatures for pH, we decide against the use of the MgCaRB *G. bulloides*-specific equation by Gray and Evans (2019) because it leads to unrealistic low temperatures (<0°C in parts of the Pleistocene) and against the use of the MgCaRB multispecies equation because it leads to a considerably larger temperature range than all other equations.

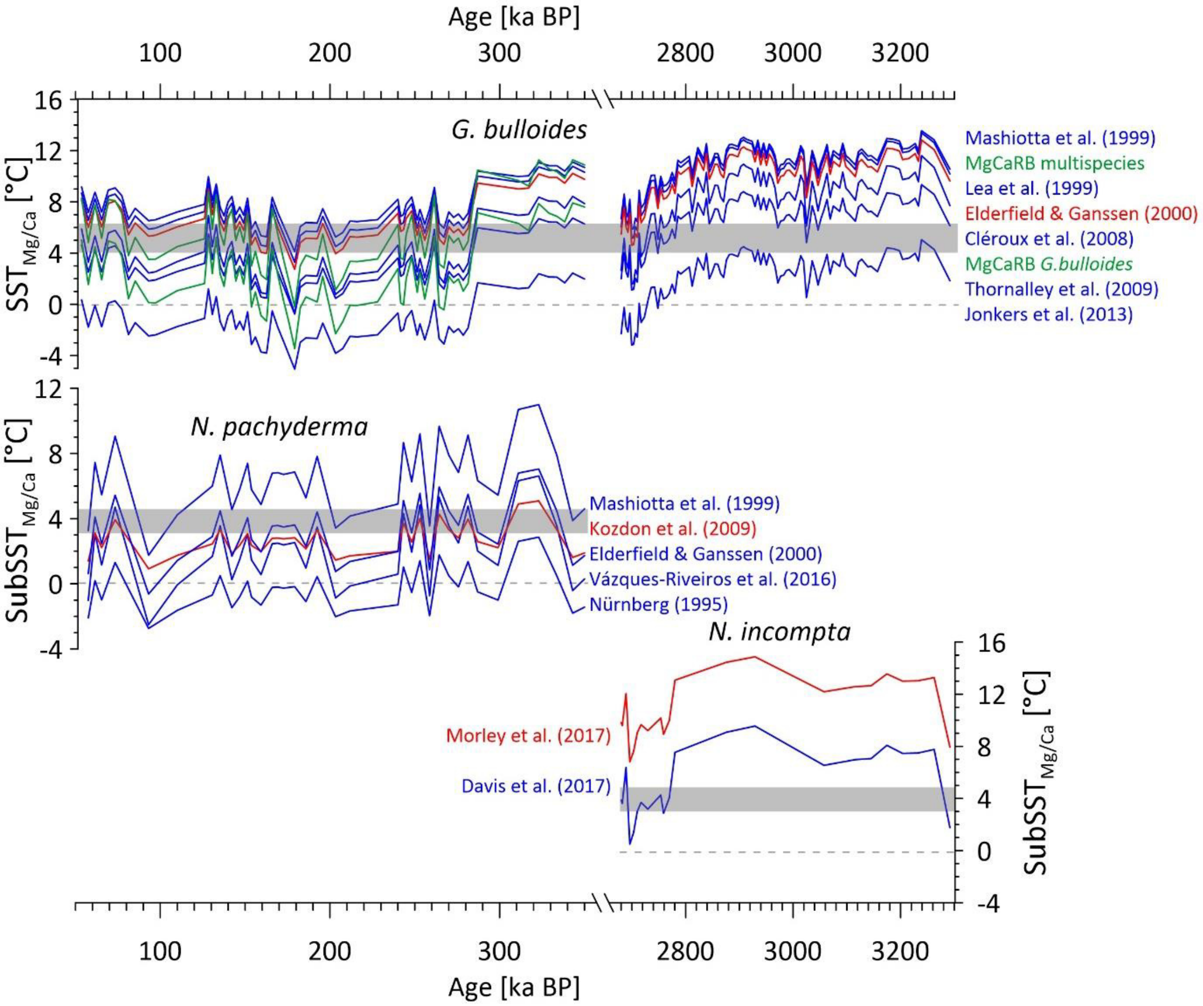

Figure 4.8: Comparison of $SST_{Mg/Ca}$ and $subSST_{Mg/Ca}$ calculated via different species-specific calibrations for *G. bulloides* (top), *N. pachyderma* (middle), and *N. incompta* (bottom). The red calibrations are used in this study. Modern annual temperature ranges (Locarnini et al., 2018) in the respective depth habitats of the individual species are marked as gray boxes. The green temperature curves for *G. bulloides* were derived with the MgCaRB tool from Gray and Evans (2019), considering local changes in salinity and pH.

Instead, we choose the species-specific equation from Elderfield & Ganssen (2000) for *G. bulloides* because it provides Holocene temperatures consistent with the modern temperature at the study site and is based on core top samples (figure 4.8). For *N. pachyderma,* we use the species-specific equation from Kozdon et al. (2009) because it provides Holocene subSSTs consistent with the modern annual subsurface temperature and is based on core top samples that were taken in a region without sea ice cover (figure 4.8). For *N. incompta,* there are fewer equations available, as this species has long been considered as right-coiling *N. pachyderma* (Darling et al., 2006). While the equation from Davis et al. (2017) is based on culturing experiments, the equation from Morley et al. (2017) is based on core top samples from subpolar waters. However, the equation of Morley et al. (2017) leads to higher *N. incompta* temperatures than *G. bulloides* temperatures. We consider this unlikely as *N. incompta* has a deeper habitat depth. Therefore, we decided to use the equation from Davis et al. (2017) (figure 4.8).

Several calibrations describe the relationship of water temperature, δ^{18}O of foraminiferal calcite, and δ^{18}O$_{sw.}$ To decide which calibration provides the most reliable results, we compared δ^{18}O$_{sw-ivc}$ derived by applying different calibrations and considered the results with regard to the modern range of δ^{18}O$_{sw}$ in the study region (figure 4.9). As discussed in chapter 4.2.3, we decided to use the equation from Shackleton (1974) for *G. bulloides* and the *N. pachyderma*-specific equation from Mulitza et al. (2003) for *N. pachyderma* and *N. incompta*.

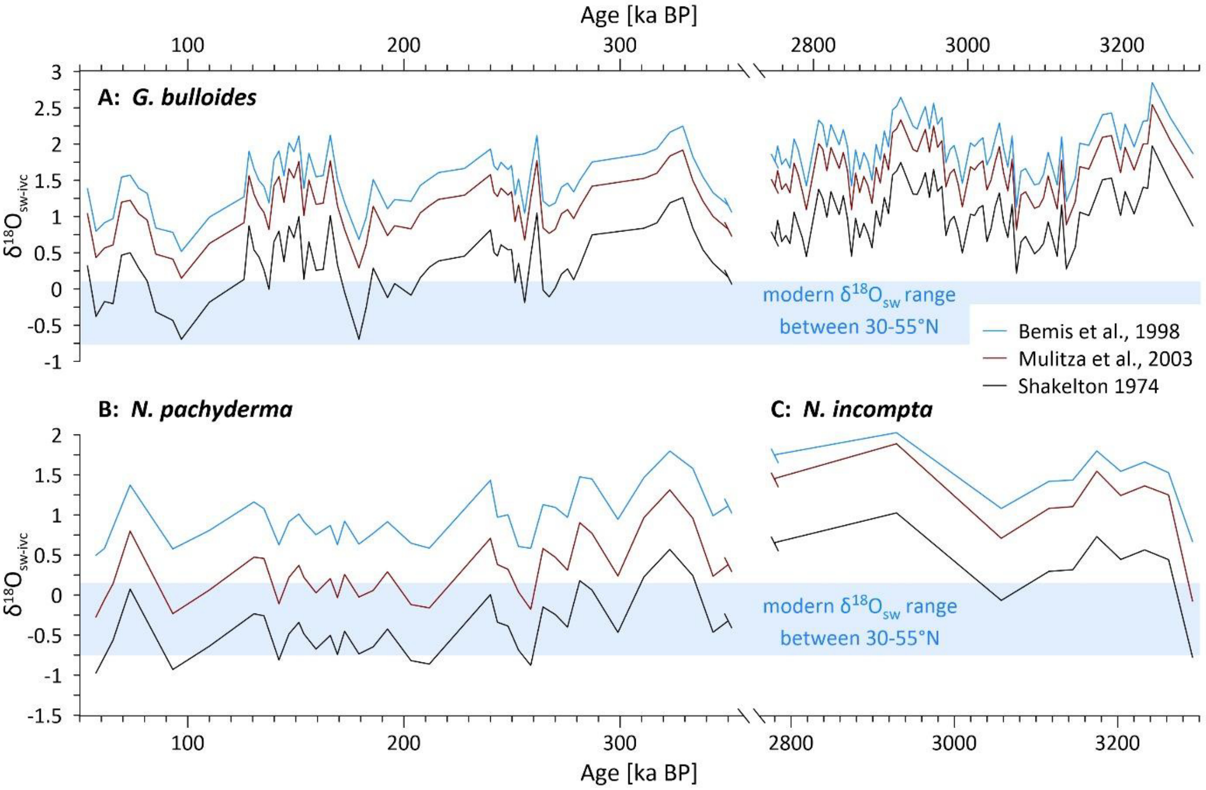

Figure 4.9: δ^{18}O$_{sw-ivc}$ calculated from combined Mg/Ca and δ^{18}O values of *G. bulloides* (A), *N. pachyderma* (B), and *N. incompta* (C) by applying calibrations of Bemis et al. (1998) (blue), Mulitza et al. (2003) (red) and Shackleton (1974) (black). Expected modern annual δ^{18}O$_{sw}$ values between 30-55°N are marked by a blue box (Locarnini et al., 2018).

4.6.3. Contamination effects and outliers

Siliciclastic material and oxide- and manganese-rich coatings can have a distinct imprint on the initial Mg/Ca values of foraminiferal calcite, thereby biasing seawater temperature reconstructions (Barker et al., 2003; Hasenfratz 2017). To determine if these contaminants have been removed sufficiently during the cleaning procedure described in chapter 4.2.2. Al, Fe, and Mn values normalized against Ca are considered. According to Barker et al. (2003), Al/Ca, Fe/Ca, and Mn/Ca values below 0.1 mmol/mol are regarded as uncritical. In core SO264-45, all Mn/Ca values of all three species and the Al/Ca and Fe/Ca values of *N. incompta* (except for the sample at 610 cm) are lower than 0.1 mmol/mol, also the Mn/Ca values of *N. pachyderma* in SO264-53 are below 0.1 mmol/mol (figures 4.10-4.13). In these cases, the cleaning procedure was sufficient, and the influence of the respective contaminants can be excluded.

Al/Ca and Fe/Ca values of *G. bulloides, N. pachyderma,* and *N. incompta* of both cores, and Mn/Ca of *G. bulloides* and *N. incompta* of core SO264-53 partly exceed 0.1 mmol/mol (figures 4.10-4.13). Therefore, we further checked for a possible correlation between high Al/Ca, Fe/Ca, Mn/Ca, and high Mg/Ca values. Figures 4.10 and 4.12 show these values plotted against each other and the calculated coefficient of determination (r^2). All r^2 values of Al/Ca and Fe/Ca are below 0.2, thus indicating that there is no significant correlation between high Al and Fe contamination and high Mg/Ca values in our data. Therefore, we consider our data free from the influence of Al or Fe contamination. However, Mn/Ca and Mg/Ca of core SO264-53 for both *G. bulloides* and *N. incompta* indicate a moderate correlation between these values. As the Mg/Ca curve of SO264-45 (no influence of Mn) and SO264-53 are similar, we assume that manganese coatings did not influence the Mg values, yet that there might have been another cause for this correlation, e.g., that manganese-rich coatings were preferentially built in periods of warmer temperatures. However, a follow-up study would be enlightening to clarify this topic further.

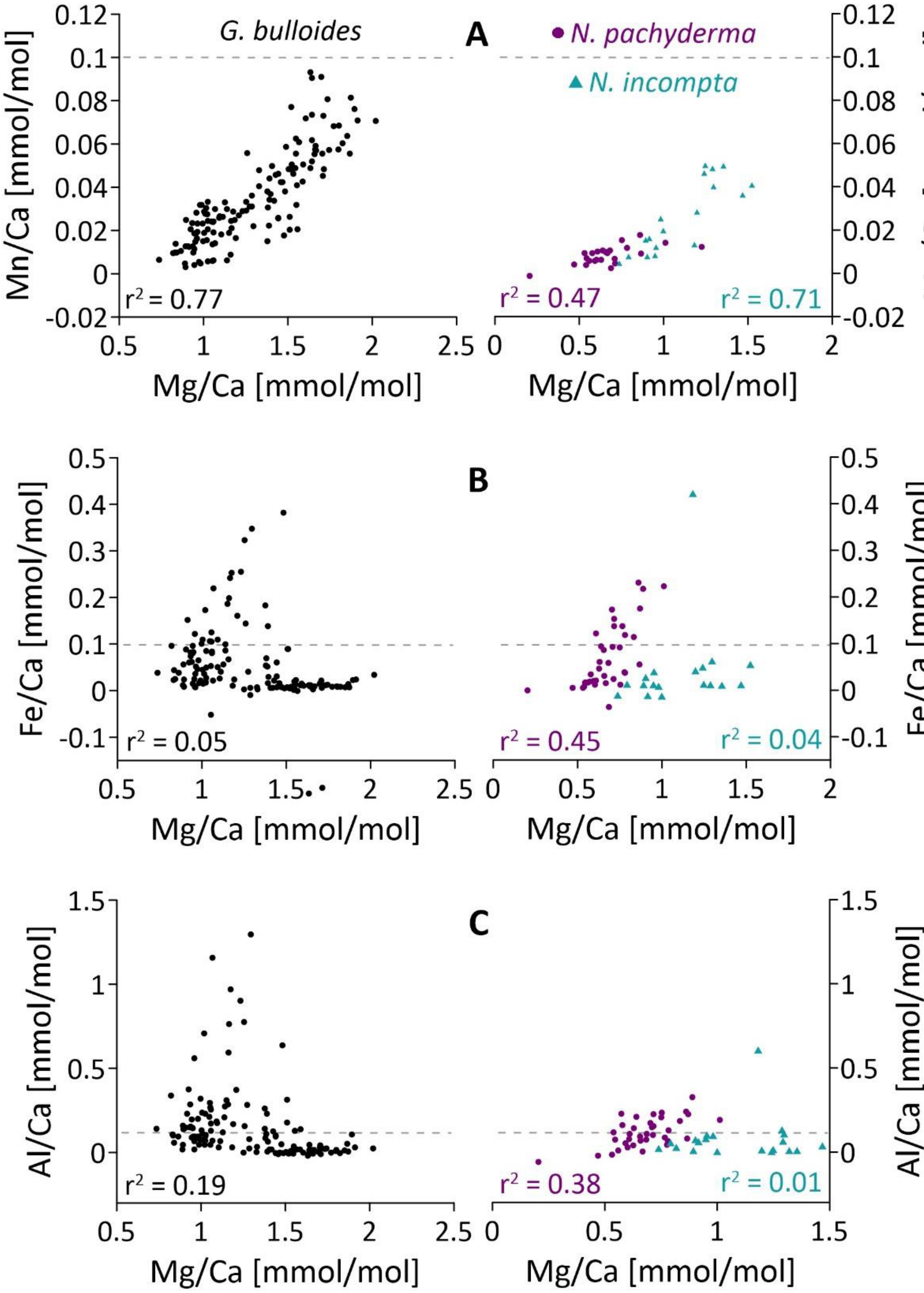

Figure 4.10: Foraminiferal Mg/Ca of *G. bulloides* (black dots), *N. pachyderma* (purple dots), and *N. incompta* (turquoise triangles) of SO264-45 vs. **A**: Mn/Ca, **B**: Fe/Ca, **C**: Al/Ca. For all species, some Fe/Ca and Al/Ca values exceed the proposed threshold of 0.1 mmol/mol (dotted lines) by (Barker et al., 2003). Yet, the coefficient of correlation (r²) is low in these cases, implying no correlation between higher Mg/Ca values and higher contamination.

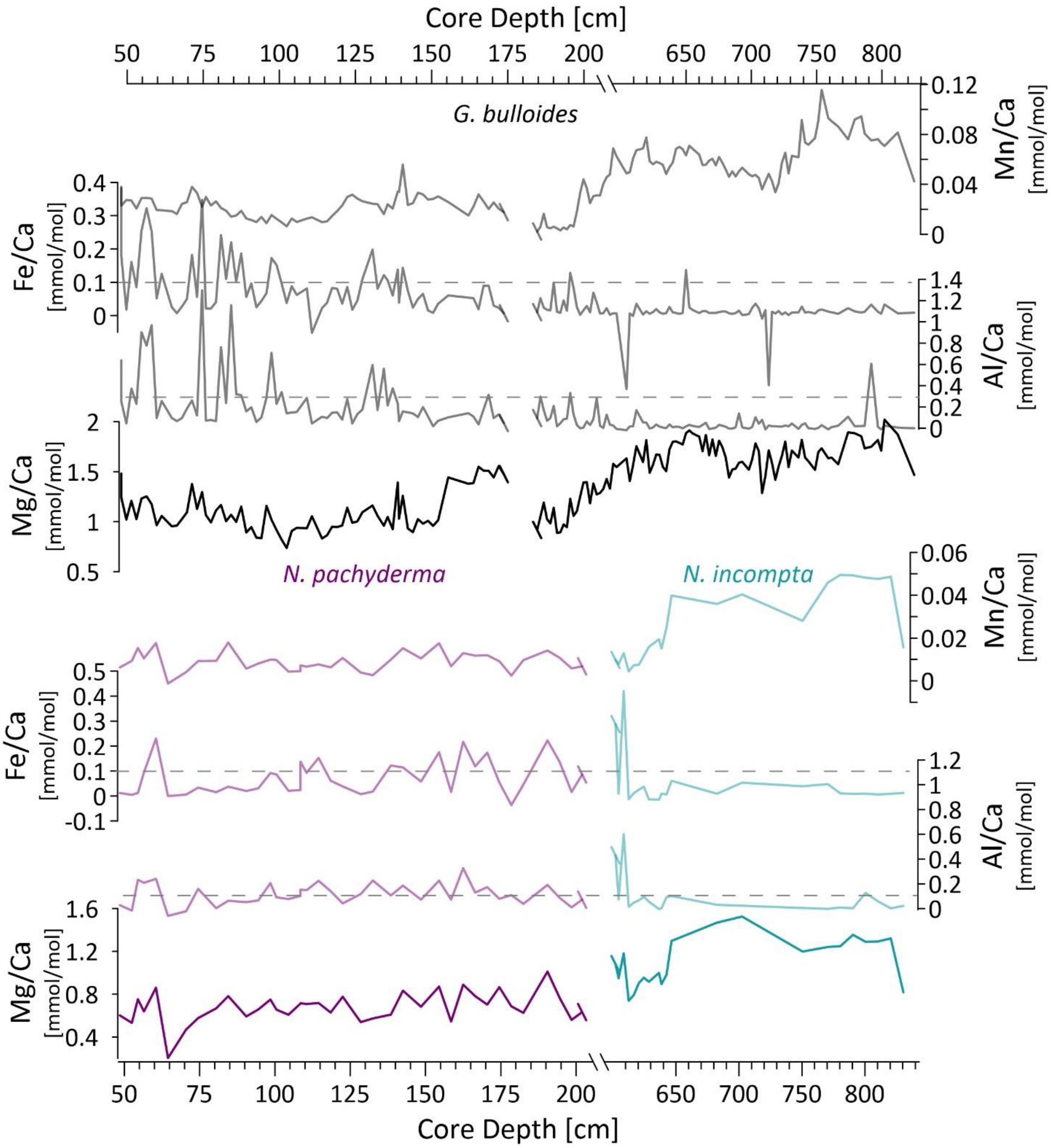

Figure 4.11: Foraminiferal Mg/Ca and contaminant elemental ratios Mn/Ca, Fe/Ca, and Al/Ca of *G. bulloides* (black), *N. pachyderma* (purple) and *N. incompta* (turquoise) vs. core depth of SO264-45. Threshold values of contamination of 0.1 mmol/mol (dotted lines), as proposed by (Barker et al., 2003), are exceeded in some core depths. Yet there is no distinct correlation between high (low) contamination and high (low) Mg/Ca, thus, no Mg/Ca values needed to be removed due to contamination.

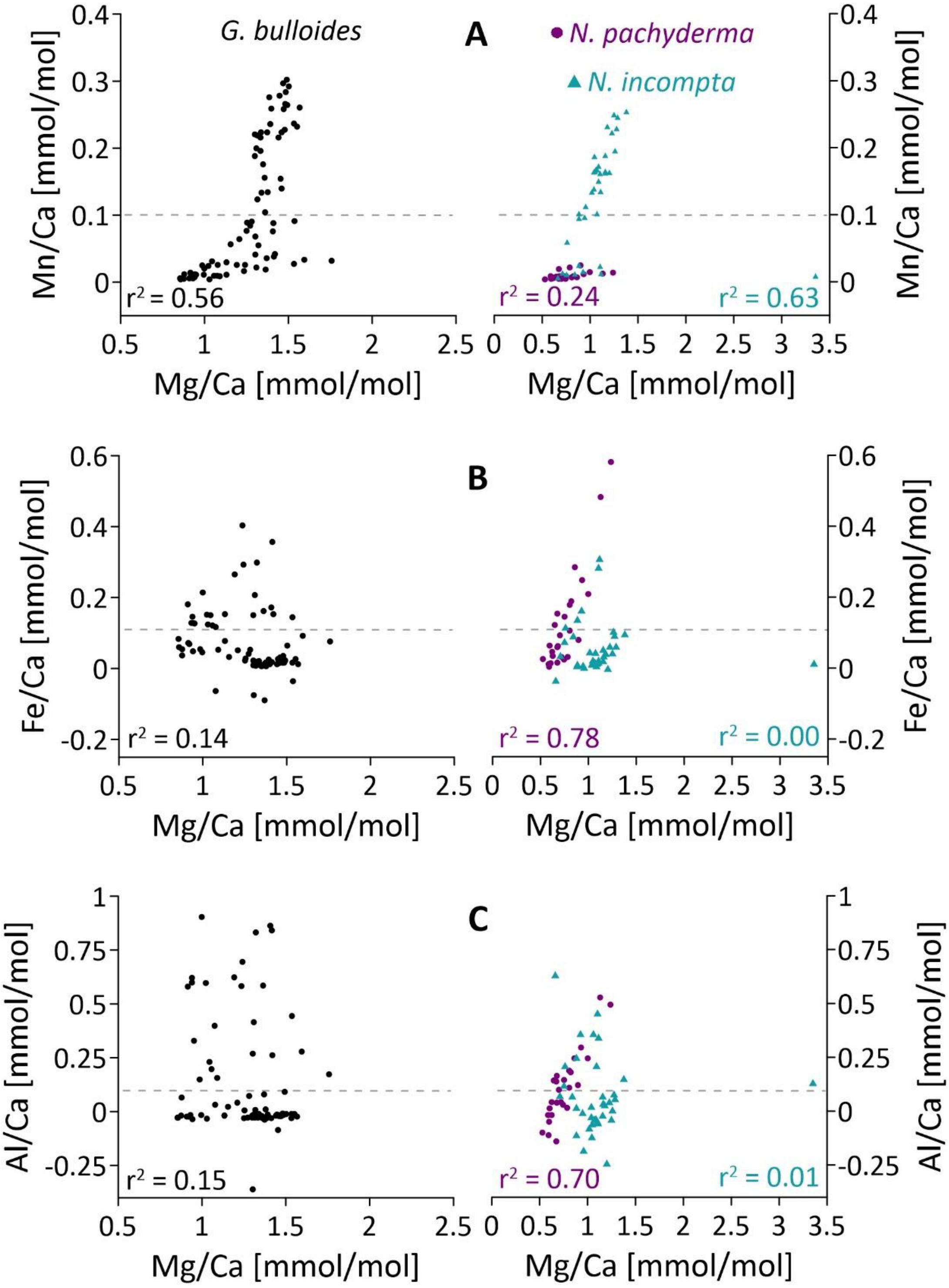

Figure 4.12: Foraminiferal Mg/Ca of *G. bulloides* (black dots), *N. pachyderma* (purple dots), and *N. incompta* (turquoise triangles) of SO264-53 vs. **A**: Mn/Ca, **B**: Fe/Ca, **C**: Al/Ca. For all species, some Mn/Ca, Fe/Ca, and Al/Ca values exceed the proposed threshold of 0.1 mmol/mol (dotted lines) by (Barker et al., 2003), yet the coefficient of correlation (r²) is low in most cases, therefore, implying no correlation between higher Mg/Ca values and higher contamination.

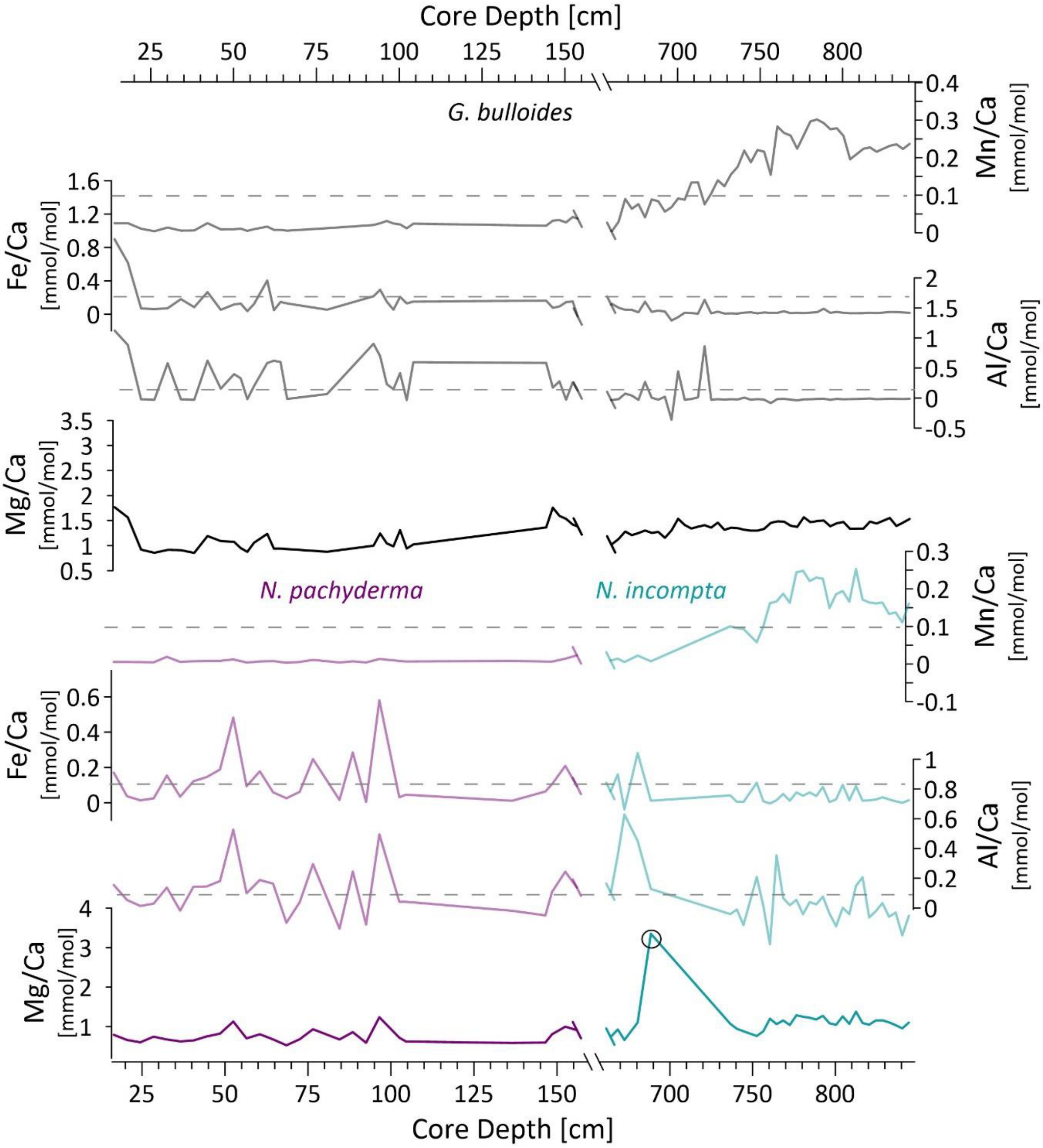

Figure 4.13: Foraminiferal Mg/Ca and contaminant elemental ratios Mn/Ca, Fe/Ca, and Al/Ca of *G. bulloides* (black), *N. pachyderma* (purple) and *N. incompta* (turquoise) vs. core depth of SO264-53. Threshold values of contamination of 0.1 mmol/mol (dotted lines), as proposed by (Barker et al., 2003), are exceeded in some core depths. There is no distinct correlation between high (low) contamination and high (low) Mg/Ca, thus, no Mg/Ca value needed to be removed due to contamination. One value of *N. incompta* was removed. A circle marks this sample with very low sample material.

4.6.4. Additional figures

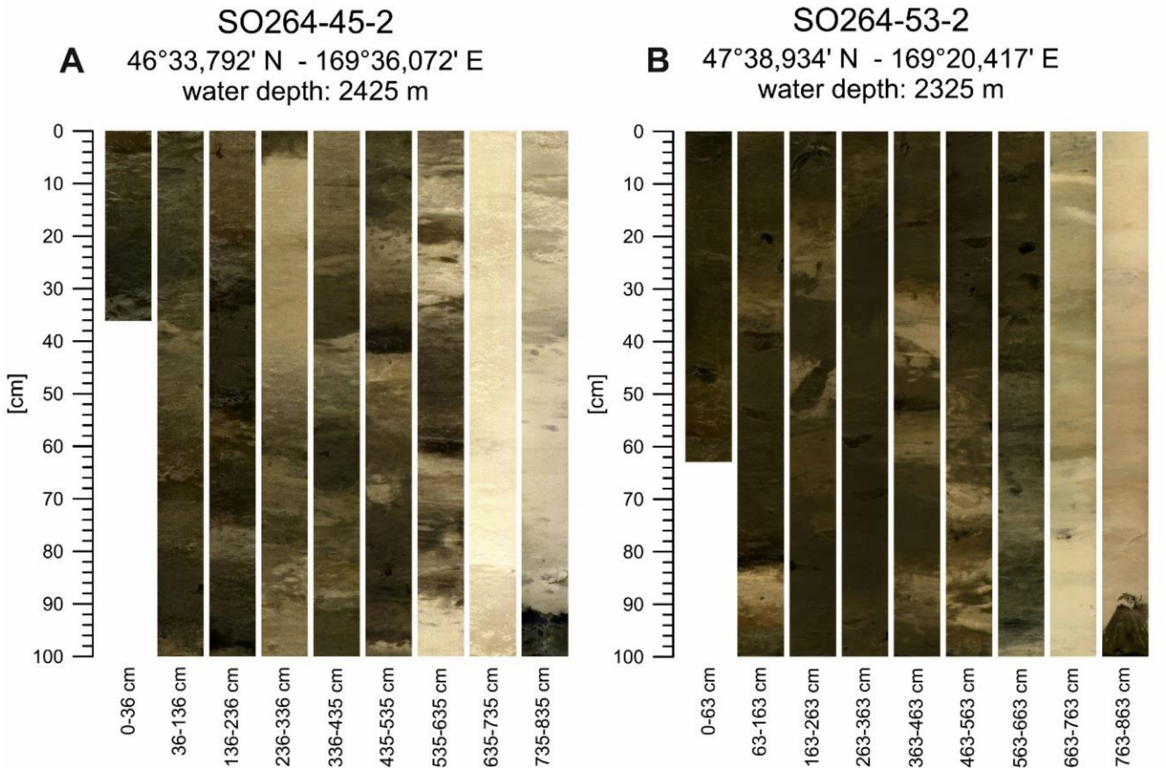

Supplementary Figure 4.14: Core pictures of SO264-45 and 53.

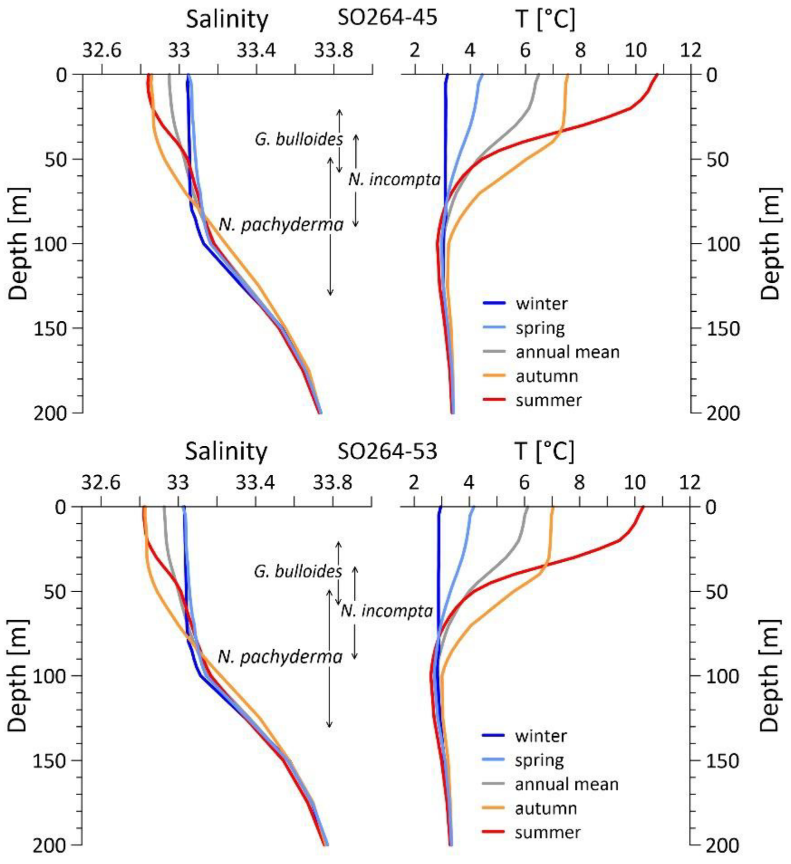

Figure 4.15: Seasonal and annual mean temperate (left) and salinity (right) profiles at 46°30’N 169°30’E (near site SO264-45; top) and at 47°50’N, 169°50’E (near site SO264-53; bottom) (Locarini et al., 2018). Black arrows indicate the main depth habitats of species.

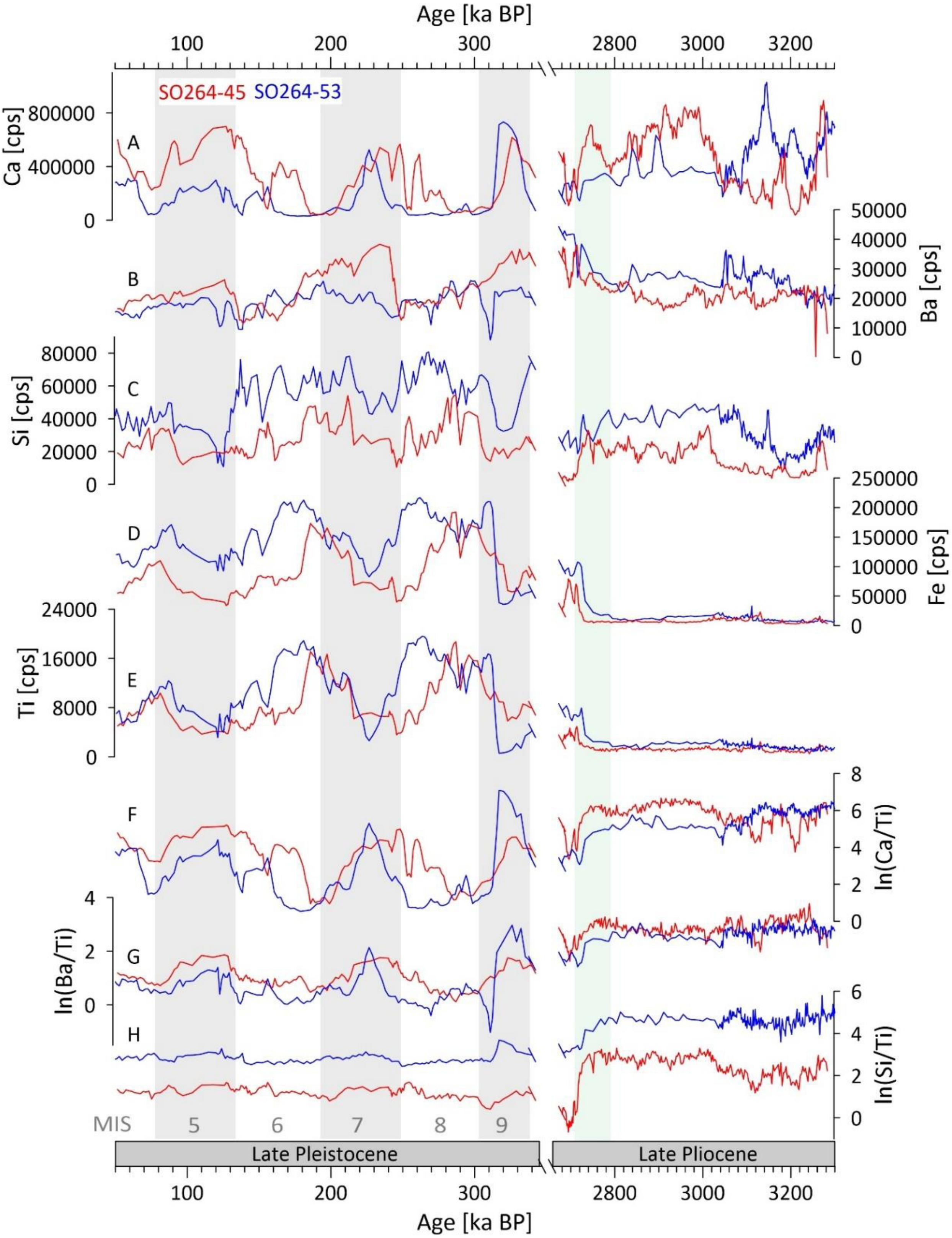

Figure 4.16: XRF-derived SO264-45 (red) and SO264-53 (blue) data. Gray shadings and numbers mark Marine Isotope Stages (MIS 9-4), while the green shading marks the time interval of the iNHG.

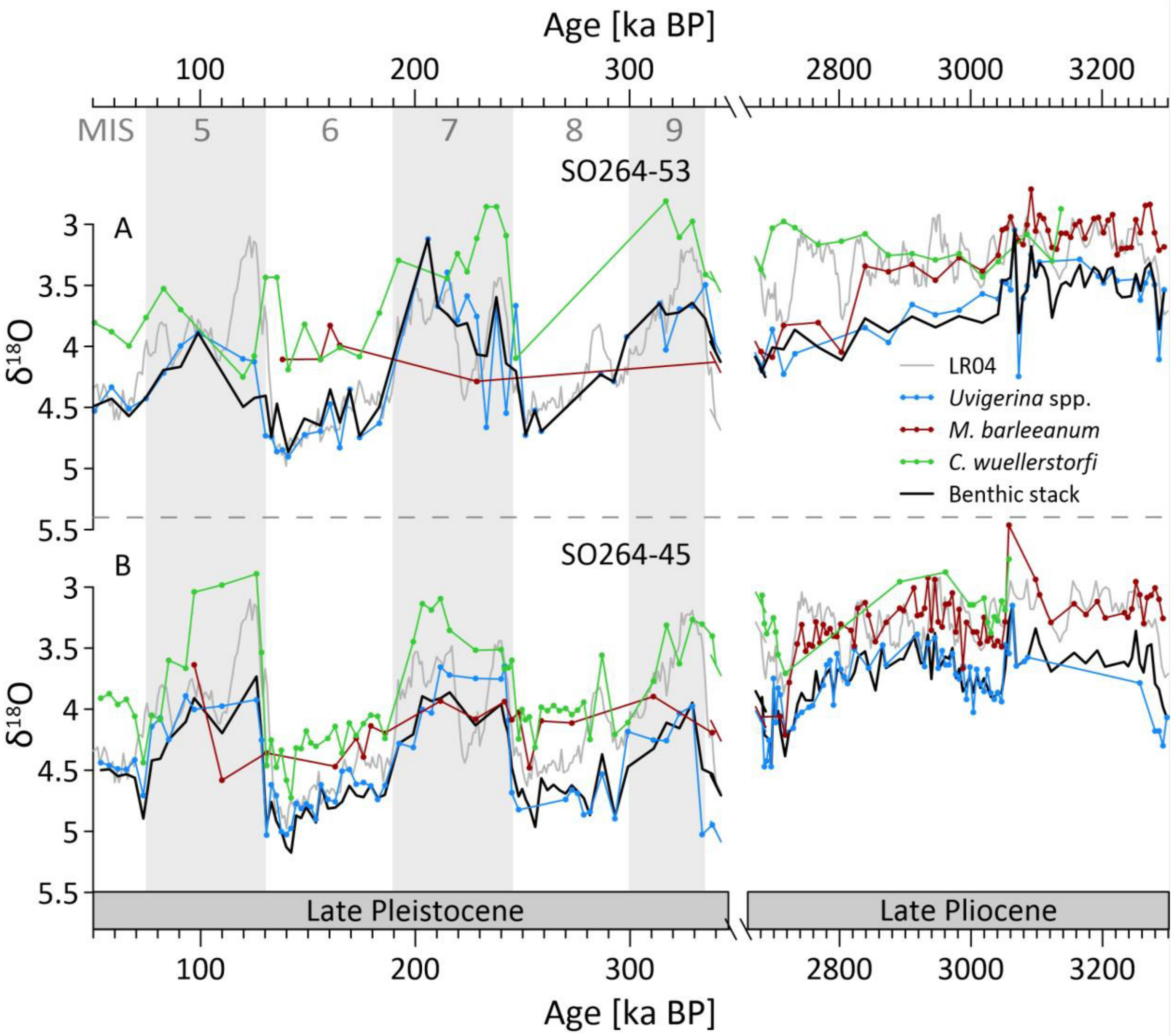

Figure 4.17: Stable oxygen isotope values ($\delta^{18}O$) of foraminiferal calcite from the benthic species *Uvigerina spp. (blue), M. barleeanum (red), and C. wuellerstorfi* (green) and the derived benthic stack (black) of SO264-45 (A) and SO264-53 (B) in comparison to the benthic isotope stack LR04 (Lisiecki and Raymo, 2005). The Gray shadings and numbers mark Marine Isotope Stages (MIS 9-4).

4.6.4. Data availability

The data presented in this chapter is available online at the Data Publisher for Earth and Environmental Science, PANGEA:

- Foraminiferal data of core SO264-45 0-650 ka
  https://doi.org/10.1594/PANGAEA.949795

- XRF data of core SO264-45 0-650 ka
  https://doi.org/10.1594/PANGAEA.949771

- Foraminiferal data of core SO264-45 from sediment depth 6.03-8.32 m
  https://doi.pangaea.de/10.1594/PANGAEA.962997

- XRF data of core SO264-45 from sediment depth 6.03-8.32 m
  https://doi.pangaea.de/10.1594/PANGAEA.963180

- Foraminiferal data of core SO264-53 from sediment depth 0.16-1.56 m and 6.48-8.47 m
  https://doi.pangaea.de/10.1594/PANGAEA.962998

- XRF data of core SO264-53 from sediment depth 0.16-1.56 m and 6.48-8.47 m
  https://doi.pangaea.de/10.1594/PANGAEA.963116

4.7. References

Abell, J. T., Winckler, G., Anderson, R. F., and Herbert, T. D. (2021). Poleward and weakened westerlies during Pliocene warmth. *Nature* 589, 70–75. doi: 10.1038/s41586-020-03062-1.

Ayers, J. M., and Lozier, M. S. (2012). Unraveling dynamical controls on the North Pacific carbon sink. *J. Geophys. Res. Ocean.* 117, 1–20. doi: 10.1029/2011JC007368.

Barker, S., Greaves, M., and Elderfield, H. (2003). A study of cleaning procedures used for foraminiferal Mg/Ca paleothermometry. *Geochemistry, Geophys. Geosystems* 4, 1–20. doi: 10.1029/2003GC000559.

Bemis, B. E., Spero, H. J., Bijma, J., and Lea, D. W. (1998). Reevaluation of the oxygen isotopic composition of planktonic foraminifera: Experimental results and revised paleotemperature equations. *Paleoceanography* 13, 150–160. doi: 10.1029/98PA00070.

Bereiter, B., Eggleston, S., Schmitt, J., Nehrbass-Ahles, C., Stocker, T. F., Fischer, H., et al. (2014). Revision of the EPICA Dome C CO2 record from 800 to 600-kyr before present. *Geophys. Res. Lett.* 42, 542–549. doi: 10.1002/2014GL061957.

Boyle, E. A., and Keigwin, L. D. (1985). Comparison of Atlantic and Pacific paleochemical records for the last 215,000 years: changes in deep ocean circulation and chemical inventories. *Earth Planet. Sci. Lett.* 76, 135–150. doi: 10.1016/0012-821X(85)90154-2.

Boyle, E., and Rosenthal, Y. (1996). Chemical Hydrography of the South Atlantic During the Last Glacial Maximum: Cd vs. δ13C. *South Atl.*, 423–443. doi: 10.1007/978-3-642-80353-6_23.

Brierley, C. M., Fedorov, A. V., Liu, Z., Herbert, T. D., Lawrence, K. T., and LaRiviere, J. P. (2009). Greatly expanded tropical warm pool and weakened Hadley circulation in the early Pliocene. *Science (80-.).* 323, 1714–1718. doi: 10.1126/science.1167625.

Brunelle, B. G., Sigman, D. M., Cook, M. S., Keigwin, L. D., Haug, G. H., Plessen, B., et al. (2007). Evidence from diatom-bound nitrogen isotopes for subarctic Pacific stratification during the last ice age and a link to North Pacific denitrification changes. *Paleoceanography* 22, 1–17. doi: 10.1029/2005PA001205.

Chalk, T. B., Hain, M. P., Foster, G. L., Rohling, E. J., Sexton, P. F., Badger, M. P. S., et al. (2017). Causes of ice age intensification across the mid-Pleistocene transition. *Proc. Natl. Acad. Sci. U. S. A.* 114, 13114–13119. doi: 10.1073/pnas.1702143114.

Chiu, T. C., and Broecker, W. S. (2008). Toward better paleocarbonate ion reconstructions: New insights regarding the CaCO3 size index. *Paleoceanography* 23, 1–7. doi: 10.1029/2008PA001599.

Cléroux, C., Cortijo, E., Anand, P., Labeyrie, L., Bassinot, F., Caillon, N., et al. (2008). Mg/Ca and Sr/Ca ratios in planktonic foraminifera: Proxies for upper water column temperature reconstruction. *Paleoceanography* 23, 1–16. doi: 10.1029/2007PA001505.

Cortese, G., Gersonde, R., Hillenbrand, C. D., and Kuhn, G. (2004). Opal sedimentation shifts in the World Ocean over the last 15 Myr. *Earth Planet. Sci. Lett.* 224, 509–527. doi: 10.1016/j.epsl.2004.05.035.

Costa, K. M., McManus, J. F., and Anderson, R. F. (2018). Paleoproductivity and Stratification Across the Subarctic Pacific Over Glacial-Interglacial Cycles. *Paleoceanogr. Paleoclimatology* 33, 914–933. doi: 10.1029/2018PA003363.

Croudace, I. W., and Rothwell, R. G. (2015). *Micro-XRF Studies of Sediment Cores*. Spinger doi: 10.1007/978-94-017-9849-5.

Darling, K. F., Kucera, M., Kroon, D., and Wade, C. M. (2006). A resolution for the coiling direction paradox in Neogloboquadrina pachyderma. *Paleoceanography* 21, 1–14. doi: 10.1029/2005PA001189.

Davis, C. V., Fehrenbacher, J. S., Hill, T. M., Russell, A. D., and Spero, H. J. (2017). Relationships Between Temperature, pH, and Crusting on Mg/Ca Ratios in Laboratory-Grown Neogloboquadrina Foraminifera. *Paleoceanography* 32, 1137–1152. doi: 10.1002/2017PA003111.

De Boer, B., Lourens, L. J., and Van De Wal, R. S. W. (2014). Persistent 400,000-year variability of Antarctic ice volume and the carbon cycle is revealed throughout the Plio-Pleistocene. *Nat. Commun.* 5, 1–8. doi: 10.1038/ncomms3999.

de la Vega, E., Chalk, T. B., Wilson, P. A., Bysani, R. P., and Foster, G. L. (2020). Atmospheric CO2 during the Mid-Piacenzian Warm Period and the M2 glaciation. *Sci. Rep.* 10, 14–21. doi: 10.1038/s41598-020-67154-8.

Dumitru, O. A., Austermann, J., Polyak, V. J., Fornós, J. J., Asmerom, Y., Ginés, J., et al. (2019). Constraints on global mean sea level during Pliocene warmth. *Nature* 574, 233–236. doi: 10.1038/s41586-019-1543-2.

Dutton, A., Carlson, A. E., Long, A. J., Milne, G. A., Clark, P. U., DeConto, R., et al. (2015). Sea-level rise due to polar ice-sheet mass loss during past warm periods. *Science (80-.).* 349. doi: 10.1126/science.aaa4019.

Eagle, M., Paytan, A., Arrigo, K. R., van Dijken, G., and Murray, R. W. (2003). A comparison between excess barium and barite as indicators of carbon export. *Paleoceanography* 18. doi: 10.1029/2002pa000793.

Elderfield, H., and Ganssen, G. (2000). Past temperature and δ18O of surface ocean waters inferred from foraminiferal Mg/Ca ratios. *Nature* 405, 442–445. doi: 10.1038/35013033.

Emelyanov (2005). Calcium Carbonate Compensation Depth (CCD). *Barrier Zo. Ocean*, 345–361. doi: 10.1007/3-540-26230-x_20.

Favorite, F. (1976). Oceanography of the subarctic Pacific region, 1960-71. *Bull Int North Pac Fish Comm* 33, 1–187. Available at: http://ci.nii.ac.jp/naid/10015636766/.

Fontanier, C., MacKensen, A., Jorissen, F. J., Anschutz, P., Licari, L., and Griveaud, C. (2006). Stable oxygen and carbon isotopes of live benthic foraminifera from the Bay of

Biscay: Microhabitat impact and seasonal variability. *Mar. Micropaleontol.* 58, 159–183. doi: 10.1016/j.marmicro.2005.09.004.

Galbraith, E. D., Jaccard, S. L., Pedersen, T. F., Sigman, D. M., Haug, G. H., Cook, M., et al. (2007). Carbon dioxide release from the North Pacific abyss during the last deglaciation. *Nature* 449, 890–893. doi: 10.1038/nature06227.

Galbraith, E. D., Kienast, M., Jaccard, S. L., Pedersen, T. F., Brunelle, B. D., Sigman, D. M., et al. (2008). Consistent relationship between global climate and surface nitrate utilization in the western subarctic Pacific throughout the last 500 ka. *Paleoceanography* 23, 1–11. doi: 10.1029/2007PA001518.

Gallagher, S. J., Kitamura, A., Iryu, Y., Itaki, T., Koizumi, I., and Hoiles, P. W. (2015). The Pliocene to recent history of the Kuroshio and Tsushima Currents: a multi-proxy approach. *Prog. Earth Planet. Sci.* 2, 1–23. doi: 10.1186/s40645-015-0045-6.

Garcia, H., Weathers, K. W., Paver, C. R., Smolyar, I., Boyer, T. P., Locarnini, R. A., et al. (2018). World Ocean Atlas 2018. Volume 4: Dissolved Inorganic Nutrients (phosphate, nitrate and nitrate+nitrite, silicate). *NOAA Atlas NESDIS 84* 84, 35.

Gargett, A. E. (1991). Physical processes and the maintenance of nutrient-rich euphotic zones. *Limnol. Oceanogr.* 36, 1527–1545. doi: 10.4319/lo.1991.36.8.1527.

Gebhardt, H., Sarnthein, M., Grootes, P. M., Kiefer, T., Kuehn, H., Schmieder, F., et al. (2008). Paleonutrient and productivity records from the subarctic North Pacific for Pleistocene glacial terminations I to V. *Paleoceanography* 23, 1–21. doi: 10.1029/2007PA001513.

Gorbarenko, Southon, J. R., Keigwin, L. D., Cherepanova, M. V., and Gvozdeva, I. G. (2004). Late Pleistocene-Holocene oceanographic variability in the Okhotsk Sea: Geochemical, lithological and paleontological evidence. *Palaeogeogr. Palaeoclimatol. Palaeoecol.* 209, 281–301. doi: 10.1016/j.palaeo.2004.02.013.

Gottschalk, J., Hodell, D. A., Skinner, L. C., Crowhurst, S. J., Jaccard, S. L., and Charles, C. (2018). Past Carbonate Preservation Events in the Deep Southeast Atlantic Ocean (Cape Basin) and Their Implications for Atlantic Overturning Dynamics and Marine Carbon Cycling. *Paleoceanogr. Paleoclimatology* 33, 643–663. doi: 10.1029/2018PA003353.

Gray, W. R., and Evans, D. (2019). Nonthermal Influences on Mg/Ca in Planktonic Foraminifera: A Review of Culture Studies and Application to the Last Glacial Maximum. *Paleoceanogr. Paleoclimatology* 34, 306–315. doi: 10.1029/2018PA003517.

Gray, W. R., Wills, R. C. J., Rae, J. W. B., Burke, A., Ivanovic, R. F., Roberts, W. H. G., et al. (2020). Wind-Driven Evolution of the North Pacific Subpolar Gyre Over the Last Deglaciation. *Geophys. Res. Lett.* 47, 1–12. doi: 10.1029/2019GL086328.

Greaves, M., Caillon, N., Rebaubier, H., Bartoli, G., Bohaty, S., Cacho, I., et al. (2008). Interlaboratory comparison study of calibration standards for foraminiferal Mg/Ca thermometry. *Geochemistry, Geophys. Geosystems* 9, 1–27. doi: 10.1029/2008GC001974.

Harada, N., Ahagon, N., Uchida, M., and Murayama, M. (2004). Northward and southward migrations of frontal zones during the past 40 kyr in the Kuroshio-Oyashio transition area. *Geochemistry, Geophys. Geosystems* 5, 1–16. doi: 10.1029/2004GC000740.

Haug, G. H., Ganopolski, A., Sigman, D. M., Rosell-Mele, A., Swann, G. E. A., Tiedemann, R., et al. (2005). North Pacific seasonality and the glaciation of North America 2.7 million years ago. *Nature* 433, 821–825. doi: 10.1038/nature03332.

Haug, G. H., Sigman, D. M., Tiedemann, R., Pedersen, T. F., and Sarnthein, M. (1999). Onset of permanent stratification in the subarctic Pacific Ocean. *Nature* 401, 779–782. doi: 779–782 (1999).

Helmke, J. P., Bauch, H. A., Röhl, U., and Kandiano, E. S. (2008). Uniform climate development between the subtropical and subpolar Northeast Atlantic across marine isotope stage 11. *Clim. Past* 4, 181–190. doi: 10.5194/cp-4-181-2008.

Herbert, T. D., Peterson, L. C., Lawrence, K. T., and Liu, Z. (2010). Tropical ocean temperatures over the past 3.5 million years. *Science (80-.).* 328, 1530–1534. doi: 10.1126/science.1185435.

Hillenbrand, C. D., and Cortese, G. (2006). Polar stratification: A critical view from the Southern Ocean. *Palaeogeogr. Palaeoclimatol. Palaeoecol.* 242, 240–252. doi: 10.1016/j.palaeo.2006.06.001.

Huang, R. X. (2015). *Oceanographic Topics: Surface/Wind Driven Circulation*. Second Edi. Elsevier doi: 10.1016/B978-0-12-382225-3.00280-2.

Isoguchi, O., Kawamura, H., and Oka, E. (2006). Quasi-stationary jets transporting surface warm waters across the transition zone between the subtropical and the subarctic gyres in the North Pacific. *J. Geophys. Res. Ocean.* 111, 1–17. doi: 10.1029/2005JC003402.

Iwasaki, S., Kimoto, K., Kuroyanagi, A., and Kawahata, H. (2017). Horizontal and vertical distributions of planktic foraminifera in the subarctic Pacific. *Mar. Micropaleontol.* 130, 1–14. doi: 10.1016/j.marmicro.2016.12.001.

Iwasaki, S., Takahashi, K., Kanematsu, Y., and Asahi, H. (2016). Deep-Sea Research II Paleoproductivity and paleoceanography of the last 4 . 3 Myrs at IODP Expedition 323 Site U1341 in the Bering Sea based on biogenic opal content. *Deep. Res. Part II* 125–126, 145–154. doi: 10.1016/j.dsr2.2015.04.005.

Jaccard, S. L., Galbraith, E. D., Sigman, D. M., and Haug, G. H. (2010). A pervasive link between Antarctic ice core and subarctic Pacific sediment records over the past 800 kyrs. *Quat. Sci. Rev.* 29, 206–212. doi: 10.1016/j.quascirev.2009.10.007.

Jaccard, S. L., Haug, G. H., Sigman, D. M., Pedersen, T. F., Thierstein, H. R., and Röhl, U. (2005). Glacial/interglacial changes in subarctic North Pacific stratification. *Science (80-.).* 308, 1003–1006. doi: 10.1126/science.1108696.

Jahn, B., Donner, B., Müller, P. J., Röhl, U., Schneider, R. R., and Wefer, G. (2003). Pleistocene variations in dust input and marine productivity in the northern Benguela

Current: Evidence of evolution of global glacial-interglacial cycles. *Palaeogeogr. Palaeoclimatol. Palaeoecol.* 193, 515–533. doi: 10.1016/S0031-0182(03)00264-5.

Jahn, Schneider, R. R., Müller, P. J., Donner, B., and Röhl, U. (2005). Response of tropical African and East Atlantic climates to orbital forcing over the last 1.7 Ma. *Geol. Soc. Spec. Publ.* 247, 65–84. doi: 10.1144/GSL.SP.2005.247.01.04.

Janecek, T. R. (2000). Data report: Late Neogene biogenic opal data for Leg 167 sites of the California margin. *Proc. Ocean Drill. Progr. Sci. Results* 167, 213–214. doi: 10.2973/odp.proc.sr.167.243.2000.

Jonkers, L., Jiménez-Amat, P., Mortyn, P. G., and Brummer, G. J. A. (2013). Seasonal Mg/Ca variability of N. pachyderma (s) and G. bulloides: Implications for seawater temperature reconstruction. *Earth Planet. Sci. Lett.* 376, 137–144. doi: 10.1016/j.epsl.2013.06.019.

Kaiser, J., Schefuß, E., Lamy, F., Mohtadi, M., and Hebbeln, D. (2008). Glacial to Holocene changes in sea surface temperature and coastal vegetation in north central Chile: high versus low latitude forcing. *Quat. Sci. Rev.* 27, 2064–2075. doi: 10.1016/j.quascirev.2008.08.025.

Kawahata, H., and Ohshima, H. (2002). Small latitudinal shift in the Kuroshio Extension (Central Pacific) during glacial times: Evidence from pollen transport. *Quat. Sci. Rev.* 21, 1705–1717. doi: 10.1016/S0277-3791(01)00150-0.

Kawahata, H., Okamoto, T., Matsumoto, E., and Ujiie, H. (2000). Fluctuations of eolian flux and ocean productivity in the mid-latitude North Pacific during the last 200 kyr. *Quat. Sci. Rev.* 19, 1279–1291. doi: 10.1016/S0277-3791(99)00096-7.

Kienast, S. S., Hendy, I. L., Crusius, J., Pedersen, T. F., and Calvert, S. E. (2004). Export production in the subarctic North Pacific over the last 800 kyrs: No evidence for iron fertilization? *J. Oceanogr.* 60, 189–203. doi: 10.1023/B:JOCE.0000038326.73943.aa.

Korff, L., von Dobeneck, T., Frederichs, T., Kasten, S., Kuhn, G., Gersonde, R., et al. (2016). Cyclic magnetite dissolution in Pleistocene sediments of the abyssal northwest Pacific Ocean: Evidence for glacial oxygen depletion and carbon trapping. *Paleoceanography* 31, 600–624. doi: 10.1002/2015PA002882.

Kotov, S., Paelike, H., Kotov, S., and Paelike, H. (2018). QAnalySeries - a cross-platform time series tuning and analysis tool. *AGUFM* 2018, PP53D-1230. Available at: https://ui.adsabs.harvard.edu/abs/2018AGUFMPP53D1230K/abstract [Accessed April 12, 2021].

Kozdon, R., Eisenhauer, A., Weinelt, M., Meland, M. Y., and Nürnberg, D. (2009). Reassessing Mg/Ca temperature calibrations of Neogloboquadrina pachyderma (sinistral) using paired δ44/40Ca and Mg/Ca measurements. *Geochemistry, Geophys. Geosystems* 10, 1–14. doi: 10.1029/2008GC002169.

Kretschmer, K., Jonkers, L., Kucera, M., and Schulz, M. (2018). Modeling seasonal and vertical habitats of planktonic foraminifera on a global scale. *Biogeosciences* 15, 4405–4429. doi: 10.5194/bg-15-4405-2018.

Kuroyanagi, A., and Kawahata, H. (2004). Vertical distribution of living planktonic foraminifera in the seas around Japan. *Mar. Micropaleontol.* 53, 173–196. doi: 10.1016/j.marmicro.2004.06.001.

Kuroyanagi, A., Kawahata, H., Nishi, H., and Honda, M. C. (2008). Seasonal to interannual changes in planktonic foraminiferal assemblages in the northwestern North Pacific: Sediment trap results encompassing a warm period related to El Niño. *Palaeogeogr. Palaeoclimatol. Palaeoecol.* 262, 107–127. doi: 10.1016/j.palaeo.2008.02.012.

Labeyrie, L., Leclaire, H., Waelbroeck, C., Cortijo, E., Duplessy, J. C., Vidal, L., et al. (1999). Temporal variability of the surface and deep waters of the northwest atlantic ocean at orbital and millennial scales. *Geophys. Monogr. Ser.* 112, 77–98. doi: 10.1029/GM112p0077.

Lamy, F., Gersonde, R., Winckler, G., Esper, O., Jaeschke, A., Kuhn, G., et al. (2014). Increased dust deposition in the Pacific Southern Ocean during glacial periods. *Science (80-.).* 343, 403–407. doi: 10.1126/science.1245424.

Lariviere, J. P., Ravelo, A. C., Crimmins, A., Dekens, P. S., Ford, H. L., Lyle, M., et al. (2012). Late Miocene decoupling of oceanic warmth and atmospheric carbon dioxide forcing. *Nature* 486, 97–100. doi: 10.1038/nature11200.

Lawrence, K. T., Herbert, T. D., Brown, C. M., Raymo, M. E., and Haywood, A. M. (2009). High-amplitude variations in North Atlantic sea surface temperature during the early Pliocene warm period. 24, 1–15. doi: 10.1029/2008PA001669.

Lawrence, K. T., Liu, Z., and Herbert, T. D. (2006). Evolution of the eastern tropical Pacific through Plio-Pleistocene glaciation. *Science (80-.).* 312, 79–83. doi: 10.1126/science.1120395.

Lawrence, K. T., Sigman, D. M., Herbert, T. D., Riihimaki, C. A., Bolton, C. T., Martinez-Garcia, A., et al. (2013). Time-transgressive North Atlantic productivity changes upon Northern Hemisphere glaciation. *Paleoceanography* 28, 740–751. doi: 10.1002/2013PA002546.

Lea, D. W., Mashiotta, T. A., and Spero, H. J. (1999). Controls on magnesium and strontium uptake in planktonic foraminifera determined by live culturing. *Geochim. Cosmochim. Acta* 63, 2369–2379. doi: 10.1016/S0016-7037(99)00197-0.

Li, X., Jiang, D., Zhang, Z., Zhang, R., Tian, Z., and Yan, Q. (2015). Mid-Pliocene westerlies from PlioMIP simulations. *Adv. Atmos. Sci.* 32, 909–923. doi: 10.1007/s00376-014-4171-7.

Lisiecki, L. E., and Raymo, M. E. (2005). A Pliocene-Pleistocene stack of 57 globally distributed benthic δ 18O records. *Paleoceanography* 20, 1–17. doi: 10.1029/2004PA001071.

Liu, Z., Altabet, M. A., and Herbert, T. D. (2008). Plio-Pleistocene denitrification in the eastern tropical North Pacific: Intensification at 2.1 Ma. *Geochemistry, Geophys. Geosystems* 9. doi: 10.1029/2008GC002044.

Locarnini, R. A., Mishonov, A. V., Baranova, O. K., Boyer, T. P., Zweng, M. M., Garcia, H. E., et al. (2018). World Ocean Atlas 2018, Volume 1: Temperature. A. Mishonov, Technical Editor. *NOAA Atlas NESDIS* 1, 52pp.

Mahowald, N. M., Muhs, D. R., Levis, S., Rasch, P. J., Yoshioka, M., Zender, C. S., et al. (2006). Change in atmospheric mineral aerosols in response to climate: Last glacial period, preindustrial, modern, and doubled carbon dioxide climates. *J. Geophys. Res. Atmos.* 111. doi: 10.1029/2005JD006653.

Malevich, S. B., Vetter, L., and Tierney, J. E. (2019). Global Core Top Calibration of δ18O in Planktic Foraminifera to Sea Surface Temperature. *Paleoceanogr. Paleoclimatology* 34, 1292–1315. doi: 10.1029/2019PA003576.

Martínez-Garcia, A., Rosell-Melé, A., Jaccard, S. L., Geibert, W., Sigman, D. M., and Haug, G. H. (2011). Southern Ocean dust-climate coupling over the past four million years. *Nature* 476, 312–315. doi: 10.1038/nature10310.

Martínez-Garcia, A., Rosell-Melé, A., McClymont, E. L., Gersonde, R., and Haug, G. H. (2010). Subpolar link to the emergence of the modern equatorial pacific cold tongue. *Science (80-.).* 328, 1550–1553. doi: 10.1126/science.1184480.

März, C., Schnetger, B., and Brumsack, H. J. (2013). Nutrient leakage from the North Pacific to the Bering Sea (IODP site U1341) following the onset of Northern Hemispheric Glaciation? *Paleoceanography* 28, 68–78. doi: 10.1002/palo.20011.

Mashiotta, T. A., Lea, D. W., and Spero, H. J. (1999). Glacial-interglacial changes in Subantarctic sea surface temperature and δ18O-water using foraminiferal Mg. *Earth Planet. Sci. Lett.* 170, 417–432. doi: 10.1016/S0012-821X(99)00116-8.

Maslin, M. A., Haug, G. H., Sarnthein, M., Tiedemann, R., Erlenkeuser, H., and Stax, R. (1995). “Northwest Pacific Site 882: The Initiation of Northern Hemisphere Glaciation,” in *Proceedings of the Ocean Drilling Program, 145 Scientific Results* doi: 10.2973/odp.proc.sr.145.119.1995.

Matsumoto, K., Oba, T., Lynch-Stieglitz, J., and Yamamoto, H. (2002). Interior hydrography and circulation of the glacial Pacific Ocean. *Quat. Sci. Rev.* 21, 1693–1704. doi: 10.1016/S0277-3791(01)00142-1.

McGee, D., Broecker, W. S., and Winckler, G. (2010). Gustiness: The driver of glacial dustiness? *Quat. Sci. Rev.* 29, 2340–2350. doi: 10.1016/j.quascirev.2010.06.009.

Mitnik, L. M., Khazanova, E. S., and Dubina, V. A. (2020). Mesoscale and synoptic scale dynamic phenomena in the Oyashio current region observed in SAR imagery. *Int. J. Remote Sens.* 41, 5861–5883. doi: 10.1080/01431161.2019.1701215.

Mohtadi, M., Romero, O. E., Kaiser, J., and Hebbeln, D. (2007). Cooling of the southern high latitudes during the Medieval Period and its effect on ENSO. *Quat. Sci. Rev.* 26, 1055–1066. doi: 10.1016/j.quascirev.2006.12.008.

Morley, A., Babila, T. L., Wright, J., Ninnemann, U., Kleiven, K., Irvali, N., et al. (2017).

Environmental Controls on Mg/Ca in Neogloboquadrina incompta: A Core-Top Study From the Subpolar North Atlantic. *Geochemistry, Geophys. Geosystems* 18, 4276–4298. doi: 10.1002/2017GC007111.

Mudelsee, M., and Raymo, M. E. (2005). Slow dynamics of the Northern Hemisphere glaciation. *Paleoceanography* 20. doi: 10.1029/2005PA001153.

Mulitza, S., Boltovskoy, D., Donner, B., Meggers, H., Paul, A., and Wefer, G. (2003). Temperature: δ18O relationships of planktonic foraminifera collected from surface waters. *Palaeogeogr. Palaeoclimatol. Palaeoecol.* 202, 143–152. doi: 10.1016/S0031-0182(03)00633-3.

Naafs, B. D. A., Hefter, J., Acton, G., Haug, G. H., Martínez-Garcia, A., Pancost, R., et al. (2012). Strengthening of North American dust sources during the late Pliocene (2.7Ma). *Earth Planet. Sci. Lett.* 317–318, 8–19. doi: 10.1016/j.epsl.2011.11.026.

Narita, H., Sato, M., Tsunogai, S., Murayama, M., Ikehara, M., Nakatsuka, T., et al. (2002). Biogenic opal indicating less productive northwestern North Pacific during the glacial ages. *Geophys. Res. Lett.* 29, 2–5. doi: 10.1029/2001GL014320.

Nishioka, J., Ono, T., Saito, H., Sakaoka, K., and Yoshimura, T. (2011). Oceanic iron supply mechanisms which support the spring diatom bloom in the Oyashio region, western subarctic Pacific. *J. Geophys. Res. Ocean.* 116, 1–17. doi: 10.1029/2010JC006321.

Nürnberg (2018). RV SONNE Fahrtbericht/Cruise Report SO264 - SONNE-EMPEROR: The Plio/Pleistocene to Holocene development of the pelagic North Pacific from surface to depth – assessing its role for the global carbon budget and Earth´s climate, Suva (Fiji) – Yokohama (Japa. *GEOMAR Report, N. Ser. 046 . GEOMAR Helmholtz-Zentrum für Ozeanforschung, Kiel, Ger.*, 1–284. doi: 10.3289/GEOMAR_REP_NS_46_2018.

Nürnberg, D. (1995). Magnesium in tests of Neogloboquadrina pachyderma sinistral from high northern and southern latitudes. *J. Foraminifer. Res.* 25, 350–368. doi: 10.2113/gsjfr.25.4.350.

Nürnberg, D. (2000). Taking the temperature of past ocean surfaces. *Science (80-.).* 289, 1698–1699. doi: 10.1126/science.289.5485.1698.

Nürnberg, D., Bijma, J., and Hemleben, C. (1996). Assessing the reliability of magnesium in foraminiferal calcite as a proxy for water mass temperatures. *Geochim. Cosmochim. Acta* 60, 803–814. doi: 10.1016/0016-7037(95)00446-7.

Nürnberg, D., and Tiedemann, R. (2004). Environmental change in the Sea of Okhotsk during the last 1.1 million years. *Paleoceanography* 19, 1–23. doi: 10.1029/2004PA001023.

Ogawa, K., Usui, T., Takatani, S., Kitao, T., Harimoto, T., Katoh, S., et al. (2006). Shipboard measurements of atmospheric and surface seawater pCO 2 in the North Pacific carried out from January 1999 to October 2000 on the voluntary observation ship MS Alligator Liberty. *Pap. Meteorol. Geophys.* 57, 37–46. doi: 10.2467/mripapers.57.37.

Pérez, M. E., Lin, H.-L., Lange, C. B., and Schneider, R. (2001). Pliocene–Pleistocene opal records off southwest Africa, Sites 1082 and 1084: a comparison of analytical techniques. *Proc. Ocean Drill. Program, 175 Sci. Results*. doi: 10.2973/odp.proc.sr.175.221.2001.

Qiu, B. (2002). The Kuroshio Extension system: Its large-scale variability and role in the midlatitude ocean-atmosphere interaction. *J. Oceanogr.* 58, 57–75. doi: 10.1023/A:1015824717293.

Qiu, B. (2019). *Kuroshio and oyashio currents. In: Cochran SJK, Bokuniewicz HJ, Yager PL (eds) Encyclopedia of Ocean Sciences*. 3rd ed. London: Elsevier Ltd. doi: 10.1016/B978-0-12-409548-9.11295-3.

Regenberg, M., Nürnberg, D., Steph, S., Groeneveld, J., Garbe-Schönberg, D., Tiedemann, R., et al. (2006). Assessing the effect of dissolution on planktonic foraminiferal Mg/Ca ratios: Evidence from Caribbean core tops. *Geochemistry, Geophys. Geosystems* 7. doi: 10.1029/2005GC001019.

Reynolds, L. A., and Thunell, R. C. (1986). Seasonal Production and Morphologic Variation of Neogloboquadrina pachyderma (Ehrenberg) in the Northeast Pacific. *Micropaleontology* 32, 1. doi: 10.2307/1485696.

Riethdorf, J. R., Max, L., Nürnberg, D., Lembke-Jene, L., and Tiedemann, R. (2013). Deglacial development of (sub) sea surface temperature and salinity in the subarctic northwest Pacific: Implications for upper-ocean stratification. *Paleoceanography* 28, 91–104. doi: 10.1002/palo.20014.

Sagawa, T., Kuroyanagi, A., Irino, T., Kuwae, M., and Kawahata, H. (2013). Seasonal variations in planktonic foraminiferal flux and oxygen isotopic composition in the western North Pacific: Implications for paleoceanographic reconstruction. *Mar. Micropaleontol.* 100, 11–20. doi: 10.1016/j.marmicro.2013.03.013.

Sánchez-Montes, M. L., McClymont, E. L., Lloyd, J. M., Müller, J., Cowan, E. A., and Zorzi, C. (2020). Late Pliocene Cordilleran Ice Sheet development with warm northeast Pacific sea surface temperatures. *Clim. Past* 16, 299–313. doi: 10.5194/cp-16-299-2020.

Sarnthein, M., Gebhardt, H., Kiefer, T., Kucera, M., Cook, M., and Erlenkeuser, H. (2004). Mid Holocene origin of the sea-surface salinity low in the subarctic North Pacific. *Quat. Sci. Rev.* 23, 2089–2099. doi: 10.1016/j.quascirev.2004.08.008.

Schiebel, R., and Hemleben, C. (2017). Planktic foraminifers in the modern ocean. *Planktic Foraminifers Mod. Ocean*, 1–358. doi: 10.1007/978-3-662-50297-6.

Schiebel, R., Spielhagen, R. F., Garnier, J., Hagemann, J., Howa, H., Jentzen, A., et al. (2017). Modern planktic foraminifers in the high-latitude ocean. *Mar. Micropaleontol.* 136, 1–13. doi: 10.1016/j.marmicro.2017.08.004.

Schlitzer, R., and Ocean Data View (2019). Ocean Data View. *Https://Odv.Awi.De*.

Science, P. (2003). Hydrographic Structure and Variability in the Kuroshio- Oyashio Transition Area. *J. Oceanogr.* 59, 389–402.

Shackleton, N. J. (1974). Attainment of isotopic equilibrium between ocean water and the benthonic foraminifera geuns *Uvigerina*: Isotopic changes in the ocean during the last glacial. *Colloq. Int. du C.N.R.S.* 219, 203–210.

Shackleton, N. J., and Hall, M. A. (1984). Oxygen and carbon isotope stratigraphy of Deep Sea Drilling Project Hole 552A: Plio-Pleistocene glacial history. *Initial reports DSDP, Leg 81, Southampt. to Azores*, 599–609. doi: 10.2973/dsdp.proc.81.116.1984.

Shackleton, N. J., Hall, M. A., and Vincent, E. (2000). Phase relationships between millennial-scale events 64,000-24,000 years ago. *Paleoceanography* 15, 565–569. doi: 10.1029/2000PA000513.

Shackleton, N. J., and Opdyke, N. D. (1973). Oxygen isotope and palaeomagnetic stratigraphy of Equatorial Pacific core V28-238: Oxygen isotope temperatures and ice volumes on a 105 year and 106 year scale. *Quat. Res.* 3, 39–55. doi: 10.1016/0033-5894(73)90052-5.

Shaffer, G., and Lambert, F. (2018). In and out of glacial extremes by way of dust−climate feedbacks. *Proc. Natl. Acad. Sci. U. S. A.* 115, 2026–2031. doi: 10.1073/pnas.1708174115.

Shigemitsu, M., Narita, H., Watanabe, Y. W., Harada, N., and Tsunogai, S. (2007). Ba, Si, U, Al, Sc, La, Th, C and 13C/12C in a sediment core in the western subarctic Pacific as proxies of past biological production. *Mar. Chem.* 106, 442–455. doi: 10.1016/j.marchem.2007.04.004.

Shimizu, Y., Yasuda, I., and Ito, S. I. (2001). Distribution and circulation of the coastal Oyashio intrusion. *J. Phys. Oceanogr.* 31, 1561–1578. doi: 10.1175/1520-0485(2001)031<1561:DACOTC>2.0.CO;2.

Sigman, D. M., Fripiat, F., Studer, A. S., Kemeny, P. C., Martínez-García, A., Hain, M. P., et al. (2021). The Southern Ocean during the ice ages: A review of the Antarctic surface isolation hypothesis, with comparison to the North Pacific. *Quat. Sci. Rev.* 254. doi: 10.1016/j.quascirev.2020.106732.

Sigman, D. M., Jaccard, S. L., and Haug, G. H. (2004). Polar ocean stratification in a cold climate. *Nature* 428, 59–63. doi: 10.1038/nature02378.1.

Studer, A. S., Martínez-Garcia, A., Jaccard, S. L., Girault, F. E., Sigman, D. M., and Haug, G. H. (2012). Enhanced stratification and seasonality in the Subarctic Pacific upon Northern Hemisphere Glaciation-New evidence from diatom-bound nitrogen isotopes, alkenones and archaeal tetraethers. *Earth Planet. Sci. Lett.* 351–352, 84–94. doi: 10.1016/j.epsl.2012.07.029.

Sun, Y., and An, Z. (2005). Late Pliocene-Pleistocene changes in mass accumulation rates of eolian deposits on the central Chinese Loess Plateau. *J. Geophys. Res. Atmos.* 110, 1–8. doi: 10.1029/2005JD006064.

Takahashi, T., Sutherland, S. C., Wanninkhof, R., Sweeney, C., Feely, R. A., Chipman, D. W., et al. (2009). Climatological mean and decadal change in surface ocean pCO2, and net sea-air CO2 flux over the global oceans. *Deep. Res. Part II Top. Stud. Oceanogr.* 56, 554–577. doi: 10.1016/j.dsr2.2008.12.009.

Talley, L. D. (1995). Some advances in understanding of the general circulation of the Pacific Ocean, with emphasis on recent U.S. contributions. *Rev. Geophys.* 33, 1335–1352. doi: 10.1029/95RG00350.

Taylor, B. J., Rae, J. W. B., Gray, W. R., Darling, K. F., Burke, A., Gersonde, R., et al. (2018). Distribution and ecology of planktic foraminifera in the North Pacific: Implications for paleo-reconstructions. *Quat. Sci. Rev.* 191, 256–274. doi: 10.1016/j.quascirev.2018.05.006.

Thompson, P. R., and Shackleton, N. J. (1980). North Pacific palaeoceanography: Late quaternary coiling variations of planktonic foraminifer neogloboquadrina pachyderma. *Nature* 287, 829–833. doi: 10.1038/287829a0.

Thornalley, D. J. R., Elderfield, H., and McCave, I. N. (2009). Holocene oscillations in temperature and salinity of the surface subpolar North Atlantic. *Nature* 457, 711–714. doi: 10.1038/nature07717.

Tjallingii, R., Röhl, U., Kölling, M., and Bickert, T. (2007). Influence of the water content on X-ray fluorescence corescanning measurements in soft marine sediments. *Geochemistry, Geophys. Geosystems* 8, 1–12. doi: 10.1029/2006GC001393.

Toggweiler, J. R., Russell, J. L., and Carson, S. R. (2006). Midlatitude westerlies, atmospheric CO2, and climate change during the ice ages. *Paleoceanography* 21. doi: 10.1029/2005PA001154.

Tukey, J. W. (1977). *Exploratory Data Analysis.* Reading, MA: Addison-Wesley.

Vázquez Riveiros, N., Govin, A., Waelbroeck, C., Mackensen, A., Michel, E., Moreira, S., et al. (2016). Mg/Ca thermometry in planktic foraminifera: Improving paleotemperature estimations for G. bulloides and N. pachyderma left. *Geochemistry, Geophys. Geosystems*, 1249–1264. doi: 10.1002/2015GC006171.Received.

Waddell, L. M., Hendy, I. L., Moore, T. C., and Lyle, M. W. (2009). Ventilation of the abyssal Southern Ocean during the late Neogene: A new perspective from the subantarctic Pacific. *Paleoceanography* 24. doi: 10.1029/2008PA001661.

Wara, M. W., Ravelo, A. C., and Delaney, M. L. (2005). Climate change: Permanent El Niño-like conditions during the Pliocene warm period. *Science (80-.).* 309, 758–761. doi: 10.1126/science.1112596.

Warren, B. A. (1983). Why is no deep water formed in the North Pacific? *J. Mar. Res.* 41, 327–347. doi: 10.1357/002224083788520207.

Weltje, G. J., and Tjallingii, R. (2008). Calibration of XRF core scanners for quantitative geochemical logging of sediment cores: Theory and application. *Earth Planet. Sci. Lett.* 274, 423–438. doi: 10.1016/j.epsl.2008.07.054.

Yasuda, I., Kouketsu, S., Katsumata, K., Ohiwa, M., Kawasaki, Y., and Kusaka, A. (2002).

Influence of Okhotsk Sea intermediate water on the Oyashio and North Pacific intermediate water. *J. Geophys. Res. Ocean.* 107, 1–11. doi: 10.1029/2001jc001037.

Yasuda, I., Okuda, K., and Shimizu, Y. (1996). Distribution and modification of North Pacific Intermediate Water in the Kuroshio-Oyashio interfrontal zone. *J. Phys. Oceanogr.* 26, 448–465. doi: 10.1175/1520-0485(1996)026<0448:DAMONP>2.0.CO;2.

Yasudomi, Y., Motoyama, I., Oba, T., and Anma, R. (2014). Environmental fluctuations in the northwestern Pacific Ocean during the last interglacial period: Evidence from radiolarian assemblages. *Mar. Micropaleontol.* 108, 1–12. doi: 10.1016/j.marmicro.2014.02.001.

Zweng, M. M., Reagan, J. R., Seidov, D., Boyer, T. P., Antonov, J. I., Locarnini, R. A., et al. (2019). World Ocean Atlas 2018, Volume 2: Salinity. *NOAA Atlas NESDIS* 2, 50.

5. Summary, Conclusion and Outlook

5.1. Summary and Conclusions

This thesis provides insights into the evolution of Pliocene and Pleistocene marine primary productivity, carbonate deposition, upper ocean temperature, salinity, and circulation in the North West Pacific. The new comprehensive geochemical and sedimentological data sets of six sediment cores presented in this thesis contribute to filling the gap in the spatial resolution of sediment archives from the North Pacific and may eventually be part of a new reference transect for this area. This thesis is divided into three scientific chapters, each addressing the respective aspects:

Scientific chapter I concentrates on changes in upper ocean hydrological development of the Northwest Pacific at the northern boundary of the Kuroshio-Oyashio transition zone during the last 650 ka. It reveals that the position of the SAF has not been stable throughout the last 650 ka but changed its position in connection to the strength and position of the Kuroshio Current/Extension as well as the Oyashio/Subarctic Current. For example, the transport of warm tropical water into the Kuroshio-Oyashio transition zone was enhanced during times of very strong La Niña-like conditions in the tropics. This enhancement caused a northward displacement of the SAF to a position north of our study site and thus a relocation of at least 5°, which is reflected by higher SSTs in the time interval 280-600 ka BP. Further, we show that such shifts of the SAF can cause very abrupt temperature changes at the location of core SO264-45, e.g., at 480 and 280 ka BP. On the other hand, an enhancement of the Oyashio Current can prevent the SAF from reaching a position north of our study site even during times of strong and persistent La Niña-like conditions in the tropics, which happened between 480 and 280 ka BP and between ~20 and 5 ka BP. Moreover, we find that glacial-interglacial variations in the Kuroshio-Oyashio transition zone also influenced the SST evolution at our study site. Yet, they are only observed in our data when the SAF was located north of our study site. In contrast to the SST, productivity at this site follows a glacial-interglacial pattern of variability with high values during the deglaciations/early interglacials and low values during glacials. Thus, the relatively small shifts of the SAF did not affect primary productivity. Changes in productivity at the study site were likely linked to glacial/interglacial variations in the subpolar marginal seas and the induced nutrient supply via the subarctic water masses during deglaciations and changes in stratification that controlled nitrate availability and utilization. Further, we show that there is no correlation between changes in productivity and terrestrial input via wind, which implies that dust fertilization did not limit productivity during this time.

Scientific chapter II investigates changes in primary productivity and the carbonate system based on four sediment cores along a transect spanning from the Hess Rise to the subarctic North Pacific over the past 500 ka. It reveals a decreasing gradient in paleo-export production and dust supply (XRF-Fe) from the north (52°N) to the south (37°N). The biogenic Ba concentration records indicate maximum export production during peak interglacials. This pattern was associated with changes in upper ocean stratification and the strength of gyre circulation rather than changes in dust supply. While there is a coherent increase in biogenic Ba, CAR, alkenone concentration, sand%, and opal% during interglacials at the northern sites, a reverse pattern of preserved carbon occurred in the southern records. This documents that the locations of the southern cores, which are also from a greater water depth, were more influenced by carbonate dissolution in connection with changes in deep Pacific carbonate chemistry responding to the global ocean carbonate budget balance than the northern cores. This is further supported by comparable patterns of the abundance of the sand fraction and the CAR resemblance to the LCDW driven carbonate abundance signal.

Scientific chapter III discusses the development of productivity, upper ocean hydrography, and terrestrial dust input in the North Pacific through a late Pliocene late Pleistocene comparison based on two sites. It shows that significantly warmer upper ocean temperatures at the sites in the Pliocene than during the Pleistocene were linked to warmer global temperatures and reduced seasonality rather than a significant northward displacement of the frontal system between the subtropical and subpolar gyre. Nevertheless, there may have been a small northward displacement of the SAF (compared to its modern position) during the Pliocene towards a position between the two study sites. This or a more gradual SST decrease with increasing latitude and thus a less pronounced SAF caused significantly higher SSTs at our northern study site compared to the study site 1° further south. Moreover, we confirm that there was no permanent halocline (at least within the upper ~130 m water depth) throughout the late Pliocene, yet we show that there was a constant thermocline. Further, we show that the intensification of Northern Hemisphere Glaciation at 2.7 Ma coincided with a simultaneous decrease in sub(SST) and productivity as well as an increase in dust input via wind. This reorganization was partly linked to the establishment of a permanent halocline and increased seasonality. The lack of permanent halocline stratification enabled a more effective upwelling of nutrients. It caused significantly higher productivity during the Pliocene than during the Pleistocene, when there was a constant halocline stratification. The increase in wind speed at ~2.7 Ma, however, was associated with a general rise in dust availability in the source regions and an intensification of the westerlies. The contrasting development of dust supply and productivity at our study sites indicates that dust fertilization neither caused the high primary productivity in the study area in the North Pacific during the late Pliocene nor did it limit primary productivity during the late Pleistocene.

5.2. Outlook

The scientific work presented in this thesis only considers snapshots of upper ocean dynamics in the North West Pacific. Many open questions that would be highly interesting to address in future work remain. For some of these open questions, more data would be needed. Yet other questions could already be addressed with the data that were initially collected for this project, which was not possible for various reasons.

The biggest obstacle for the investigations was the development of reliable age models. As discussed in the respective scientific chapters, several sediment cores along the Emperor Seamount chain do not show continuous sedimentation but are disturbed by hiatuses. This led us to abandon some cores for which several attempts of developing an age model with different proxies in collaboration with *MARUM – Center for Marine Environmental Sciences*, the University of Bremen, and the Alfred-Wegner-Institute - Helmholtz Centre for Polar and Marine Research in Bremerhaven were undertaken, yet without providing satisfying results. Further, there are large time gaps in the age models of SO264-45 and -53 because distinct age tie points are missing. Therefore scientific chapter III focuses on two relatively short time intervals of the late Pliocene and the late Pleistocene rather than including the evolution of the upper ocean dynamics during the mid-Pleistocene transition, which would be highly insightful.

An improvement of these age models, especially the exact dating of the start and end points of the hiatuses, e.g., through the use of additional dating techniques, for example, uranium–thorium dating of calcium carbonate (age limit 500 ka) or biostratigraphy could therefore immensely contribute to a more complete record of the sediments. Regarding this, there is promising work currently undertaken by the working group of V. Ponomareva, who is dating tephra layers that may enable future progress on the age models.

With such improvements in the age models, there is much potential for the use of the already partly discussed cores of this thesis. If they are combined, e.g., by a stack or further supported with other cores of cruise SO264, an investigation of the complete evolution of the North Pacific through the mid-Pleistocene transition may be possible. Additionally, the presumed very high age of some records may allow the analysis of changes during the Pliocene in more detail and with more precise knowledge of the timing of certain events.

Yet besides reaching further back in time, an investigation of more cores along the transect between Hess Rise and the subarctic North Pacific may further clarify the extent of shifts in the frontal system as supposed in scientific chapter I. Moreover, in scientific chapter I, it is suggested that changes in Oyashio Current strength contributed to and weakened shifts of the frontal system. Yet, due to the lack of data monitoring the behavior of the Oyashio Current on longer time scales, it is currently not possible to make precise predictions. Thus, a study concentrating on variations of the Oyashio Current strength and spatial variability during the Pleistocene would be insightful. Similarly, information on the variability of the Kuroshio Extension, ideally measured by a combination of proxies in several regions or gained through modeling could help to support the hypothesis of a link between the tropical Pacific (ENSO-related surface temperature gradient) and the frontal system in the Kuroshio-Oyashio transition zone. Regarding this, also changes in the Pacific Decadal Oscillation (PDO) and its influences on the temperature development at our study site, as well as the position of the frontal system, would be interesting to discuss and would contribute to the discussion. Yet studies investigating PDO variability on longer time scales would be needed.

Moreover, the influence of changes in deep-water carbon chemistry is addressed in scientific chapter II. However, an impact on carbon preservation was only observed at two study sites and could not be discussed in detail. It would be interesting to determine more precisely at what depth dissolution takes place along the Emperor Seamount chain and to what extent it influenced the preservation of foraminiferal calcite in shallower water depths. Further, a consideration of the deep water carbon chemistry in the context of glacial-interglacial cycles would be needed. These investigations may help future studies address dissolution impacts more precisely and may make such studies more reliable.

Lastly, the ecology of the foraminiferal species used in this study is essential for interpreting reconstructed SST and subSST. The distribution of foraminifera in the water column, specific depth habitats, and seasonal occurrence significantly influence derived temperature and salinity approximations (see chapter 2.7.1). Several studies have addressed these topics and show that species' behavior can show wide regional variations. Therefore, it is crucial to consider regional investigations, yet up to now there are only few ecological studies regarding foraminiferal species from the North Pacific. Therefore, detailed studies of the ecology of the foraminiferal species used in this study would be highly beneficial.

6. Acknowledgments

During the last four years, I experienced much support and encouragement from colleagues at GEOMAR and AWI. Without you, this work would not have been possible! A big thank you goes out:

- To Dirk, for being my supervisor and first reviewer. With letting me be part of the Sonne-Emperor project, you made it possible for me to join the extraordinary SO264 Expedition that will always stay in my mind as a colorful memory. It was very helpful that you always had an open door, have been there for discussions, and of course, for your scientific expertise. Thank you also for your comments and ideas on my manuscripts; they immensely helped to improve my scientific interpretations and writing.
- To Lester, for being there for (not only) scientific discussions, bringing up new ideas, giving encouragement, and supporting me with my Lab work in Bremerhaven.
- To Martin, for your great personal support and positivity, for keeping track of my overall project, and believing in me. This really kept me motivated.
- To Julia, for fruitful discussions, encouragement, new ideas, and most importantly, for showing me the right direction at a point where I couldn't see the finishing line.
- To Nadine and Sebastian, as well as all Hiwis and interns who were associated with the project, I would not have been able to accomplish such a big data set without your support. Thank you very much for all your work for this project, the general help, and the lovely chats in between. It was a pleasure to work with you.
- To JC, spending endless hours in the lab with you and having fruitful discussions was fun. It was so good to have someone to discuss ongoing work and especially to talk about the things that went wrong or did not make sense at the first site.
- To Kristin and Eleni, for your great support, feedback, new ideas, and encouragement.
- To Meike, for the tremendous support during the final weeks.
- To Martina for being there and guiding me through the administrative jungle. Moreover, the chats with you always reminded me that there is a world outside the institute.
- To All former and current colleagues from GEOMAR who were there for chats, laughs, and lunch breaks at the Schwentine.

PhD life… It is not easy to stay strong and confident when you have to handle drawbacks, when unforeseeable problems hinder you from achieving goals on time, when you get told that your work is not good enough, and you might not achieve what you are aiming for. So you try to work harder, longer hours, cut off holidays, and start to abandon things you love. And even if you allow yourself free time, you get pangs of remorse because you could be working. Just the everyday life of a PhD student. Yet everyone needs time to recharge. And confidence can't grow just from within. Thus, the greatest thanks goes to all the people who kept me sane and happy during these years and reminded me that regardless of what happens at work, life is worth enjoying. That really meant a lot to me and supported me way more than you might think. Thank you: Ute, Rainer, Janine, Kirsten, Moritz, Benji, Bengt, Carlotta, Max, Friedrich; Svantje, Lisa D., Ellen, Mareike F., Maike, Merle; Jana, Lilli, Juliane,; Mareike K., Steffen, Lisa B., Felix, Sarina, Jacky, Peer, Nina, Edel, Timo, Luisa, Thore, Edel, Tjördis and Mäli. Thank you very much Eva and Neele!